

The Hydro–Support:
An Elasto–Hydrostatic Thrust Bearing
with
Mixed Lubrication

Ron van Ostayen

The Hydro–Support: An Elasto–Hydrostatic Thrust Bearing with Mixed Lubrication

PROEFSCHRIFT

ter verkrijging van de graad van doctor
aan de Technische Universiteit Delft,
op gezag van de Rector Magnificus prof. dr. ir. J.T. Fokkema,
voorzitter van het College voor Promoties,
in het openbaar te verdedigen op maandag 16 december, 2002 om 13:30 uur
door

Ronald Adrianus Johannes VAN OSTAYEN

werktuigkundig ingenieur
geboren te Roosendaal

Dit proefschrift is goedgekeurd door de promotor:

Prof. dr. ir. D.J. Rixen

Toegevoegd promotor:

Dr. ir. A. van Beek

Samenstelling promotiecommissie:

Rector Magnificus,	voorzitter
Prof. dr. ir. D.J. Rixen,	Technische Universiteit Delft, promotor
Dr. ir. A. van Beek,	Technische Universiteit Delft, toegevoegd promotor
Prof. dr. ir. P. de Baets,	Universiteit van Gent, België
Prof. dr. ir. J. Blaauwendraad,	Technische Universiteit Delft
Prof. dr. ir. M.J.W. Schouten,	Technische Universiteit Eindhoven
Prof. dr. ir. K. van der Werff,	Technische Universiteit Delft
Dr. ir. G.J.J. van Heijningen,	vml. Technische Universiteit Delft (1996)
Prof. ir. J. Klein Woud,	Technische Universiteit Delft, reservelid

Title: The Hydro-Support: An Elasto-Hydrostatic Thrust Bearing with Mixed Lubrication
Author: van Ostayen, R.A.J.
Subject headings: Elasto-hydrostatic lubrication, mixed lubrication, bearing design, numerical modelling, finite element method
Copyright: R.A.J. van Ostayen, Roosendaal, the Netherlands, 2002
Print: Ponsen & Looijen BV, Wageningen
ISBN: 90-370-0204-8

aan mijn ouders

The 'classic' solution for the support of a translating lock-gate, the wheel-on-rail support, has relatively high construction as well as inspection and maintenance costs. An alternative support which has previously been developed for use in the Prins Willem-Alexander lock is the so-called 'hydro-support', a hydrostatic thrust bearing that slides on an elastic track and is connected to the lock-gate by an elastic support. After a running-in period, this support shows low friction.

In this thesis several methods to further improve this type of support have been studied. The direction of these improvements has been guided by the following observation: The typical dimensions and manufacturing standards of the bearing and the track are in conflict. On the large scale of a lock-gate, a hydrostatic bearing typically requires sliding surfaces with a surface waviness smaller than 0.1 mm/m. However, the track can not be manufactured easily with a surface waviness smaller than typically 0.5 mm/m. This means that contact between the bearing and track will be inevitable. In this thesis, methods have been studied to use this contact in order to improve the performance (namely reduced flow rate and pumping power) of the hydro-support.

A mathematical model has been developed, incorporating the elastic deformation of the track, bearing and support, and the partial contact and hydrostatic lubricating film between the bearing and track. Several track waviness models have been developed, among others a random periodic surface waviness. Furthermore the concept of an 'ideal' support has been introduced, which under compression exhibits a reaction pressure equal to the hydrostatic pressure in a lubricating film with a constant height.

Not only has this mathematical model been developed in this thesis, it has also been implemented in a numerical program and used to test the influence of a number of design parameters on the performance of a hydro-support. It has been shown that, using the contact between the sliding surfaces, the tilting stiffness of a bearing with 1 small recess is comparable to that of the 4-recess bearing. Additionally, a 1 recess bearing requires a smaller or even no restrictor and therefore a smaller supply pump.

Furthermore, it has been shown that the hydro-fender with its large length/width ratio has comparable or even better performance than the circular hydro-foot, while requiring a narrower track.

In addition, it has been shown that, for a given load, a hydro-fender with a small bearing thickness and with a standard elastic support design exhibits a smaller flow rate and larger bearing coefficient than a bearing with an ideal support design.

Finally, using the results of these parametric studies, a procedure has been developed for the design of hydro-supports. This procedure has been used in two examples.

De 'klassieke' oplossing voor de geleiding van een translerende sluisdeur, de wiel op rail geleiding, heeft relatief hoge constructiekosten en inspectie- en onderhoudskosten. Een alternatieve geleiding, die eerder ontwikkeld werd voor gebruik in de Prins Willem-Alexandersluis, is de zogenaamde 'hydro-geleiding', een hydrostatisch druklager dat over een elastische glijbaan glijdt en verbonden is aan de sluisdeur door een elastische oplegging. Na een inlooperperiode heeft deze geleiding een lage wrijving.

In dit proefschrift zijn verschillende methoden om deze geleiding verder te verbeteren bestudeerd. De richting van deze verbeteringen is gestuurd door de volgende observatie: De typische afmetingen en fabricagetechnieken van het lager en de glijbaan zijn in conflict. Indien toegepast in een sluis, vereist het hydrostatisch lager typisch loopvlakken met een oppervlakte golving die geringer is dan 0.1 mm/m. Echter, het is niet eenvoudig de glijbaan te maken met een oppervlakte golving die geringer is dan 0.5 mm/m. Dit betekent dat contact tussen het lager en de glijbaan onvermijdelijk zal zijn. In dit proefschrift zijn methoden bestudeerd om dit contact te gebruiken en zo de eigenschappen en prestaties van de hydro-geleiding te verbeteren (verminderde volumestroom en pompvermogen).

Een wiskundig model is ontwikkeld waarin de elastische vervorming van de glijbaan, lager en oplegging, en het partiële contact en de hydrostatische smeerfilm tussen het lager en de glijbaan, zijn opgenomen. Verscheidene glijbaan onvlakheidsmodellen zijn ontwikkeld, waaronder een random, periodieke oppervlakte onvlakheid. Verder is het concept van de 'ideale' oplegging geïntroduceerd, die als gevolg van een uniforme indrukking een reactiedruk heeft die gelijk is aan de hydrostatische druk in een smeerfilm met een constante hoogte.

In dit proefschrift is dit wiskundig model niet alleen ontwikkeld, maar ook geïmplementeerd in een numeriek programma dat gebruikt is om de invloed van verschillende onwerpparameters op de eigenschappen van de hydro-geleiding te bestuderen. Het is aangetoond dat, gebruik makend van het contact tussen de loopvlakken, de kantelstijfheid van een lager met 1 kamer vergelijkbaar is aan die van een 4-kamer lager.

Daarnaast heeft een 1-kamer lager een kleinere of zelfs geen restrictor nodig en kan daardoor volstaan worden met een kleinere voedingspomp.

Ook is aangetoond dat de hydro-fender met zijn grotere lengte/breedte verhouding, vergelijkbare of zelfs betere prestaties vertoont dan de hydro-voet, terwijl volstaan kan worden met een smallere glijbaan.

Verder wordt getoond dat, bij een gegeven belasting, een hydro-fender met een dunner lager en een standaard elastische oplegging een lagere volumestroom en een hogere lagercoëfficiënt heeft dan hetzelfde lager met een 'ideale' oplegging.

Tot slot is, gebruik makend van de resultaten van het parameteronderzoek, een procedure ontwikkeld voor het ontwerp van hydro-geleidingen. Ter illustratie is deze procedure in twee voorbeelden gebruikt.

Abstract		vii
Samenvatting		ix
Contents		xi
List of Symbols		xv
1 Introduction		1
1.1 Reading guide to this thesis		5
2 The Prins Willem–Alexander lock		7
2.1 The hydrostatic bearing		9
2.2 The rubber support		11
2.3 The track		12
2.4 Friction measurements in situ		12
3 Introduction to the model development		15
4 Hydro–support with rigid surfaces		19
4.1 1-Recess hydro–foot		19
4.1.1 Parallel pad coefficients		21
4.1.2 Tilted pad coefficients		23

CONTENTS

4.2	1-Recess hydro-fender	26
4.2.1	Parallel pad coefficients (infinite fender)	27
4.2.2	Parallel pad coefficients (finite fender)	29
4.2.3	Tilted pad coefficients	34
4.3	Properties of the hydro-support including supply	44
5	Track deformation and surface description	49
5.1	Track deformation	50
5.2	Track surface description	54
5.3	Surface roughness description	60
5.4	Conclusion	62
6	Mixed lubrication	63
6.1	Nominal and effective film height	65
6.2	Local contact area fraction \bar{a}_c	67
6.3	Reduced contact pressure \bar{p}_c	71
6.4	Coefficient of friction c_f	73
6.5	Conclusion	74
7	Full film lubrication	75
8	Bearing deformation	83
9	Rubber support	89
9.1	3D deformation	91
9.1.1	Hydro-foot	91
9.1.2	Hydro-fender	95
9.2	Constant pressure approximation	98
9.2.1	Hydro-foot	99
9.2.2	Hydro-fender	104
9.3	Support shape optimization	104
9.3.1	Reduction of peak stresses	107
9.3.2	Optimization of normal stresses	109
9.4	Conclusion	110

10	Experimental data	111
10.1	Hydro-foot data	111
10.2	Hydro-fender data	113
10.2.1	10:1 length/width ratio fender	113
10.2.2	2:1 length/width ratio fender	117
11	Introduction to the numerical study	119
12	Iterative numerical procedure	123
12.1	Support pressure calculation	124
12.2	Displacements and contact pressure calculation	125
12.3	Coupled solution	128
12.4	Height step procedure	130
13	Introduction to the parameter study	133
13.1	Reference fender geometry	134
14	Bearing geometry	141
14.1	Bearing length/width ratio	141
14.2	Bearing thickness	141
14.3	Constant load, variable bearing length/width ratio and recess pressure .	148
15	Recess geometry	153
15.1	Number of recesses	153
15.2	Recess width	158
15.3	Recess pressure	158
16	Track parameters	165
16.1	Surface waviness	165
16.1.1	Fender position on track	165
16.1.2	Different random track surfaces	167
16.1.3	Waviness amplitude	169
16.2	Track thickness	169

CONTENTS

17 'Ideal' support	175
17.1 Support type: solid or 'ideal'	175
18 Parameter study summary	179
19 Design tools	181
19.1 Example I: PWA-lock	184
19.2 Example II: west lock Terneuzen	185
20 Conclusion	187
20.1 Recommendations for further research	188
A Operation point, material properties and dimensions of the PWA-lock hydrofoot	191
B Bearing attitude	193
C Thermal effects	195
C.1 Heat transfer coefficient	196
C.2 Model I: Adiabatic track model	198
C.3 Model II: Flash temperature model	200
C.4 Model III: Dutch Department of Public Works model	202
C.5 Model IV: Modified Dutch Department of Public Works model	204
C.6 Conclusion	205
D Matrices for the Lee–Ren contact model	207
Bibliography	209
Acknowledgements	225
Curriculum Vitae	227

LIST OF SYMBOLS

A	surface area	$[m^2]$
A_c	contact area	$[m^2]$
\bar{A}_c	non-dimensional contact area	$[-]$
\bar{a}_c	local contact area	$[-]$
A_e	effective bearing surface area	$[m^2]$
A_{eI}, A_{eII}	effective area of parts I and II	$[m^2]$
\bar{A}_e	non-dimensional effective bearing surface area	$[-]$
$[A_i]$	contact area matrix	$[-]$
a_{mn}	amplitude of surface wave mn	$[m]$
a_s	support edge shape parameter	$[-]$
a_x, a_y, a_z	distance between load vector and bearing rotation center	$[m]$
B	bearing width	$[m]$
B_s	support width	$[m]$
b	recess width	$[m]$
c	specific heat capacity	$[J/kgK]$
c_b	bearing coefficient	$[-]$
c_f	coefficient of friction	$[-]$
C	heat transfer coefficient parameter	$[-]$
D	plate constant	$[Nm]$
D	bearing diameter	$[m]$
d	recess diameter	$[m]$
D_s	support diameter	$[m]$
d_s	support recess diameter	$[m]$
E'	reduced modulus of elasticity	$[N/m^2]$
E_b, E_t, E_s	Young's modulus of elasticity (bearing, track, support)	$[N/m^2]$
E_t^*	track elasticity constant	$[N/m^3]$
\bar{E}_t	effective track modulus of elasticity	$[-]$

LIST OF SYMBOLS

E_a, E_b	modulus of elasticity of contacting materials a and b	$[N/m^2]$
e	compression of the support	$[m]$
F	friction force	$[N]$
F_c, F_h	friction force (contact, hydrostatic)	$[N]$
$[G_i]$	true film height matrix	$[-]$
G_s	support shear modulus	$[N/m^2]$
H	power dissipation	$[W]$
H	surface hardness	$[N/m^2]$
\vec{H}	surface hardness vector	$[N/m^2]$
\mathcal{H}	non-dimensional hardness number	$[-]$
h	nominal film height	$[m]$
h_c	center film height	$[m]$
h_{eff}	effective film height	$[m]$
h_r	recess height	$[m]$
h_0	reference film height	$[m]$
h_{PWA}	typical measured track surface waviness	$[m]$
h_{old}	nominal film height in previous iteration	$[m]$
h_s	track waviness step height	$[m]$
h_t	effective film height	$[m]$
h_{wav}	track surface waviness	$[m]$
k_{sx}, k_{sy}	support tilting stiffness	$[Nm/rad]$
K	heat transfer coefficient parameter	$[-]$
$K_t(x, y)$	kernel deformation function	$[m/N]$
L	bearing length	$[m]$
L_x, L_y	roughness/waviness evaluation lengths in x and y direction	$[m]$
M	number of wave components in x-direction	$[-]$
M_{Fx}, M_{Fy}	tilting moment due to friction	$[Nm]$
M_{sx}, M_{sy}	support tilting moment	$[Nm]$
$\overline{M}_x, \overline{M}_y$	tilting moment	$[Nm]$
\overline{M}	non-dimensional tilting moment	$[-]$
N	number of wave components in y-direction	$[-]$
n	heat transfer coefficient parameter	$[-]$
O	bearing circumference	$[m]$
P	power surface roughness	$[m^3]$
p	(effective) pressure	$[N/m^2]$
\bar{p}	non-dimensional pressure	$[-]$
\mathcal{P}_c	non-dimensional pressure number	$[-]$
p_c	average pressure increase due to contact	$[N/m^2]$
\bar{p}_c	reduced contact pressure increase due to contact	$[-]$
p_c^*	average contact pressure	$[N/m^2]$
p_h	hydro-dynamic/static pressure	$[N/m^2]$
\bar{p}_h	non-dimensional hydro-dynamic/static pressure	$[-]$

p_{old}	effective pressure in previous iteration	$[N/m^2]$
p_r	recess pressure	$[N/m^2]$
p_{sup}	supply pressure	$[N/m^2]$
Q	flow rate	$[m^3/s]$
\overline{Q}	non-dimensional flow rate	$[-]$
Q_I, Q_{II}	flow rate from parts I and II	$[N]$
Q	heat flow rate	$[W]$
Q_0	reference flow rate	$[m^3/s]$
q_r	radial flow rate per unit width	$[m^3/ms]$
q_x, q_y	flow rate per unit width in x- and y-direction	$[m^2/s]$
r	radial coordinate	$[m]$
R^*	radius of curvature of surface asperities	$[m]$
\overline{R}_h	non-dimensional hydraulic resistance lubricating film	$[-]$
R_q	RMS profile roughness	$[m]$
R_r	hydraulic resistance restrictor	$[m^5/Ns]$
\overline{R}_s	non-dimensional support recess radius	$[-]$
S	support slenderness parameter	$[-]$
S	surface auto-covariance function	$[m^2]$
S_{q_a}, S_{q_b}	surface roughness of contacting surfaces a and b	$[m]$
S_q	(combined) RMS surface roughness	$[m]$
T	temperature	$[K]$
T_a	ambient temperature	$[K]$
T_L	temperature at end of track	$[K]$
T_{max}	maximum temperature	$[K]$
t_b, t_t, t_s	height (bearing, track, support)	$[m]$
t_c	contact distance	$[m]$
U	bearing velocity	$[m/s]$
U_a, U_b	velocity of surfaces a and b	$[m/s]$
u_a, u_b	vertical displacement of surfaces a and b	$[m]$
u_b, u_t	deformation (bearing, track)	$[m]$
u_g	gate displacement	$[m]$
W	load	$[N]$
W_I, W_{II}	load on parts I and II	$[N]$
W_0	reference load	$[N]$
W_c	contact load	$[N]$
\overline{W}_c	non-dimensional contact load	$[-]$
W_h	hydrostatic load	$[N]$
W_s	support load	$[N]$
x	coordinate along the track	$[m]$
\overline{x}	non-dimensional coordinate along the track	$[-]$
x_s	track waviness step position	$[m]$
y	coordinate transverse to the track	$[m]$
\overline{y}	non-dimensional coordinate transverse to the track	$[-]$

LIST OF SYMBOLS

z	coordinate perpendicular to the track	[m]
\bar{z}	non-dimensional coordinate perpendicular to the track	[-]
z_b, z_t	surface position (bearing, track)	[m]
z_a, z_b	initial position of contacting surfaces a and b	[m]

Greek symbols

α	heat transfer coefficient	[W/m ² K]
$\alpha, \alpha_x, \alpha_y$	bearing tilting angle	[rad]
α_{x0}, α_{y0}	support top surface tilting angle	[rad]
$\bar{\alpha}$	non-dimensional bearing tilting angle	[-]
β	pressure ratio	[-]
β	auto-correlation length	[m]
β	thermal expansion coefficient	[1/K]
β_0	reference pressure ratio	[-]
ϵ	relative error	[-]
ϵ_{\max}	maximum relative error	[-]
ϵ_H	relative error in nominal film height	[-]
ϵ_P	relative error in effective pressure	[-]
ϵ	strain	[-]
ϵ	non-dimensional compression	[-]
ϵ_x, ϵ_y	relative excentricity load	[-]
η	viscosity	[Ns/m ²]
Γ	non-dimensional power dissipation number	[-]
γ	amplitude surface wave attenuation factor	[-]
γ	asperity aspect ratio	[-]
$\vec{\gamma}_A$	asperity aspect ratio vector for contact area	[-]
$\vec{\gamma}_G$	asperity aspect ratio vector for true film height	[-]
ϕ_{xmn}, ϕ_{ymn}	phase shift surface wave mn in x- and y-direction	[-]
$\lambda, \lambda_x, \lambda_y$	surface roughness/waviness wave length	[m]
λ_x, λ_y	modified auto-correlation length	[m]
λ	heat conduction coefficient	[W/mK]
Λ	film thickness number	[-]
ν_a, ν_b	Poisson ratio of contacting materials a and b	[-]
ν_b, ν_t, ν_s	Poisson ratio (bearing, track, support)	[-]
ω_H	underrelaxation factor for nominal film height iteration	[-]
ω_P	underrelaxation factor for effective pressure iteration	[-]
$\Phi(z)$	complement of the cumulative probability distribution function	[m ²]
ϕ	angle	[rad]
$\phi(z)$	roughness height distribution function	[m]
ϕ_f	shear term correction factor	[-]
ϕ_{fp}	pressure term correction factor	[-]

ϕ_{fs}	shear term correction factor	[-]
ϕ_{px}, ϕ_{py}	pressure term correction factor	[-]
ϕ_s	shear term correction factor	[-]
Φ_s	shear term correction factor function	[-]
ψ	plasticity index (Williamson)	[-]
ψ^*	plasticity index (Greenwood–Williamson)	[-]
ψ_p	polymer plasticity index	[-]
ρ	mass density	$[kg/m^3]$
$\rho(x)$	roughness autocorrelation function	$[m]$
σ	stress	$[N/m^2]$
$\bar{\sigma}$	non-dimensional stress	[-]
$\tilde{\sigma}$	scaled stress	[-]
σ_y	yield stress	$[N/m^2]$
σ_r	reference stress	$[N/m^2]$
$\sigma_{xx}, \sigma_{zz}, \sigma_{xz}$	stress components (cartesian)	$[N/m^2]$
$\bar{\sigma}_{xx}, \bar{\sigma}_{zz}, \bar{\sigma}_{xz}$	non-dimensional stress components (cartesian)	[-]
$\sigma_{rr}, \sigma_{zz}, \sigma_{rz}$	stress components (cylindrical)	$[N/m^2]$
$\bar{\sigma}_{rr}, \bar{\sigma}_{zz}, \bar{\sigma}_{rz}$	non-dimensional stress components (cylindrical)	[-]
τ	time	$[s]$
τ_b	summed loading time	$[s]$
τ_c	temperature time constant	$[s]$
τ_L	total sliding time	$[s]$
τ_r	reference time	$[s]$
τ_x, τ_y	shear stress in x- and y-direction	$[N/m^2]$

Dimensionless Groups

Gr	Grasshof number	$[\frac{g\beta\rho^2\Delta TD^3}{\eta^2}]$
Nu	Nusselt number	$[\frac{\alpha D}{\lambda}]$
Pr	Prandtl number	$[\frac{\eta c}{\lambda}]$
Re	Reynolds number	$[\frac{\rho UD}{\eta}]$

CHAPTER 1

Introduction

Navigation locks are used to transport ships across height differences in water ways. A basic navigation lock consists of a lock-chamber closed by two lock-gates. Frequently, particularly in larger locks, rolling lock-gates are used to close the lock-chamber. These gates are supported by a wheel-on-rails support and, when opening, ride sideways along these rails into an alcove in the side of the lock-chamber. The wheel-on-rail support has several drawbacks:

- Rolling gates are heavy and even with the weight of the gate distributed on a large number of wheels, the wheels are usually highly loaded;
- In order to distribute the total weight evenly on the wheels, a load distribution mechanism (bogie system) is employed. As a result, the support exposes many moving parts (wheels, bearings, load distribution mechanism) to a corrosive environment, namely (salt) water.
- Furthermore the positioning of the support under water results in high inspection and maintenance costs (table 1.1).

The Civil Engineering Division of the Dutch Directorate-General of Public Works and Water Management initiated a study into the possibilities to reduce the maintenance costs and down-time and improve the performance and life span of the lock-gate support. The three primary methods to achieve this goal are:

- The reduction of the contact pressure between the moving parts by using the maximum of the available surface area;
- The reduction of the number of moving parts, particularly under water;

Table 1.1: Maintenance costs per rolling door per year in k€ (data: Dutch Directorate-General of Public Works and Water Management).

<i>Once every 8 years, gate maintenance:</i>	
Renewal of shafts and seals	46
Replacing bearings	52
Protection carriage, replacing zinc anodes	9
Partition chamber and dry gate	36
Overhaul hydraulic cylinders	24
Overhaul hydraulic system	36
Removing and replacing gate	
(Total 160 k€, attribute 75% of this sum to gate protection, and 25% to support gate maintenance:)	40
Total (every 8 years)	243
Total (per year)	30.3
<i>Once every 30 years, replacement of the gate support:</i>	
Replacing wheels	364
Replacing rails	91
Total (every 30 years)	455
Total (per year)	15.2
Total per gate per year	45.5

- Providing access to the lock-gate support without completely removing the lock-gate.

In order to meet these goals an alternative lock-gate support method has been developed: A water lubricated, hydrostatic thrust bearing sliding on a track, the so-named 'hydro-support'. If this hydrostatic bearing has a length/width ratio close to 1, it is called 'hydro-foot'. A bearing with a length/width ratio much larger than 1 is called 'hydro-fender'. Using a supply pump, water is pumped under high pressure between the bearing and the track, thereby lifting the bearing (and thus the lock-gate) on a thin film of water, enabling the lock-gate to slide with very little friction on the track. Figure 1.1 is a schematic view of a navigation lock where the rolling supports of the lock-gates have been replaced by hydro-feet.

In order to allow tilting of the lock-gate relative to the track, the hydro-support is connected to the lock-gate using a flexible rubber hinge. This tilting can be caused by water currents (e.g. due to the tide) or by misalignment of the track with respect to the lock-gate. The materials of the track and the hydro-support have been selected in order to provide the best tribological performance (low friction, low wear).

A number of studies have been performed in corporation between the Laboratory of Tribology of the University of Technology Delft and the Dutch Directorate-General

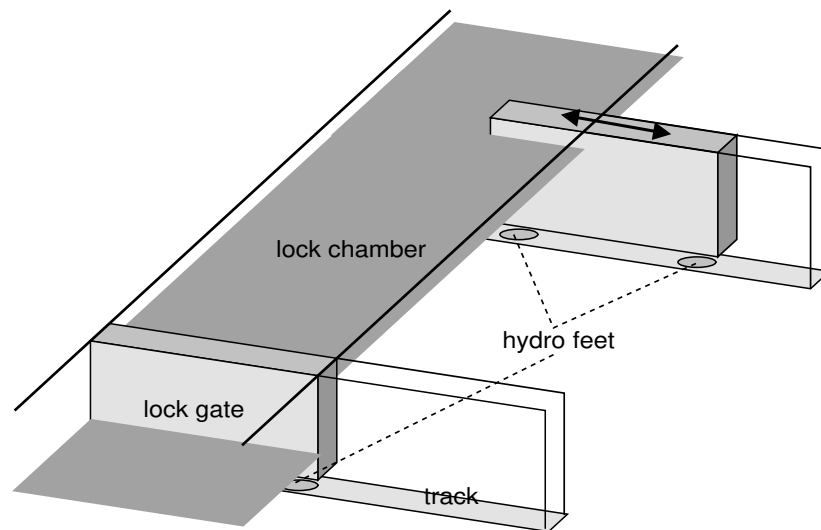


Figure 1.1: Schematic view of a lock with gates supported by hydro-feet on tracks.

of Public Works and Water Management, Civil Engineering Division which has also financed these studies.

In some preliminary publications the possibility of the replacement of the rolling support by the hydro-support has been suggested (Ros, 1987a) and the first test results have been studied (Ros, 1993a,b). Then, during the research project 'Glijdeur' (Sliding door) (VAN BEEK AND DAANE, 1995; VAN HEIJNINGEN, 1991) the application of the hydro-foot in substitution for the rolling support has been studied further. The result of this research was the application of a 4-recess hydro-foot in the new Prins Willem-Alexander lock (PWA-lock) which was put into use in 1995 in the 'Oranje' lock complex near Amsterdam (REINSHAGEN, 1991; VAN TOL, 1992). The use of the hydro-feet addresses the first two of the drawbacks to the traditional rolling support that were mentioned previously, namely the high surface pressure and the large number of moving parts under water. The third drawback, the high inspection and maintenance costs, has been addressed in the construction of the PWA-lock by mounting the hydro-feet on a separate part of the lock-gate. This part can be removed from the lock-gate without lifting the lock-gate as a whole. In the next chapter, the hydro-feet as used in the PWA-lock are studied in more detail. The theory used in the design of this hydro-foot was based on the assumptions that both track and bearing are perfectly plane and rigid and that contact between bearing and track does not occur.

The elastic deformation of the hydro-foot and hydro-fender as a result of the hydrostatic pressure was studied in the research project 'Hydrofilm', the PhD-research of van Beek (VAN BEEK, 1995). In this study it has been suggested that the contact between a flexible bearing and track can be used to improve the performance of the bearing without greatly increasing the friction force as a result of this contact.

After the hydro-foot was put into use in the PWA-lock, measurements showed that, as had actually been expected in the design stage, there is always some contact between the bearing and the track. In fact, due to the large track surface waviness and the thin lubricating water film, partial contact between the bearing and the track is inevitable. This aspect has been taken into account in the present research project 'HydroContact' (Ros, 1996). As the name of this project 'HydroContact' indicates, the inevitable occurring contact between the bearing and the track is taken into account and, if possible, is used to improve the performance of the lock-gate support. In the present research a number of possibilities to improve and simplify the design of the hydro-foot are studied:

- The 1-recess bearing. The hydro-feet in the PWA-lock have 4 recesses (sometimes called chambers) to which the water is supplied (see also the next chapter). From these recesses the water flows through the lubricating film to the water surrounding the bearing. In chapters 4 and 15 the properties of hydrostatic bearings with recesses are studied in more detail. In summary: The load capacity of a hydrostatic bearing increases with an increased total recess area, and the use of more recesses, each separately supplied with water, increases the tilting stiffness of the bearing.

In the 1-recess bearing obviously only 1 recess needs to be supplied with water. The hydraulic installation is therefore much more simple than that for the 4-recess bearing. If the supply pump characteristic is chosen carefully, the use of the supply restrictor can be dropped and the pump can be connected to the recess directly. This in turn enables the use of a pump with a lower output pressure because of the fact that the pressure drop across the restrictor is no longer present.

- The no-recess bearing. The deformation of the elastic track as a result of the hydrostatic pressure is sufficient to form a pseudo-recess in the track. This recess is therefore not constructed in the bearing but is formed during operation under the bearing in the track. Due to this deformation it is expected that the contribution of the contact forces between the bearing and the track to the total load will reduce. This contribution is expressed in the contact force ratio. The contact force ratio is defined as the fraction of the total load on the bearing which is carried by contact between the bearing and the track. The bearing coefficient which is approximately directly proportional to the contact force ratio, will also become smaller. The bearing coefficient is defined as the ratio between the total friction force (both contact and hydrodynamic) and the total load on the bearing. The no-recess bearing also has a larger surface which could potentially improve the hydrodynamic load carrying capability, that is the load carrying capability which results from the pressure rise in the water film as a result of the velocity difference between the bearing and the track.

Furthermore, the forming of the pseudo-recess in the track as a result of the hydrostatic pressure will also result in a better start-up performance of the bearing.

When the lock-gate has moved to one of its end positions (gate completely closed or open) the water supply is stopped and the remaining water in the water film will be forced out and the contact between the bearing and the track will reach a maximum. After a restart of the hydraulic installation, the pressure in the (small) recess will rise and the track will indent. As a consequence the recess will grow, the hydrostatic pressure will be applied to a larger area, the track will deform some more, the recess will grow some more, etcetera. This process will continue until the recess area and hydrostatic pressure are large enough to carry most of the load and the bearing will lift from the track.

- The elastic bearing. The bearing of the PWA-lock is made of steel and has a thickness of 120 mm. This bearing will barely deform due to the occurring contact or the hydrostatic pressure. A thinner bearing will deform more and possibly follow the waviness of the track better, resulting in a smaller contact force ratio and a reduced total flow.
- Other bearing geometries. In stead of a circular hydro-support (the so-called hydro-foot) as was used in the PWA-lock, a bearing with a larger length/width ratio can be used (the hydro-fender). The slender shape of the bearing enables the use of a smaller track. The hydro-fender can also be used to support a moving lock-gate against the horizontal load of the fall, waves and wind. In this case the hydro-fender is part of the horizontal seal of the lock-gate. Other applications are the support of ship lifts, harbor cranes and movable bridges.

1.1 Reading guide to this thesis

In chapters 3 to 9 a mathematical model is developed describing the behavior of an elastic, axial thrust bearing sliding on an elastic track. This bearing is connected to the lock-gate by an elastic support. Contact between the non-smooth track and the bearing will occur and is taken into account.

In chapter 10 some experiments with hydro-support are presented. The results will be used to make some (mainly qualitative) observations on the properties of hydro-supports.

In chapters 11 and 12 a computer program is developed which is used to calculate the properties and behavior of such a bearing. Particularly the development of a stable and converging algorithm is described in this part.

In chapters 13 to 18 the program developed in the previous part, is used to calculate the properties of the hydro-foot and the hydro-fender. The influence of several parameters is studied.

In chapters 19 and 20 the results from the previous part are used to derive design guides, graphs and formulas which can be used to design a hydro-foot or hydro-

CHAPTER 1. INTRODUCTION

fender for a given application. Furthermore the conclusions and recommendations for further research are presented in this part.

CHAPTER 2

The Prins Willem–Alexander lock

The port of Amsterdam is connected to the North Sea by a 36.8 km long canal, the North Sea Canal. In order to maintain a constant water level and to reduce the influence of the tide in this canal, it is closed at both ends by a lock complex, the North Sea Lock Complex near IJmuiden and the Oranje Lock Complex (figure 2.1) at Schellingwoude near Amsterdam.

In order to deal with the increase in shipping, the PWA-lock has been added to the complex and put into use in March 1995. This new lock has a length of 200 m, an effective width of 24.10 m and the depth is approximately equal to 4.70 m depending on the water level.



Figure 2.1: Aerial view of the Oranje Lock Complex. In the foreground the new PWA-lock can be seen.

In order to close the lock, two gates move from bays in the side of the lock into the lock itself (figure 2.2). The classic method to support this kind of lock gate is to use a wheel-on-rail support. In the PWA-lock, for the first time in the world, self

correcting so-called ‘hydro-feet’ have been designed and used to support the lock gates. ‘Hydro-foot’ is the name given to the type of hydrostatic bearing used in this lock gate: A flexible circular hydrostatic bearing connected to the lock gate by a highly elastic rubber support and sliding on a track made from a synthetic material. ‘Hydro-fender’ is the name given to a similar bearing but with a (much) more slender shape.



Figure 2.2: Placing of a lock-gate in the PWA-lock.

In case of the PWA-lock, the bearing is made from stainless steel and the track from Ultra High Molecular Weight Poly Ethylene (UHMWPE). This material combination has been selected because of the excellent friction and wear characteristics. A ‘reversed’ material combination (UHMWPE bearing and stainless steel track) would have increased the elasticity of the bearing and rubber support combination considerably, and therefore increase the capability of the bearing to follow surface waviness. However, there are several reasons not to use this ‘reversed’ material combination:

- The use of a stainless steel track would increase the possibility of galvanic corrosion considerably, because of the large stainless steel surface area exposed to (salt) water on a steel reinforced concrete foundation.
- In case of an accidentally damaged track surface (pits and grooves due to dropped anchors, rocks, etc.), this damage would in term damage and cause wear to the UHMWPE bearing on each passage.
- In contrast, if an UHMWPE track is used, surface waviness and damages are slowly removed by the repeated passage of the stainless steel bearing.

The lock gate is supported by two hydro-feet each at one end of the gate (figure 2.3). These hydro-feet can be removed for inspection and maintenance without lifting the gate as a whole. The gate is then supported by two fixed feet.



Figure 2.3: Bottom of the lock-gate. The hydro-foot and the fixed foot closest to the camera are clearly visible.

The dry weight of the door is equal to 1800 kN, and when placed in the water it is, depending on the water level, approximately 500 kN. Assuming an equal distribution of the weight on both hydro-feet, the load on each hydro-foot is therefore equal to 250 kN. The nominal velocity with which the gates are opened and closed is equal to 0.24 m/s. Pertinent dimensions, material properties and operating conditions of the PWA-lock have been collected in appendix A.

The following parts of the lock gate support are described in more detail:

- The hydrostatic bearing
- The rubber support
- The track

2.1 The hydrostatic bearing

The hydro-static bearings under the lock-gate are required to carry the weight of the submerged lock-gate with preferably as little contact between the bearing and the

track as possible. The lock–gate has some leeway in its alcove and can therefore tilt relative to the track. This tilt can be caused by the water current in the lock, or by height differences between the water levels inside and outside the lock. (Note, that although strictly speaking different water levels should only occur when the gates are closed, it is common practise to open a lock–gate when there is still a water level difference between the inside and outside of the lock.) The tilt of the lock–gate is partly accommodated to by the rubber support and partly by the lubricating film between the bearing and the track. In order to ensure that most of this tilt is accommodated to by the rubber support it is necessary that the tilting stiffness of the lubricating film is much larger than that of the rubber support.

The hydro–foot as used in the PWA–lock is a 4-recess hydrostatic bearing with a supply pump supplying each of the recesses with water through an orifice restrictor (figure 2.4). The 4-recess bearing was selected because of the higher expected tilting stiffness compared to that of an 1-recess bearing. A disadvantage of the 4-recess bearing is the fact that either 4 restrictors or 4 separate supply pumps are required.

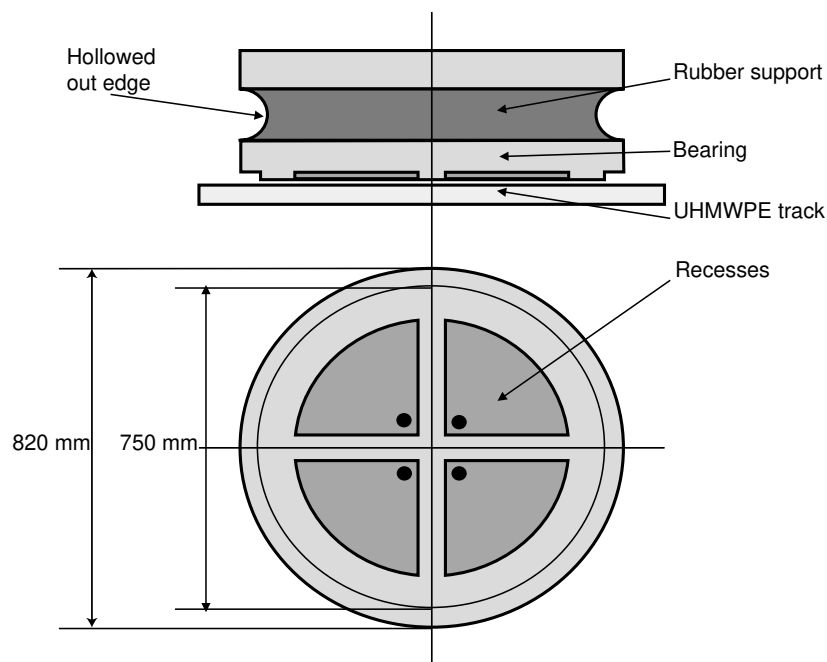


Figure 2.4: Hydro–foot used in the PWA–lock. The hydro–foot consists of a steel sole with four recesses and supply holes and is supported by a rubber ring. The hydro–foot slides on a UHMWPE track.

The nominal film height is 0.1 mm, the nominal load for each hydro–foot 250 kN. The nominal supply pressure p_{sup} supplied by the pump is equal to $20 \cdot 10^5 \text{N/m}^2$. The hydraulic resistance R_r of the restrictor is selected as to ensure a nominal recess–supply pressure ratio β of 0.4. The volumetric flow rate Q for each bearing is approximately equal to $10 \text{ m}^3/\text{h}$. The design of the hydro–feet and hydraulic installation is described

in VAN HEIJNINGEN (1991). This design is based on calculations where a full lubricating film was assumed (no contact) and the bearing and the track were assumed to be rigid.



Figure 2.5: Testing of the hydro-foot. These tests have been carried out above water and the water supplied to the bearing can be seen squirting out.

2.2 The rubber support

The bearing is elastically connected to the lock gate using a rubber support. This support is a ring with an external diameter of 820 mm, an internal diameter of 290 mm and a height of 80 mm. In order to prevent high edge stresses the internal and external surfaces of the ring are hollowed out (see figure 2.4). The support is ring shaped due to the fact that water has to be supplied to the bearing. This water is supplied through pipes that run through the hollow center of the support.

The axial stiffness of the rubber supports used in the PWA-lock at the nominal load (≈ 250 kN) is approximately 50 kN/mm. The compression of the support at this point is approximately equal to 5 mm. The axial and tilting stiffness of the rubber supports have been measured (BAKKER-RUBBER, 1994). The variation between the different supports used in the PWA-lock is large (figure 2.6).

The tilting stiffness at this nominal load is approximately equal to 1.75 MNm/rad. This tilting stiffness is very low compared to that of the lubricating film, which is approximately 36.0 MNm/rad (see section 15.1). Therefore any tilt of the gate relative to the track is largely taken up by the support. The water film between the hydro-foot and the track remains approximately parallel.

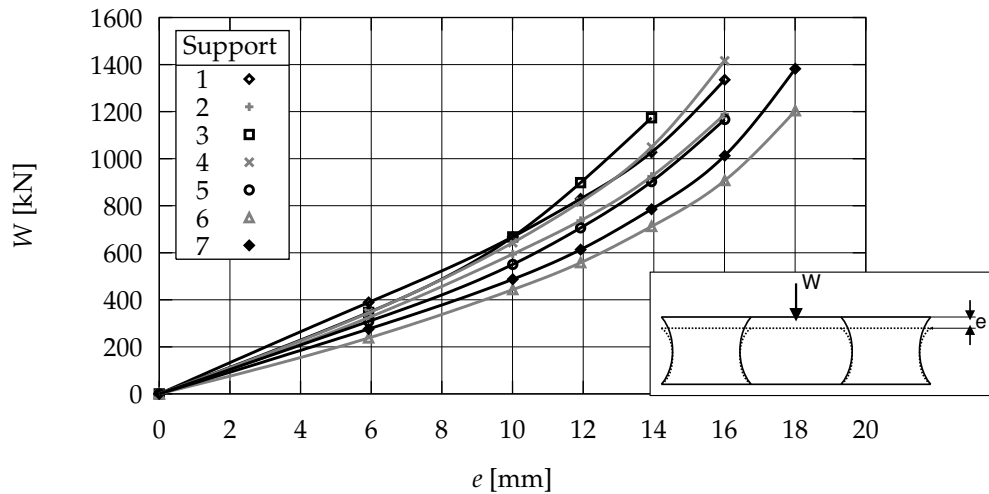


Figure 2.6: Axial stiffness of 7 rubber supports produced for the PWA-lock. The dimensions of the rubber support are given in appendix A

2.3 The track

The track along which the hydro-foot slides is an UHMWPE track fixed on a concrete foundation. During the opening and closing of the lock gate the hydro-foot slides on top of this track. The width of the track is equal to 1.1 m and the height is 0.07 m.

The track surface isn't perfectly plane. Figure 2.7 shows the surface waviness of a test track (ABT-WEST, 1991; HOLLANDIA, 1994). The amplitude of the surface waviness within a hydro-foot diameter (0.75 m) is clearly much larger than the nominal lubricating water film thickness (0.1 mm). The surface waviness of the tracks actually used in the PWA-lock have a comparable amplitude of about 0.3 mm.

2.4 Friction measurements in situ

In the design stage of the hydro-foot for the PWA-lock it was recognized that partial contact between the hydro-foot and the track would occur due to the fact that the nominal film height (0.1 mm) is much smaller than the amplitude of the track surface waviness (0.3 mm/m). Yet, at the time, the hydro-foot was designed using calculations where no contact between hydro-foot and track was assumed to occur.

From the moment the PWA-lock was put into use, monitoring measurements were performed periodically, in which the force required to open or close the lock gates was measured (KLOPPENBURG ET AL., 1997, 1998, 1999). This force consists partly of an inertia force during acceleration and deceleration of the gate, partly of a drag force due to the gate moving through the water and partly of a friction force between the

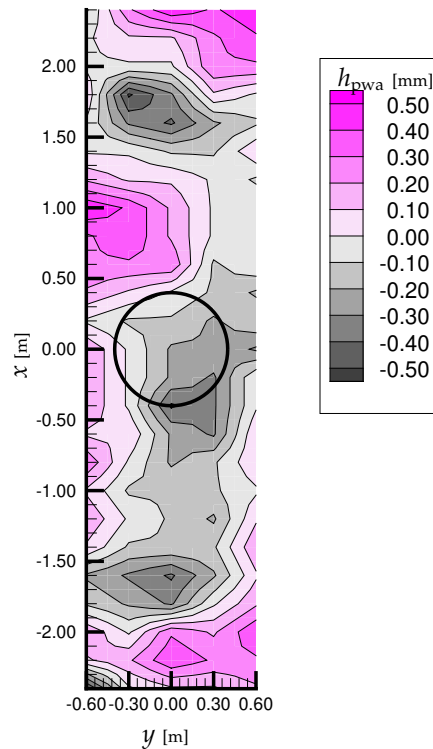


Figure 2.7: Height of the surface of a test track compared to a plane reference surface. The surface has been measured on a grid of 0.2 m along the length of the track and 0.3 m across.

hydro-foot and the track and partly of a friction force in other supports. Using several initial measurements, at several sliding velocities, the contribution of the friction force between the hydro-foot and the track is calculated.

The classic designation for the ratio of the friction force and the load is friction coefficient. However in this thesis a distinction is made between the *friction* coefficient c_f and the *bearing* coefficient c_b . The friction coefficient is the ratio of the friction force due to contact and the load carried in contact. The bearing coefficient however, is the ratio of the total friction force and the total load. This definition therefore, is identical to the classic definition of the friction coefficient.

If the weight of the gate is fully carried by the hydrostatic pressure in the lubricating water film, this friction force and thus the bearing coefficient will be very small. The experiments (see for instance figure 2.8) show that the initial bearing coefficient c_b was initially much higher than can be expected in case of a total separation of hydro-foot and track.

Secondly, the experiments show a decline of the measured bearing coefficient particularly during the first two years of use. These two facts confirm the assumption that (partial) contact between and deformation and wear of the hydro-foot and track occur. After a period of use of three years, the bearing coefficient has dropped to about 0.003 for the west gate and 0.007 for the east gate.

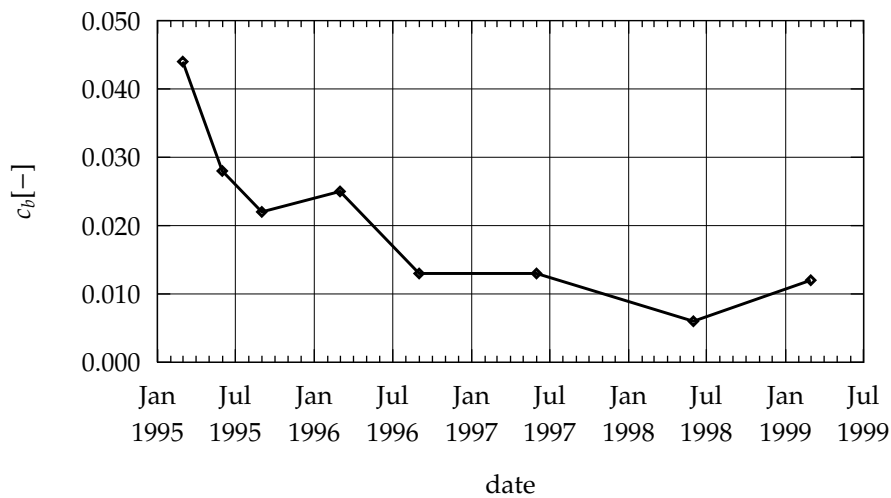


Figure 2.8: Reduction in time of the average bearing coefficient of the east gate. The bearing coefficient is measured during the opening of the gate and the average sliding speed during these measurements is 0.24 m/s.

After a running-in period, the coefficient of friction between stainless steel and UHMWPE under water, and with a contact pressure of $1.0 \cdot 10^6 \text{ N/m}^2$, is approximately equal to 0.1. If the weight of the lock gate is carried fully by the contact between the hydro-foot and the track (no hydrostatic pressure) the bearing coefficient will become equal to the coefficient of friction of stainless steel and UHMWPE. If the weight of the gate is partly carried by the hydrostatic pressure in the lubricating water film the bearing coefficient will be less than the coefficient of friction. A bearing coefficient of 0.05 implies that approximately 50% of the load is carried by contact, a bearing coefficient of 0.007 implies that only 7% of the load is carried by contact. After three years of use the bearing is almost fully hydrostatically lubricated.

A track surface waviness smaller than that present in the PWA-lock is difficult and expensive to realize. Because of this reason, contact between the bearing and the track is practically unavoidable. Among other things, this was the reason to perform the present study and study the possibilities to improve the design of the hydro-foot, taking into account this contact between the hydro-foot and the track.

CHAPTER 3

Introduction to the model development

The purpose of the present study is the development of methods, graphs and formulae for the design of hydro-supports. In the following chapters a mathematical model is developed in order to describe the behavior and properties of a hydro-support.

As was mentioned in the introduction (chapter 1), a hydro-support is a water lubricated, hydrostatic thrust bearing sliding on a track. If the hydro-support has a length/width ratio approximately equal to 1.0, it is called a hydro-foot. If the length/width ratio is (much) larger than 1.0, it is called a hydro-fender.

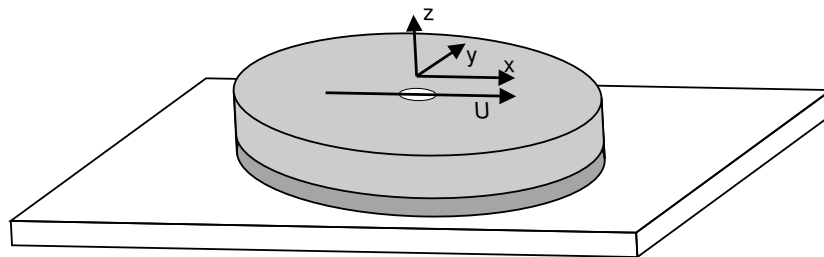


Figure 3.1: Geometry and coordinate system. A hydro-foot, consisting of a steel sliding-sole and a rubber support, slides with a velocity U on top of a track.

The bearing is connected to the moving part (for instance a lock gate) by a flexible rubber hinge or support. The primary function of this support is to enable the bearing to tilt relative to the moving part. Secondly, it supports the elastic deformation of the bearing.

It is assumed that due to inevitable manufacturing limitations, the track has a surface waviness with a substantially greater amplitude than the nominal lubricating film thickness between the bearing and the track. This will result in repeated contact

between the bearing and the track. It is assumed that the load on the bearing is constant and non-dynamic. Both the bearing and the track are assumed to deform elastically under the prevailing load.

The hydro-support is elastically connected to the lock gate with a rubber support. This elastic hinge will allow the bearing to maintain an attitude relative to the lock gate in such a way that the forces above and below the bearing are in equilibrium.

The load W on top of the bearing is in equilibrium with the hydrostatic and contact pressures between the bearing and the track.

$$W = \iint_A p \, dA \quad (3.1)$$

where p is the effective pressure between the bearing and the track, consisting of the hydrostatic and contact pressures and A is the total surface area of the bearing. In chapters 6 and 7 the relations describing these pressures will be presented.

Both the deformation of the bearing and the attitude of the bearing in relation to the moving part and the track are determined by the forces acting on the bearing. If the resulting load on the underside of the bearing is a-symmetric, a tilting moment will occur. Due to this tilting moment the bearing will tilt relative to the top plane of the rubber support. In appendix B this effect is studied in more detail. In this thesis it is assumed that the tilting moment will remain negligible and that therefore the bearing will remain parallel relative to the track. In order to ensure that this assumption is acceptable, the wavelength of the components of the surface waviness has been limited to the bearing width (see chapter 5 for a description of the track surface waviness). This assumption substantially reduces the numerical complexity and makes the parametric study performed in the chapters 13 to 18 feasible.

In a previous study both the hydro-foot and hydro-fender have been studied in particular with respect to the tilting stiffness and the influence of an elastic surface on its performance (VAN BEEK, 1995; VAN BEEK AND DAANE, 1995; VAN BEEK AND LEPIC, 1996; VAN BEEK AND VAN OSTAYEN, 1997; VAN BEEK AND SEGAL, 1991, 1997a,b). However these studies were limited to the no-contact situation.

In CASTELLI ET AL. (1967) a hydrostatic thrust bearing with a compliant (rubber) surface has been studied. Comparable bearings were studied by DOWSON AND TAYLOR (1967); GUPTA (1974).

The mathematical model developed to describe the behavior and properties of a hydro-support is described in the following chapters:

- Hydro-support with rigid surfaces (chapter 4). If the surfaces of the hydro-support are assumed to be both rigid and plane, the properties of the hydro-support are fairly easy to calculate. The results for this rigid, plane hydro-support are used as a reference in this study.

-
- Track deformation and surface description (chapter 5). Both the track and the bearing will deform elastically due to the load. In this chapter the deformation of the track is studied.

One of the typical properties of the hydro-support as studied in this thesis, is the relative large surface waviness of one of the surfaces. The description of this surface waviness is also part of this chapter.

- Mixed lubrication (chapter 6). In the contact areas between bearing and track the contact pressure carries part of the load on the bearing.
- Full film lubrication (chapter 7). The hydrostatic pressure in the lubricating film is described by the Reynolds' equation. Due to the contact occurring between bearing and track, surface roughness effects must be taken into account. Surface roughness will partially obstruct the flow in the lubricating film.
- Bearing deformation (chapter 8). It is assumed that due to the load, the bearing will deform elastically. Because it is assumed that a thin bearing will show better compliance to the track surface waviness, we will study the deformation of the thin bearing in particular.
- Rubber support (chapter 9). The rubber support will deform elastically due to the load. In this chapter the normal stress on top of the bearing due to the compression of the support, is calculated. Furthermore, the concept of the 'ideal' support is introduced.

The results of the mathematical model can be partially verified with the results of several experiments on both hydro-feet and hydro-fenders (chapter 10).

If the hydrostatic supply of the hydro-support is not active, the load will be carried completely by the contact forces between the bearing and the track. In this case, at high sliding speeds, the resulting friction could result in a substantial temperature rise of the bearing and the track. A preliminary study into this temperature rise is presented in appendix C. This possible temperature rise is of particular interest for bearings with a smaller thickness and at high sliding speeds. However, the sliding speeds for typical applications of the hydro-support are fairly low and therefore it is assumed that the temperature rise will remain within acceptable limits. In addition, because of the low sliding speeds, it is assumed that the hydrodynamic pressure rise in the lubricating film can be neglected compared to the hydrostatic pressure. In any case, the hydrodynamic pressure has a positive effect on the total pressure distribution and can safely be neglected. In the parametric studies in this thesis the sliding velocity is therefore set to zero.

In the next chapters the mathematical model for the description of the hydro-support will be developed.

CHAPTER 4

Hydro-support with rigid surfaces

The properties of a hydro-support with elastic, non-smooth surfaces are dependent on a lot of parameters. The determination of these properties can only be performed using involved numerical calculations. However, if a number of assumptions is made, the determination of these properties can be performed using analytical methods or simple numerical methods. These assumptions are:

- The surfaces are rigid (non-elastic).
- The surfaces are smooth (no surface waviness or roughness).
- The surfaces are plane.
- The support has a zero velocity.

In this chapter the properties of both hydro-foot and hydro-fender are determined using these simplifying assumptions. The results will be used in later chapters as reference for the more involved numerical calculations.

4.1 1-Recess hydro-foot

The hydro-foot is a hydro-fender with a circular shape. For this shape it is a natural choice to use a cylindrical coordinate system (r, ϕ) to describe the properties of the lubricating film where the origin of the coordinate system is located in the center of the film. If it is assumed that (1) the hydro-foot has rigid and parallel surfaces a constant distance h_0 apart, (2) the hydro-foot has zero velocity, (3) the hydro-foot has 1 recess, then balance of mass yields:

$$\frac{\partial}{\partial r}(rq_r) = 0 \tag{4.1}$$

where r is the radial coordinate and with q_r the flow rate per unit width for a fluid with constant viscosity η and pressure distribution p_h :

$$q_r = -\frac{h_0^3}{12\eta} \frac{\partial p_h}{\partial r} \quad (4.2)$$

Substitution of equation 4.2 into equation 4.1 yields a simplified, axi-symmetric form of the Reynolds' equation (see for instance BASSANI AND PICCIGALLO (1992)).

$$\frac{\partial}{\partial r} \left(-\frac{h_0^3 r}{12\eta} \frac{\partial p_h}{\partial r} \right) = 0 \quad (4.3a)$$

The Reynolds' equation will be further examined in chapter 7. Basically, the Reynolds' equation is an expression of the conservation of mass in a fluid continuum in which a number of assumptions valid for thin fluid films have been introduced.

It is assumed that the pressure in the recess is constant and equal to p_r and the ambient pressure is equal to 0. Thus the boundary conditions to equation 4.3a are:

$$p_h(d/2) = p_r \quad (4.3b)$$

$$p_h(D/2) = 0 \quad (4.3c)$$

where d is the diameter of the recess and D is the outer diameter of the bearing (figure 4.1).

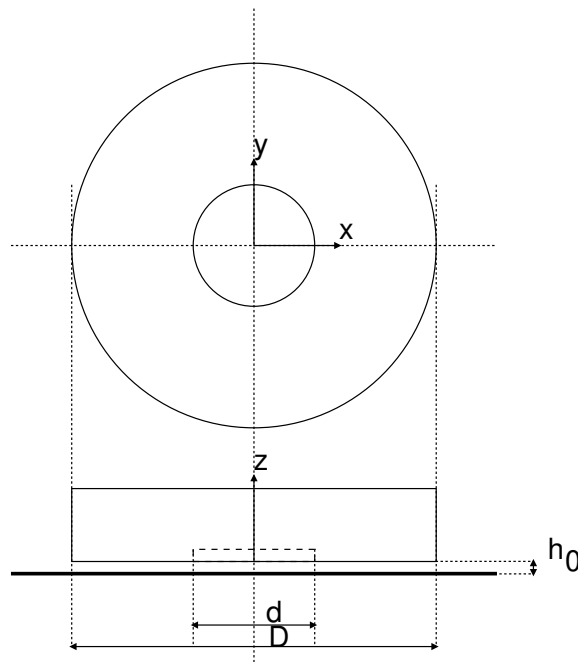


Figure 4.1: Schematic view of a 1-recess hydro-foot

The solution of equation 4.3a yields the axi-symmetric hydrostatic pressure distribution p_h in the lubricating film (figure 4.2):

$$p_h(r) = \begin{cases} p_r & \text{for } r \leq d/2 \\ p_r \frac{\ln(2r/D)}{\ln(d/D)} & \text{for } d/2 < r < D/2 \end{cases} \quad (4.4)$$

and the flow rate q_r follows from the substitution of this result in equation 4.2:

$$q_r(r) = -\frac{p_r h_0^3}{12\eta} \frac{1}{r \ln(d/D)} \quad (4.5)$$

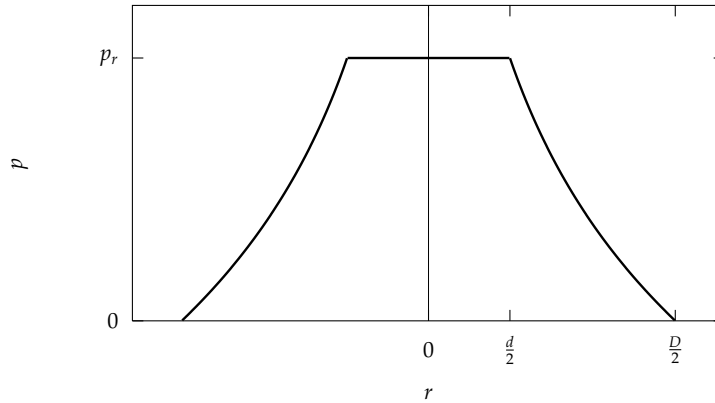


Figure 4.2: Pressure distribution for the hydro-foot with rigid, parallel surfaces.

4.1.1 Parallel pad coefficients

The properties of a hydrostatic bearing can be expressed using the so-called pad coefficients (BASSANI AND PICCIGALLO, 1992). These pad coefficients are the non-dimensional effective bearing area \bar{A}_e which is a measure of the load capacity, the non-dimensional hydraulic resistance \bar{R}_h which is a measure of the flow and the non-dimensional power dissipation number Γ which is a measure of the power dissipation.

The total load on the bearing can be found by integrating the hydrostatic pressure (equation 4.4) over the bearing area:

$$W = 2\pi \int_0^{D/2} p_h r dr = p_r \frac{\pi}{4} D^2 \frac{1 - (d/D)^2}{2 \ln(D/d)} \quad (4.6)$$

This can be restated as:

$$W = p_r A \bar{A}_e \quad (4.7)$$

with A the total bearing area:

$$A = \frac{\pi}{4} D^2 \quad (4.8)$$

and introducing the non-dimensional effective bearing area \bar{A}_e :

$$\bar{A}_e = \frac{1 - (d/D)^2}{2 \ln(D/d)} \quad (4.9)$$

Note that in this case the load W is independent of the film height h_0 . The film height is largely determined by the flow supplied to the bearing by the supply pump at the given supply pressure.

The total flow rate Q through the lubricating film follows from the flow rate per unit width (equation 4.5) and is equal to:

$$Q = \pi D q_{r(r=D/2)} = \frac{p_r h_0^3}{\eta} \frac{\pi}{6 \ln(D/d)} \quad (4.10)$$

Introducing the hydraulic resistance R_h and the dimensionless hydraulic resistance \bar{R}_h :

$$Q = \frac{p_r}{R_h} = \frac{p_r h_0^3}{\eta} \frac{1}{\bar{R}_h} \quad (4.11)$$

yields:

$$\frac{1}{\bar{R}_h} = \frac{\pi}{6 \ln(D/d)} \quad (4.12)$$

The power H required to pump the lubricating fluid from the recess to the surroundings is:

$$H = Q p_r = \frac{p_r^2 h_0^3}{\eta} \frac{1}{\bar{R}_h} \quad (4.13)$$

Eliminating p_r from this equation using equation 4.7 yields:

$$H = \frac{W^2 h_0^3}{A^2 \eta} \Gamma \quad (4.14)$$

introducing the dimensionless power dissipation number Γ .

$$\Gamma = \frac{1}{\bar{A}_e^2 \bar{R}_h} \quad (4.15)$$

Note that \bar{A}_e , \bar{R}_h and therefore Γ are only dependent on the geometry of the bearing.

For a given load, film thickness and bearing area, a minimum value for Γ results in a minimal power loss (figure 4.3). The optimal recess/bearing diameter ratio d/D resulting in a minimal power loss is 0.5291. Keep in mind that this power loss is not the total required pumping power. In practise, an important part of the pumping power is lost in the restrictor.

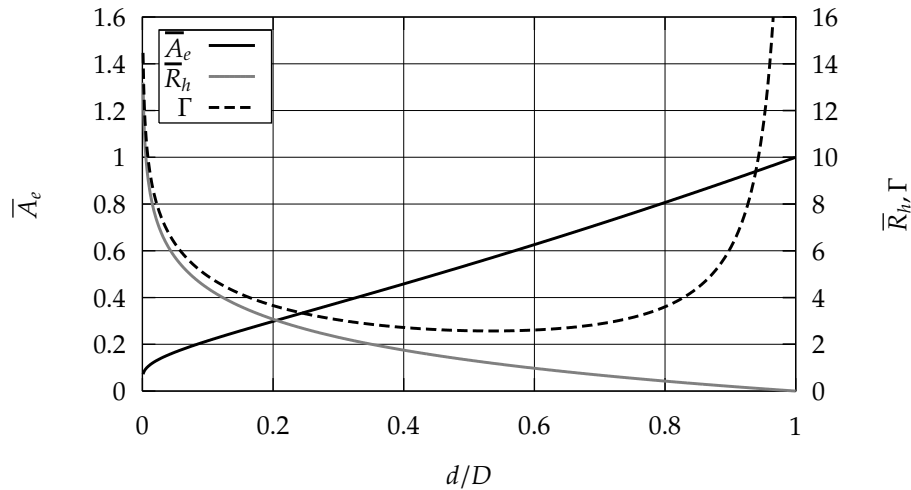


Figure 4.3: Pad coefficients of the 1-recess hydro-foot: Non-dimensional effective area \bar{A}_e , non-dimensional hydraulic resistance \bar{R}_h and power dissipation number Γ .

4.1.2 Tilted pad coefficients

The properties of a tilted 1-recess hydro-foot can only be determined by numerical solution of the Reynolds' equation. Therefore a numerical program has been developed using Sepran, a general purpose finite element program and subroutine library (SEGAL, 1993b). This program calculates the pressure distribution, volume flow rate and load of the hydro-support with rigid and plane bearing surfaces.

In figure 4.4 the effective bearing area \bar{A}_e and hydraulic resistance \bar{R}_h calculated using the analytical result (equation 4.7) are compared with \bar{A}_e and \bar{R}_h calculated using the numerical method. The similarity between both results is excellent.

The numerical program is used to calculate the effective area \bar{A}_e and hydraulic resistance \bar{R}_h for a tilted bearing. The angle of the tilt is denoted by $\bar{\alpha}$, where a value of 0 means no tilt and a value of 1 means maximum tilt, i.e. at the edge of the bearing the film height is reduced to 0:

$$\bar{\alpha} = \frac{\alpha \frac{D}{2}}{h_0} \quad (4.16)$$

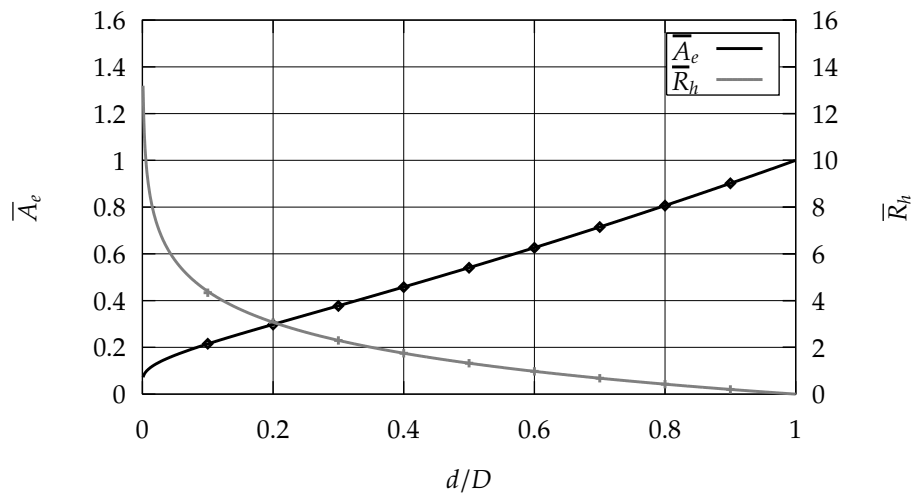


Figure 4.4: Comparison numerical and analytical calculated effective area \bar{A}_e and hydraulic resistance \bar{R}_h . The lines represent the analytical solution, the symbols represent the numerical solution.

with h_0 being the film height in the center of the bearing (not taking into account the recess depth).

The influence of tilt on the effective bearing area \bar{A}_e is small (figure 4.5), on the hydraulic resistance \bar{R}_h somewhat larger (figure 4.6). These numerical results have been accurately curve-fitted by BASSANI AND PICCIGALLO (1992).

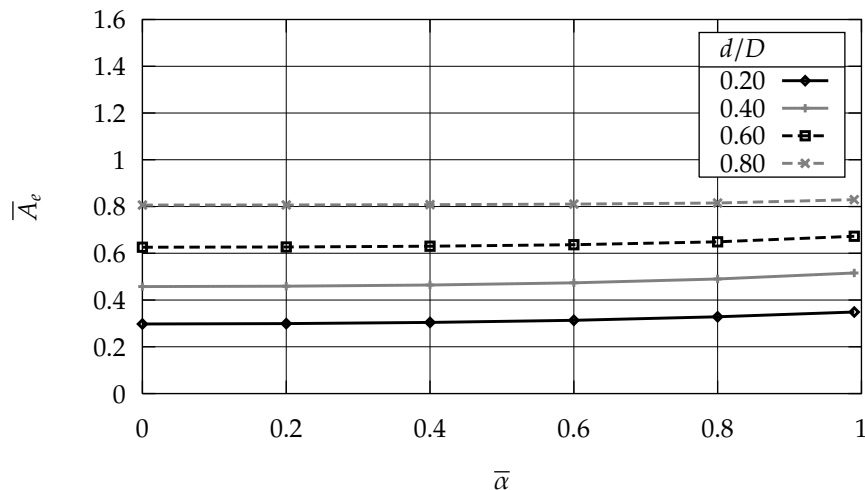


Figure 4.5: Effective area \bar{A}_e of the tilted 1-recess hydro-foot as function of the tilt angle $\bar{\alpha}$.

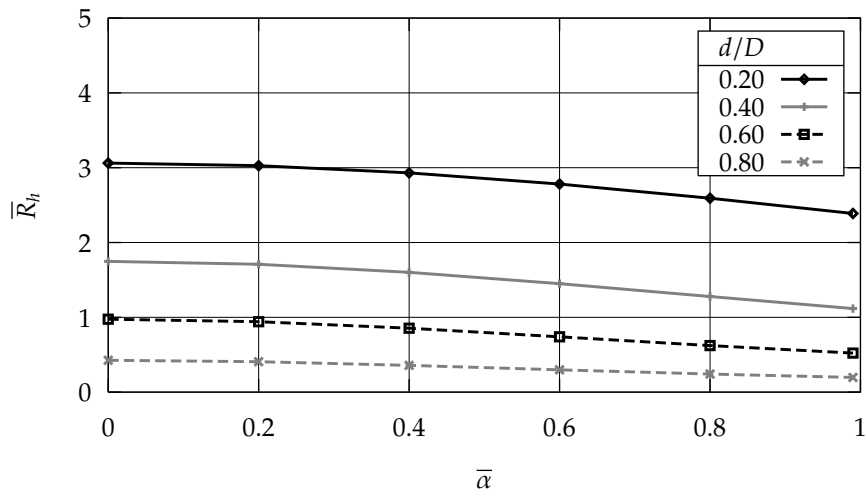


Figure 4.6: Hydraulic resistance \bar{R}_h of the tilted 1-recess hydro-foot as function of the tilt angle $\bar{\alpha}$.

Figure 4.7 shows the pressure distribution in the lubricating film for a maximal tilted bearing. The pressure distribution is eccentric and the pressure contours are displaced in the direction of the minimal film thickness located at coordinates $(0, -1)$.

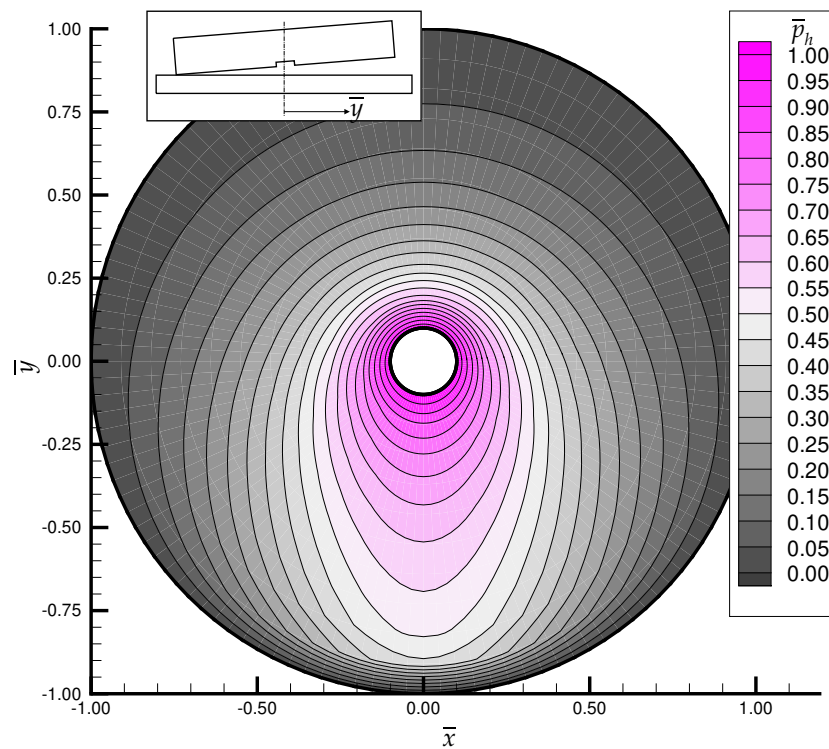


Figure 4.7: Pressure distribution $\bar{p}_h = p_h/p_r$ of a 1-recess hydro-foot with maximum tilt.

4.2 1-Recess hydro-fender

The hydro-fender is a hydro-support with a long shape. In previous studies, a simple rectangular shape has been studied, both analytically (see e.g. BASSANI AND PICCIGALLO (1992)) and experimentally (see chapter 10 or SCHUT (1991a); VISSER (1989a,b)). However, it was shown that this shape exhibits large end effects, in that the flow is irregular or even blocked at the ends of the bearing. Instead of the simple rectangle a different fender shape is studied in the present study.

The hydro-fender studied here (figure 4.8) can be divided in 3 distinct parts viz. 1 rectangular center part (II) and 2 semi-circular end parts (Ia and Ib). The total length of the fender is L , the width B and therefore the length of the central rectangular part $L - B$. The recess width is equal to b .

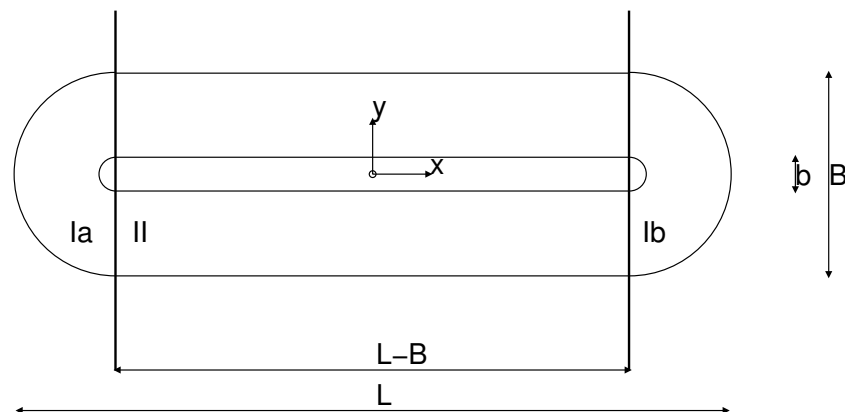


Figure 4.8: Schematic view of a 1-recess hydro-fender

Using the same assumptions that were used in the previous section for the hydro-foot (rigid, plane surfaces, zero velocity and one recess), the properties of the hydro-fender can be approximated.

It is assumed that by approximation, the hydrostatic pressure and flow in the 3 parts of the fender can be studied separately:

- Semi-circular end parts Ia and Ib. The pressure and flow are considered to be equal to those under the circular hydro-foot. The pad coefficients of this shape have been studied in the previous sections.
- Rectangular center part II. It is assumed that in this part the flow is perfectly perpendicular to the long axis of the fender. The pad coefficients of this shape will be studied in the next section.

4.2.1 Parallel pad coefficients (infinite fender)

It is assumed that, in the central part II of the hydro-fender (figure 4.8), the pressure and flow are approximately equal to those under an infinitely long rectangular pad.

The width of this pad is B , the recess width is equal to b . In the direction of the long axis of the fender (x -coordinate) the pressure and flow are constant. Perpendicular to the long axis of the fender (y -coordinate) the pressure is described using the 1-dimensional Reynolds' equation:

$$\frac{\partial}{\partial y} \left(\frac{-h_0^3}{12\eta} \frac{\partial p_h}{\partial y} \right) = 0 \quad (4.17a)$$

The pressure in the recess is assumed to be constant and equal to p_r . The boundary conditions for the Reynolds' equation for $y < 0$ are:

$$p_h(-B/2) = 0 \quad (4.17b)$$

$$p_h(-b/2) = p_r \quad (4.17c)$$

and for $y > 0$:

$$p_h(b/2) = p_r \quad (4.17d)$$

$$p_h(B/2) = 0 \quad (4.17e)$$

where b and B are the widths of the recess and fender respectively.

The solution of this equation is easily obtained and shows a linear drop from the recess pressure to the zero ambient pressure at the edge of the fender (figure 4.9):

$$p_h(y) = \begin{cases} p_r \left(\frac{B+2y}{B-b} \right) & \text{for } -B/2 \leq y < -b/2 \\ p_r & \text{for } -b/2 \leq y \leq b/2 \\ p_r \left(\frac{B-2y}{B-b} \right) & \text{for } b/2 < y \leq B/2 \end{cases} \quad (4.18)$$

If we now consider a part of the infinite fender, with length L , the load W carried by the pressure in this part is equal to:

$$W = L \int_{-B/2}^{B/2} p_h dy = p_r BL \frac{1}{2} (1 + b/B) \quad (4.19)$$

and, using equation 4.7 and noting that the bearing area of this part is equal to BL , the dimensionless effective area \bar{A}_e becomes:

$$\bar{A}_e = \frac{1}{2} (1 + b/B) \quad (4.20)$$

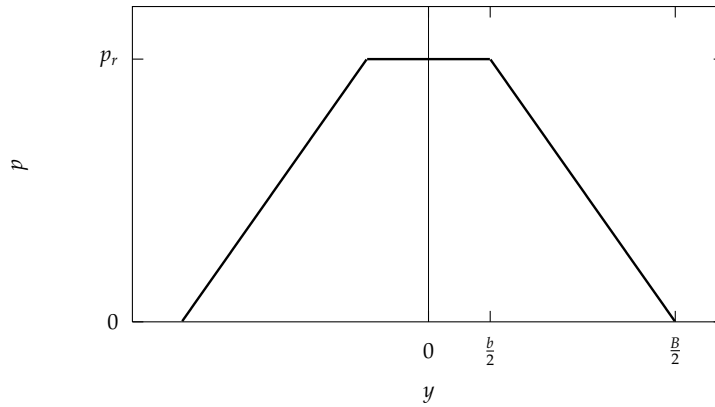


Figure 4.9: Pressure distribution for the infinitely long hydro-fender with rigid, parallel surfaces.

The flow Q from this part is equal to:

$$Q = 2L \frac{h_0^3}{12\eta} \frac{2p_r}{B-b} = \frac{p_r h_0^3}{\eta} \frac{L/B}{3(1-b/B)} \quad (4.21)$$

and thus, using equation 4.11, the dimensionless hydraulic resistance \bar{R}_h is equal to:

$$\bar{R}_h = \frac{3(1-b/B)}{L/B} \quad (4.22)$$

The power dissipation H in this part is equal to:

$$H = Qp_r = \frac{p_r^2 h_0^3}{\eta} \frac{L/B}{3(1-b/B)} \quad (4.23)$$

and therefore, using equation 4.15, the dimensionless power dissipation number Γ is equal to:

$$\Gamma = \frac{1}{\bar{A}_e^2 \bar{R}_h} = \frac{4L/B}{3(1+b/B)^2(1-b/B)} \quad (4.24)$$

In figure 4.10, the dimensionless effective area \bar{A}_e , hydraulic resistance \bar{R}_h and power dissipation number Γ are presented as a function of the recess to bearing width ratio b/B . Note, that contrary to that of the circular hydro-foot (figure 4.3), the power dissipation number does *not* increase to infinite for small b/B . In fact, although the power dissipation number reaches a minimum value 1.125 for $b/B = 0.33$, for $b/B = 0$ this value is just equal to 1.33. It is therefore possible to choose a small value of b/B without the penalty of a large increase in power dissipation.

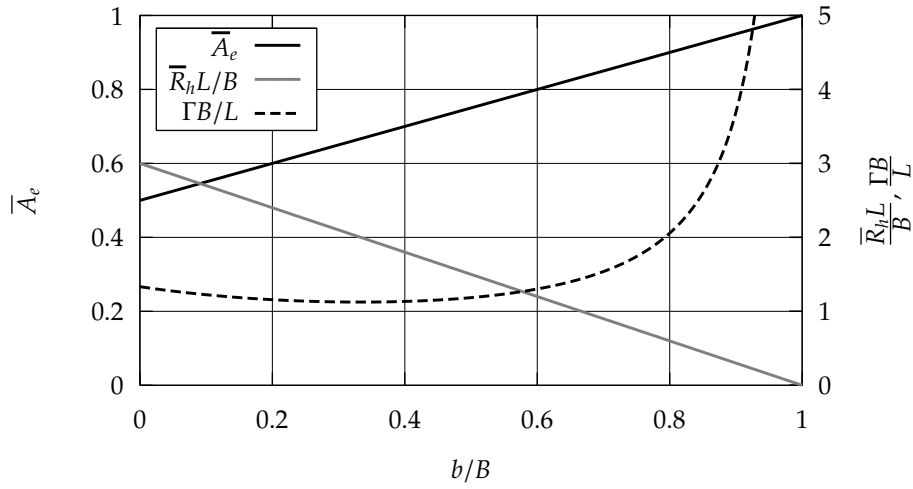


Figure 4.10: Pad coefficients of the infinite 1-recess hydro-fender: Non-dimensional effective area \bar{A}_e , non-dimensional hydraulic resistance \bar{R}_h and power dissipation number Γ .

4.2.2 Parallel pad coefficients (finite fender)

In the previous sections 4.1.1 and 4.2.1 the pad coefficients of respectively the circular bearing and the infinite rectangular bearing, have been derived. In this section the pad coefficients of the finite fender as shown in figure 4.8 will be approximated using these results.

As was stated previously, it is assumed that the hydrostatic pressure and flow in the 3 parts of the fender can be studied separately:

- Semi-circular end parts Ia and Ib. The pressure (and therefore the load) and flow in these parts are assumed to be equal to those under the circular hydro-foot (section 4.1.1).
- Rectangular center part II. The pressure (and therefore the load) and flow in this part are assumed to be equal to those under the infinitely long rectangular hydro-fender (section 4.2.1).

The load W on the fender is now equal to the sum of the loads on the fender parts (Ia, Ib and II):

$$W = p_r A \bar{A}_e = p_r (A_I \bar{A}_{eI} + A_{II} \bar{A}_{eII}) = p_r (A_I + A_{II}) \bar{A}_e \quad (4.25)$$

where A_I, A_{II} and $\bar{A}_{eI}, \bar{A}_{eII}$ are the surface areas and dimensionless effective areas of respectively part I (that is parts Ia and Ib combined) and part II.

Using equations 4.9, 4.8 and 4.20, the load W becomes equal to:

$$W = p_r B^2 \left(\frac{\pi}{4} \frac{1 - (b/B)^2}{2 \ln(B/b)} + \frac{1}{2} (L/B - 1)(1 + b/B) \right) \quad (4.26)$$

and the total dimensionless effective area \bar{A}_e :

$$\bar{A}_e = \frac{A_I \bar{A}_{eI} + A_{II} \bar{A}_{eII}}{A_I + A_{II}} = \frac{\frac{\pi}{4} \frac{1 - (b/B)^2}{2 \ln(B/b)} + \frac{1}{2} (L/B - 1)(1 + b/B)}{\frac{\pi}{4} + (L/B - 1)} \quad (4.27)$$

Note that the length of the central rectangular part II is $L - B$ instead of L so naturally, the equations from section 4.2.1 have been modified accordingly.

Figure 4.11 shows the dimensionless effective area \bar{A}_e of the hydro-fender for several bearing length/width ratios L/B versus the recess/bearing width b/B ratio. In this figure both the results of the approximation (equation 4.27) and the results of 'exact' finite element calculations are presented. Both methods yield the same results with a very small margin of error.

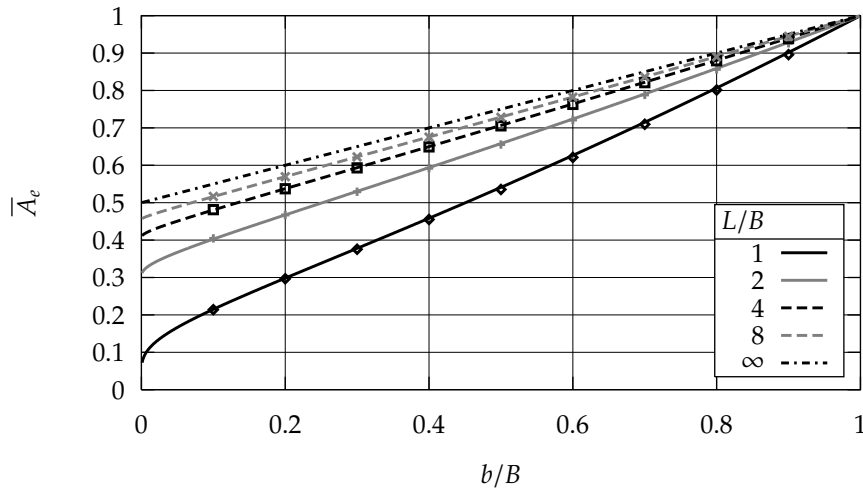


Figure 4.11: Effective area A_e of the 1-recess hydro-fender. The lines represent the analytical approximation, the symbols represent the numerical finite element solution.

The dimensionless effective area \bar{A}_e increases for higher values of L/B . Therefore, given a certain bearing area A , the load increases with increased bearing length/width ratio.

Using equations 4.10 and 4.21, the flow rate Q from the fender becomes equal to:

$$Q = Q_I + Q_{II} = \frac{p_r h_0^3}{\eta} \left(\frac{\pi}{6 \ln(B/b)} + \frac{L/B - 1}{3(1 - (b/B))} \right) \quad (4.28)$$

The dimensionless hydraulic resistance \bar{R}_h becomes:

$$1/\bar{R}_h = Q \frac{p_r h_0^3}{\eta} = \frac{\pi}{6 \ln(B/b)} + \frac{L/B - 1}{3(1 - (b/B))} \quad (4.29)$$

Figure 4.12 shows the dimensionless hydraulic resistance \bar{R}_h of the hydro-fender for several bearing length/width ratios versus the recess/bearing width ratio. The approximation (equation 4.29) and the finite element calculations yield the same results. It can be concluded that the model used to calculate the load and flow rate of the hydro-fender is sufficiently accurate.

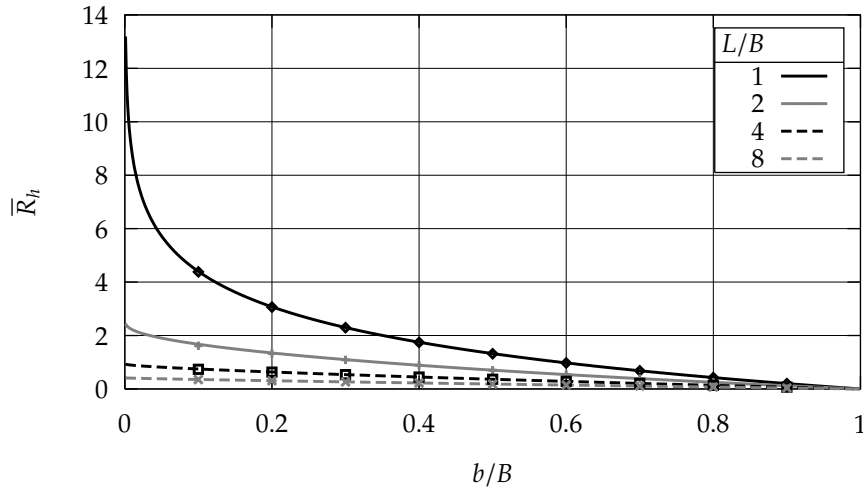


Figure 4.12: Dimensionless hydraulic resistance \bar{R}_h of the 1-recess hydro-fender. The lines represent the analytical approximation, the symbols represent the numerical solution.

Using equation 4.28, the power dissipation H is equal to:

$$H = p_r Q = \frac{p_r^2 h_0^3}{\eta} \left(\frac{\pi}{6 \ln(B/b)} + \frac{L/B - 1}{3(1 - (b/B))} \right) \quad (4.30)$$

Similar to equation 4.15, a dimensionless power dissipation number can be introduced, relating the required pumping power to the bearing load:

$$\Gamma = \frac{1}{\bar{A}_e \bar{R}_h} \quad (4.31)$$

with \bar{A}_e and \bar{R}_h given by respectively equations 4.27 and 4.29.

In figures 4.13 and 4.14 Γ is presented as a function of b/B and L/B . All fenders show a minimal value of Γ for a certain 'optimal' recess/bearing width ratio. This optimal ratio

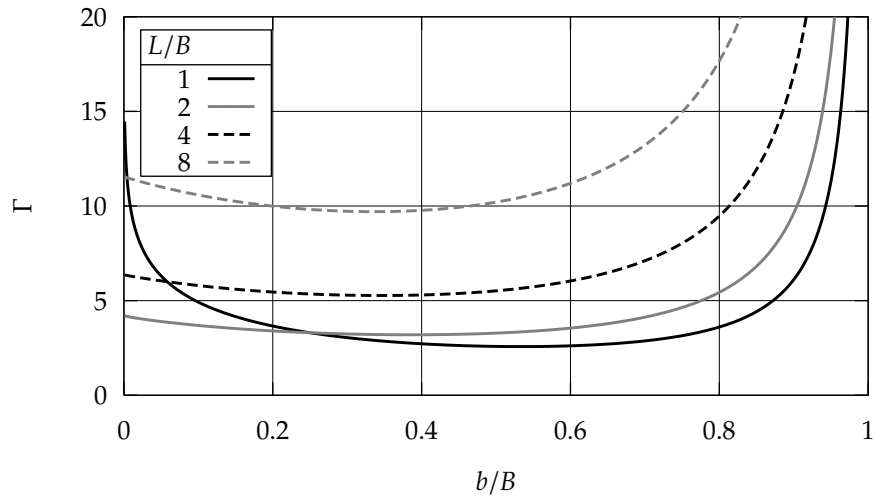


Figure 4.13: Dimensionless power dissipation number Γ for the 1-recess hydro-fender as a function of the recess/bearing width ratio b/B .

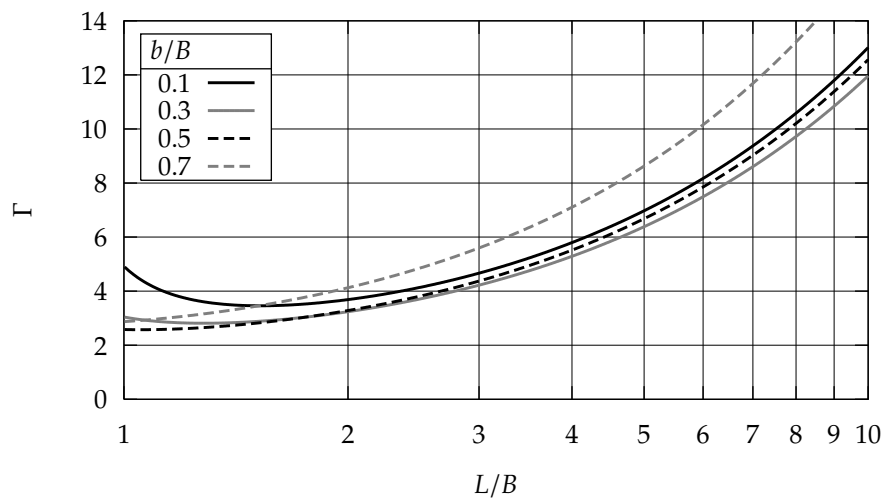


Figure 4.14: Dimensionless power dissipation number Γ for the 1-recess hydro-fender as a function of the bearing length/width ratio L/B .

varies between $b/B = 0.33$ for large values of L/B and $b/B = 0.5291$ for small values of L/B . For all values of b/B the power dissipation number Γ increases for larger values of L/B .

In figures 4.13 and 4.14 the power dissipation of fenders with equal load and surface area, but different lengths and recess widths have been compared. Looking at these figures one could conclude that the hydro-fender with the smaller length/width ratio has the advantage due to the lower power dissipation. However, after the bearing width, and thus the track width, has been chosen, the designer is free to choose any bearing length. It is therefore expedient, to not only compare hydro-fenders with identical surface area, but also those with identical bearing width. Repeating equation 4.14 and introducing the bearing width B yields:

$$H = \frac{W^2 h_0^3}{A^2 \eta} \Gamma = \frac{W^2 h_0^3}{B^4 \eta} \frac{B^4 \Gamma}{A^2} \quad (4.32)$$

In figure 4.15 the modified power dissipation number $B^4 \Gamma / A^2$ shows a decrease in power dissipation for larger values of L/B .

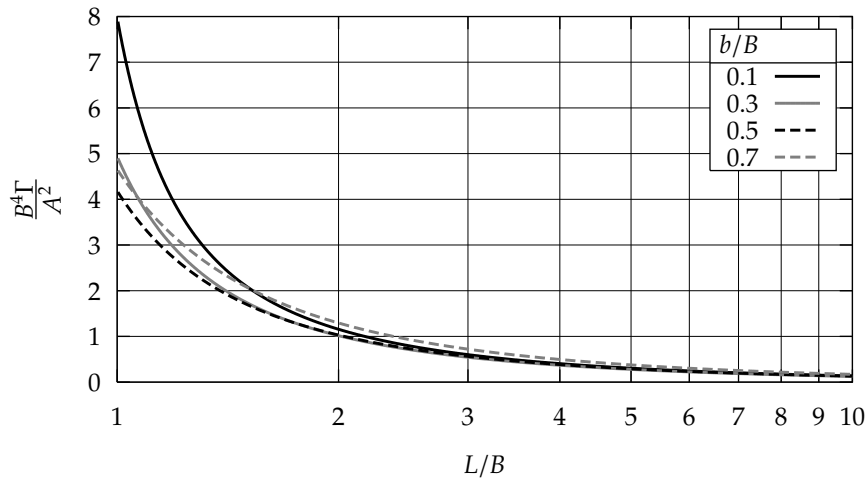


Figure 4.15: Modified dimensionless power dissipation number $B^4 \Gamma / A^2$ for the 1-recess hydro-fender as a function of the bearing length/width ratio L/B .

The load and flow of an arbitrary hydrostatic bearing can be expressed using the dimensionless bearing area \bar{A}_e and hydraulic resistance \bar{R}_h (equations 4.7 and 4.11). In order to compare the flow of different hydro-fenders with the same load, equation 4.7 can be substituted into equation 4.11:

$$Q = \frac{W h_0^3}{A \eta} \frac{1}{\bar{A}_e \bar{R}_h} \quad (4.33)$$

or:

$$\frac{QA\eta}{Wh_0^3} = \frac{1}{\overline{A_e R_h}} \quad (4.34)$$

or for bearings with constant bearing width B :

$$\frac{QB^2\eta}{Wh_0^3} = \frac{B^2}{\overline{AA_e R_h}} \quad (4.35)$$

In figures 4.16 and 4.17 these dimensionless flow numbers have been presented as function of the bearing length. Figure 4.17 shows that for bearings with a constant

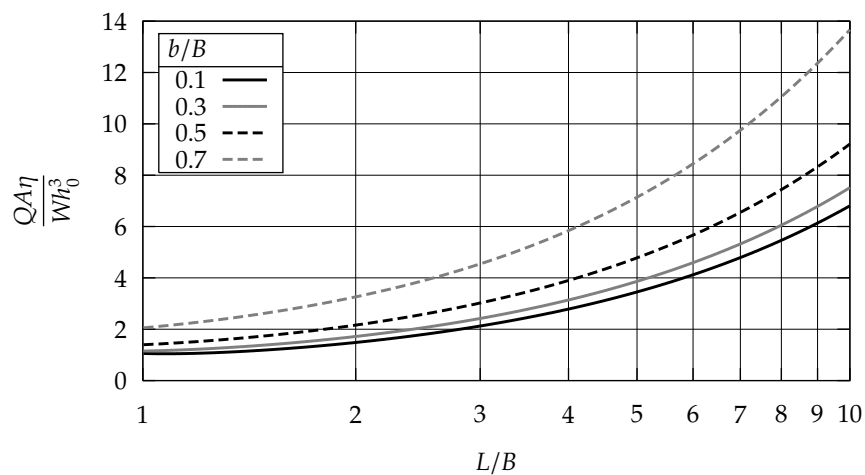


Figure 4.16: Dimensionless flow for constant *surface area* $QA\eta/Wh_0^3$ versus the bearing length L/B .

width and load, the flow Q decreases for increasing values of L/B . However, values larger than 4 do not result in a substantial further decrease. The recess pressure *will* decrease further and therefore the pumping power required will decrease also (see figure 4.15).

4.2.3 Tilted pad coefficients

The analytical model used in the previous section cannot be extended easily to take into account the properties of the tilted hydro-fender. However, it was shown that the numerical calculations yield results that are approximately equal to those obtained using the analytical model. In this section the numerical program will be used to study the influence of the following parameters on the properties of the tilted hydro-fender:

- Bearing length/width ratio L/B .

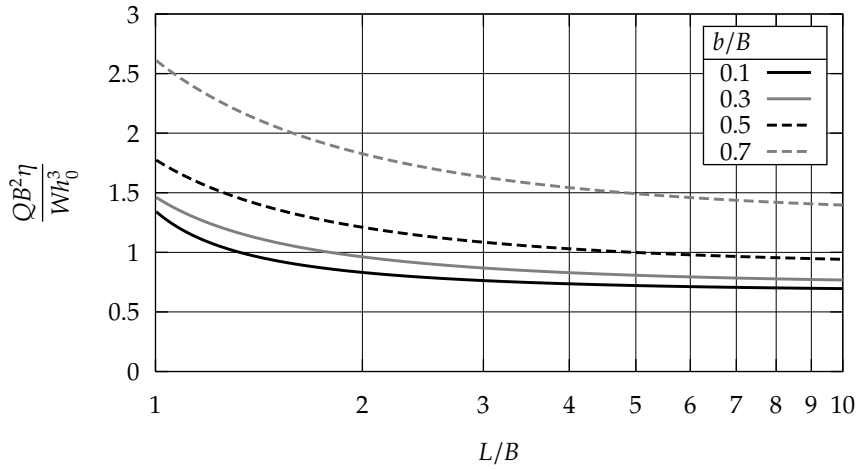


Figure 4.17: Dimensionless flow for constant bearing width $QB^2\eta/Wh_0^3$ versus the bearing length L/B .

- Recess/bearing width ratio b/B .
- Tilt angles in x - and y -direction, α_x and α_y . Similar to the dimensionless tilt angle $\bar{\alpha}$ for the hydro-foot (equation 4.16), the following dimensionless tilt angles have been defined:

$$\bar{\alpha}_x = \frac{\alpha_x^L}{h_0} \quad (4.36a)$$

$$\bar{\alpha}_y = \frac{\alpha_y^B}{h_0} \quad (4.36b)$$

The following properties are studied:

- Non-dimensional effective area \bar{A}_e .
- Relative eccentricities in x - and y -direction, ϵ_x and ϵ_y , where

$$\epsilon_x = \frac{\iint_A p_h x dA}{\frac{L}{2} \iint_A p_h dA} \quad (4.37a)$$

$$\epsilon_y = \frac{\iint_A p_h y dA}{\frac{B}{2} \iint_A p_h dA} \quad (4.37b)$$

- Hydraulic resistance \bar{R}_h .

Tilt in x -direction

If the hydro-fender is tilted along the x -direction the pressure distribution (figure 4.18) is largely similar to that of the non-tilted hydro-fender. Only the pressure in the semi-circular end part that is tilted towards the track shows a clearly modified pressure distribution.

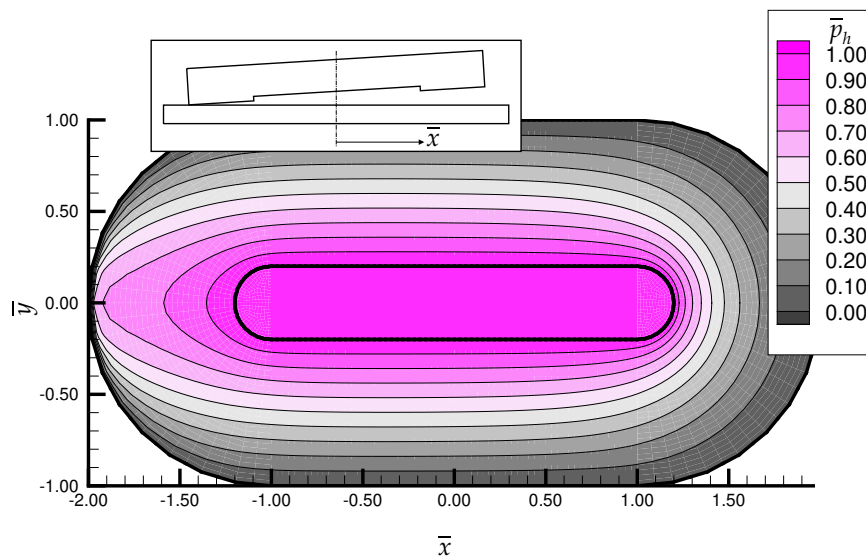


Figure 4.18: Pressure distribution $\bar{p}_h = p_h/p_r$ of a 1-recess hydro-fender with maximum tilt along the x -axis.

As a result the dimensionless effective area \bar{A}_e isn't much influenced by the tilting of the hydro-fender in x -direction. Figure 4.19 shows \bar{A}_e for various values of the bearing length/width ratio L/B versus the dimensionless tilting angle $\bar{\alpha}_x$. This angle is 0 for parallel surfaces and 1 for the maximal tilted bearing. Figure 4.20 shows the dimensionless effective area \bar{A}_e for various values of the recess/bearing width ratio b/B versus the dimensionless tilting angle $\bar{\alpha}_x$.

As one would expect, the eccentricity ϵ_x increases for larger tilt angles $\bar{\alpha}_x$. The maximum eccentricity (for tilt angle $\bar{\alpha}_x = 1.0$) increases for smaller values of L/B (figure 4.21) and b/B (figure 4.22). This means that the tilting stiffness in x -direction for hydro-fenders with a larger L/B ratio is smaller than that of hydro-fenders with a smaller L/B ratio.

The hydraulic resistance \bar{R}_h is influenced by the tilting of the hydro-fender in x -direction. This influence increases for smaller L/B (figure 4.23) and smaller b/B (figure 4.24).

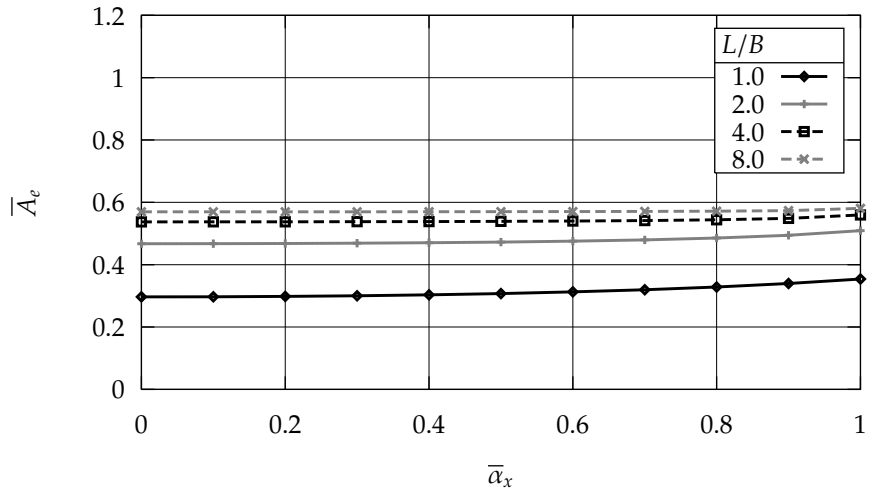


Figure 4.19: Effective area \bar{A}_e of the tilted 1-recess hydro-fender versus the tilting angle $\bar{\alpha}_x$ for various values of L/B . ($b/B = 0.2$)

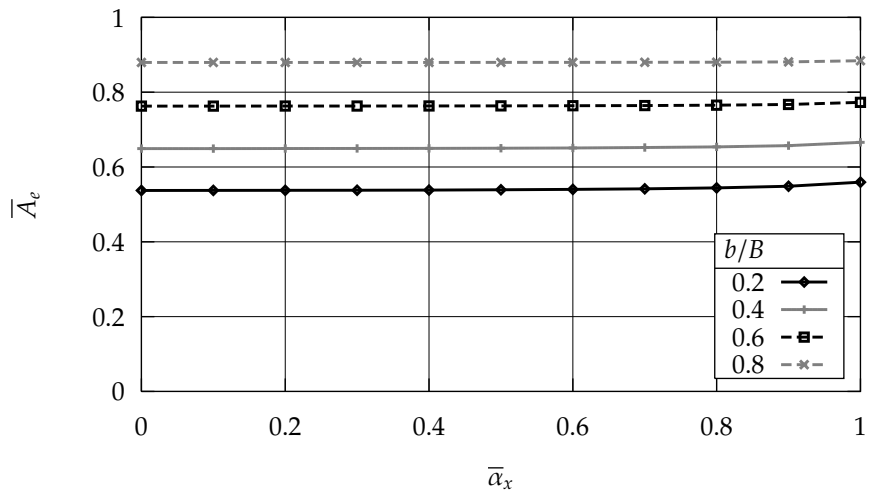


Figure 4.20: Effective area \bar{A}_e of the tilted 1-recess hydro-fender versus the tilting angle $\bar{\alpha}_x$ for various values of b/B . ($L/B = 4.0$)

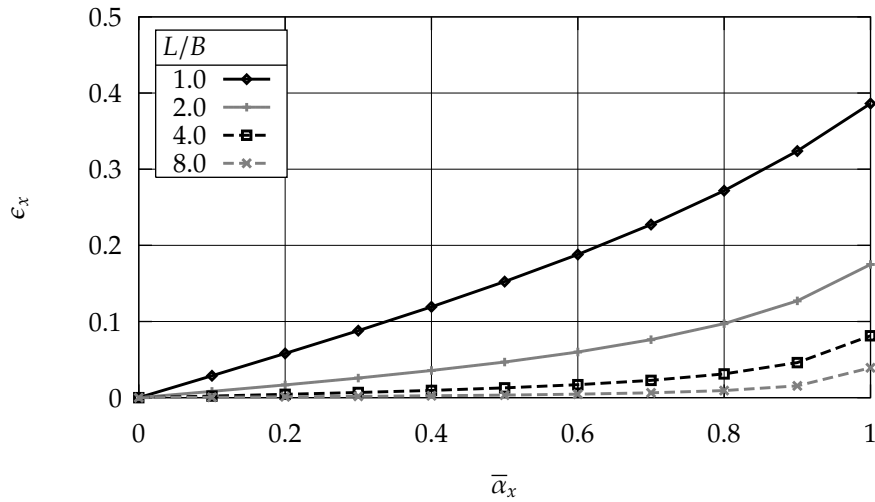


Figure 4.21: Relative eccentricity ϵ_x of the tilted 1-recess hydro-fender versus the tilting angle $\bar{\alpha}_x$ for various values of L/B . ($b/B = 0.2$)

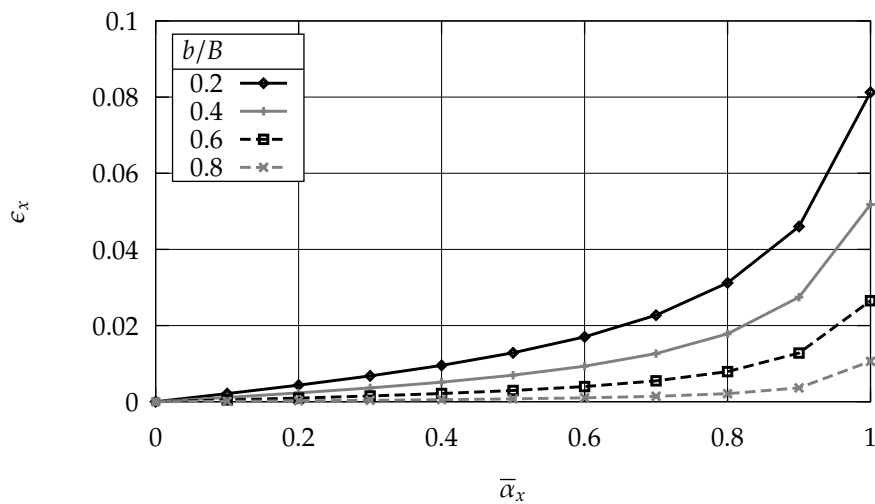


Figure 4.22: Relative eccentricity ϵ_x of the tilted 1-recess hydro-fender versus the tilting angle $\bar{\alpha}_x$ for various values of b/B . ($L/B = 4.0$)

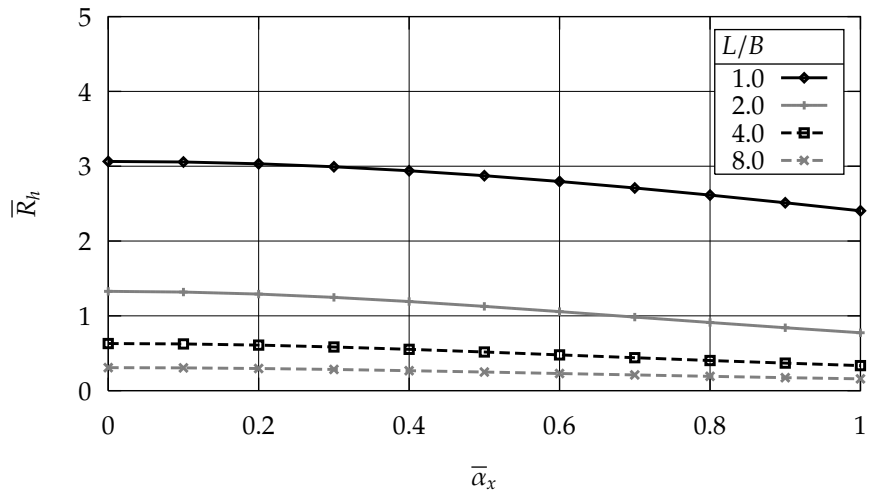


Figure 4.23: Hydraulic resistance \bar{R}_h of the tilted 1-recess hydro-fender versus the tilting angle $\bar{\alpha}_x$ for various values of L/B . ($b/B = 0.2$)

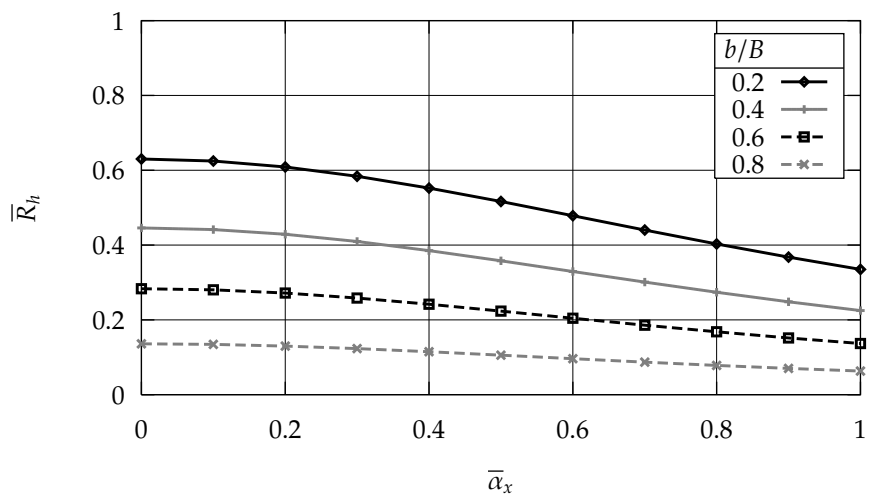


Figure 4.24: Hydraulic resistance \bar{R}_h of the tilted 1-recess hydro-fender versus the tilting angle $\bar{\alpha}_x$ for various values of b/B . ($L/B = 4.0$)

Tilt in y -direction

The lock-gate can be tilted in its supports due to the water height difference on both sides of the door. This tilt is largely compensated by the rubber support between the lock-gate and the bearing, but must also be partly compensated by the lubricating film under the bearing.

If the hydro-fender is tilted in the y -direction the pressure distribution (figure 4.25) is substantially different from that of the non-tilted hydro-fender.

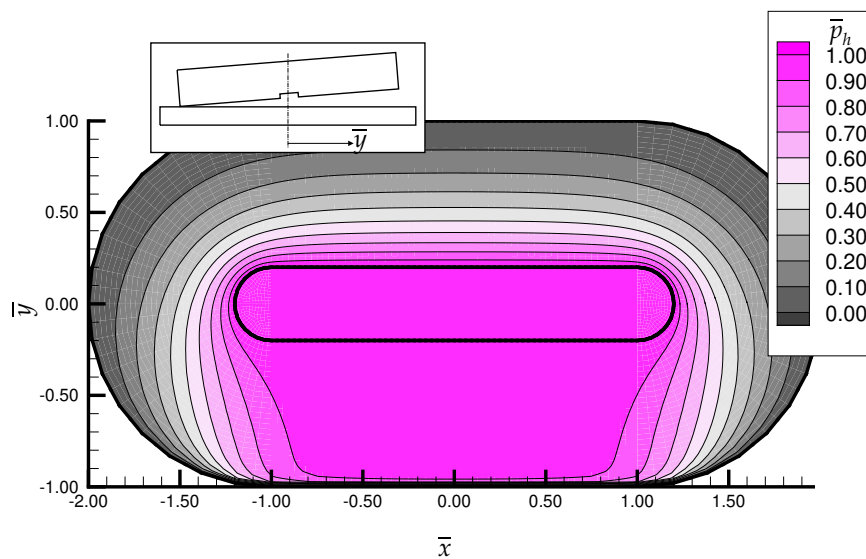


Figure 4.25: Pressure distribution $\bar{p}_h = p_h/p_r$ of a 1-recess hydro-fender with maximum tilt along the y -axis.

However the influence of this tilt on the effective area remains fairly limited. The influence of the tilt angle $\bar{\alpha}_y$ increases for larger values of L/B (figure 4.26). This can be explained by the fact that the pressure distribution is mainly influenced in the center rectangular part of the hydro-fender and obviously this part becomes larger for larger values of L/B . The influence of the tilt angle $\bar{\alpha}_y$ increases for smaller values of b/B (figure 4.27). This can be explained by the fact that the pressure distribution can only vary in the lubricating film, not in the recess. For larger values of b/B the lubricating film becomes smaller and so the possible variation of the pressure distribution.

The eccentricity ϵ_y increases for increased tilt angle $\bar{\alpha}_y$. The maximum eccentricity (for tilt angle $\bar{\alpha}_y = 1.0$) increases slightly for larger values of L/B (figure 4.28). The bearing length/width ratio therefore has only a small influence on the tilting stiffness in y -direction of the hydro-fender. The maximum eccentricity decreases for larger values of b/B (figure 4.29). In order to obtain a larger tilting stiffness a smaller recess/bearing width ratio b/B is required.

The hydraulic resistance \bar{R}_h is influenced by the tilting of the hydro-fender in y -

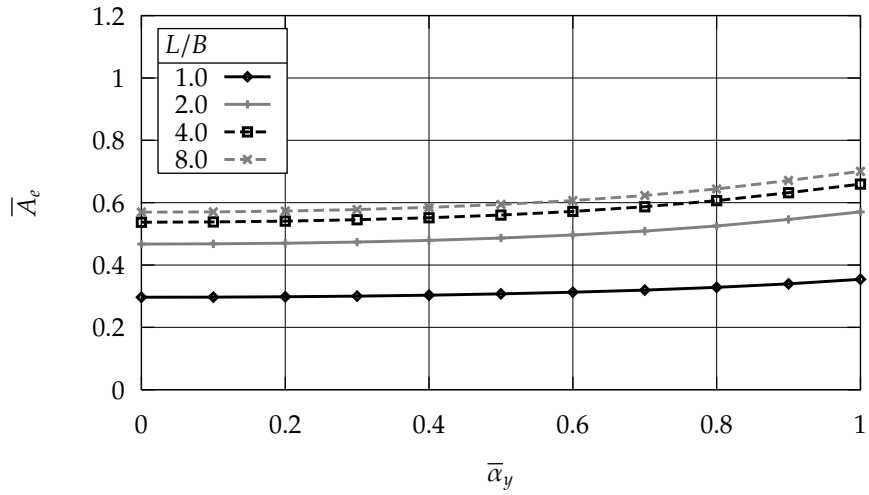


Figure 4.26: Effective area \bar{A}_e of the tilted 1-recess hydro-fender versus the tilting angle $\bar{\alpha}_y$ for various values of L/B . ($b/B = 0.2$)

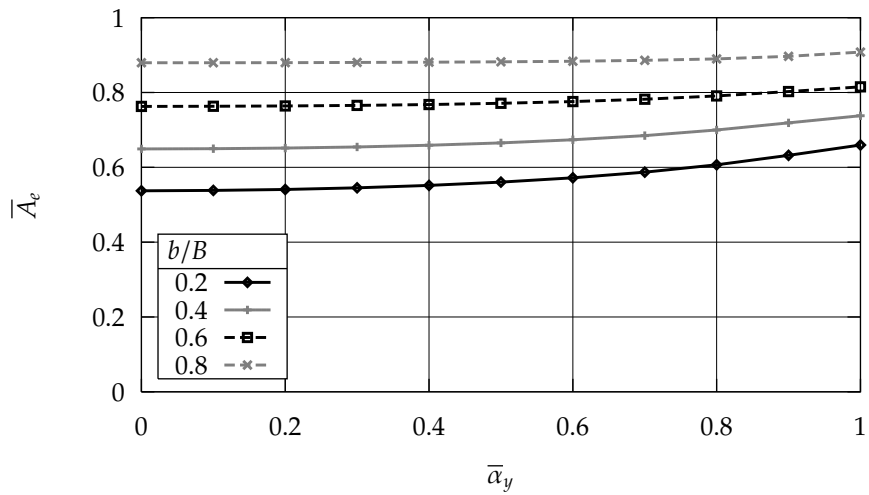


Figure 4.27: Effective area \bar{A}_e of the tilted 1-recess hydro-fender versus the tilting angle $\bar{\alpha}_y$ for various values of b/B . ($L/B = 4.0$)

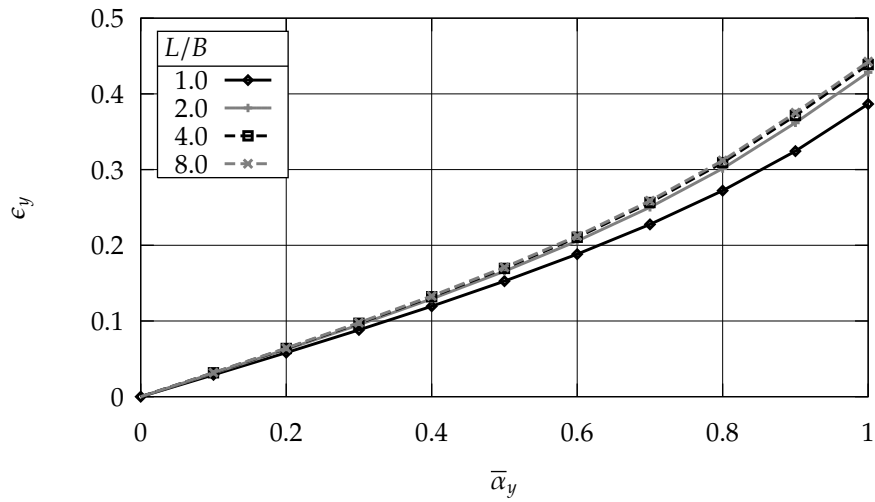


Figure 4.28: Relative eccentricity ϵ_y of the tilted 1-recess hydro-fender versus the tilting angle $\bar{\alpha}_y$ for various values of L/B . ($b/B = 0.2$)

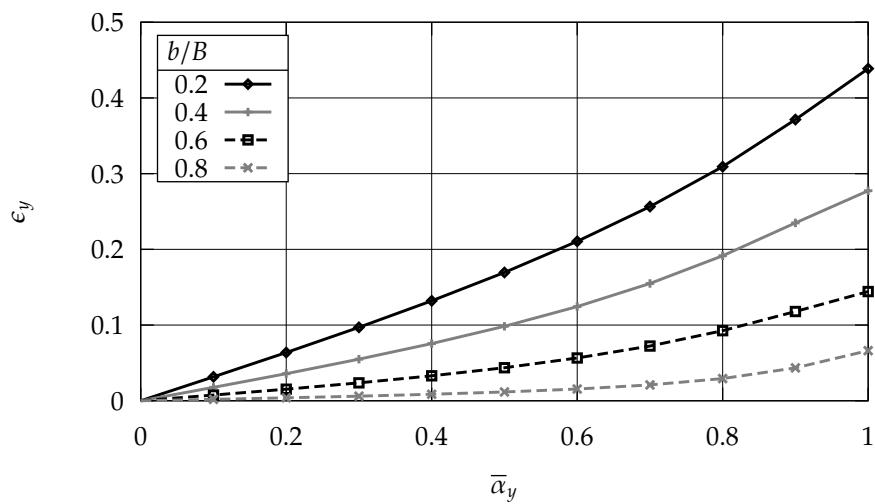


Figure 4.29: Relative eccentricity ϵ_y of the tilted 1-recess hydro-fender versus the tilting angle $\bar{\alpha}_y$ for various values of b/B . ($L/B = 4.0$)

direction. This influence increases for smaller L/B (figure 4.30) and smaller b/B (figure 4.31).

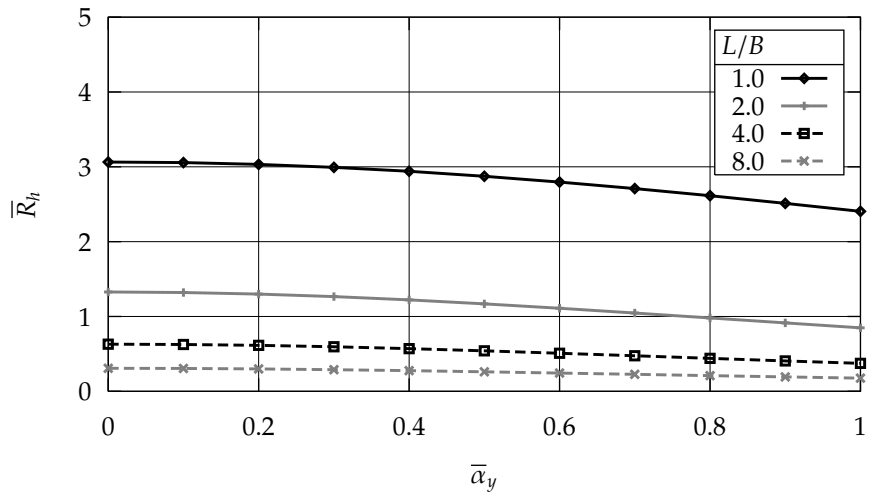


Figure 4.30: Hydraulic resistance \bar{R}_h of the tilted 1-recess hydro-fender versus the tilting angle $\bar{\alpha}_y$ for various values of L/B . ($b/B = 0.2$)

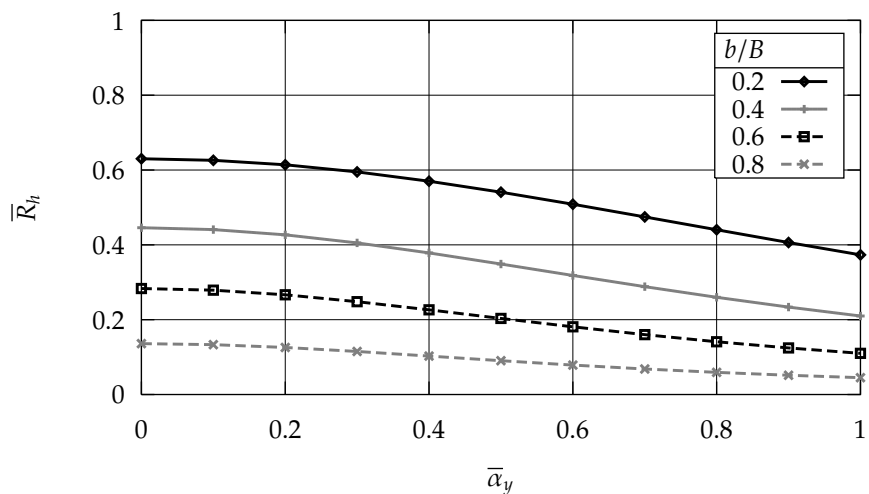


Figure 4.31: Hydraulic resistance \bar{R}_h of the tilted 1-recess hydro-fender versus the tilting angle $\bar{\alpha}_y$ for various values of b/B . ($L/B = 4.0$)

4.3 Properties of the hydro-support including supply

Up to now in this thesis, the properties of the rigid hydro-fender have been studied *excluding* the supply and possible restrictor. In practise however, these properties are largely determined by the combination of the bearing, the restrictor and the supply pump. In particular, for rigid bearing surfaces, the film height is independent of the load (see equations 4.7 and 4.26) and only determined by the flow rate supplied by the pump at a given recess pressure.

The lubricating fluid is pumped by a hydraulic pump through one or more restrictors and bearing recesses into the lubricating film. The function of the restrictor is primarily to increase the axial stiffness of the bearing. If the film height is decreased the flow resistance in the film will increase compared to that of the restrictor. As a result the recess pressure and film pressure will increase resulting in a higher load on the bearing.

A second function of the restrictor is the increase of the tilting stiffness of the multi-recess bearing. More recesses give the bearing tilting stiffness due to the fact that a tilt of the bearing results in a difference between the recess pressures that results in moment that reduces the bearing tilt.

A characteristic property in this regard is the recess/supply pressure ratio β :

$$\beta = \frac{p_r}{p_{\text{sup}}} \quad (4.38)$$

In the classic hydrostatic (multi-recess) thrust bearing design this pressure ratio β is usually chosen to be approximately 0.6.

The volume flow rate through the restrictor is a function of the pressure difference across the restrictor. There are numerous different types of restrictor (BASSANI AND PICCIGALLO, 1992).

In this thesis 3 basic, different types of supply are studied:

- Constant pressure supply. This type of supply maintains a constant recess pressure, independent of the required flow.
- Constant flow supply. This type of supply maintains a constant flow, independent of the resulting recess pressure.
- Laminar restrictor. This type of restrictor consists usually of a long, narrow hole through which a laminar flow flows. The flow is linearly dependent on the pressure difference:

$$Q = (p_{\text{sup}} - p_r) / R_r \quad (4.39)$$

with R_r the hydraulic resistance of the restrictor.

In order to study the properties of rigid hydro-fender including the supply, equations 4.7, 4.11 and 4.39 are repeated here, but rewritten to include the pressure ratio β (equation 4.38).

$$W = \beta p_{\text{sup}} A \bar{A}_e \quad (4.40a)$$

$$Q = \frac{\beta p_{\text{sup}} h^3}{\eta} \frac{1}{R_h} \quad (4.40b)$$

$$Q = p_{\text{sup}} (1 - \beta) / R_r \quad (4.40c)$$

For a given bearing geometry and supply, A , \bar{A}_e , \bar{R}_h , R_r and p_{sup} are constants, whereas h , W , Q and β vary depending on the operating conditions. In a given reference situation, the film height is assumed to be equal to h_0 , the load to W_0 , the flow rate to Q_0 and the pressure ratio to β_0 . Comparing an arbitrary operating point to this reference situation yields (from equation 4.40a):

$$W_0 = \beta_0 p_{\text{sup}} A \bar{A}_e \quad (4.41a)$$

$$W = \beta p_{\text{sup}} A \bar{A}_e \quad (4.41b)$$

and therefore:

$$\frac{W}{W_0} = \frac{\beta}{\beta_0} \quad (4.42a)$$

Similarly from equations 4.40b, respectively 4.40c:

$$\frac{Q}{Q_0} = \frac{\beta}{\beta_0} \left(\frac{h}{h_0} \right)^3 \quad (4.42b)$$

$$\frac{Q}{Q_0} = \frac{1 - \beta}{1 - \beta_0} \quad (4.42c)$$

Now the properties of our basic supply types can be derived, yielding expressions for the load and flow as function of the film height:

- Constant pressure supply: The recess pressure and therefore β is constant ($\beta = \beta_0$). For the load follows from equation 4.42a:

$$\frac{W}{W_0} = 1 \quad (4.43a)$$

and for the flow from equation 4.42b:

$$\frac{Q}{Q_0} = \left(\frac{h}{h_0} \right)^3 \quad (4.43b)$$

- Constant flow supply: The flow is constant ($Q = Q_0$) and therefore from equation 4.42b follows:

$$\frac{\beta}{\beta_0} = \left(\frac{h_0}{h}\right)^3$$

Substituting into equation 4.42a yields:

$$\frac{W}{W_0} = \left(\frac{h_0}{h}\right)^3 \quad (4.44a)$$

The flow rate by definition is now:

$$\frac{Q}{Q_0} = 1 \quad (4.44b)$$

- Laminar restrictor: First an expression for β as function of h is derived. Equating equations 4.42b and 4.42c yields:

$$\frac{\beta}{\beta_0} \left(\frac{h}{h_0}\right)^3 = \frac{1 - \beta}{1 - \beta_0}$$

or:

$$\frac{\beta}{\beta_0} = \frac{1}{\beta_0 + \left(\frac{h}{h_0}\right)^3 (1 - \beta_0)} \quad (4.45)$$

Substituting into 4.42a yields for the load:

$$\frac{W}{W_0} = \frac{1}{\beta_0 + \left(\frac{h}{h_0}\right)^3 (1 - \beta_0)} \quad (4.46a)$$

and substituting into 4.42b yields for the flow:

$$\frac{Q}{Q_0} = \frac{\left(\frac{h}{h_0}\right)^3}{\beta_0 + \left(\frac{h}{h_0}\right)^3 (1 - \beta_0)} \quad (4.46b)$$

From these 2 equations it is clear that the constant pressure supply and the constant flow supply can be considered to be asymptotes of this type of supply. The constant recess pressure supply is obtained by choosing a nominal pressure ratio $\beta_0 = 1$ and the constant flow rate by choosing a $\beta_0 = 0$.

Figures 4.32 and 4.33 show the load and flow rate respectively for a number of different pressure ratios β_0 versus the relative film height h/h_0 . The axial stiffness of the bearing is higher for smaller values of β_0 . However, a small pressure ratio β_0 means that a large fraction of the supply power is dissipated in the restrictor. Another method to obtain a large axial stiffness is to use a constant flow rate supply.

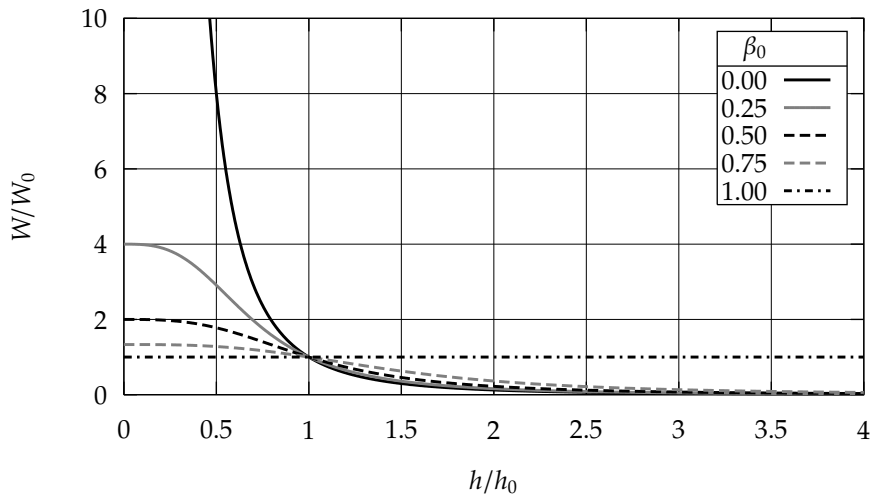


Figure 4.32: Load capacity W of a hydro-support relative to a reference point (h_0, W_0, β_0) .

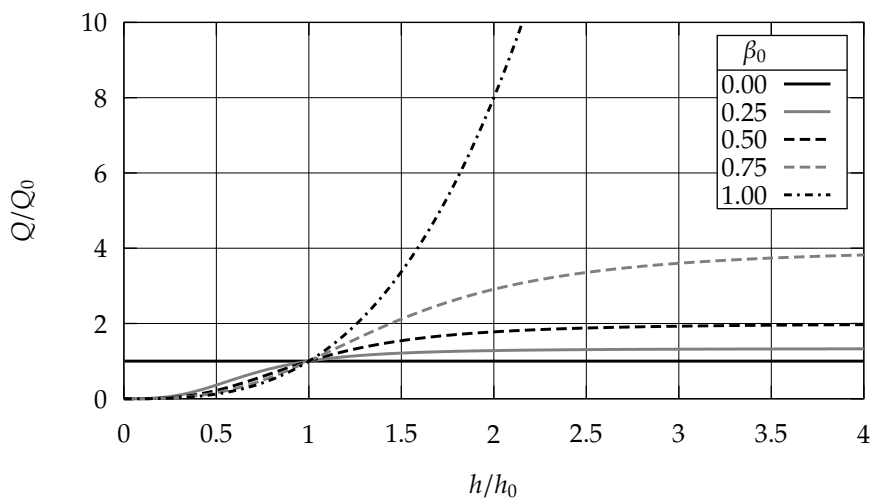


Figure 4.33: Flow rate Q of a hydro-support relative to a reference point (h_0, Q_0, β_0) .

CHAPTER 5

Track deformation and surface description

The hydrostatic bearing slides on a track. This track is made of a polymer and fixed to a concrete foundation. Ideally the track surface is perfectly smooth and plane, however there are several reasons why in practise this isn't feasible:

- The surface of the concrete foundation on which the track is fixed, isn't perfectly plane. This surface waviness of the foundation is partly passed on to the surface of the track.
- The track itself isn't perfectly plane or smooth. Surface waviness and roughness will occur during the production process of the track and to a certain extent be unavoidable.
- Due to the length required, the track will most likely consist of a number of parts that are joined (imperfectly) head to tail. So a surface height difference between two consecutive parts will probably occur.
- In use, damage may occur to the track surface. For instance, a ships anchor could drop on the track resulting in a groove or indentation of the track surface.

The track is made from a visco-elastic material. Therefore the track will deform due to the load of the bearing on the track. Furthermore, the track is fixed on a foundation, usually made from concrete, which will also deform as a result of the load. The influence of the foundation can be split into two components:

- Local deformation of the foundation within the contour of the bearing: It is assumed that, due to the large difference of the Youngs' moduli of the concrete foundation ($\approx 4 \cdot 10^{10} \text{N/m}^2$) and the UHMWPE track ($\approx 1 \cdot 10^9 \text{N/m}^2$), the combined deformation of the track and its foundation is primarily the result of the deformation of the track. The contribution of the local deformation of the foundation will be neglected.

- Global deformation of the foundation: The foundation which consists of a concrete plate or beam, will bend as a result of the load. Locally, within the contour of the bearing, this will result in an angle of the track relative to the gate. The rubber support between the bearing and the gate will deform to accommodate this angle.

In the next section a model is derived to describe the deformation of the track.

5.1 Track deformation

Ideally the hydro-support slides on a track fully separated from this track by a water film. In this case the wear of the surface materials is very low. The surface materials are selected for their tribological properties in case this water film is absent e.g. due to pump failure. In wet conditions the material combination of stainless steel and Ultra-High-Molecular-Weight-Poly-Ethylene (UHMWPE) exhibits very low wear and friction. For this reason the track in the PWA-lock is made from UHMWPE, the bearing from stainless steel.

The mechanical behavior of polymers like UHMWPE is time and temperature dependent and non-linear. A complete description of this behavior should incorporate a smooth transition between the linear elastic to the visco-elastic and visco-plastic region. A large number of different constitutive equations have been proposed in order to describe different aspects of this material behavior. Basic models describing *visco-elastic* material behavior are the Maxwell model, the Voigt model and the “standard linear” model, all of which can be depicted as combinations of linear springs and dashpots (FUNG, 1994). Combined with models describing the *visco-plastic* behavior of the polymer a complete constitutive model for the material behavior can be derived. In BERGSTRÖM ET AL. (2002) some of the more recently developed models have been compared for their accuracy in cyclic loading conditions. However, in this thesis it is assumed that the track will only deform elastically and plastic deformation will be ignored.

The following simple empirical visco-elastic result between the uni-axial strain ϵ and stress σ in an UHMWPE test-rod, has been proposed (Ros, 1984):

$$\epsilon = \left(\frac{\sigma}{\sigma_r}\right) \log_{10} \left(\frac{\tau}{\tau_r}\right) \quad (5.1)$$

with the loading time τ , reference time τ_r and corresponding reference stress σ_r . For the UHMWPE used in the PWA-lock the reference stress $\sigma_r = 1.0 \cdot 10^9 \text{N/m}^2$ and reference time $\tau_r = 0.190 \text{s}$ were found. Note that this relation produces unrealistic values for ϵ for times τ smaller than τ_r , in which case ϵ becomes negative for positive values of σ . Relation 5.1 has been derived using experiments with very large values for τ ($\approx 2.0 \cdot 10^5 \text{s}$) and should only be used in these conditions. The material of the track in

the PWA–lock however, is loaded for ≈ 3 s at each passage. In this case, relation 5.1 should not be used.

The manufacturer of the UHMWPE track material provides a constant value for the modulus of elasticity of $1.0 \cdot 10^9 \text{ N/m}^2$. In the model, this constant value will be used and the track is therefore assumed to behave linear elastic instead of visco–elastic/plastic. In section 16.2 the influence of the track modulus of elasticity will be studied. It will be shown that on a track with surface waviness, the variation of the bearing coefficient and flow is small for different values of the track modulus of elasticity. In contrast, the dependence on the exact track surface waviness geometry (16.1.2) is large. However, this track surface waviness can only be specified in an average sense, not deterministically. The variation of the results due to the different track moduli of elasticity can therefore be neglected compared to the variation of the results due to the *unknown* different surface wavinesses. Therefore, it is assumed that any visco–elastic effects in the material behavior may be neglected and that the use of the linear elastic material model is justified.

The track deforms due to the pressure caused by the hydrostatic water film and the partial contact on the track. Generally, the indentation at a point (x, y) of the surface is dependent on the pressure on the surface:

$$u_t(x, y) = - \iint_S p_t(\xi, \eta) K_t(x - \xi, y - \eta) d\xi d\eta \quad (5.2)$$

with the indentation of the track $u_t(x, y)$ at point (x, y) , pressure on the track $p_t(\xi, \eta)$ at point (ξ, η) and a kernel $K_t(x - \xi, y - \eta)$ relating both quantities. The minus sign in equation 5.2 is a result of the fact that a positive pressure p on the track results in an indentation u_t in the negative direction.

The relation between the surface pressure and surface indentation of the track (that is the kernel K_t from equation 5.2) can be obtained using different models:

- The deformation of the track is calculated using a numerical, full 3D elasticity calculation. This method is accurate but costly.
- The deformation of the track is calculated using the thin layer model (DRAGONI AND STROZZI, 1993; KALKER, 1990; STROZZI, 2000). As the name indicates this method can be used when a thin elastic layer on a rigid foundation is loaded with a distributed load on a relatively large area. The model is based on a series approximation of the track indentation (DRAGONI AND STROZZI, 1993). In this case the indentation u_t of an elastic layer with thickness t_t , modulus of elasticity E_t and Poisson's ratio ν_t as a result of a pressure p_t is equal to:

$$u_t(x, y) = - \frac{(1 + \nu_t)(1 - 2\nu_t)}{E_t(1 - \nu_t)} t_t p_t(x, y) = - \frac{1}{E_t^*} p_t(x, y) \quad (5.3)$$

Thus, the indentation at point (x, y) is only dependent on the pressure at that point. The model is only valid for compressible materials. The Poisson ratio

for UHMWPE is approximately equal to 0.46 (WRIGHT ET AL., 1991) and therefore UHMWPE is nearly incompressible. The applicability of the thin layer model must therefore be examined.

Figure 5.1 shows the indentation of a track surface calculated using both methods. The pressure on the track is the hydrostatic pressure of the lubricating film. The recess pressure is equal to $10 \cdot 10^5 \text{N/m}^2$, the track thickness t_t is equal to 0.07 m and other properties and dimensions are equal to those in the PWA-lock (appendix A). No contact is assumed.

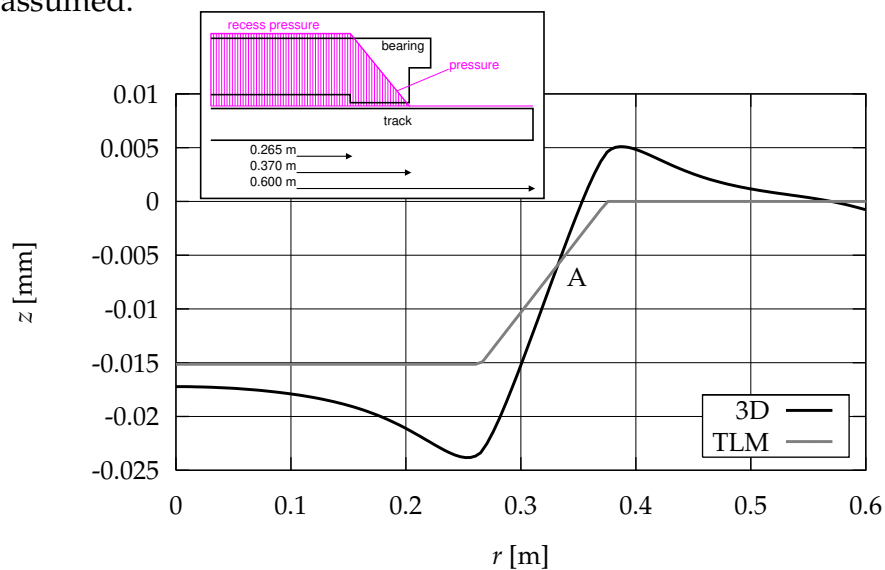


Figure 5.1: Indentation of the PWA-lock track calculated using the Thin Layer Model (TLM) and the full 3D linear elastic model (3D) as a result of the hydrostatic pressure (recess pressure $10 \cdot 10^5 \text{N/m}^2$, track thickness 0.07 m). For other pertinent dimensions and properties of the track see appendix A.

There is some similarity between the results of both models. However, compared to the thin layer model, the ‘exact’ 3D solution shows a large groove at the recess edge and a large ridge at the bearing edge. These features are caused by the large pressure gradient differences at these points. The first order approximation of the deformation used in the thin layer model shows a large deviation here. Note however that the nominal lubricating film thickness ($\approx 0.1 \text{mm}$) is more than 4 times the maximum indentation ($\approx 0.025 \text{mm}$) of the track.

Using the results in figure 5.1, we can verify the assumption made previously that the time dependent behavior of the material can be neglected. The time dependent stress component in the material is determined by the rate of strain in the material. The bearing is sliding with a constant speed of 0.24 m/s along the track. The rate of deformation is at its maximum approximately in the middle of the lubricating film (point A in figure 5.1). In point A, the gradient of the deformation is approximately

(using the 3D model result):

$$\frac{0.032 \text{ mm}}{0.105 \text{ m}} = 3 \cdot 10^{-4} \quad (5.4)$$

If we assume that the strain is uniform across the track, then the rate of strain in point A can be approximated:

$$\dot{\epsilon} = \frac{3 \cdot 10^{-4}}{0.07 \text{ m}} \cdot 0.24 \text{ m/s} = 1 \cdot 10^{-3} 1/\text{s} \quad (5.5)$$

This strain rate is very low, comparable to that used in a typical tension or compression test used to determine the modulus of elasticity ($0.25 \cdot 10^{-3} 1/\text{s}$, see JEBBINK (1996)). Therefore, we can assume that the time dependent behavior in the deformation of the track can be neglected.

Figure 5.2 shows the vertical stress σ_{zz} in the track, calculated using the ‘exact’ 3D model. The thin layer model assumes a constant σ_{zz} through the thickness of the track. It is clear that at the positions with a large pressure gradient difference this assumption is less valid.

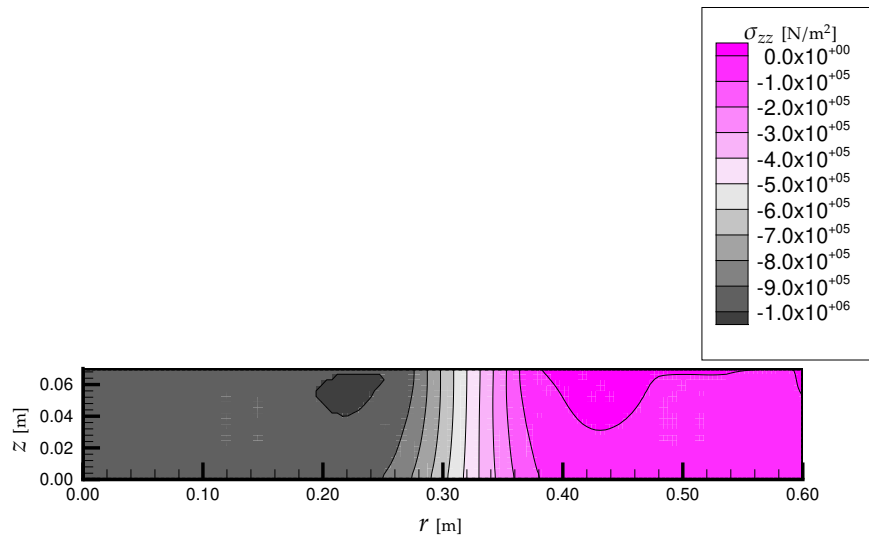


Figure 5.2: Stress σ_{zz} [N/m²] in the track.

The use of the full 3D model is less numerically efficient than the use of the thin layer model. At best, it requires the determination of a stiffness matrix for the track, followed by a condensation of this matrix to a smaller surface stiffness matrix in which only the unknown track surface displacements are represented. This surface stiffness matrix must then be used at each iteration to determine the indentation of the track due to the distributed hydrostatic and contact pressures.

As was stated earlier, in chapter 16 it is shown that, on a track with surface waviness, the influence of the track thickness and elasticity is fairly limited compared to the

influence of other parameters (in particular, the surface waviness geometry) in the model. Therefore, the numerically more efficient thin layer model can be used, instead of the full 3D model without substantial loss of accuracy.

5.2 Track surface description

As stated before, the track surface isn't perfectly smooth or plane. In practise the surface waviness is even substantially larger than the nominal film thickness of the lubricating film. For instance, the surface waviness of the track in the PWA-lock is approximately equal to 0.5 mm/m, the nominal film height 0.1 mm.

Because of this surface waviness partial contact will occur between the bearing and the track, carrying a fraction of the total load. The extent of this partial contact is dependent on the surface texture of the track. The surface texture of a surface can be separated into three parts: error of form (I), surface waviness (II) and surface roughness (III). In figure 5.3 a power spectrum of a typical engineering surface is presented. The power spectrum is essentially a presentation of the contribution of wave-components with different wave lengths to the surface roughness (THOMAS, 1999). The distinction

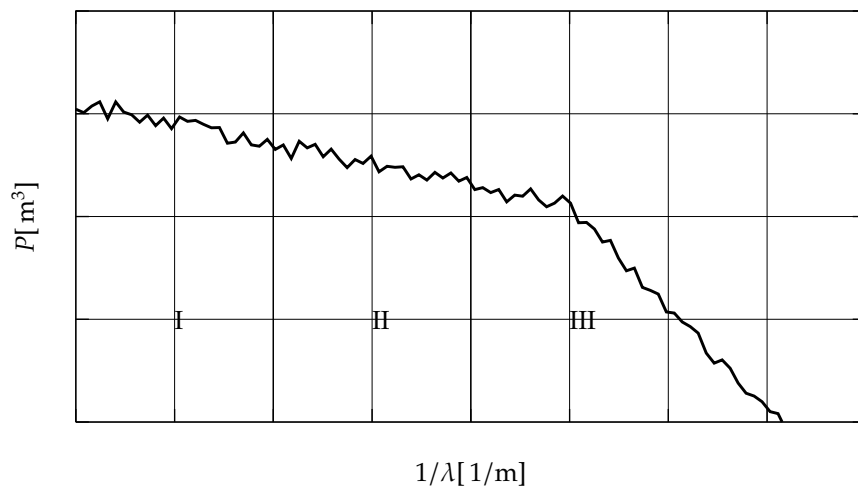


Figure 5.3: Power spectrum of a typical surface texture: (I) Error of form, (II) Waviness (III) Roughness.

between these different types of surface texture is based on their wave length λ . Errors of form have a very large wave length, surface waviness has a smaller wave length and surface roughness has a very small wave length. The transition from one type of surface texture to the next isn't exactly defined. In the present study this transition is defined by the numerical model: Surface textures that can just be represented on the mesh used in the numerical calculations will be called surface waviness. Surface

textures with a larger wave length will be called error of form, surface textures with a shorter wave length surface roughness.

In order to describe the track surface texture first a number of different textures is recognized:

- Tilt of the lock-gate: Due to the water level difference on both sides of the lock-gate, the gate will be tilted in its support. In the model this tilt can be translated into a tilt or misalignment of the track relative to the bearing.
- Height difference between adjacent track parts: Figure 5.4 shows the height differences measured at the joints between track parts in the PWA-lock. The track parts are connected using finger joints. The line $b - a$ denotes the height difference measured at the end of the fingers of track part a between the track parts a and b . Conversely, the line $a - b$ denotes the height difference measured from the end of the fingers of track part b .

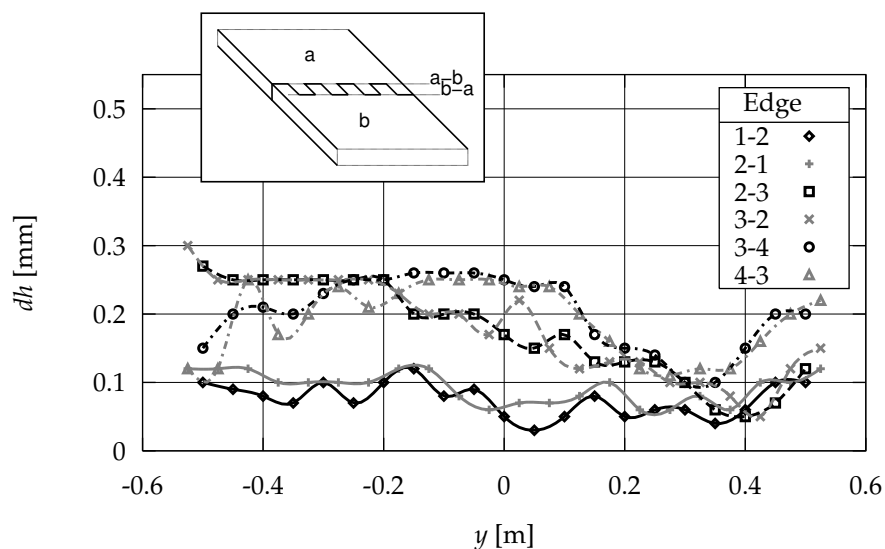


Figure 5.4: Height differences between adjacent track sections. The height differences between track parts a and b are measured both at the end of the fingers of part a (line $b - a$) and of part b (line $a - b$).

- Surface waviness on a track part: This waviness is partly due to the surface waviness of the foundation that is passed on to the track surface and partly due to height variations in the track part itself. Figure 5.5 shows the height variation measured on a test track for the PWA-lock.
- Roughness: Surface texture with a very short wave length is called surface roughness.

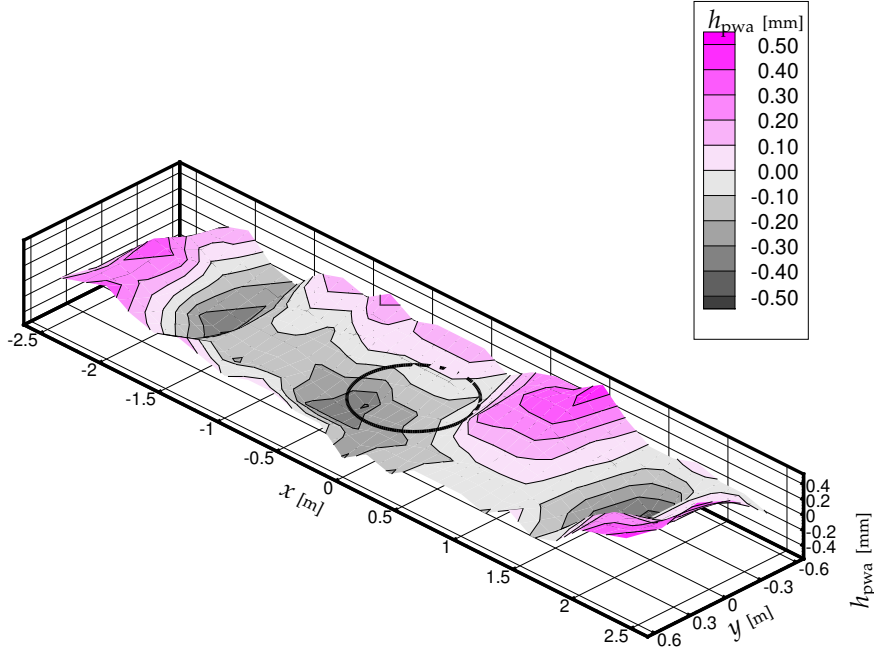


Figure 5.5: The height of the surface [mm] of a test track relative to a plane reference surface. The surface has been measured on a grid of 0.2 m along the track and 0.3 m across.

In this thesis a surface waviness model is assumed that provides a simple approximation of the true surface waviness as for instance shown in 5.5. A general method to describe a surface waviness is given by KALKER ET AL. (1995):

$$h_{\text{wav}}(x, y) = \sum_{m=0}^M \sum_{n=0}^N a_{mn} \gamma^{m+n} \cos\left(\frac{2\pi mx}{\lambda_x} + \phi_{xmn}\right) \cos\left(\frac{2\pi ny}{\lambda_y} + \phi_{ymn}\right) \quad (5.6)$$

This surface consists of $(M+1)(N+1)$ components. λ_x and λ_y are the wave lengths of the components with the largest wave lengths and M and N the number of components in x and y direction respectively. The surface described by equation 5.6 is random but periodic. The amplitude parameters a_{mn} , phase parameters ϕ_{xmn} , ϕ_{ymn} are chosen randomly from:

$$\begin{cases} a_{mn} = 0 & \text{If } m = 0 \text{ and } n = 0 \\ 0 \leq a_{mn} \leq A & \text{Otherwise} \end{cases} \quad (5.7a)$$

and:

$$0 \leq \phi_{xmn}, \phi_{ymn} \leq 2\pi \quad (5.7b)$$

The attenuation parameter γ is given a value of 0.8, which, according to KALKER ET AL. (1995), produces a realistic rough surface. The attenuation parameter γ denotes the

measure with which the amplitude of high frequency components and thus small wavelength components (or components with large values of m or n) decrease compared to low frequency components.

For the description of surface *roughness* the surface autocovariance function has been introduced (THOMAS, 1999):

$$S(x, y) = \frac{1}{L_x L_y} \int_0^{L_x} \int_0^{L_y} z(x', y') z(x' + x, y' + y) dx' dy' \quad (5.8)$$

The root mean square (RMS) surface roughness is defined as:

$$S_q^2 = S(0, 0) = \frac{1}{L_x L_y} \int_0^{L_x} \int_0^{L_y} z^2(x', y') dx' dy' \quad (5.9)$$

with L_x and L_y the evaluation lengths in x and y direction respectively. This roughness parameter is comparable to the RMS *profile* roughness R_q :

$$R_q^2 = \frac{1}{L} \int_0^L z^2(x') dx' \quad (5.10)$$

that is measured along a line on the surface, contrary to S_q that is measured on the surface.

If these definitions are used for the surface *waviness* generated with equation 5.6, it has been shown (KALKER ET AL., 1995) that the surface autocovariance function $S(x, y)$ of this surface is given by:

$$S(x, y) = \frac{1}{4} \sum_{m=0}^M \sum_{n=0}^N a_{mn}^2 \gamma^{2(m+n)} \cos\left(\frac{2\pi mx}{\lambda_x}\right) \cos\left(\frac{2\pi ny}{\lambda_y}\right) \quad (5.11a)$$

and the RMS surface roughness S_q by:

$$S_q^2 = \frac{1}{4} \sum_{m=0}^M \sum_{n=0}^N a_{mn}^2 \gamma^{2(m+n)} \quad (5.11b)$$

Surface roughness will be further discussed in the next section 5.3. Note however that equation 5.6 is used in this study to describe surface *waviness* whereas this equation was introduced in KALKER ET AL. (1995) to describe surface *roughness*. It is therefore assumed that surface waviness and surface roughness can be described using the same general equation.

Figure 5.6 shows an example of a surface generated with equation 5.6. This surface and the measured surface waviness in figure 5.5 are fairly similar in shape as they both show separated peaks and valleys randomly distributed on the surface.

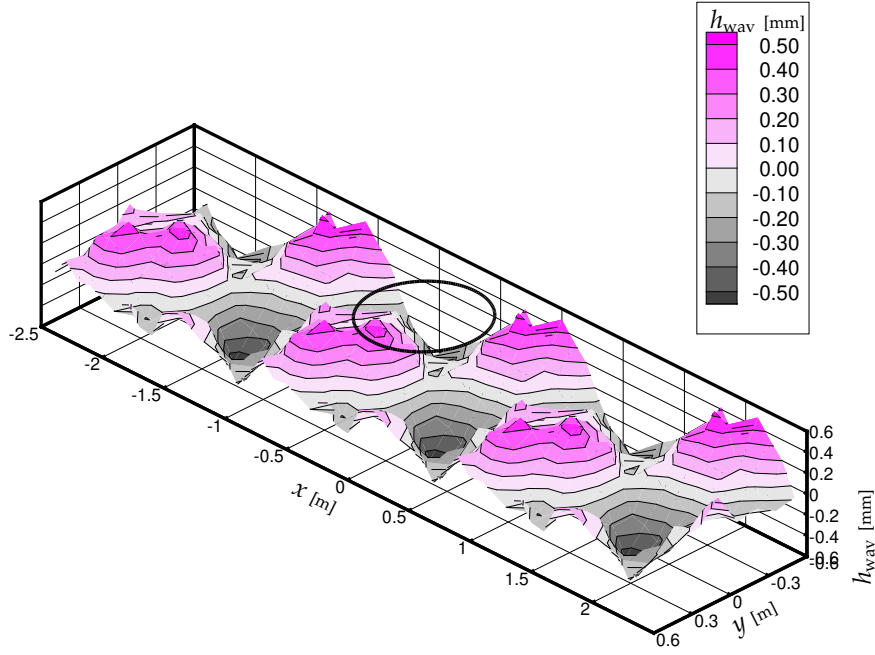


Figure 5.6: Track surface with a periodic random waviness.

Equation 5.6 can also be used to generate a basic surface waviness using a suitable choice of parameters:

- Surface with a single wave in x -direction:

$$h_{\text{wav}}(x, y) = a_{10}\gamma \cos\left(\frac{2\pi x}{\lambda_x} + \phi_{x10}\right) \quad (5.12)$$

where $M = 1, N = 0$ and $a_{10} \neq 0$ and $\phi_{y10} = 0$.

- Surface with a single wave in x and y -direction:

$$h_{\text{wav}}(x, y) = a_{11}\gamma \cos\left(\frac{2\pi x}{\lambda_x} + \phi_{x11}\right) \cos\left(\frac{2\pi y}{\lambda_y} + \phi_{y11}\right) \quad (5.13)$$

where $M = 1, N = 1$ and $a_{10} = 0, a_{01} = 0, a_{11} \neq 0$.

A basic surface which cannot easily be obtained using equation 5.6 is the step waviness:

$$h_{\text{wav}}(x, y) = \begin{cases} h_s/2 & \text{if } x < x_s \\ -h_s/2 & \text{otherwise} \end{cases} \quad (5.14)$$

where h_s is the step height and x_s the position of the step.

In the numerical model every type of surface waviness described above has been implemented:

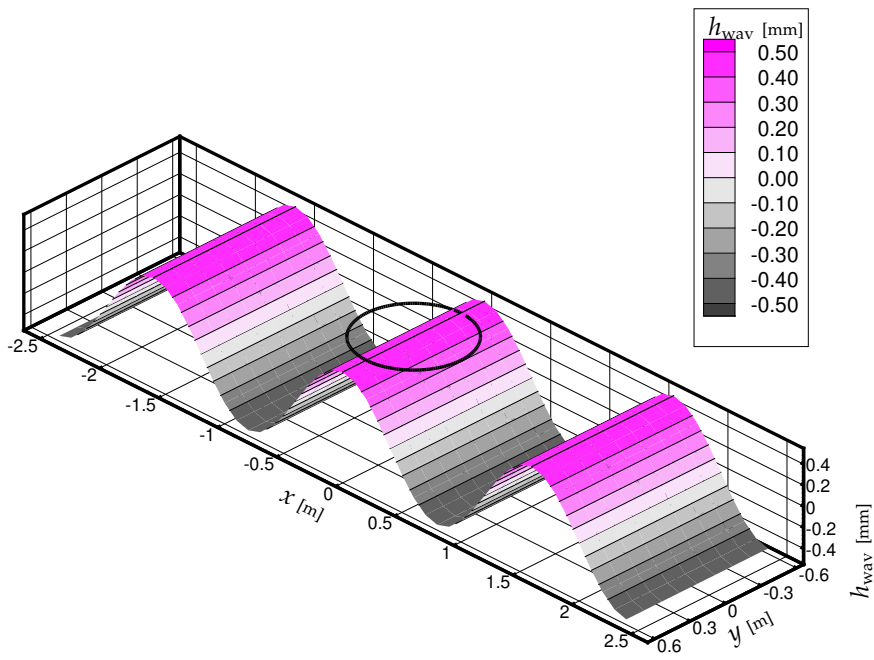


Figure 5.7: Track surface with a periodic 1-D waviness.

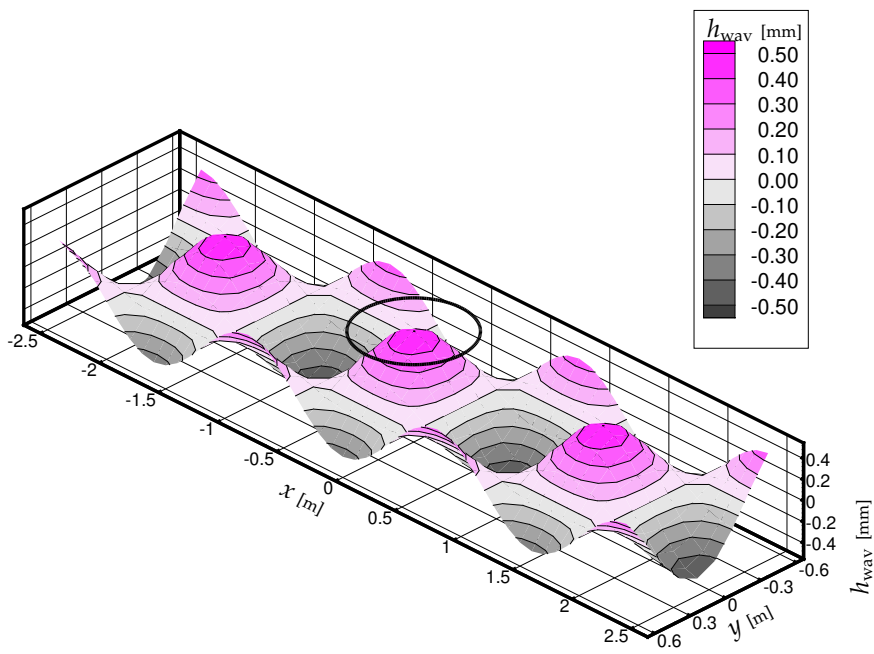


Figure 5.8: Track surface with a periodic 2-D waviness.

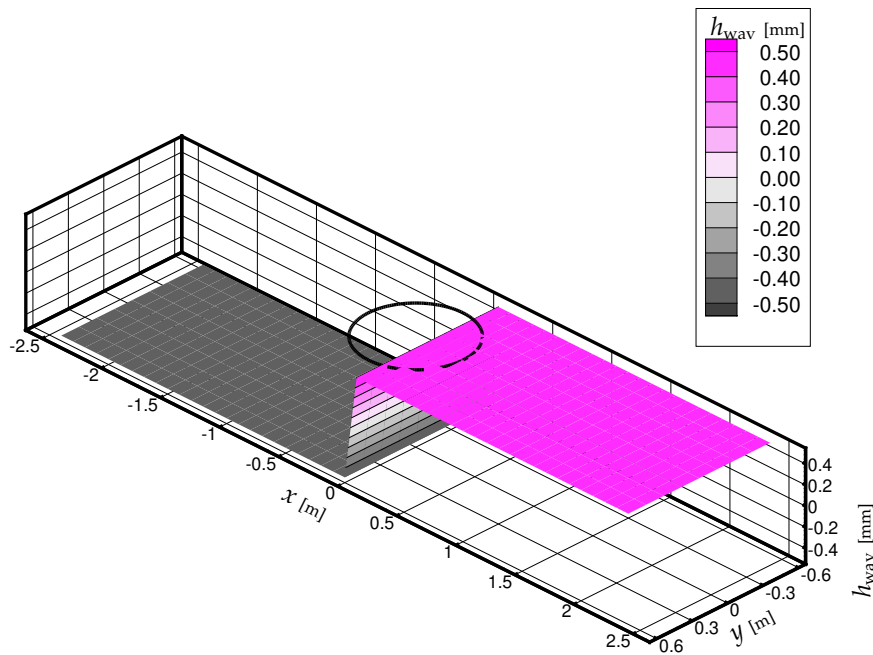


Figure 5.9: Track surface with a single step.

- A random periodic surface (equation 5.6).
- Surface with a single wave in x -direction (equation 5.12).
- Surface with a single wave in x and y -direction (equation 5.13).
- Surface with a step (equation 5.14).

5.3 Surface roughness description

In the previous section a deterministic model for a basic surface waviness has been presented. In contrast, the surface roughness is usually described by a stochastic model (ARCHARD, 1974; THOMAS, 1999). Recently a fractal surface roughness has been developed based on the observation that surface roughness seems to be similar on different scales (MAJUMDAR AND BHUSHAN, 1990, 1991; SAHOO AND CHOWDHURY, 2000). WHITEHOUSE (2001) has recently shown some limitations of this fractal surface description.

It is assumed that the surface roughness height is normally distributed (figure 5.10). A reference plane is defined to be the average or mean plane through this roughness profile. Thus the roughness height probability density function $\phi(z)$ of the surface is equal to:

$$\phi(z) = \frac{1}{S_q \sqrt{2\pi}} \exp\left(-\frac{1}{2} \left(\frac{z}{S_q}\right)^2\right) \quad (5.15)$$

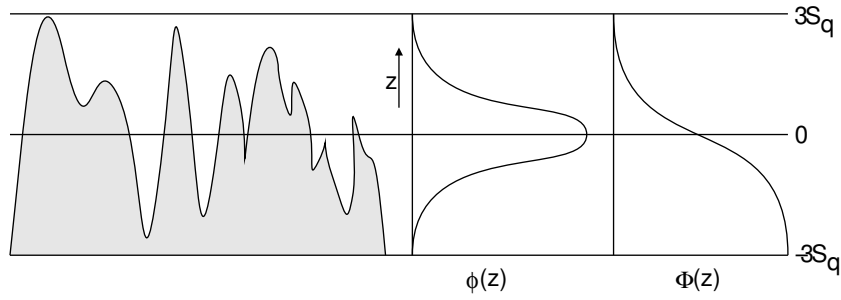


Figure 5.10: Rough surface with the corresponding roughness distribution.

The probability that a point on the surface has a height between h and $h + \Delta h$ relative to the reference plane is then equal to $\phi(h)\Delta h$. The probability that a point on the surface has a height larger than h is then equal to the complement of the cumulative probability distribution function $\Phi(h)$:

$$\Phi(z) = \int_z^{\infty} \phi(z') dz' = \frac{1}{2} \left(1 - \operatorname{erf} \left(\frac{z}{\sqrt{2}S_q} \right) \right) \quad (5.16)$$

with the error function $\operatorname{erf}(x)$ defined as:

$$\operatorname{erf}(x) = \frac{2}{\sqrt{\pi}} \int_0^x e^{-x'^2} dx' \quad (5.17)$$

This means that the probability that a point on the surface has a height higher than 0, S_q and $3S_q$, is equal to 0.5, 0.159 and 0.00135 respectively.

When two rough surfaces with a normal height distribution with RMS roughness S_{q_a} and S_{q_b} make contact, the cumulative height distribution is comparable to the contact of a smooth surface and a surface with a normal height distribution with RMS roughness S_q :

$$S_q = \sqrt{S_{q_a}^2 + S_{q_b}^2} \quad (5.18)$$

The roughness of a surface is not only defined by its RMS roughness value but also by the periodicity of the roughness. This periodicity can be expressed by the so-called auto-correlation function $\rho(x)$:

$$\rho(x) = \frac{1}{R_q^2} \frac{1}{L-x} \int_0^{L-x} z(x')z(x+x') dx' \quad (5.19)$$

If the surface roughness is non-isotropic (due to the manufacturing process used or due to wear) this auto-correlation function is dependent on the direction in which it is measured.

It has been shown in THOMAS (1999) that for some manufacturing processes the auto-correlation function $\rho(x)$ of the resulting surface can be approximated using an exponential function:

$$\rho(x) = \exp(-x/\beta) \tag{5.20}$$

with β the auto-correlation length.

In case of a non-isotropic surface roughness the auto-correlation lengths in x and y direction will differ, and are equal to β_x and β_y , respectively. The asperity aspect ratio of the surface roughness γ is given by:

$$\gamma = \frac{\beta_x}{\beta_y} \tag{5.21}$$

5.4 Conclusion

In this chapter the first parts of the mathematical model which will be used to study the behavior of the hydro-support, have been presented. These parts are all related to the modelling of the track: The first part is a model for the indentation of the track, the so-called thin layer model. The second part is a description of the surface waviness and surface roughness of the track. The surface waviness is described using a deterministic description, the surface roughness using a stochastic description (figure 5.11).

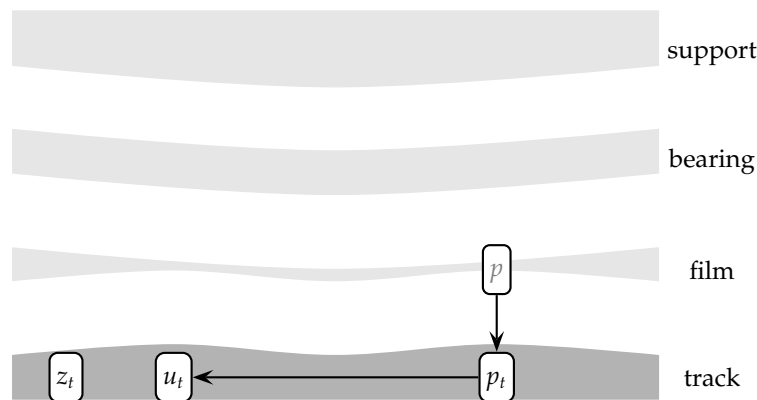


Figure 5.11: Component of the model described in this chapter: The track.

In the next chapter the interaction of the track surface and the bearing surface in mixed lubrication will be studied.

If the load on the bearing is too great and/or the surface waviness too high, contact between the bearing and the track will occur in multiple contact areas (figure 6.1). In

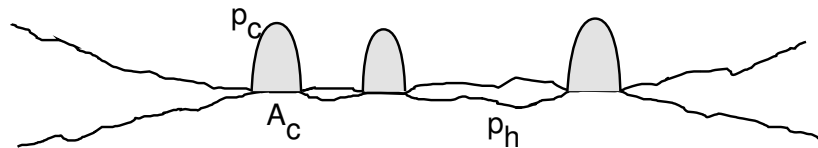


Figure 6.1: Thin lubricating film with rough surfaces and partial contact.

this case the total load applied to the bearing is carried partially by the mechanical contact in these areas and partially by the hydrostatic fluid pressure in the full-film areas separating these contact areas. The contact load fraction (or dimensionless contact load) \bar{W}_c is defined as the ratio of the load carried by contact W_c and the total load W :

$$\bar{W}_c = \frac{W_c}{W} \quad (6.1)$$

Similarly, the contact area fraction (or dimensionless contact area) \bar{A}_c is defined as the ratio of the contact area A_c and the total area A :

$$\bar{A}_c = \frac{A_c}{A} \quad (6.2)$$

The symbol \bar{a}_c will subsequently be used for the *local* contact area fraction which is defined as the local contact area per unit area. The following relation between \bar{a}_c and \bar{A}_c holds:

$$\bar{A}_c = \frac{1}{A} \iint_A \bar{a}_c dA \quad (6.3)$$

A distinction can be made between microscopic contact areas and macroscopic contact areas. A microscopic contact area occurs where *roughness* peaks or asperities of both surfaces come into contact. In these areas no fluid flow is possible. A macroscopic contact area occurs where *waviness* peaks of both surfaces come into contact. The actual contact in these areas occurs in a (large) number of microscopic contact areas separated by areas where no contact occurs. Therefore in a macroscopic contact area the area that is actually in contact (true contact area) is smaller than the apparent contact area. The lubricating fluid is still present in valleys and pits between the surfaces and it is assumed that the fluid can continue to flow between the actual (microscopic) contact spots. In this thesis when contact areas are mentioned it is assumed that these are *macroscopic* contact areas.

In the contact areas between bearing and track, mixed lubrication is present: Part of the load is carried by hydrostatic fluid pressure, part by contact pressure. The hydrostatic fluid pressure distribution p_h is described by the Reynolds' equation and will be examined in chapter 7. The contact pressure will be studied in this chapter. Both these components of mixed lubrication have been studied separately extensively in the past, the combination of these components in mixed lubrication has been studied less frequently. Mixed lubrication has been the subject of conferences (DOWSON ET AL., 1984) and papers (AI ET AL., 1998; FULLER, 1954; GELINCK, 1999; HU AND ZHU, 2000; JIANG ET AL., 1998; LO, 1994; OH, 1986; WANG AND CHENG, 1995; ZHAI AND CHANG, 1998), in all of which it is assumed that mixed lubrication can be regarded as the sum of the two basic components. For the calculation of these components, various methods are employed.

The total pressure p on the track and bearing is equal to (figure 6.2a, b):

$$p = \bar{a}_c p_c^* + (1 - \bar{a}_c) p_h^* \quad (6.4)$$

where the first and second term on the right hand side represent the contribution of the contact pressure and the hydrostatic pressure to the total pressure respectively.

The actual average contact pressure p_c^* is defined as the average contact pressure per unit *contact* area. The actual average hydrostatic pressure p_h^* is defined as the average hydrostatic pressure per unit *full-film* area. p_c^* and p_h^* can be rewritten using:

$$p_c^* = \frac{p_c}{\bar{a}_c} + p_h \quad (6.5a)$$

$$p_h^* = p_h \quad (6.5b)$$

with p_h the hydrostatic pressure and p_c the average pressure *raise* due to contact (figure 6.2b, c, d). Substituting these relations into 6.4 yields:

$$p = p_h + p_c \quad (6.6)$$

In the following sections relations for the nominal and effective film height (h and h_t respectively), the contact pressure *raise* p_c and the local contact area fraction \bar{a}_c are presented. The equations describing the hydrostatic fluid pressure p_h are presented in the next chapter.

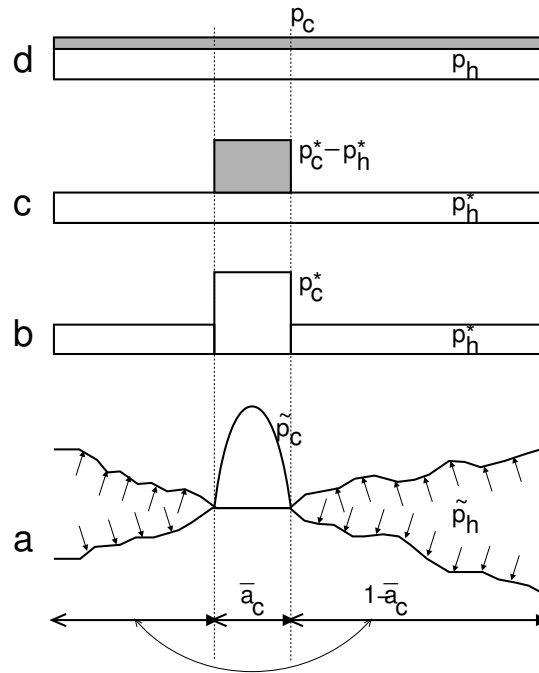


Figure 6.2: The mixed lubrication model. In a contact point the contact pressure is \tilde{p}_c (figure a), or averaged p_c^* (figure b). The local pressure *raise* is then equal to $p_c^* - p_h^*$ (figure c) or averaged over the total surface p_c (figure d). It is assumed that the hydrostatic pressure surrounding the contact point is constant, and thus $\tilde{p}_h = p_h^* = p_h$.

6.1 Nominal and effective film height

The gap between the bearing and the track is dependent on:

- The initial gap of the undeformed surfaces. This gap is defined by the distance between the track surface position z_t and the bearing surface position z_b .
- The *global* track and bearing deformations (u_t and u_b respectively) due to the hydrostatic and contact pressures.
- The *local* (roughness) surface deformations due to the hydrostatic and contact pressures.

The nominal film height h (sometimes called compliance) is defined as the distance between the mean planes of the *undeformed* surface roughness of both surfaces. It is the result of the initial gap and the global deformations (figure 6.3):

$$h = (z_b + u_b) - (z_t + u_t) \quad (6.7)$$

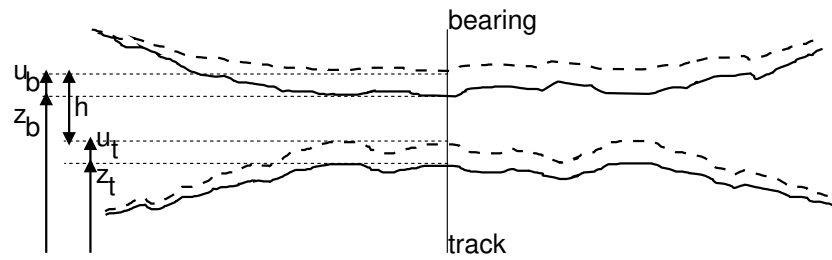


Figure 6.3: Nominal film height h

However, the gap between the bearing and the track is also dependent on the roughness and deformation of that roughness. The definition of the so-called effective or true film height h_t takes this effect into account. The effective film height is defined as the ratio of the volume of a small part of the lubricating film and the area of that part of the film, that is the distance between the mean planes of the *deformed* surface roughness of both surfaces. The effective film height can be regarded as an average height of the film and will prove useful in the calculation of the hydrostatic pressure p_h .

If the surfaces do not make contact the effective film height h_t is equal to the nominal film height h . But if the surfaces do make contact the effective film height will be larger than the nominal film height (WILSON AND MARSAULT, 1998). The nominal film height can even become negative while the effective film height always remains strictly non-negative.

In CHENGWEI AND LINQING (1989) a model is presented for the effective film height. It is assumed that, in contact, only the roughness peaks actually in contact deform and the roughness profile surrounding that contact remains unchanged. In this case the effective film height can easily be defined as a function of the nominal film height h and the combined roughness of the surfaces S_q (see equation 5.18):

$$\frac{dh_t}{dh} = \int_{-\infty}^h \phi(h') dh' \quad (6.8)$$

where $\phi(h)$ is the height distribution function of the combined surface roughness.

For a normal surface height distribution (equation 5.15) this integral can be solved:

$$\frac{dh_t}{dh} = \frac{1}{2} \left(1 + \operatorname{erf} \left(\frac{1}{\sqrt{2}} \frac{h}{S_q} \right) \right) \quad (6.9)$$

with the error function $\operatorname{erf}(x)$ again defined as:

$$\operatorname{erf}(x) = \frac{2}{\sqrt{\pi}} \int_0^x e^{-x'^2} dx' \quad (6.10)$$

Solution of the differential equation 6.9 yields a relation for the effective film height h_t as a function of the nominal film height h :

$$\frac{h_t}{S_q} = \frac{1}{2} \frac{h}{S_q} \left(1 + \operatorname{erf} \left(\frac{1}{\sqrt{2}} \frac{h}{S_q} \right) \right) + \frac{1}{\sqrt{2\pi}} e^{-\frac{1}{2} \left(\frac{h}{S_q} \right)^2} \quad (6.11)$$

In figure 6.4 this relation is presented. The asymptotic solutions of this relation can be identified: For large nominal film height h the effective film height h_t is approximately equal to the nominal film height, for negative nominal film height h the effective film height approaches zero.

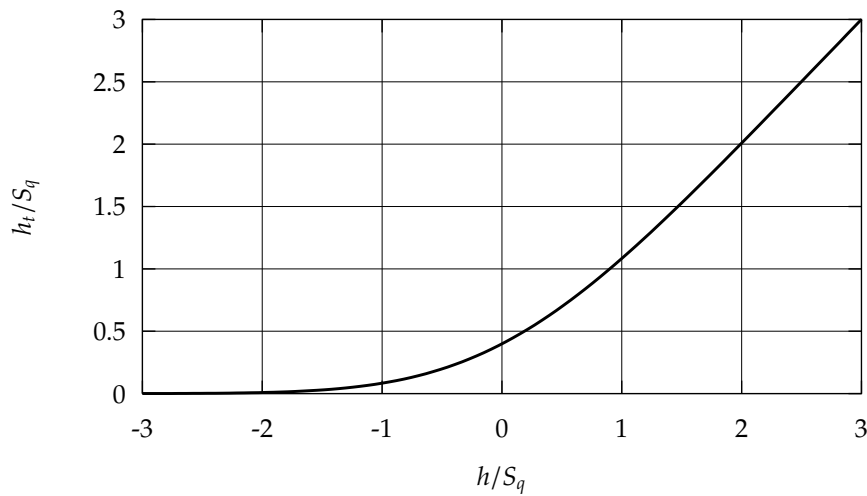


Figure 6.4: The effective film height h_t versus the nominal film height h and the surface roughness S_q .

6.2 Local contact area fraction \bar{a}_c

The contact of two tribological elements with rough surfaces will result in a global (or bulk) deformation of these elements and in a local deformation of the surface roughness. In literature many models have been presented describing the contact between rough surfaces (see for instance a recent survey of the most important models by LIU ET AL. (1999)). These models can be divided using different criteria. One such criterion is the type of roughness deformation (plastic, elastic or elastic/plastic) and another criterion is the type of mathematical approach used (stochastic, deterministic).

When bodies are placed in contact, the true area of contact is very small compared to the apparent contact area. Early studies assumed that due to this small true contact area the contact pressure would rapidly exceed the hardness of the softer of the contacting materials and thus would result in *plastic* deformation of the roughness peaks

(BOWDEN AND TABOR, 2001). This model is also in accordance with the classic friction laws formulated by Leonardo da Vinci (1452-1519), which were later rediscovered by Amontons (1663-1705):

- The force of friction is directly proportional to the applied load.
- The force of friction is independent of the apparent area of contact.

However later it was discovered that, assuming a realistic surface roughness height distribution, any type of roughness deformation (plastic, elastic or elastic/plastic) would be in accordance with these friction laws.

In order to determine the mode of the roughness deformation, the so-called plasticity index ψ^* has been introduced (GREENWOOD AND WILLIAMSON, 1966):

$$\psi^* = \left(\frac{E^*}{H}\right) \left(\frac{S_q}{R^*}\right)^{\frac{1}{2}} \quad (6.12)$$

with H the hardness of the softest material, S_q the standard deviation of the *asperity* height distribution and R^* the radius of curvature of the asperities and E^* the composite modulus of elasticity of the material combination:

$$\frac{1}{E^*} = \frac{1 - \nu_a^2}{E_a} + \frac{1 - \nu_b^2}{E_b} \quad (6.13)$$

A different expression for the plasticity index ψ was introduced by WILLIAMSON (1971):

$$\psi = \left(\frac{E^*}{H}\right) \left(\frac{S_q}{\beta}\right) \quad (6.14)$$

with S_q the standard deviation of the height distribution (or surface roughness) and β the correlation distance of the auto-correlation function of the surface roughness (equation 5.20). A plasticity index specifically for polymer materials ψ_p was introduced by BHUSHAN (1984):

$$\psi_p = \left(\frac{E^*}{\sigma_y}\right) \left(\frac{S_q}{R^*}\right)^{\frac{1}{2}} \quad (6.15)$$

with σ_y the yield stress of the softest material:

$$H \approx 3\sigma_y \quad (6.16)$$

The mode of deformation is determined by the value of the plasticity index:

$$\begin{cases} \psi^*, \psi < 1 & \text{predominately elastic} \\ \psi^*, \psi > 1 & \text{predominately plastic} \end{cases} \quad (6.17)$$

where a value of 1 indicates that 98% of the contact points is elastic and the remaining 2% will have yielded internally.

Given the mode of deformation a model for the roughness deformation can be developed. A seminal paper was published by GREENWOOD AND WILLIAMSON (1966) in which an elastic, stochastic contact model was presented. In their model the rough surface was modelled as a large number of hemispherically tipped asperities with an identical radius of curvature and with a Gaussian distributed asperity height distribution. Furthermore, elastic (Hertzian) and mutually independent deformation of the asperities was assumed. Relations for the true area of contact and contact pressure were derived as a function of the separation between the surfaces. This so-called Greenwood–Williamson model (GW-model) is still in use today (see for instance GELINCK (1999); GELINCK AND SCHIPPER (1998, 2000)). In a number of papers some of the basic geometrical assumptions in the GW-model have been relaxed and the model improved (GREENWOOD AND TRIPP, 1971; ONIONS AND ARCHARD, 1972; WHITEHOUSE AND ARCHARD, 1970). CHANG ET AL. (1987) extended the GW-model to include elastic/plastic deformation (CEB-model). More recently elastic/plastic deformation was included in LEE AND REN (1996); POLYCARPOU AND ETSION (1999).

In these papers the surface roughness is described using a stochastic model where a distribution function of the surface heights was assumed, possible in conjunction with an auto-correlation function for the surface heights. The disadvantage if this type of surface description is that it is dependent on the sample length and the resolution of the measuring device. Therefore a scale-invariant method has been proposed to describe surface roughness, the fractal geometry surface description (MAJUMDAR AND BHUSHAN, 1990). This surface description has subsequently been used to study the elastic/plastic contact between surfaces (KOMVOPOULOS AND YE, 2001; MAJUMDAR AND BHUSHAN, 1991; YAN AND KOMVOPOULOS, 1998). A critical comparison of both surface description methods (stochastic and fractal) has recently been published (WHITEHOUSE, 2001).

Most models assume that the deformation of nearby roughness peaks do not influence each other. This assumption is only valid for small contact area fractions. Recently some studies have been performed using advanced numerical methods where contact between surfaces has been studied assuming both elastic and plastic deformation of the surfaces and interaction between roughness asperities (LEE AND REN, 1996). In these studies the contact area fraction is dependent on a hardness parameter \mathcal{H} :

$$\mathcal{H} = \frac{2.3 (3\sigma_y)\beta_x}{\pi \pi E^* S_q} \quad (6.18)$$

where β_x and β_y denote the auto-correlation lengths of the roughness profile in x resp. y -direction and S_q the combined roughness of the surfaces.

Introducing equation 6.16 in 6.18:

$$\mathcal{H} = \frac{2.3 H\beta_x}{\pi E^* S_q} = \frac{0.733}{\psi} \quad (6.19)$$

In LEE AND REN (1996) relations for the true contact area \bar{a}_c and the effective film height h_t are presented as function of γ , \mathcal{H} and \mathcal{P}_c with \mathcal{P}_c equal to:

$$\mathcal{P}_c = \frac{2.3 p_c \beta_x}{\pi E^* S_q} \quad (6.20)$$

The true contact area is equal to (figure 6.5):

$$\bar{a}_c(\gamma, \mathcal{H}, \mathcal{P}_c) = \sum_{i=1}^4 \left\{ \gamma_A^T [A_i] \vec{\mathcal{H}} \right\} \mathcal{P}_c^i \quad (6.21a)$$

and the average gap:

$$\frac{h_t(\gamma, \mathcal{H}, \mathcal{P}_c)}{S_q} = \exp \left\{ \sum_{i=0}^4 \left\{ \gamma_G^T [G_i] \vec{\mathcal{H}} \right\} \mathcal{P}_c^i \right\} \quad (6.21b)$$

where:

$$\vec{\mathcal{H}}^T = \begin{bmatrix} 1 & \mathcal{H}^{-1} & \mathcal{H}^{-2} & \mathcal{H}^{-3} \end{bmatrix} \quad (6.22)$$

$$\gamma_G^T = \begin{bmatrix} 1 & \gamma^{-1} & \gamma^{-2} & \gamma^{-3} \end{bmatrix} \quad (6.23)$$

$$\gamma_A^T = \begin{bmatrix} 1 & \gamma & \gamma^2 & \gamma^3 \end{bmatrix} \quad (6.24)$$

and $[A_i]$, $[G_i]$ are matrices filled with constants obtained from curve-fits of the numerical results. The matrices have previously been presented in LEE AND REN (1996), but for completeness have been repeated here in appendix D.

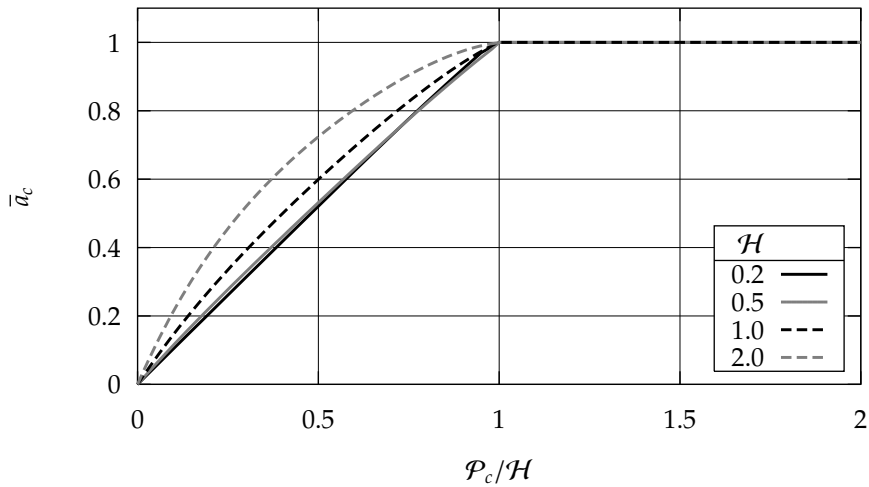


Figure 6.5: Contact area fraction \bar{a}_c versus the reduced pressure $\mathcal{P}_c/\mathcal{H}$ (model by Lee).

The hardness parameter \mathcal{H} is approximately equal to 0.5 for an UHMWPE surface as encountered in the present study for a representative roughness S_q of $10.0 \cdot 10^{-6} \text{m}$ and auto-correlation length β_x of $0.2 \cdot 10^{-3} \text{m}$. Because of this low value for the hardness parameter \mathcal{H} the contact area fraction is approximately proportional to the reduced contact pressure $\bar{p}_c = \mathcal{P}_c / \mathcal{H} = p_c / H$ (see figure 6.5):

$$\bar{a}_c = \begin{cases} \bar{p}_c & \text{if } \bar{p}_c < 1 \\ 1 & \text{otherwise} \end{cases} \quad (6.25)$$

6.3 Reduced contact pressure \bar{p}_c

The contact area fraction is dependent on the distance between the surfaces. The smaller the distance, the larger the contact area fraction. The nominal distance h between the surfaces is:

$$h = (z_a + u_a) - (z_b + u_b) \quad (6.26)$$

where z_a and z_b are the initial positions and u_a and u_b the displacements of the surfaces.

Contact between the surfaces starts when the nominal distance h between the surfaces is approximately equal to $3S_q$ (see previous chapter, figure 5.10 and equation 5.16). The contact area fraction \bar{a}_c increases with decreasing h until for a nominal distance approximately equal to $-3S_q$ the contact area fraction \bar{a}_c is equal to 1. Assuming the same type of deformation as was used for equation 6.9 it has been shown in CHENGWEI AND LINQING (1989) that the contact area fraction \bar{a}_c is equal to (figure 6.6):

$$\bar{a}_c = \frac{1}{2} \left(1 - \operatorname{erf} \left(\frac{1}{\sqrt{2}} \frac{h}{S_q} \right) \right) \quad (6.27)$$

Combining equations 6.27 and 6.25 yields a relation for the reduced contact pressure \bar{p}_c as a function of the nominal surface distance h based on Lee's contact model (figure 6.7):

$$\bar{p}_c = \frac{1}{2} \left(1 - \operatorname{erf} \left(\frac{1}{\sqrt{2}} \frac{h}{S_q} \right) \right) \quad (6.28)$$

Figure 6.7 shows that for negative values of h the reduced contact pressure \bar{p}_c is limited to 1 in Lee's model.

Unfortunately, LEE AND REN (1996) do not provide a relation between the nominal film height h and the effective film height h_t . Furthermore, no direct relation between the effective film height h_t and the contact area fraction \bar{a}_c has been given. It is possible however, to use equations 6.21a and 6.21b to find this relation numerically. In figure 6.8 this relation is presented for different values of \mathcal{H} .

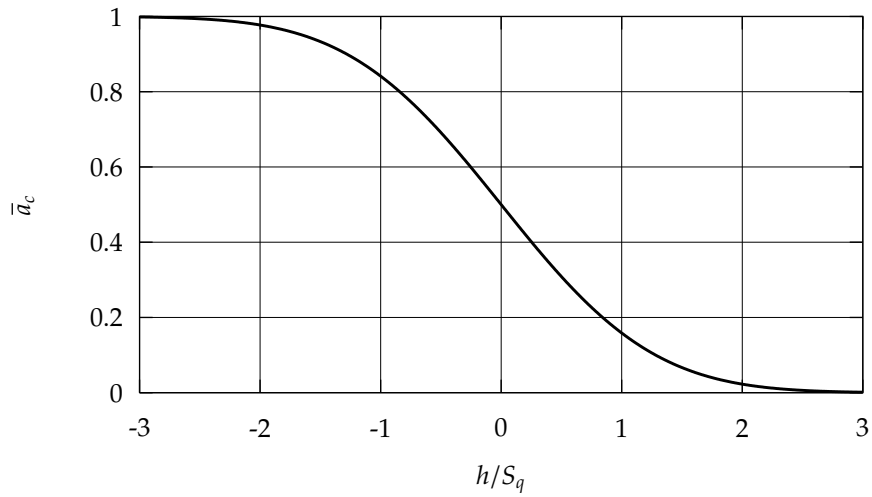


Figure 6.6: Contact area fraction \bar{a}_c versus the nominal film height h and the surface roughness S_q .

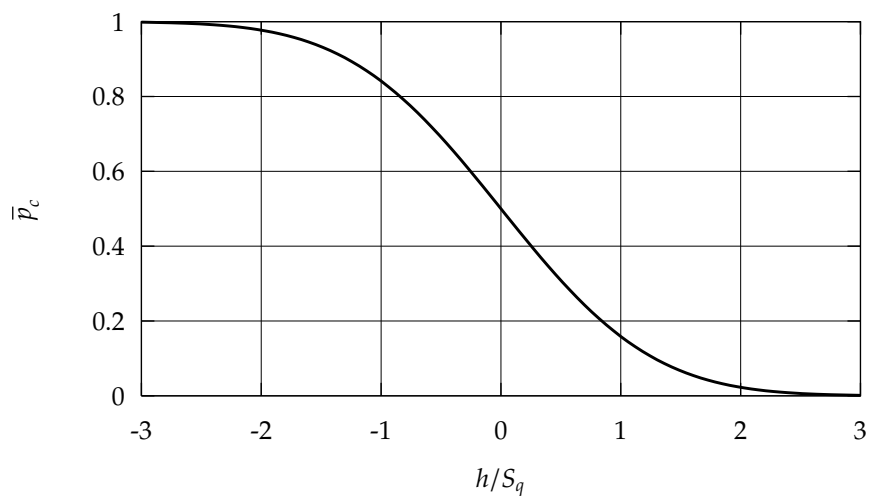


Figure 6.7: Contact pressure \bar{p}_c versus the nominal film height h and the surface roughness S_q .

In the previous section, the equations derived by CHENGWEI AND LINQING (1989) have been used to provide the relation between the nominal film height h and the effective film height h_t and the contact area fraction \bar{a}_c (respectively equations 6.11 and 6.27). Combining these equations again yields a relation between h_t and \bar{a}_c (figure 6.8). The

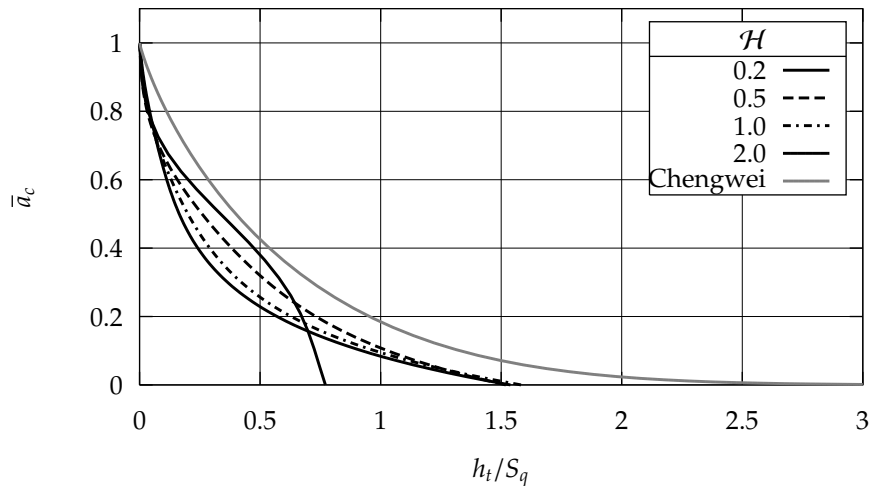


Figure 6.8: Contact area fraction \bar{a}_c versus the effective film height h_t and surface roughness S_q .

difference between both models is probably caused by the fact that in the simple deformation model proposed by CHENGWEI AND LINQING (1989), the deformation of the asperity peaks does not influence the gaps in between, whereas in the numerical model of LEE AND REN (1996) this influence is taken into account.

6.4 Coefficient of friction c_f

The coefficient of friction c_f of a polymer–metal combination is dependent on a large number of parameters, such as load, sliding speed, material properties and surface geometry (BARRETT ET AL., 1992).

HONSELAAR (1993) has performed experiments to determine the coefficient of friction of UHMWPE on steel under water for different loads and sliding speeds (see figure 6.9). For the application examined in this thesis the contact pressures are expected to remain relatively low. A constant value of 0.1 will be used for the coefficient of friction of the steel–UHMWPE material combination in these conditions.

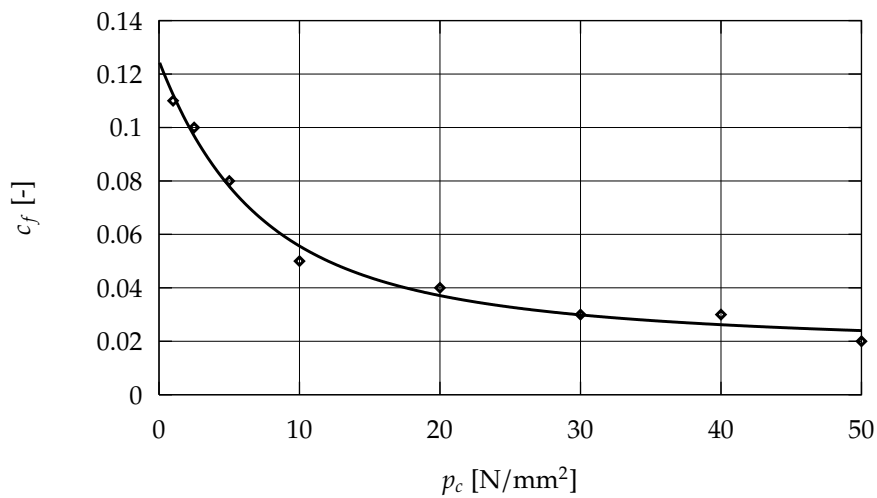


Figure 6.9: Coefficient of friction c_f of UHMWPE versus the contact pressure p_c for a sliding speed of 0.1 m/s and a surface roughness (R_a) of the steel surface equal to 0.5 μm .

6.5 Conclusion

In this chapter, equations for the nominal film thickness, the effective film thickness, the contact area, and contact load have been derived. These equations partly describe the mixed lubricated contact between the track and the bearing (figure 6.10).

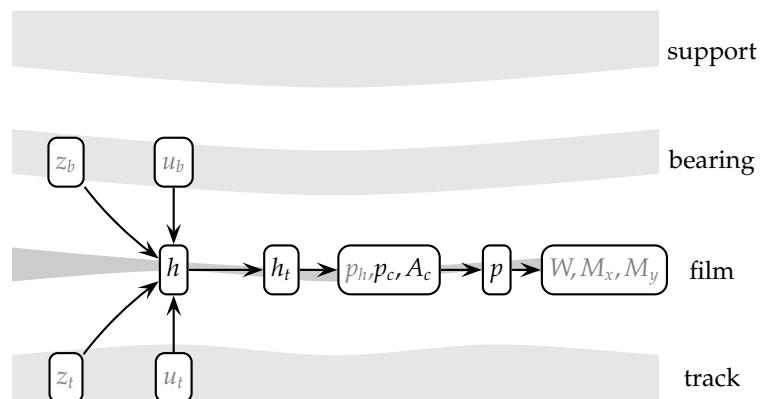


Figure 6.10: Components of the model described in this chapter: The mixed lubricated contact between track and bearing.

The hydrostatic pressure is the final component of the description of the mixed lubricated contact. This will be studied in the next chapter.

CHAPTER 7

Full film lubrication

When two surfaces have to move relative to each other, often a lubricating fluid film is used to separate the surfaces. In order to carry a load, a fluid pressure in the lubricating film must be present. There are several methods to build up fluid pressure in a lubricating film:

- The lubricant can be injected at a certain point into the film under high pressure using an external supply.
- The pressure in the fluid film will increase when the fluid is forced by the surface movement into a convergent film.

The pressure in a lubricating film can be described using the basic fluid flow equations (conservation of mass, conservation of impulse and conservation of energy (BIRD ET AL., 2002)). However, the numerical effort required to solve these equations for a typical lubrication problem is very large. Recent developments in computer and computational fluid dynamics (CFD) software design have made this solution feasible, if not practical. For instance, in CHEN AND HAHN (1998) this method has been used to calculate the pressure in a lubricating film.

Using a number of assumptions, the pressure in a lubricating film can be described by the Reynolds' equation. This equation was first derived by Reynolds (REYNOLDS, 1886). DOWSON (1962) derived a more general version of this equation, more recently BOOKER (1989) derived a general form of the Reynolds' equation particularly suited for the finite element method.

The Reynolds' equation is derived using basic equations describing fluid flow: conservation of mass and conservation of impulse. The typical geometry of a lubricating film can be described by two dimensions: A very small dimension perpendicular to the plane of the film, large dimensions in the plane of the film.

Conservation of mass in a column extending from one surface to the other, yields:

$$\frac{\partial q_x}{\partial x} + \frac{\partial q_y}{\partial y} = 0 \quad (7.1)$$

with q_x and q_y the mass flows through this column in x and y direction respectively.

Using the so-called thin film assumptions these mass flows can be derived from the equations describing conservation of impulse (DOWSON, 1962):

- The lubricating film is defined by two dimensions: a large transverse dimension L and a small dimension h perpendicular to the film (film thickness). It is assumed that the ratio between these dimensions is very small.
- There are no body forces acting on the fluid (such as gravity forces, magnetic forces or centrifugal forces).
- The pressure is constant perpendicular to the film.
- There is no velocity difference between the surfaces and the fluid against the surfaces. That is, the fluid 'sticks' to the surfaces.
- The fluid acts 'Newtonian', that is, there is a linear relation between shear stress and shear velocity.
- The viscosity and density are constant perpendicular to the film.
- Inertia forces in the fluid can be neglected compared to the viscous forces.
- The flow is laminar.
- The flow is stationary.

The mass flows in the film can now be described by:

$$q_x = \frac{-\rho h^3}{12\eta} \frac{\partial p_h}{\partial x} + \frac{\rho(U_a + U_b)h}{2} \quad (7.2a)$$

$$q_y = \frac{-\rho h^3}{12\eta} \frac{\partial p_h}{\partial y} \quad (7.2b)$$

with fluid pressure p_h , film height h , fluid viscosity η , fluid density ρ and surface velocities of both surfaces a and b in x -direction U_a and U_b . It is assumed that the velocity in y -direction is zero.

Substituting equation 7.2 in equation 7.1 yields the Reynolds' equation, so-called after Osborne Reynolds who first derived this equation (REYNOLDS, 1886):

$$\frac{\partial}{\partial x} \left(\frac{-\rho h^3}{12\eta} \frac{\partial p_h}{\partial x} + \frac{\rho(U_a + U_b)h}{2} \right) + \frac{\partial}{\partial y} \left(\frac{-\rho h^3}{12\eta} \frac{\partial p_h}{\partial y} \right) = 0 \quad (7.3)$$

Given a known film geometry h and an unknown fluid pressure p_h this equation presents a 2nd order partial differential equation in p_h . Thus the solution of this equation yields the fluid pressure p_h .

The shear stresses acted by the fluid on the surfaces is given by:

$$\tau_x = -\frac{h}{2} \frac{\partial p_h}{\partial x} \pm \frac{\eta(U_a - U_b)}{h} \quad (7.4a)$$

$$\tau_y = -\frac{h}{2} \frac{\partial p_h}{\partial y} \quad (7.4b)$$

where τ_x and τ_y denote the shear stresses in x and y direction. The lower symbol of the \pm in equation 7.4a (minus sign) is valid for the lower surface a, the upper symbol (plus sign) for the upper surface b.

The load W on the fluid film can be calculated by integrating the pressure over the surface. The tilting moments M_x and M_y as a result of the fluid pressure and with respect to the origin, can be found by integrating the first moment of the pressure over the surface:

$$W = \iint_A p_h dA \quad (7.5a)$$

$$M_x = \iint_A xp_h dA \quad (7.5b)$$

$$M_y = \iint_A yp_h dA \quad (7.5c)$$

If the basic assumptions used in the derivation of the Reynolds' equation 7.3 hold, the Reynolds' equation is valid for smooth and rough surfaces (figure 7.1). Surface roughness where these assumptions remain valid is usually called Reynolds' roughness.

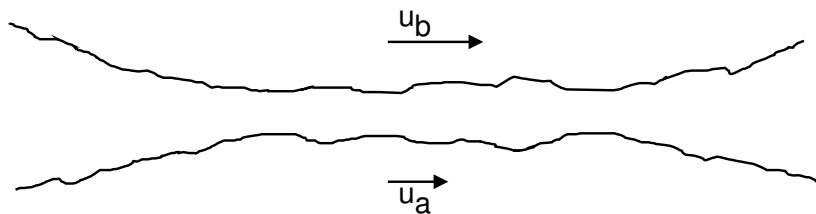


Figure 7.1: Lubricating film with rough surfaces.

Surface roughness disturbs the flow of the fluid in the lubricating film. In an extreme situation contact between two roughness peaks can impede the flow completely.

In order to solve the Reynolds' equation 7.3 for rough surfaces, the film height in every point of the film has to be known. Surface roughness however, is usually merely known in an average or stochastic manner. Lubrication of rough surfaces has been studied extensively in the past (DOWSON ET AL., 1977). In order to cope with surfaces with a stochastic roughness an adapted Reynolds' equation has been proposed (BERTHE AND GODET, 1973; CHENG, 1984; CHRISTENSEN, 1971; CHRISTENSEN AND TØNDER, 1973; ELROD, 1979; HARP AND SALANT, 2001; KNOLL ET AL., 1998; PATIR AND CHENG, 1978a,b; TRIPP, 1982; WILSON AND MARSAULT, 1998).

In particular, in the research by PATIR AND CHENG (1978a,b) a simple modified Reynolds' equation (the so-called *PC* rough Reynolds' equation) has been proposed, in which flow factors have been used to take the influence of the surface roughness into account. Very recently, a modified version of this rough Reynolds' equation has been presented (HARP AND SALANT, 2001, 2002), in which cavitation between asperities is also taken into account. An important drawback of both these rough Reynolds' equations is the fact that they use the *nominal* height of the film (that is the distance between the *undeformed* surfaces (see chapter 6)). At high loads, the nominal film height can become zero or even negative and the rough Reynolds' equations proposed by PATIR AND CHENG (1978a,b) and HARP AND SALANT (2001, 2002) become insoluble.

In WILSON AND MARSAULT (1998) the effective or average film height h_t (chapter 6) has been used in the formulation of a new rough Reynolds' equation. The average film height is always larger or equal to zero, and therefore this rough Reynolds' equation (the so-called *WM* rough Reynolds' equation) remains soluble. Instead of equations 7.2 the relations for the mass flow become:

$$q_x = -\phi_{p_x} \frac{\rho h_t^3}{12\eta} \frac{\partial p_h}{\partial x} + \frac{\rho(U_a + U_b)h_t}{2} + \phi_s \frac{\rho(U_a - U_b)S_q}{2} \quad (7.6a)$$

$$q_y = -\phi_{p_y} \frac{\rho h_t^3}{12\eta} \frac{\partial p_h}{\partial y} \quad (7.6b)$$

where flow factors ϕ_{p_x} , ϕ_{p_y} and ϕ_s have been introduced to take surface roughness effects into account. The surface roughness S_q is the combined roughness of both surfaces according to equation 5.18.

Compared to equations 7.2 an extra shear term is added to q_x that takes into account the fluid mass flow carried with the moving surface in roughness valleys and pits. The flow factors ϕ_{p_x} and ϕ_{p_y} are factors correcting the pressure term for roughness effects. The flow factors in equation 7.6a are dependent on the material combination of both surfaces (in particular the elasticity of both surfaces) and on the roughness geometry and orientation.

The summed surface roughness S_q is given by:

$$S_q = \sqrt{S_{q_a}^2 + S_{q_b}^2} \quad (7.7)$$

with S_{q_a} and S_{q_b} the surface roughness of surface a and b respectively.

In general, the pressure correction factors ϕ_{p_x} and ϕ_{p_y} are dependent on the material properties and the roughness geometry and the effective film height. It has been shown in WILSON AND MARSAULT (1998) that if it is assumed that the roughness doesn't exhibit an orientation (isotropic) and the surfaces are rigid, the flow factors in both directions are equal and given by:

$$\phi_p = 1 - .9e^{-.56\Lambda} \quad (7.8a)$$

with Λ the film thickness number:

$$\Lambda = h_t/S_q \quad (7.8b)$$

In figure 7.2 these flow factors (WILSON AND MARSAULT, 1998) (WM) are plotted together with the flow factors of PATIR AND CHENG (1978a,b) (PC). Note that for this plot, the PC flow factors have been transformed from the original nominal film height description to an effective film height description using equation 6.11.

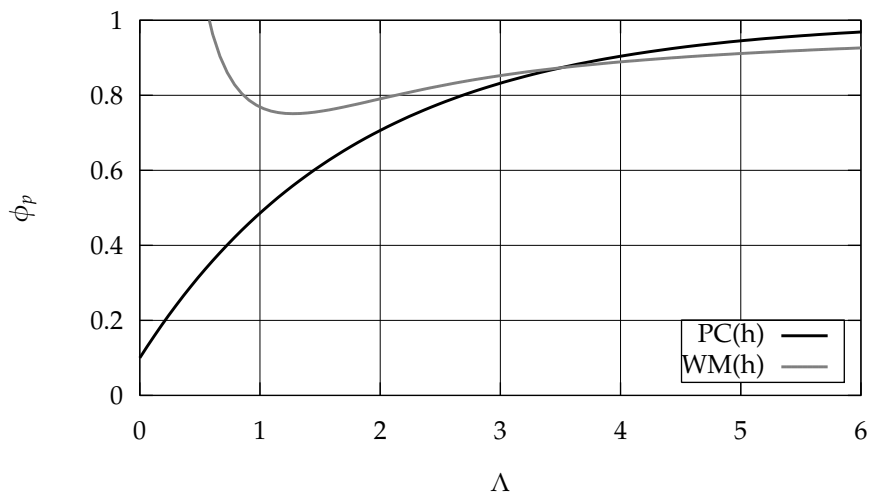


Figure 7.2: Pressure correction factor ϕ_p for an isotropic rough surface calculated using PATIR AND CHENG (1978b) (PC) and WILSON AND MARSAULT (1998) (WM).

The shear flow correction factor ϕ_s is given by (WILSON AND MARSAULT, 1998) (figure 7.3):

$$\phi_s = \left(\left(\frac{S_{q_a}}{S_q} \right)^2 - \left(\frac{S_{q_b}}{S_q} \right)^2 \right) \Phi_s(\Lambda) \quad (7.8c)$$

$$\Phi_s = \begin{cases} 1.899\Lambda^{.98}e^{-.92\Lambda+.05\Lambda^2} & \text{if } \Lambda \leq 5 \\ 1.126e^{-.25\Lambda} & \text{if } \Lambda > 5 \end{cases} \quad (7.8d)$$

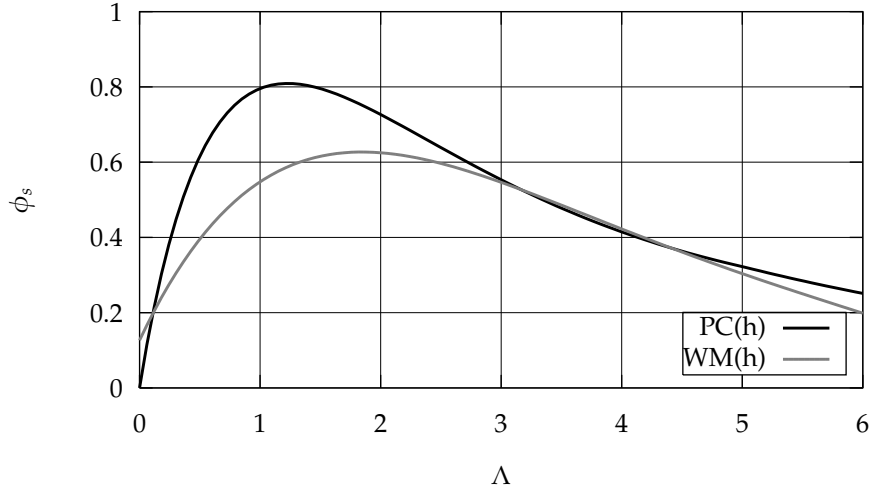


Figure 7.3: Shear correction factor Φ_s for an isotropic rough surface calculated using PATIR AND CHENG (1978b) (PC) and WILSON AND MARSAULT (1998) (WM).

In figure 7.3 this shear flow correction factor (WILSON AND MARSAULT, 1998) (WM) is plotted together with the flow factor of PATIR AND CHENG (1978a,b) (PC).

If equations 7.6a are introduced into equation 7.1 the rough Reynolds' equation is the result:

$$\frac{\partial}{\partial x} \left(-\phi_{px} \frac{h_t^3}{12\eta} \frac{\partial p_h}{\partial x} + \frac{(U_a + U_b)h_t}{2} + \frac{\phi_s(U_a - U_b)S_q}{2} \right) + \frac{\partial}{\partial y} \left(-\phi_{py} \frac{h_t^3}{12\eta} \frac{\partial p_h}{\partial y} \right) = 0 \quad (7.9)$$

Note that in these studies the deformation of the surfaces, and in particular, the deformation of the surface roughnesses, was not taken into account. In a recent study (KNOLL ET AL., 1998) it was shown that, for isotropic surface roughness, due to elastic deformation of the surfaces, the pressure correction factors ϕ_{px} and ϕ_{py} are approximately equal to 1. In all further calculations in this thesis it will be assumed that these factors are all equal to 1.

The hydrodynamic shear stresses on the rough surfaces are given by:

$$\tau_x = \phi_{fp} \frac{h}{2} \frac{\partial p}{\partial x} \pm (\phi_f \pm \phi_{fs}) \frac{\eta(U_a - U_b)}{h} \quad (7.10a)$$

$$\tau_y = \phi_{fp} \frac{h}{2} \frac{\partial p}{\partial y} \quad (7.10b)$$

where ϕ_{fp} , ϕ_f and ϕ_{fs} are shear correction factors. Again, the lower sign in the \pm sign is valid for the lower surface, the upper sign for the upper surface. In practise these

shear correction factors are approximately equal to (PATIR AND CHENG, 1978a,b):

$$\phi_{fp} = 1 \quad (7.11a)$$

$$\phi_f = 1 \quad (7.11b)$$

$$\phi_{fs} = 0 \quad (7.11c)$$

Due to the very small sliding speeds of the supports studied in this thesis, the hydrodynamic friction force (which is linear dependent on the sliding speed), will be negligible small compared to the contact friction force.

In this chapter the rough Reynolds' equation has been presented as a means to calculate the hydrostatic pressure between the track and the bearing (see figure 7.4).

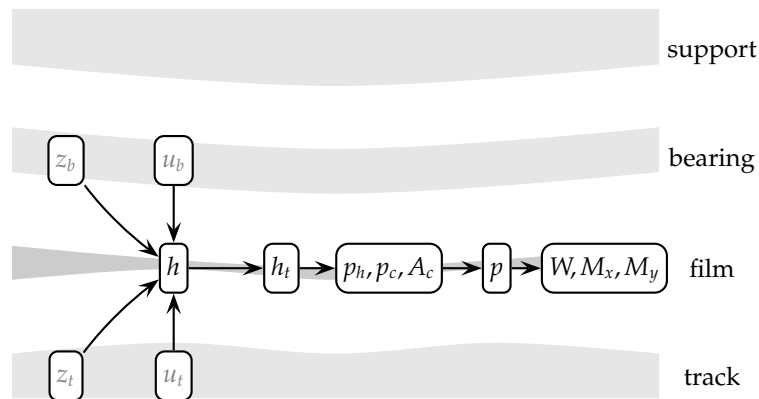


Figure 7.4: Components of the model described in this and the previous chapter: The mixed lubricated film.

In this and the previous chapters, the components of the model pertaining to parts of the hydro-support located below the bearing have been studied. In the next chapter, the deformation of the bearing will be studied.

CHAPTER 8

Bearing deformation

The hydro-support is made of a (thin) bearing supported by a highly elastic rubber support. The bearing will deform due to the load on the bearing. This load consists of 3 elements:

- The pressure p on the underside of the bearing. This is the combined pressure of the hydrostatic pressure p_h and the contact pressure raise p_c between the bearing and the track (equation 6.6).
- The pressure on top of the bearing. This is the reaction pressure p_s of the rubber support as a result of the compression of the rubber support.

Thus the total bearing pressure p_b is given by:

$$p_b = p - p_s \quad (8.1)$$

Due to the fact that the total load on top of the bearing and the total load on bottom of the bearing are in equilibrium the following must hold:

$$\iint_A p_b dA = 0 \quad (8.2)$$

Depending on the relative thickness of the bearing and the load distribution on the bearing, the deformation of the bearing can be described using a thin plate model (Kirchhoff theory), a thick plate model (Reisner–Mindlin theory) or a full 3D elastic model. The use of a plate model has preference because of the reduced numerical complexity (2D calculation versus 3D). Furthermore it is assumed that the in-plane displacements of the bearing are zero.

According to the Kirchhoff theory ZIENKIEWICZ AND TAYLOR (2000*b*), if the bearing is relatively thin and the load distribution on the bearing is smooth and distributed on a large surface area, the deformation due to shear can be neglected and the vertical deformation of the bearing u_b as a result of the distributed load p_b can be calculated using the bi-harmonic equation:

$$D \left(\frac{\partial^2}{\partial x^2} + \frac{\partial^2}{\partial y^2} \right) \left(\frac{\partial^2}{\partial x^2} + \frac{\partial^2}{\partial y^2} \right) u_b = p_b \quad (8.3)$$

where D is the plate constant:

$$D = \frac{E_b t_b^3}{12(1 - \nu_b^2)} \quad (8.4)$$

with the modulus of elasticity E_b , Poisson's ratio ν_b and the plate thickness t_b . The Kirchhoff plate theory is characterized by the fact that a plane normal to the midplane of the plate before deformation, remains normal to the midplane after the deformation.

If the bearing is thicker, the deformation due to shear cannot be neglected, and a thick plate model according to the Reissner–Mindlin theory can be used (ZIENKIEWICZ AND TAYLOR, 2000*b*). This model can be used up to a bearing thickness/length ratio of approximately 0.2 (HUGHES AND TEZDUYAR, 1981). The Reissner–Mindlin plate theory is characterized by the fact that a plane normal to the midplane of the plate before deformation, does *not* remain normal to the midplane after the deformation.

In case of a very thick bearing or a very localized load, the use of a plate model isn't possible. In this case, planes normal to the midplane of the plate before the deformation, do not remain normal or even plane after the deformation. Here, for maximum accuracy, a full 3D elastic model should be used. However, if in the hydro-support systems studied in this thesis, the bearing thickness becomes very large, the deformation of that bearing will be negligible compared to the deformation of the track. The same observation is valid for the deformation due to a localized load. So, even in this case, the Reissner–Mindlin plate theory can be used with little overall loss of accuracy.

In order to compare the full 3D elastic and thick plate models, the deformation of the PWA–lock bearing has been calculated with both models using the finite element program SEPRAN (SEGAL, 1993*b*). In this thesis we are primarily interested in bearings with a thickness smaller than that in the PWA–lock, and this calculation can therefore be considered, in this respect, to be an upper limit. If the similarity between both models is acceptable in this case, it will certainly be acceptable for bearings with a relatively smaller thickness.

For these calculations it is assumed that the hydrostatic pressure is given by equation 4.4 with a recess pressure of $10 \cdot 10^5 \text{N/m}^2$. The support of the PWA–lock bearing is ring-shaped with inner and outer diameters of 0.29 m and 0.82 m respectively. In the next chapter the reaction pressure of a ring-shaped support as a result of a uniform

compression is approximated using equation 9.12. Furthermore, the support reaction pressure is in balance with the hydrostatic pressure.

For this load on the bearing, the maximum deformation is approximately $0.02 \cdot 10^{-3} \text{m}$ (figure 8.1). There is a difference between the plate (plate) calculation and the axis-symmetric 3D (3D) calculation. This difference is caused by:

- The hydrostatic pressure on the inside edge of the recess (point A in figure 8.1) causes a reduction of the deformation of the bearing. A calculation (3D(2)) where this pressure is absent exhibits a deformation that is comparable to the deformation calculated using plate elements (plate).
- The calculation using plate elements assumes a symmetric distribution of the bearing thickness below and above a neutral plane. However in reality, the bearing is asymmetric and therefore exhibits a higher stiffness than the plate calculation predicts.

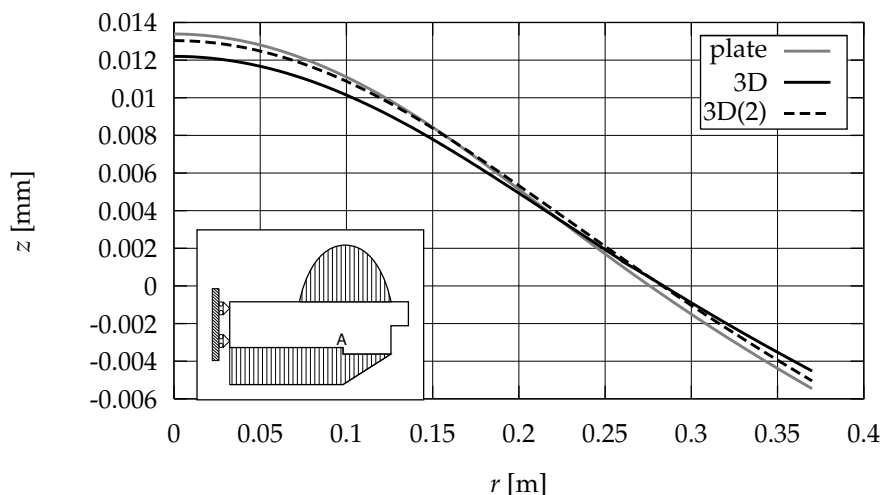


Figure 8.1: Deformation of the bearing due to a recess pressure of $10 \cdot 10^5 \text{N/m}^2$. This deformation has been calculated using both plate elements (plate) and axis-symmetric strain elements (3D and 3D(2)). In 3D(2) the pressure on the inside edge of the recess (A) has been neglected.

An advantage of the 3D model is the fact that local stresses in the bearing can be studied in more detail than with the thick plate model. For instance, the vertical stress in the bearing σ_{zz} is presented in figure 8.2. As expected, the stress on the bottom and top of the bearing are the same as the applied hydrostatic and reaction pressures. However, due to the sharp edge in the recess corner, large stress gradients occur at this corner. In practise, although the stresses in the bearing are well below the maximum allowable stresses, it is advisable to chamfer this corner in order to reduce these stress gradients.

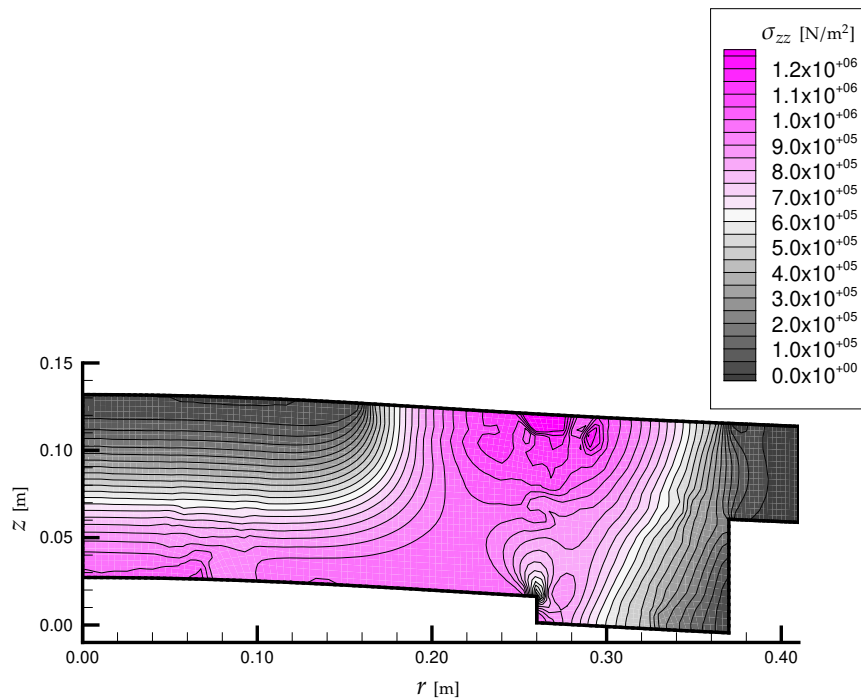


Figure 8.2: Vertical deformation and stress distribution σ_{zz} [N/m²] in the bearing. The deformation of the bearing is scaled by a factor of 1000. The maximum deformation is approximately equal to 0.02 mm. The boundary conditions are the same as in figure 8.1.

In this chapter the deformation of the bearing has been studied. This deformation has been calculated using both a full 3D description and using the Reisner–Mindlin plate model. In this thesis the Reisner–Mindlin plate model (HUGHES AND TEZDUYAR, 1981) will be used for further calculations. The accuracy is acceptable both for thin and thick bearings and the numerical efficiency is better than that of the full 3D model (figure 8.3).

In the next chapter the last part of the hydro–support will be modelled, that is the rubber support.

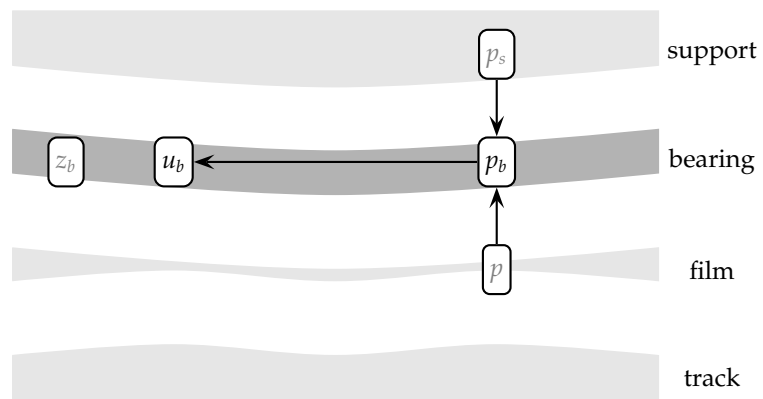


Figure 8.3: Components of the model described in this chapter: The bearing.

CHAPTER 9

Rubber support

The hydrostatic bearing is connected to the lock–gate by a highly elastic rubber support. This support acts as a hinge between the bearing and the lock–gate and has to absorb any tilt between these parts with preferably a minimum tilting moment. This tilt can be a result of:

- tilting of the lock–gate due to a water level difference on both sides of the gate. (transverse direction)
- a non–level track surface, for instance due to an error in the track’s foundation or fixation. (transverse direction)
- large scale waviness of the track surface. (transverse and/or longitudinal direction)

The demands put on this support are:

minimal tilting moment. The main demand of the support is, as stated above, the hinge function between bearing and lock–gate. A minimal tilting moment as a result of tilt means that the hinge function is performed optimally.

allowable mechanical load and deformation. The rubber support is continuously loaded with the weight of the lock–gate. This load must remain (also after a longer period of time) below the maximum allowed load on the support. Also the shear stress on the interface between the bearing and the support and between the lock–gate and the support must remain below an upper limit. This in order to ensure a good continuous connection between the parts.

transport of water. A secondary function of the support is to allow water to be supplied to the bearing. The water for the hydrostatic bearing is pumped by a supply

pump in the lock-gate to the bearing. For this reason the support of the PWA-lock is not a disc but a ring, where the water is supplied to the bearing via pipes running through the center hollow part of the ring (figure 9.1a). A disadvantage of the ring compared to the disc is the fact that the ring has a larger tilting stiffness than the massive disc for the same axial stiffness. Another possibility to supply water through the support, is to manufacture the water supply conduits directly in the support (figure 9.1b).

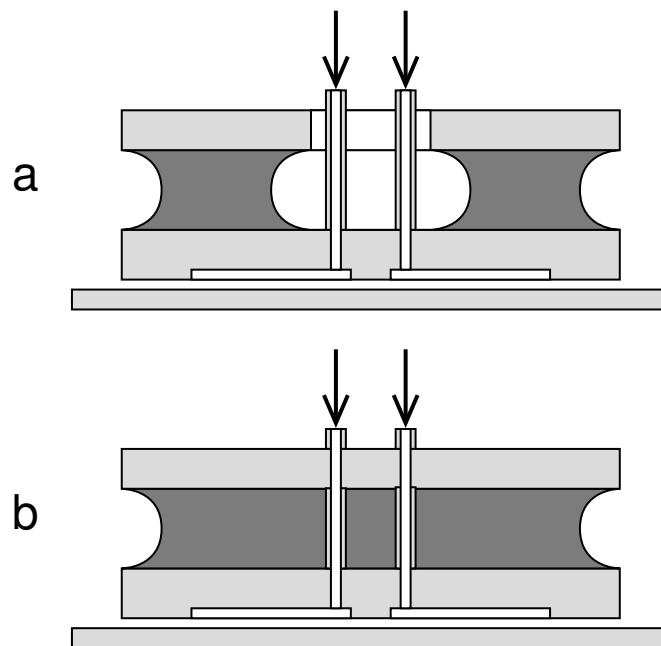


Figure 9.1: (a) hollow ring support allowing (rigid) supply conduits to run through, (b) solid disc support with (flexible) supply conduits inserted in the support

reaction pressure opposing the hydrostatic and contact pressure. The bearing deforms as a result of the hydrostatic and contact pressures under the bearing and the reaction pressure of the support on top of the bearing. In particular a thin bearing has to be locally supported against the hydrostatic and contact pressures.

The support deforms as a result of the load on the bearing. This load is equal to approximately 50% of the total submerged weight of the lock-gate. Due to the fact that the axial stiffness of the support is much lower than that of the lubricating film, the support will compress much more than the nominal film thickness of the film (approximately 100 times). This means that any variation in the nominal film thickness due to track surface waviness and bearing deformation will only result in a relatively small extra deformation of the support. Therefore, in this study it is assumed that the axial stiffness of the support can be calculated assuming a uniform compression of the

support, neglecting any small variations due to track surface waviness and bearing deformation.

The stresses and strains in a rubber block bonded to two rigid end plates have been studied by GENT ET AL. (1974); GENT AND LINDLEY (1959); GENT AND MEINECKE (1970); HALL (1971); LINDLEY (1975, 1979*a,b*); LING ET AL. (1995); SHARIFF (1988, 1989).

The deformation and stresses in the support can be calculated using different methods. In this study two methods have been used and compared:

- Full 3D calculation based on Rayleigh's analogue.
- Reduced 2D calculation based on the constant pressure approximation.

9.1 3D deformation

The properties of the rubber support can be calculated with a full 3D calculation using a finite element program (SEPRAN). Although the deformation of rubber is strongly non-linear for large deformations, the material can be considered to deform linear for strains up to approximately 10% (GENT AND MEINECKE, 1970). Furthermore it is assumed that the rubber is perfectly incompressible (Poisson's ratio $\nu_s = 0.5$).

Using these two assumptions the analogue between incompressible elastic deformation and incompressible fluid flow (RAYLEIGH, 1896) can be used to calculate the deformations and stresses in the rubber support. Rayleigh's analogue states that the deformation of an incompressible elastic body is analogous to the flow velocity of an incompressible fluid within a geometry defined by that body. The shear modulus of the elastic material is analogous to the viscosity of the fluid.

These calculations have been performed both for the circular support and for a transverse cross-section of an infinitely long hydro-fender support.

9.1.1 Hydro-foot

In this section the stresses in a circular support of a hydro-foot are calculated using a finite element program and Rayleigh's analogue.

The results are dependent on the geometry. As an example the stresses in a massive, circular support with a constant thickness and a thickness/diameter ratio of 1/10 have been calculated. The support is assumed to be fixed to two rigid surfaces on top and bottom of the support. The edge of the support is free.

As a result of a uniform compression of the support the axi-symmetric normal stress at the top and bottom surfaces becomes approximately parabolic and the axi-symmetric shear stress at the surfaces increases approximately linearly from the center to the edge

(figure 9.2). As stated above, it is assumed that the stress is linearly dependent on the strain. Therefore all stresses and pressures presented in this chapter have been scaled and made dimensionless using:

$$\bar{\sigma} = \frac{\sigma}{E_s \epsilon} \quad (9.1a)$$

$$\bar{p} = \frac{p}{E_s \epsilon} \quad (9.1b)$$

with $\bar{\sigma}$ and σ the dimensionless and non–dimensionless stress component, \bar{p} and p the dimensionless and non–dimensionless pressure and E_s the modulus of elasticity and ϵ the uniform strain calculated using:

$$\epsilon = \frac{e}{t_s} \quad (9.2)$$

where e is the compression and t_s the initial height of the support.

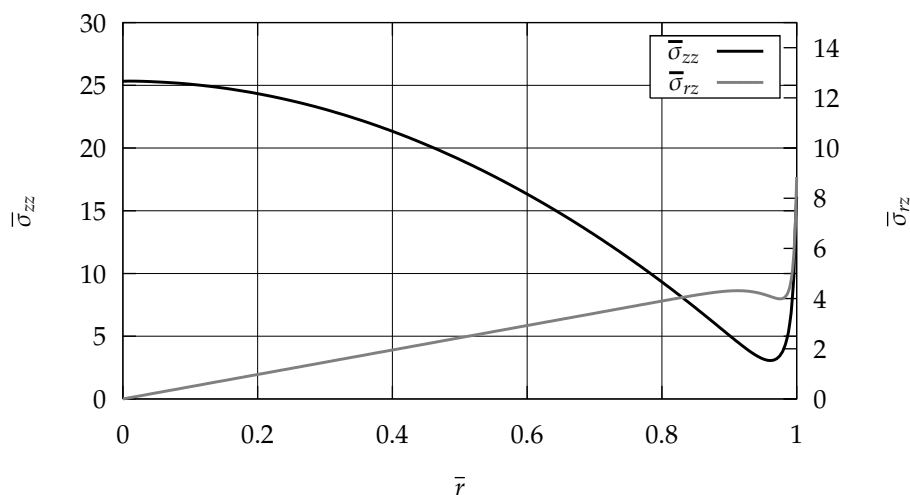


Figure 9.2: The vertical stress $\bar{\sigma}_{zz}$ and shear stress $\bar{\sigma}_{rz}$ at the interface of a circular rubber support with a rectangular cross section and the rigid bearing for a uniform compression.

The dimensionless radial stress $\bar{\sigma}_{rr}$, vertical stress $\bar{\sigma}_{zz}$, shear stress $\bar{\sigma}_{rz}$ and hydrostatic pressure \bar{p} in a cross–section are shown in figures 9.3, 9.4, 9.5 and 9.6 respectively. This last figure shows that the hydrostatic pressure \bar{p} is approximately constant for constant r in a large part of the support. This fact will be used in the development of the constant pressure approximation in section 9.2.

All these figures show that there are large peak stresses at the corners of the support that are located both at the edge and on the interface of the support and the rigid surfaces. These peak stresses can result in a failure of the bond between the support

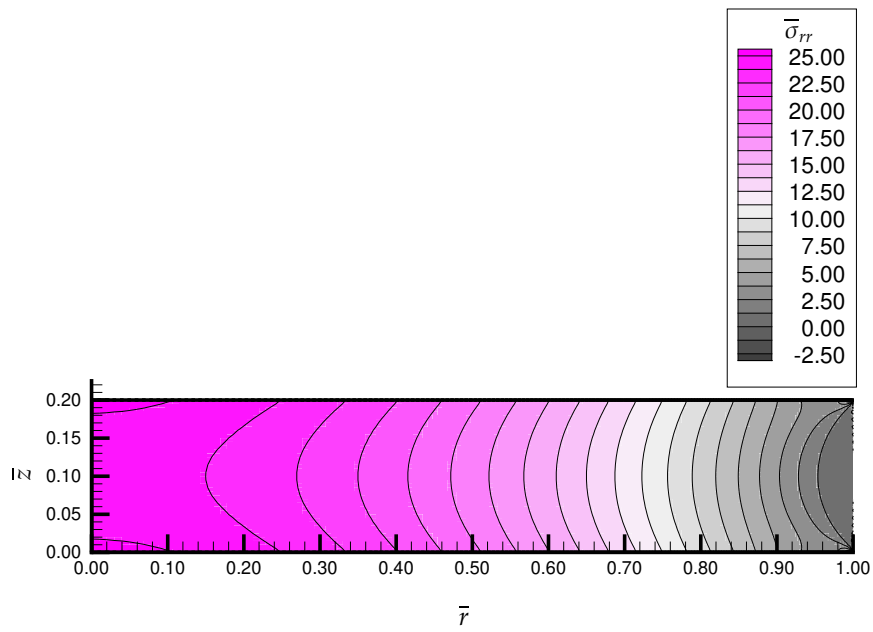


Figure 9.3: The radial stress $\bar{\sigma}_{rr}$ in a circular rubber support with a rectangular cross section for a uniform compression ϵ .

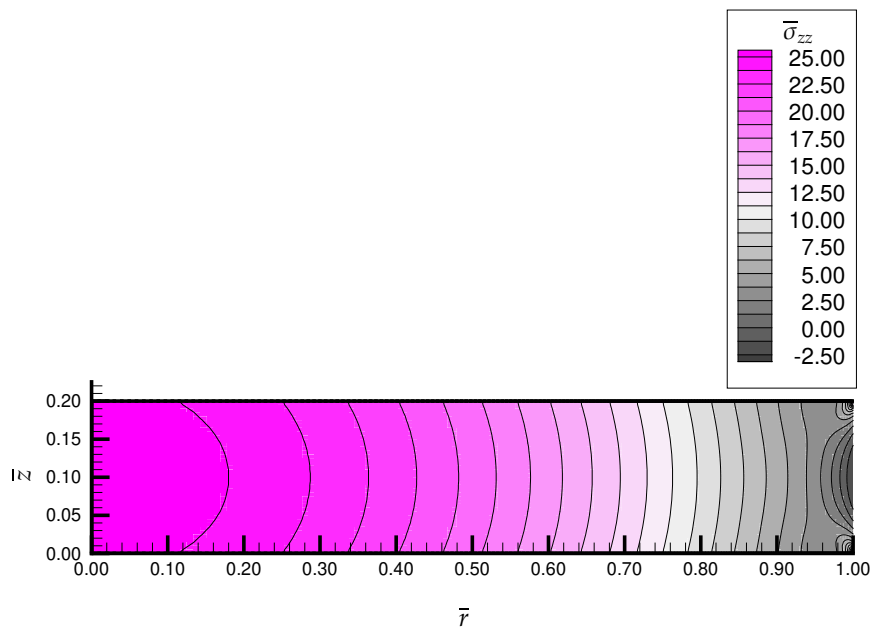


Figure 9.4: The vertical stress $\bar{\sigma}_{zz}$ in a circular rubber support with a rectangular cross section for a uniform compression ϵ .

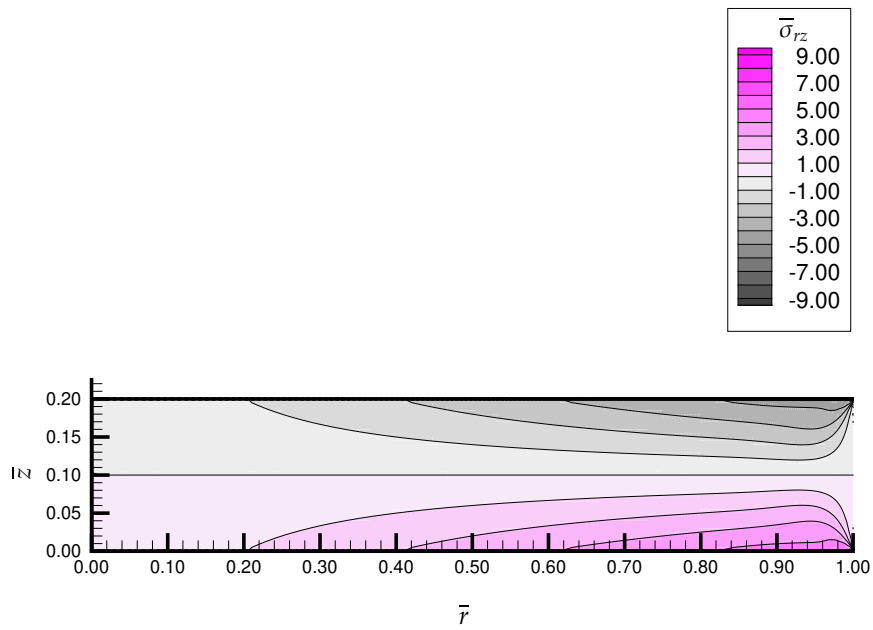


Figure 9.5: The shear stress $\bar{\sigma}_{rz}$ in a circular rubber support with a rectangular cross section for a uniform compression ϵ .

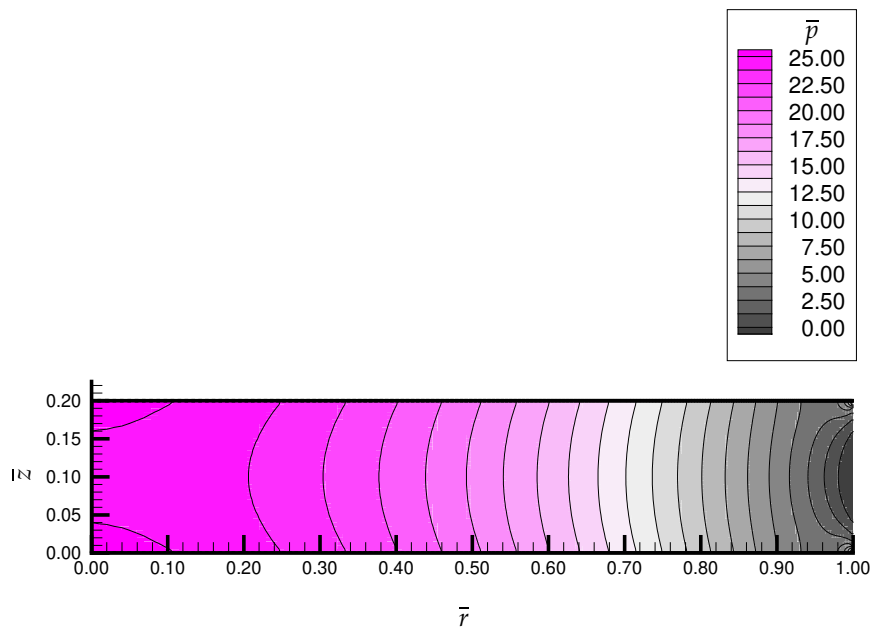


Figure 9.6: The hydrostatic pressure \bar{p} in a circular rubber support with a rectangular cross section for a uniform compression ϵ .

and the rigid metal surfaces. Later (section 9.3) we will study possibilities to reduce these peak stresses.

In the next section the same calculations have been carried out for a cross-section of the support of an infinitely long hydro-fender.

9.1.2 Hydro-fender

In this section the stresses in a cross-section of the support of an infinitely long hydro-fender are calculated using a finite element program and Rayleigh's analogue. The support has a constant height and therefore the cross-section is rectangular.

The results are dependent on the geometry. As an example the stresses in a massive support with a constant thickness and a thickness/width ratio of 1/10 have been calculated. The support is assumed to be fixed to two rigid surfaces on top and bottom of the support. The edge of the support is free.

As a result of a uniform compression of the support the normal stress at the top and bottom surfaces becomes approximately parabolic and the shear stress at the surfaces increases approximately linearly from the center to the edge (figure 9.7). These results are qualitatively the same as those for the hydro-foot support (figure 9.2) however the maximum values for the normal stress (50 versus 25) and the shear stress (10 versus 5, disregarding the edge stress peak) have doubled.

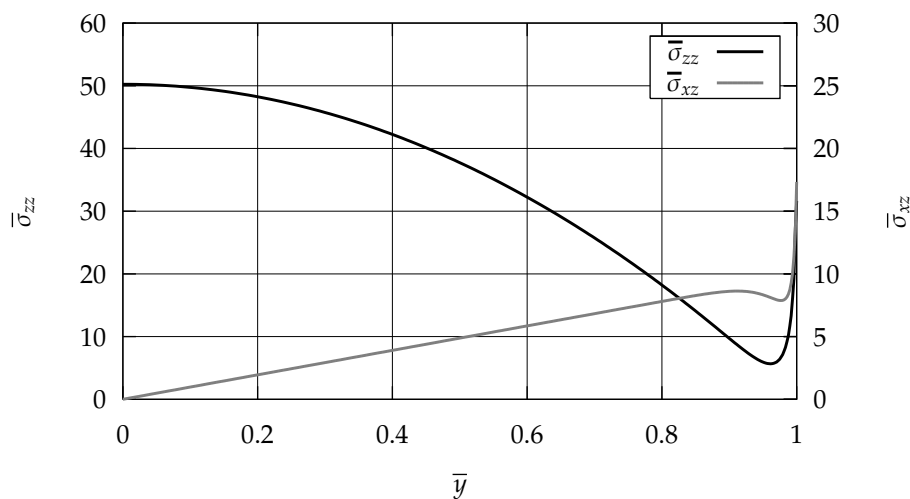


Figure 9.7: The vertical stress $\bar{\sigma}_{zz}$ and shear stress $\bar{\sigma}_{xz}$ at the interface of an infinitely long rubber support with a rectangular cross section and the rigid bearing for a uniform compression.

The dimensionless transverse stress $\bar{\sigma}_{xx}$, vertical stress $\bar{\sigma}_{zz}$, shear stress $\bar{\sigma}_{xz}$ and hydrostatic pressure \bar{p} in a cross-section are shown in figures 9.8, 9.9, 9.10 and 9.11 respectively.

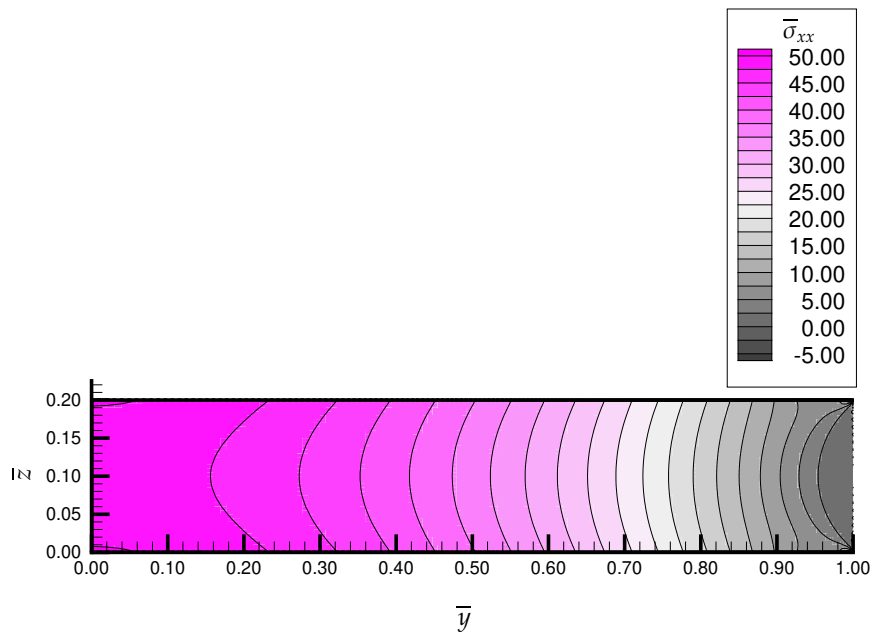


Figure 9.8: The horizontal stress $\bar{\sigma}_{xx}$ in an infinitely long rubber support with a rectangular cross section for a uniform compression ϵ .

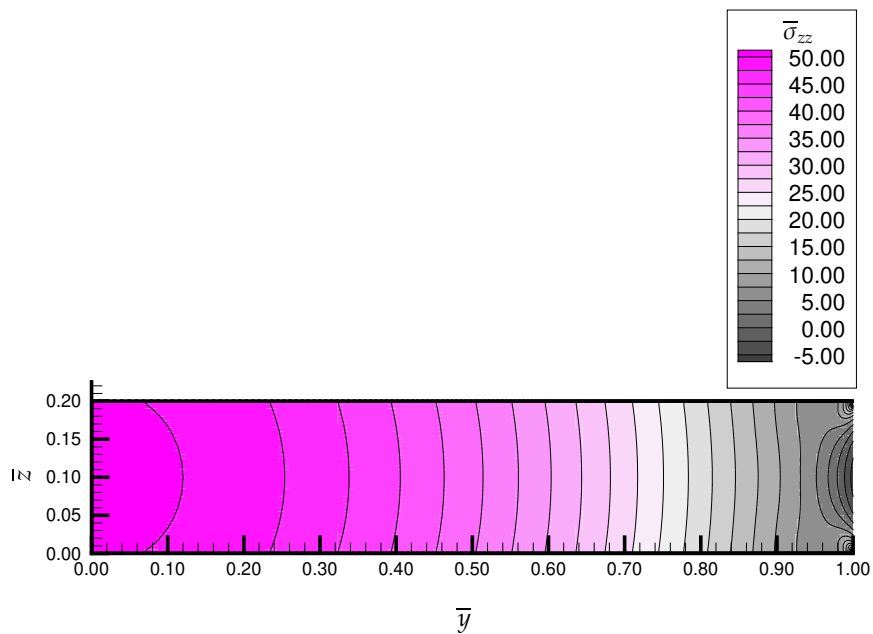


Figure 9.9: The vertical stress $\bar{\sigma}_{zz}$ in an infinitely long rubber support with a rectangular cross section for a uniform compression ϵ .

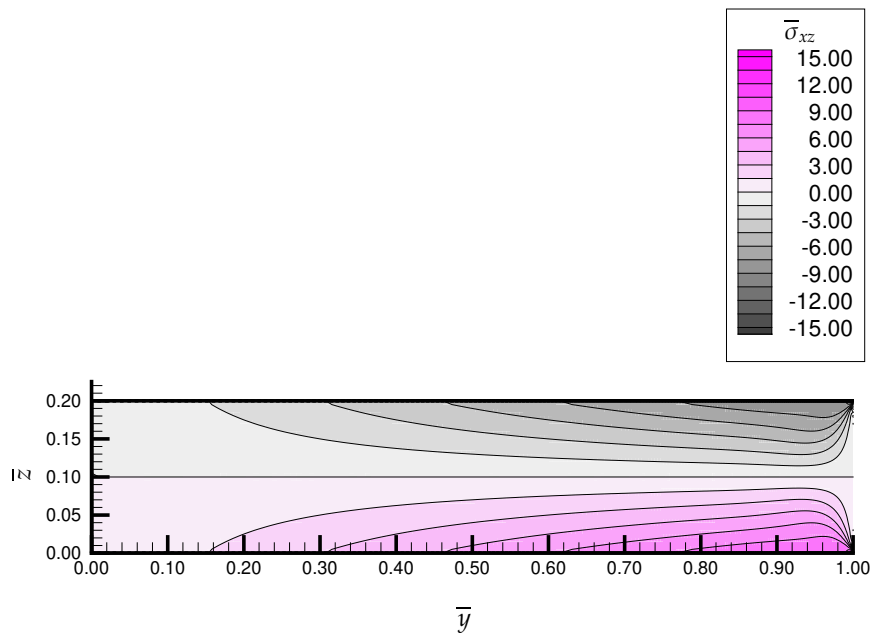


Figure 9.10: The shear stress $\bar{\sigma}_{xz}$ in an infinitely long rubber support with a rectangular cross section for a uniform compression ϵ .

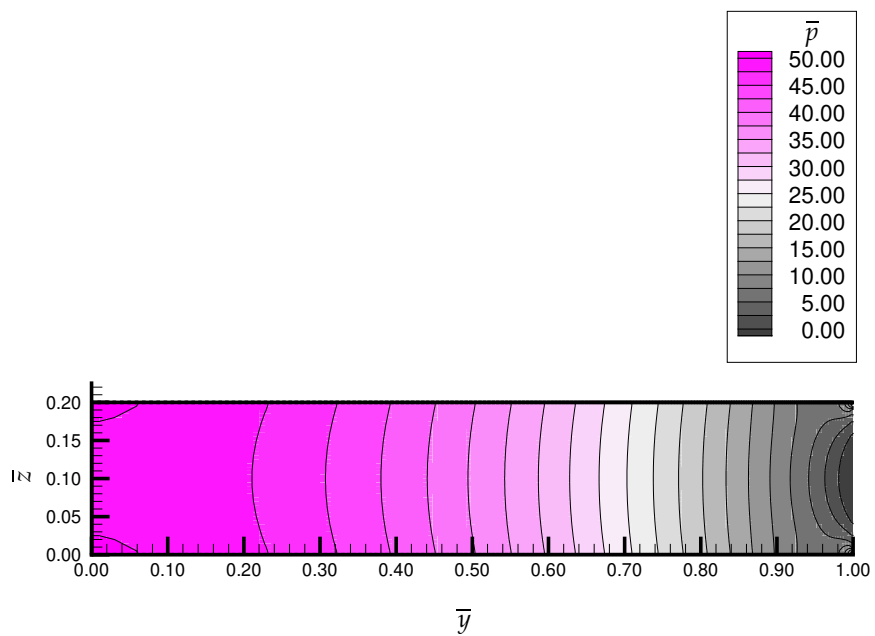


Figure 9.11: The hydrostatic pressure \bar{p} in an infinitely long rubber support with a rectangular cross section for a uniform compression ϵ .

Just as was the case for the circular support these figures show large peak stresses at the outer edge of the support. Also, figure 9.11 shows that the hydrostatic pressure \bar{p} is approximately constant for constant x in a large part of the support. This fact will be used in the next section where the constant pressure assumption is used to simplify the stress calculation in the rubber support.

9.2 Constant pressure approximation

We have seen that as a result of compression, the hydrostatic pressure in the rubber support is approximately constant across the height of the support (figures 9.6 and 9.11). Using this fact, the constant pressure approximation as derived by (GENT AND LINDLEY, 1959; GENT AND MEINECKE, 1970), can be used to calculate the stress and strain in the support. This model has been derived using a number of assumptions:

- The rubber body considered has a small height relative to its other dimensions.
- The top and bottom surfaces of the body are fixed to rigid surfaces.
- The rubber is perfectly incompressible. (Poisson's ratio $\nu_s = 0.5$)
- Originally plane, horizontal cross-sections remain plane under deformation.
- The hydrostatic pressure is constant across the height of the body.

In GENT AND MEINECKE (1970) it has been shown that, using this constant pressure approximation, the normal stress on the top and bottom planes of a rubber body with height t_s as a result of a uniform compression e , can be approximated using:

$$\sigma_{zz} = E_s \epsilon + p \tag{9.3}$$

with σ_{zz} the normal stress, E_s modulus of elasticity, ϵ the strain as a result of a constant, uniform compression:

$$\epsilon = \frac{e}{t_s} \tag{9.4}$$

and p the hydrostatic pressure. The hydrostatic pressure p is equal to the solution to the 2^e order partial differential equation (GENT AND MEINECKE, 1970):

$$\frac{\partial}{\partial x} \left(-\frac{t_s^3}{12G_s} \frac{\partial p}{\partial x} \right) + \frac{\partial}{\partial y} \left(-\frac{t_s^3}{12G_s} \frac{\partial p}{\partial y} \right) = e \tag{9.5}$$

The striking similarity between this and the Reynolds' equation used to calculate the pressure in a lubricating film is obvious.

In general, the shear modulus G_s of a linear elastic material is related to the modulus of elasticity E_s and Poisson's ratio ν_s of that material:

$$G_s = \frac{E_s}{2(1 + \nu_s)} \quad (9.6)$$

For an incompressible material $\nu_s = 0.5$ and thus:

$$G_s = \frac{E_s}{3} \quad (9.7)$$

Using this property equation 9.5 becomes:

$$\frac{\partial}{\partial x} \left(-\frac{t_s^3}{4E_s} \frac{\partial p}{\partial x} \right) + \frac{\partial}{\partial y} \left(-\frac{t_s^3}{4E_s} \frac{\partial p}{\partial y} \right) = e \quad (9.8)$$

The load W and tilting moments M_x and M_y on the support can be calculated using:

$$W = \iint_A \sigma_{zz} dA \quad (9.9a)$$

$$M_x = \iint_A x \sigma_{zz} dA \quad (9.9b)$$

$$M_y = \iint_A y \sigma_{zz} dA \quad (9.9c)$$

In the following sections equation 9.8 will be used to calculate the hydrostatic pressure as a result of compression of the hydro-foot and hydro-fender supports. These results will be compared to the finite element results of section 9.1.

9.2.1 Hydro-foot

In this section the normal stress between the support and the bearing of a hydro-foot are calculated using the constant pressure approximation. Here it will be assumed that the support is not a massive disc with a rectangular cross-section, but a ring (like in the PWA-lock) (figure 9.12). The ring has outside diameter D_s , inside diameter d_s and height t_s . In case of a uniform compression equation 9.8 can be rewritten to its axi-symmetric form:

$$\frac{1}{r} \frac{\partial}{\partial r} \left(-\frac{t_s^3 r}{4E_s} \frac{\partial p}{\partial r} \right) = e \quad (9.10)$$

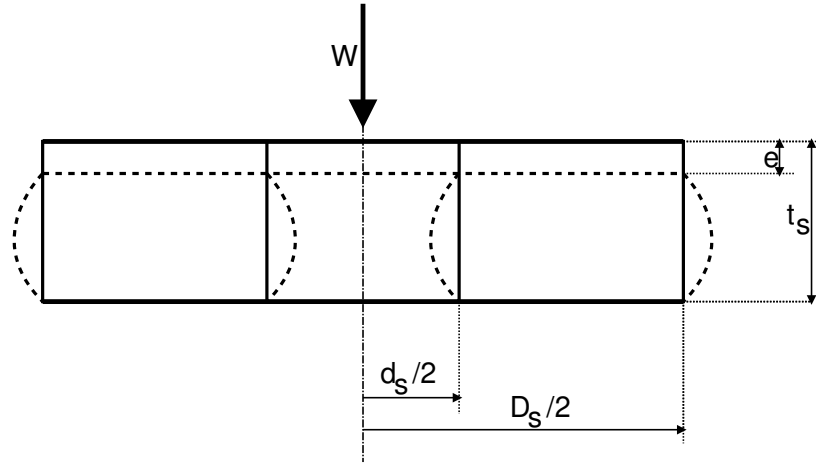


Figure 9.12: compression e of a rubber ring given a load W .

Introducing the boundary conditions:

$$p(d_s/2) = 0 \quad (9.11a)$$

$$p(D_s/2) = 0 \quad (9.11b)$$

and then solving this equation and introducing the relative compression $\epsilon = e/t_s$ and dimensionless coordinate $\bar{r} = 2r/D_s$ yields:

$$p(\bar{r}) = E_s \epsilon S^2 \left(1 - \bar{r}^2 - (1 - \bar{R}_s^2) \frac{\ln(\bar{r})}{\ln(\bar{R}_s)} \right) \quad (9.12)$$

and therefore (using equation 9.3):

$$\sigma_{zzL}(\bar{r}) = E_s \epsilon \left(1 + S^2 \left(1 - \bar{r}^2 - (1 - \bar{R}_s^2) \frac{\ln(\bar{r})}{\ln(\bar{R}_s)} \right) \right) \quad (9.13)$$

where the subscript L in σ_{zzL} stands for 'linear' and where S is a slenderness parameter:

$$S = \frac{D_s}{2t_s} \quad (9.14)$$

and $\bar{R}_s = d_s/D_s$ the ratio between the inner and outer radius of the support. Figure 9.13 compares the normal stress on the top surface of a massive circular support ($\bar{R}_s = 0$) calculated with equation 9.13 and the full 3D model (see also figure 9.2):

$$\sigma_{zzL}(\bar{r}) = E_s \epsilon \left(1 + S^2 (1 - \bar{r}^2) \right) \quad (9.15)$$

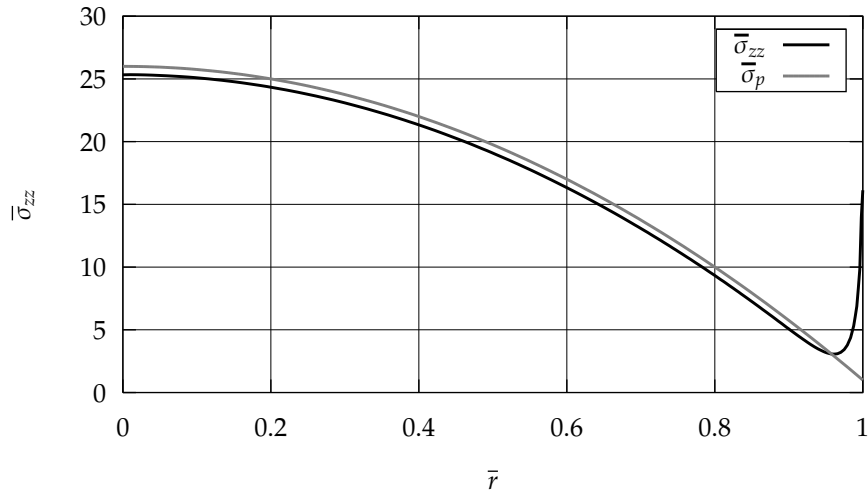


Figure 9.13: The vertical stress of a massive ($\bar{R}_s = 0$) circular rubber support with a rectangular cross section calculated with a full 3D model $\bar{\sigma}_{zz}$ compared to the stress calculated with the constant pressure approximation $\bar{\sigma}_p$.

Integrating equation 9.13 over the surface area of the support, the load W_L becomes:

$$\frac{4W_L}{\pi D_s^2 E_s} = \epsilon(1 - \bar{R}_s^2) \left(1 + \frac{S^2}{2} \left(1 + \bar{R}_s^2 + \frac{1 - \bar{R}_s^2}{\ln(\bar{R}_s)} \right) \right) \quad (9.16)$$

Equation 9.16 is valid for small deformations ϵ . It is possible to derive the load for larger deformations if the deformed geometry is taken into account. In this case the σ_{zzNL} is given by:

$$\sigma_{zzNL} = \frac{E_s}{3} \left(\frac{1}{(1 - \epsilon)^2} - (1 - \epsilon) \right) + p_{NL} \quad (9.17)$$

where the first term denotes the stress due to a *large* uniform compression (GENT AND LINDLEY, 1959) and the second term the accompanying hydrostatic pressure which is the solution of a modified version of equation 9.10:

$$\frac{1}{r} \frac{\partial}{\partial r} \left(-\frac{t_s^3(1 - \epsilon)^3 r}{4E_s} \frac{\partial p_{NL}}{\partial r} \right) = e \quad (9.18)$$

In this equation, the support height in the differential equation is corrected for the compression, so t_s is replaced by $t_s(1 - \epsilon)$. The solution to this partial differential equation is given by:

$$p_{NL}(\bar{r}) = E_s \frac{\epsilon}{(1 - \epsilon)^3} S^2 \left(1 - \bar{r}^2 - (1 - \bar{R}_s^2) \frac{\ln(\bar{r})}{\ln(\bar{R}_s)} \right) \quad (9.19)$$

and therefore the stress $\sigma_{zz_{NL}}$ is equal to:

$$\sigma_{zz_{NL}}(\bar{r}) = E_s \left(\frac{1}{3} \left(\frac{1}{(1-\epsilon)^2} - (1-\epsilon) \right) + \frac{\epsilon}{(1-\epsilon)^3} S^2 \left(1 - \bar{r}^2 - (1 - \bar{R}_s^2) \frac{\ln(\bar{r})}{\ln(\bar{R}_s)} \right) \right) \quad (9.20)$$

Integrating this equation over the surface area of the support, gives the load on the support for large deformations:

$$\frac{4W_{NL}}{\pi D_s^2 E_s} = (1 - \bar{R}_s^2) \left(\frac{1}{3} \left(\frac{1}{(1-\epsilon)^2} - (1-\epsilon) \right) + \frac{\epsilon}{(1-\epsilon)^3} \frac{S^2}{2} \left(1 + \bar{R}_s^2 + \frac{1 - \bar{R}_s^2}{\ln(\bar{R}_s)} \right) \right) \quad (9.21)$$

In figure 9.14 the load on the rubber supports used in the PWA-lock versus the compression is shown. For the nominal load of $250 \cdot 10^3 \text{N}$ the compression is approximately $6 \cdot 10^{-3} \text{m}$. In this case the linear model is sufficient. At higher loads the non-linear model is better.

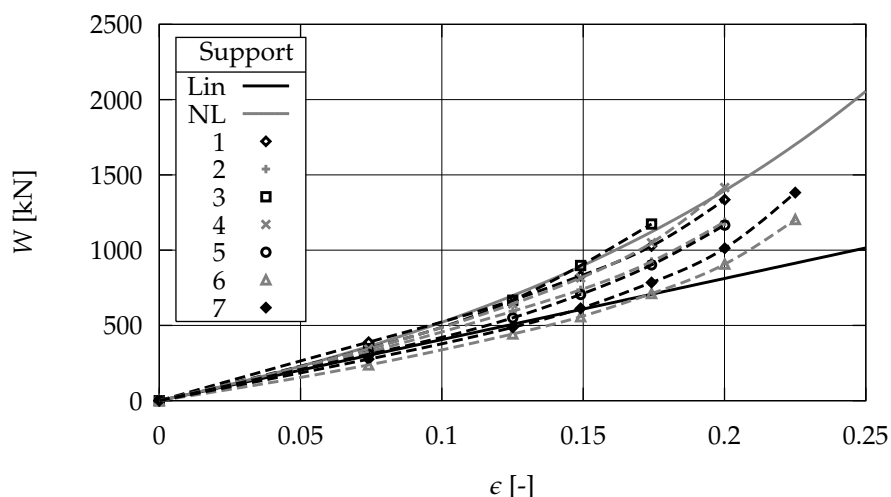


Figure 9.14: Compression of the PWA-lock rubber support. Linear (equation 9.16) and non-linear (equation 9.21) model compared with experimental data of 7 rubber supports (BAKKER-RUBBER, 1994).

Again using the linear approximation, it is possible to derive a relation for the tilting stiffness of the circular ring support (figure 9.15). For this analysis a cylindrical coordinate system (r, ϕ) is used with the angle ϕ defined relative to the angle of maximum tilt. This means that for a given tilting angle α the compression e on the top plane of the support in a point (r, ϕ) is given by:

$$e(r, \phi) = ar \cos(\phi) \quad (9.22)$$

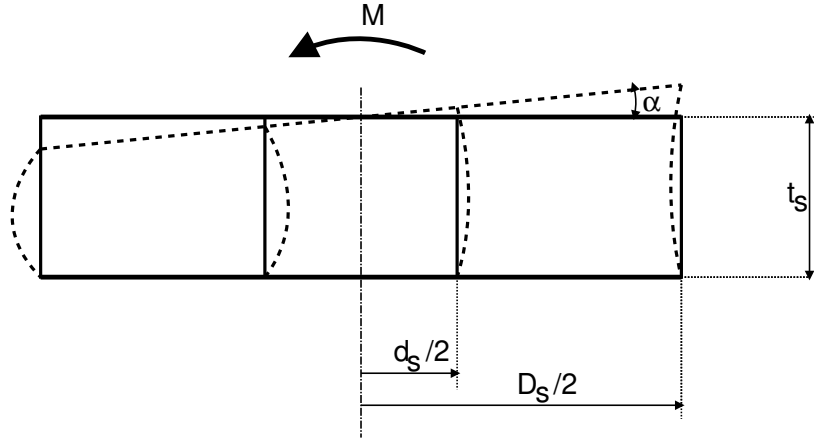


Figure 9.15: Tilt α of a rubber ring given a tilting moment M .

In this case the normal stress on the support is given by:

$$\sigma_{zz} = \frac{E_s \alpha r \cos(\phi)}{h} + p \quad (9.23)$$

where the first term denotes the vertical stress due to a uniform rotation and the second term p the accompanying hydrostatic pressure which follows from equation 9.8 which reads in cylindrical coordinates:

$$\frac{\partial}{r \partial r} \left(-\frac{t_s^3 r}{4E_s} \frac{\partial p}{\partial r} \right) + \frac{\partial}{r \partial \phi} \left(-\frac{t_s^3}{4E_s r} \frac{\partial p}{\partial \phi} \right) = \alpha r \cos(\phi) \quad (9.24)$$

Introducing the boundary conditions:

$$p(d_s/2, \phi) = 0 \quad (9.25a)$$

$$p(D_s/2, \phi) = 0 \quad (9.25b)$$

and $\bar{r} = 2r/D$, $S = D_s/2t_s$ and $\bar{\alpha} = \alpha S$ and solving for p yields:

$$p(\bar{r}, \phi) = E_s \bar{\alpha} \bar{r} \cos(\phi) \frac{S^2}{2} \left(1 - \bar{r}^2 + \bar{R}_s^2 \left(1 - \frac{1}{\bar{r}^2} \right) \right) \quad (9.26)$$

and therefore:

$$\sigma_{zz}(\bar{r}, \phi) = E_s \bar{\alpha} \bar{r} \cos(\phi) \left(1 + \frac{S^2}{2} \left(1 - \bar{r}^2 + \bar{R}_s^2 \left(1 - \frac{1}{\bar{r}^2} \right) \right) \right) \quad (9.27)$$

Integrating this equation using:

$$M = \int_{d_s/2}^{D_s/2} \int_{-\pi}^{\pi} \sigma_{zz} r^2 \cos(\phi) d\phi dr \quad (9.28)$$

gives the tilting moment M for a given tilting angle $\bar{\alpha}$ and geometry S, \bar{R}_s :

$$\frac{4M}{\pi D_s^3 E_s} = \frac{1}{8} \bar{\alpha} (1 - \bar{R}_s^2) \left(1 + \bar{R}_s^2 + \frac{S^2}{6} (1 - \bar{R}_s^2)^2 \right) \quad (9.29)$$

The calculated tilting stiffness for the PWA–lock support of $1.72 \cdot 10^6 \text{Nm/rad}$ agrees very well with the tilting stiffness measured for the actual PWA–lock hydro–foot supports (BAKKER-RUBBER, 1994).

9.2.2 Hydro–fender

In this section the constant pressure approximation is applied to the rubber support of the hydro–fender. It is assumed that the support is massive with constant height and hollowed outer edges.

Analogous to the calculation for the hydro–foot in the previous section, the normal stress σ_{zz} between the infinitely long support with rectangular cross–section and the bearing due to compression $\epsilon = e/t_s$ can be calculated and is found to be equal to:

$$\sigma_{zz_L}(\bar{y}) = E_s \epsilon \left(1 + \frac{1}{2} S^2 (1 - \bar{y}^2) \right) \quad (9.30)$$

with dimensionless coordinate $\bar{y} = \frac{y}{B/2}$ and a slenderness parameter S :

$$S = \frac{B}{t_s} \quad (9.31)$$

Figure 9.16 shows this result and the result of the full 3D calculation.

The constant pressure approximation can also be applied to a support with a finite length/width ratio. In this case equation 9.8 can be solved numerically. Figure 9.17 shows the normal stress of a support with length/width ratio equal to 2. Figures 9.18 and 9.19 show the same for a length/width ratio 4 and 8 respectively.

These calculations show that for an increasing length/width ratio, the normal stress approaches that of the infinitely long support. Furthermore it is clear that the fender can be divided into 3 parts: a central part with approximately constant normal stress and two end parts where the normal stress is reduced to zero. These end parts are approximately as long as they are wide.

9.3 Support shape optimization

The supports that have been considered until now have a simple shape: a massive rubber circular (hydro–foot) or rectangular (hydro–fender) block with a rectangular

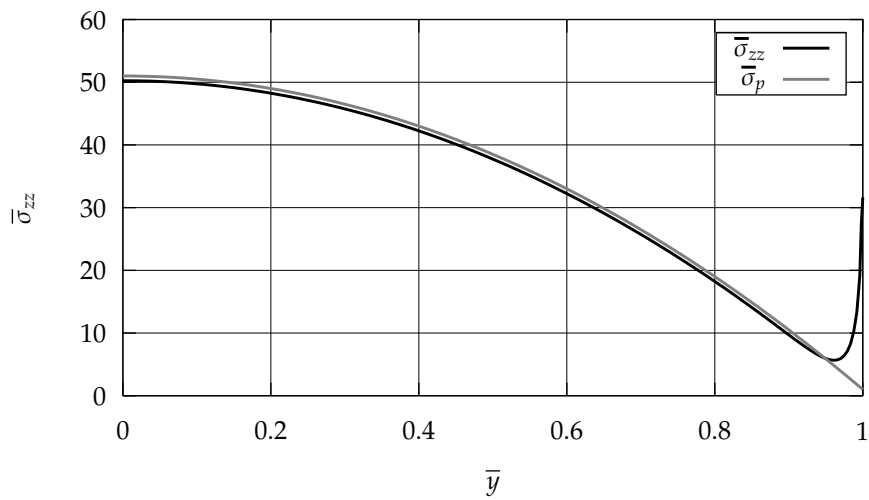


Figure 9.16: The vertical stress $\bar{\sigma}_{zz}$ in an infinitely long rubber support and uniform compression versus the position $\bar{y} = \frac{y}{B/2}$ compared with the constant pressure approximation $\bar{\sigma}_p$.

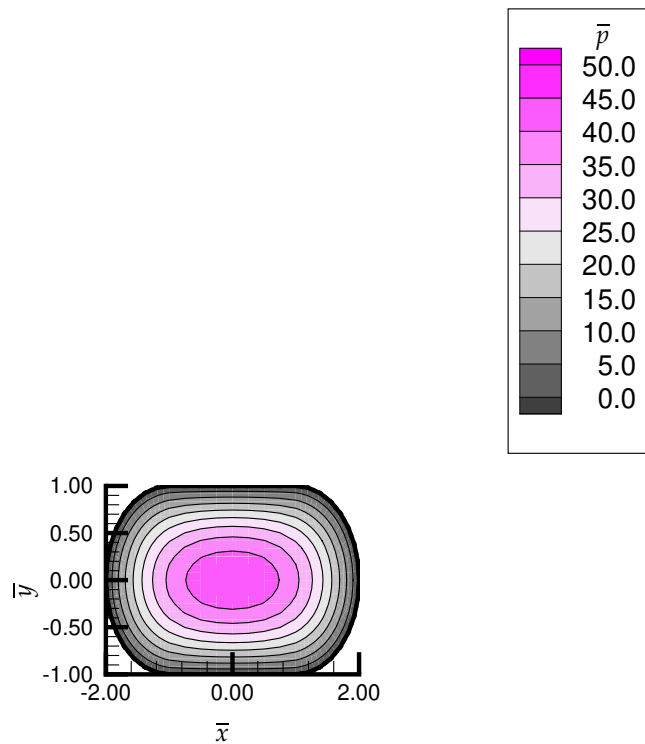


Figure 9.17: The vertical stress $\bar{\sigma}_{zz}$ in a rubber support with a length/width ratio of 2 and with a rectangular cross section given a uniform compression ϵ . The maximum value is equal to 45.5.

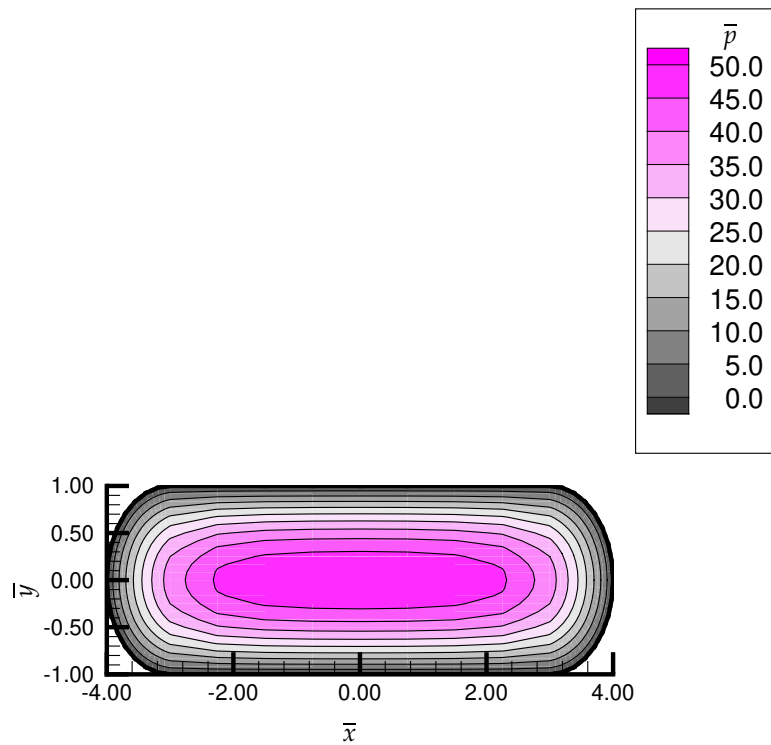


Figure 9.18: The vertical stress $\bar{\sigma}_{zz}$ in a rubber support with a length/width ration of 4 and with a rectangular cross section given a uniform compression ϵ . The maximum value is equal to 49.8.

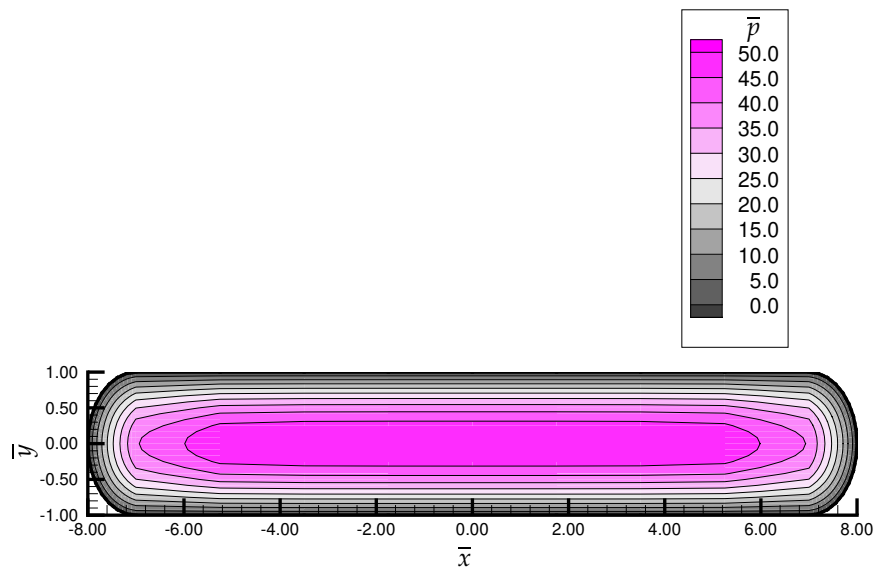


Figure 9.19: The vertical stress $\bar{\sigma}_{zz}$ in a rubber support with a length/width ration of 8 and with a rectangular cross section given a uniform compression ϵ . The maximum value is equal to 50.0. (Compare with figure 9.16)

vertical cross-section. This type of support exhibits high peak stresses at the edge of the support. In the next section a method to reduce these peak stresses is investigated. Furthermore, in section 9.3.2 it is postulated that, in particular for the (very) thin bearing, there exists an 'ideal' support with a very specific reaction pressure. The 'ideal' support ensures a parallel lubricating film, even for non-smooth surfaces.

9.3.1 Reduction of peak stresses

The calculations in section 9.1 show that as a result of compression large peak stresses occur at the outer edge points of the support. These peak stresses (in particular the shear stresses) can cause the bonding between the support and the rigid end plates to fail. In order to reduce these peak stresses the edge of the support can be hollowed out. Figure 9.20 shows (half) a vertical cross-section of a support with an increasingly hollowed out edge. This edge shape is described by the polynomial:

$$\bar{B}_s(\bar{z}) = 1 - a_s \bar{z}(1 - \bar{z}) \quad (9.32)$$

where the parameter a_s is increased from 0 to increase the hollow and:

$$\bar{B}_s = \frac{B_s}{B} \quad (9.33)$$

$$\bar{z} = \frac{z}{t_s} \quad (9.34)$$

with B_s the support width, which, due to the hollowed out edge, is a function of the z-coordinate.

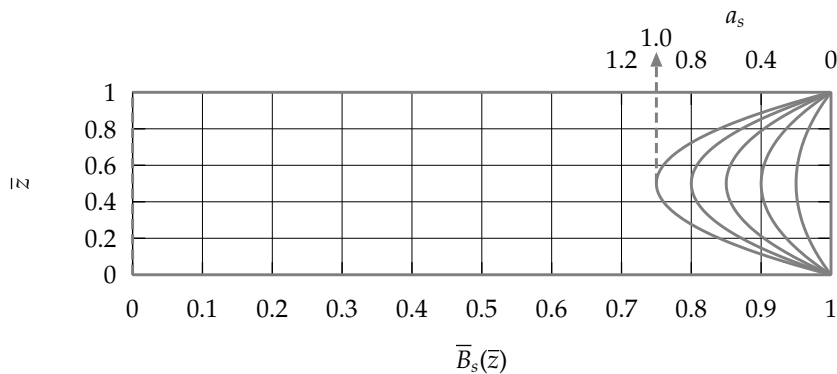


Figure 9.20: Half cross section of the infinitely long rubber support with a hollowed edge for 6 values of a_s increasing from 0 to 1.

If the hollow is increased the peak stresses are reduced until for a value of the parameter $a_s = 0.4$ both the normal stress $\tilde{\sigma}_{zz}$ (figure 9.21) and the shear stress $\tilde{\sigma}_{xz}$ (figure 9.22) show no peak stresses at the edge. These calculations have been performed using the

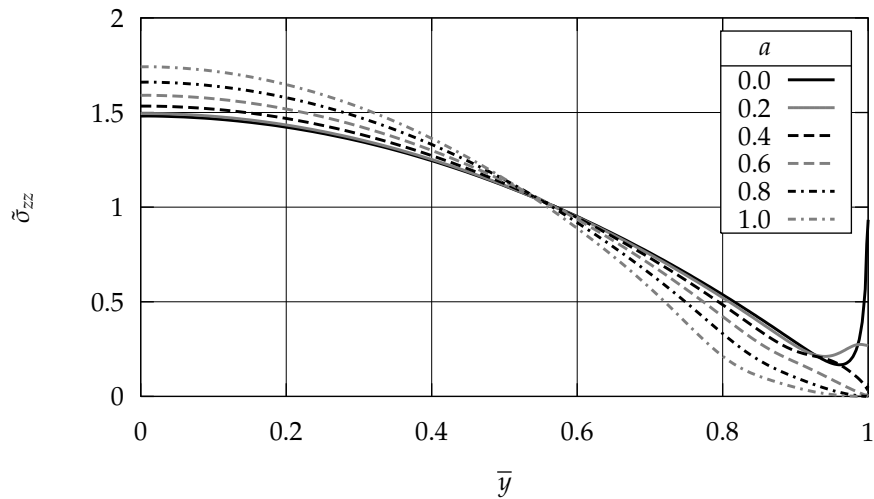


Figure 9.21: The vertical stress $\tilde{\sigma}_{zz}$ in an infinitely long rubber support with uniform compression ϵ versus the position $\bar{y} = \frac{y}{B/2}$. The amount with which the edge is hollowed out is the parameter.

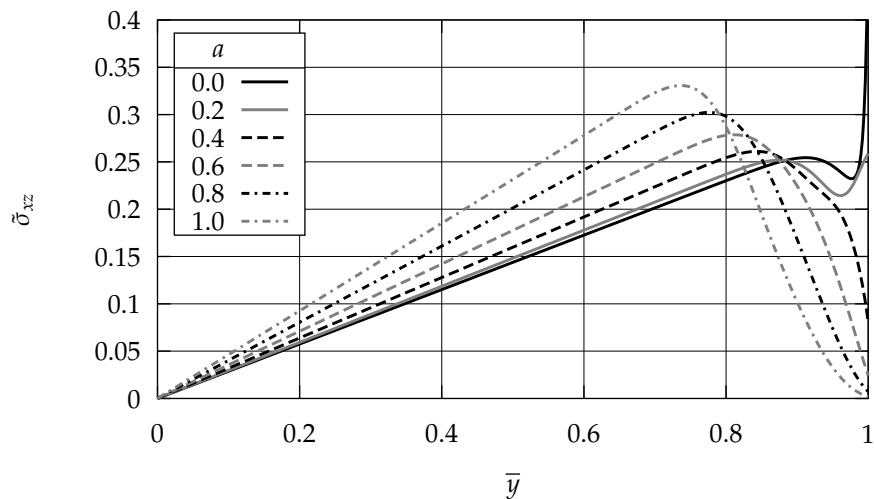


Figure 9.22: The shear stress $\tilde{\sigma}_{xz}$ in an infinitely long rubber support with uniform compression ϵ versus the position $\bar{y} = \frac{y}{B/2}$. The amount with which the edge is hollowed out is the parameter.

full 3D model previously used in section 9.1.2. Contrary to the previous figures in this chapter, the stresses in figures 9.21 and 9.22 have not been scaled using equations 9.1a. Instead, in order to evaluate the effect of the hollowed edge the following scaling has been used:

$$\tilde{\sigma} = \frac{\sigma A}{W} \quad (9.35)$$

with A the surface area of the support and W the load. Therefore, the curves in figures 9.21 and 9.22 present the stress for constant load.

9.3.2 Optimization of normal stresses

In the previous section the problem of the peak stresses was studied. In this section the relation between the normal stresses of the support on top of the bearing and the hydrostatic and contact pressure on the bottom of the bearing is studied.

The reaction pressure of a support with a rectangular cross-section due to a uniform compression, reaches a maximum in the center of the support and reduces to the edge parabolically (figures 9.2 and 9.7). At the same time, if we assume that the lubricating film remains parallel, the hydrostatic pressure in the lubricating film is constant in the center of the bearing (recess pressure) and starting at the edge of the recess, drops (approximately) linearly to ambient pressure at the edge of the bearing. This means that, although the *forces*, that is the pressures integrated over the bearing surface, on top and bottom of the bearing will be in equilibrium, the *pressures* may differ locally.

Particularly a thin bearing will deform due to this difference and the parallel lubricating film will not be maintained. A parallel lubricating film is to be preferred because of the minimal chance of contact and a minimal flow rate.

Ideally the reaction pressure of the rubber support should be equal to the hydrostatic pressure in a parallel lubricating film. Combined with a perfectly elastic bearing this would ensure a constant parallel film even on a track with substantial surface waviness.

The rubber support is compressed by the load on the bearing. This compression is much larger (≈ 100 times) than the nominal height of the lubricating film. The variation in compression due to the passage of a surface peak is relatively small compared to the initial compression. The reaction pressure of the support therefore remains approximately the same regardless of a small local indentation.

As stated above, the 'ideal' support has a reaction pressure due to compression identical to the hydrostatic pressure in a parallel lubricating film. The geometry of this 'ideal' support is yet unknown. The constant pressure approximation (equations 9.3 and 9.8) can be used here to determine the variable height of this 'ideal' support. In this case the pressure is known and the height is the unknown variable.

The design of this 'ideal' support using this approach is beyond the scope of this thesis. However, the properties of the hydro-support with the 'ideal' support will be calculated and compared with those of the standard support in chapter 17.

9.4 Conclusion

In this chapter the reaction pressure of the rubber support on top of the bearing has been calculated, using both a full 3D approach and a constant pressure approximation (figure 9.23).

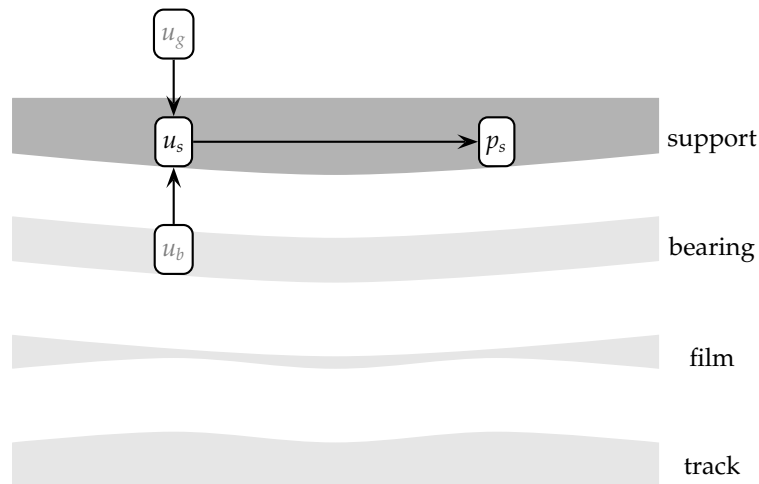


Figure 9.23: Components of the model described in this chapter: The rubber support.

Both methods produce comparable results.

The full 3D method shows high peak stresses at the edges of the support. These peak stresses can be alleviated by hollowing the edge of the support.

It is assumed that it is possible to design an ‘ideal’ support, that is a support with a reaction pressure due to compression that is identical to the hydrostatic pressure in the hydrostatic bearing with equidistant surfaces. It is assumed that the use of this support will ensure that the film height remains approximately parallel even when traversing surface peaks.

The properties of a hydro-support with this ‘ideal’ support and with a massive support with rectangular cross-section will be studied in the continuation of this thesis. In case of the rectangular support the edge will be hollowed out to reduce the peak stresses.

All components of the mathematical model describing the hydro-support, have been presented in the previous chapters. In the next chapter some experimental results are described that can be used to, at least qualitatively, verify the results of the model.

In the previous chapters a model has been presented to describe the properties of the hydro-support. There are some experimental data available to validate this model. The force required to move the lock-gates of the PWA-lock has been measured periodically. Additionally, model tests have been performed to examine the behavior of hydro-fenders.

10.1 Hydro-foot data

The PWA-lock in the 'Oranje' lock complex near Amsterdam has been put into use in March 1995. As from that date the forces required to open and close the lock-gates have been measured periodically (KLOPPENBURG ET AL., 1997, 1998, 1999). The force required to open a lock-gate is composed of a number of different components:

- Inertia forces required to accelerate/decelerate the lock-gate.
- The hydrodynamic friction force of the lock-gate in relation to the water in the lock-chamber.
- The friction force of the transverse guidance.
- The friction forces of the hydro-feet on the track.

The contributions of these components to the total force have been determined using calibration measurements (see e.g. KLOPPENBURG ET AL. (1997)).

We are particularly interested in the last component, the friction forces of the hydro-feet on the track. Combined with the load on the hydro-feet which is equal to the weight

of the lock-gate in water, these friction forces give information about the bearing coefficient and thus the contact load fraction.

Figure 10.1 shows the measured bearing coefficient c_b of the east gate in the PWA-lock at different times and for different sliding speeds and directions (opening and closing). It is clear from these measurements that the bearing coefficient is more or

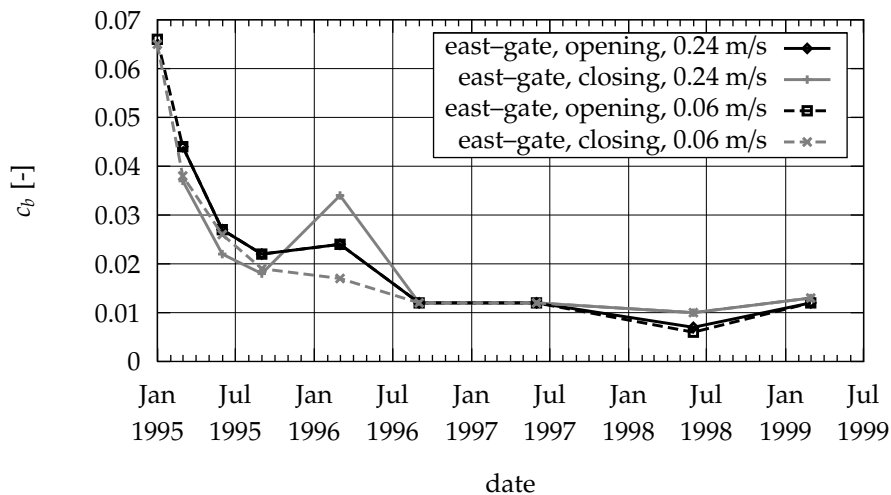


Figure 10.1: The average bearing coefficient c_b of the east-gate of the PWA-lock measured during opening and closing and with two sliding speeds: 0.24 m/s and 0.06 m/s. The irregular results in March '96 were probably caused by the growth of algae on the east gate track.

less independent on the sliding speed and direction but it is dependent on the point in time when the measurement was taken. Initially, the measured bearing coefficient was approximately 0.065, however after a few years of use this bearing coefficient has dropped to approximately 0.007. Assuming a coefficient of friction of 0.1 for the wet steel/UHMWPE combination this means that the contact load fraction has dropped from initially 65% to 7%.

Figure 10.2 shows the measured bearing coefficient of the east gate and west gate of the PWA-lock at a constant speed of 0.24 m/s. Since the lock was put into use, the west gate has shown a markedly lower bearing coefficient. This difference is probably caused by a higher track waviness and a higher friction in the transverse guidance in the east gate. This larger friction is probably caused by the fact that this gate has more room to tilt, causing a larger normal force on the guidance and thus a larger friction force. The values in figures 10.1 and 10.2 are averages obtained during one gate movement. The standard deviation was approximately 0.02 during the first measurements and reduced to about 0.01 in subsequent measurements.

After 3 years of use the bearing coefficient has dropped to 0.003 for the west gate and 0.007 for the east gate. Furthermore the measurements show that particularly in the

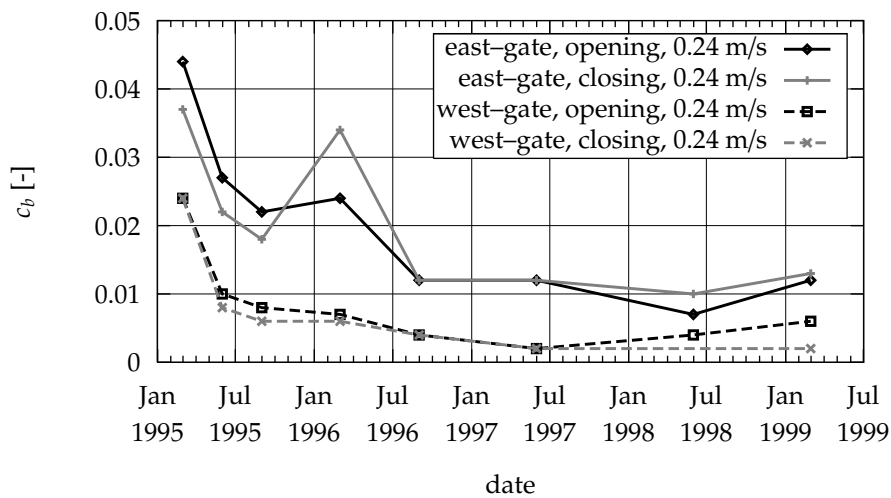


Figure 10.2: The average bearing coefficient c_b of the east-gate and west-gate of the PWA-lock measured during opening and closing with the sliding speed equal to 0.24 m/s.

first year, the bearing coefficient has dropped considerably due to running in. This fact confirms our assumption that initially a large fraction of the load is carried by contact between the bearing and the track.

The results of these measurements have been used to validate (primarily qualitatively) the model presented in the previous chapters.

10.2 Hydro-fender data

In this section the results of a number of experiments on hydro-fenders are summarized. These experiments are extensively described in a number of reports (SCHUT, 1991a; VISSER, 1989a,b). The fenders used in these experiments are all n-recess bearings and have a rectangular bearing shape. The hydro-fenders modelled in this thesis are mostly 1-recess bearings and have a rounded bearing shape. The results of the experiments mentioned above will therefore primarily be used qualitatively.

Experiments have been performed on two types of hydro-fender: hydro-fenders with a 10:1 length/width ratio and hydro-fenders with a 2:1 length/width ratio.

10.2.1 10:1 length/width ratio fender

Hydro-fenders with a 10:1 length/width ratio (length: 1.0 m, width: 0.1 m) and a thin bearing ($0.8 \cdot 10^{-3}$ m and $1.5 \cdot 10^{-3}$ m have been tested (VISSER, 1989a,b). These hydro-fenders have 6 recesses in a 3×2 arrangement (figure 10.3). In a large number of

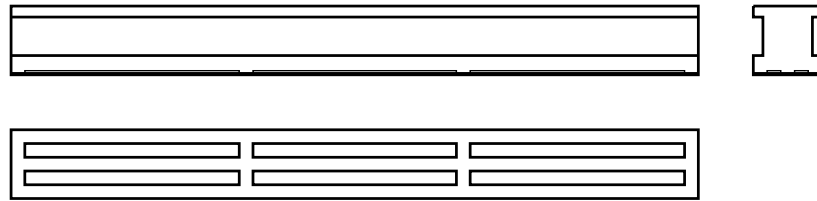


Figure 10.3: Schematic view of the 10:1 fender.

tests these hydro-fenders appear to function well with a bearing coefficient of 0.01 (approximately 10% contact force ratio). However the flow of the water leaving the bearing is more irregular for the thin bearing (figures 10.4 and 10.5) than it is for the thick bearing (figures 10.6 and 10.7).

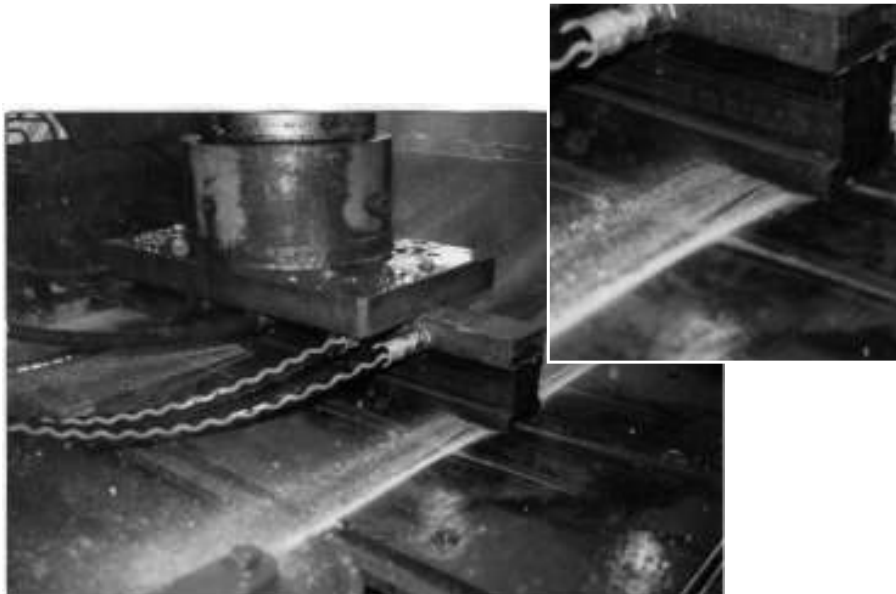


Figure 10.4: 10:1 fender with bearing thickness of 0.8 mm (view I).

The figures show that the flow from the end of the bearing is almost completely blocked. This is caused by the geometry of the rubber support which has a flat edge at the bearing end. A flat edge of the support leads to high peak stresses at the edge. A hollowed edge would reduce these peak stresses (see chapter 9).

Furthermore, after a long experiment these thin bearings appeared to bend outwards in the center of the recess and came loose of the rubber support (figure 10.8). This was caused by the fact that the depth of the recesses was higher than the bearing thickness and continued partly in the rubber support. The pressure on the side of the recess resulted in a force outwards of the recess resulting in the deformation mentioned above.

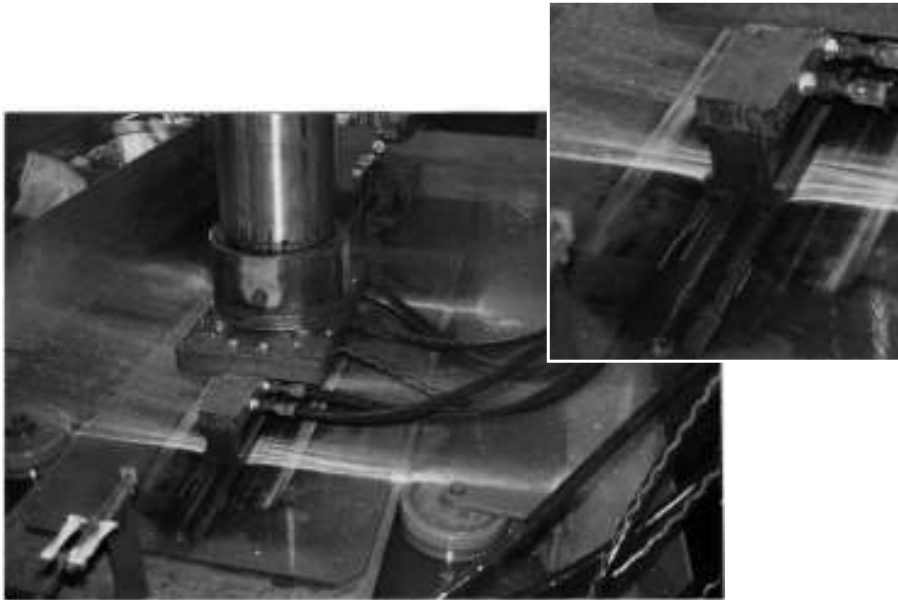


Figure 10.5: 10:1 fender with bearing thickness of 0.8 mm (view II).

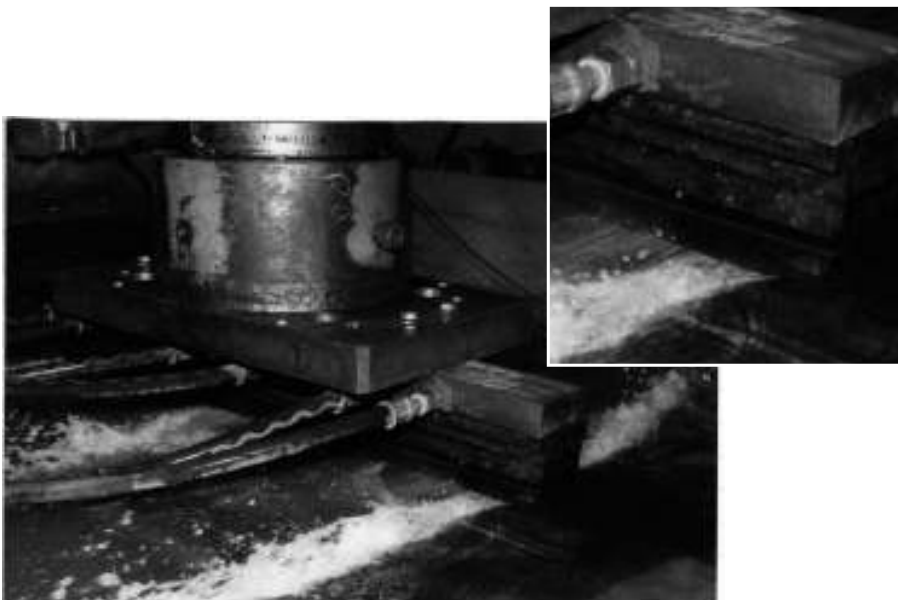


Figure 10.6: 10:1 fender with bearing thickness of 1.5 mm (view I).



Figure 10.7: 10:1 fender with bearing thickness of 1.5 mm (view II).



Figure 10.8: 10:1 fender with bearing thickness of 0.8 mm. The bearing is bend outward and the bonding between the bearing and the support has failed.

10.2.2 2:1 length/width ratio fender

Hydro-fenders with an approximate 2:1 length/width ratio (length: 0.686 m, width: 0.3 m) and different bearing thicknesses ($5 \cdot 10^{-3}$ m, $22 \cdot 10^{-3}$ m, $30 \cdot 10^{-3}$ m, and $60 \cdot 10^{-3}$ m) have been tested (SCHUT, 1991a). These hydro-fenders have 4 recesses in a 2×2 arrangement (figure 10.9).

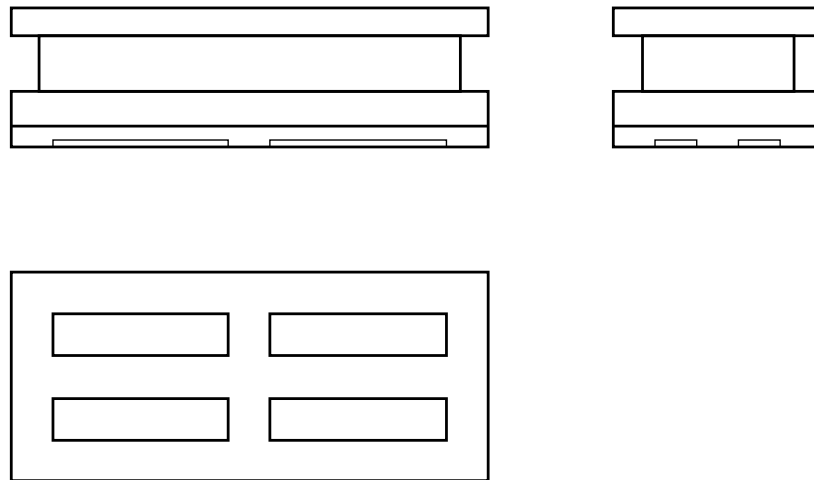


Figure 10.9: Schematic view of the 2:1 fender.

The bearing coefficient of these bearings increases with a decreased bearing thickness (table 10.1). For the thin bearing, the flow of the water out of the bearing is again very

bearing thickness	average bearing coefficient
5 mm	0.020
22 mm	0.007
30 mm	0.006
60 mm	0.006

Table 10.1: Average bearing coefficient for different bearing thicknesses.

irregular (figures 10.10 and 10.11). There is substantial flow at the ends of the bearing but hardly any flow in the center of the bearing.

Hydro-fenders with a thinner bearing are better capable to cross surface waviness. In table 10.2 the average bearing coefficient is shown while crossing surface waviness of different heights.

Again the results of these experiments are primarily used qualitatively in order to evaluate the results of the model. Especially the distribution of the film height and the flow under the bearing and the bearing coefficient of the hydro-support are studied.

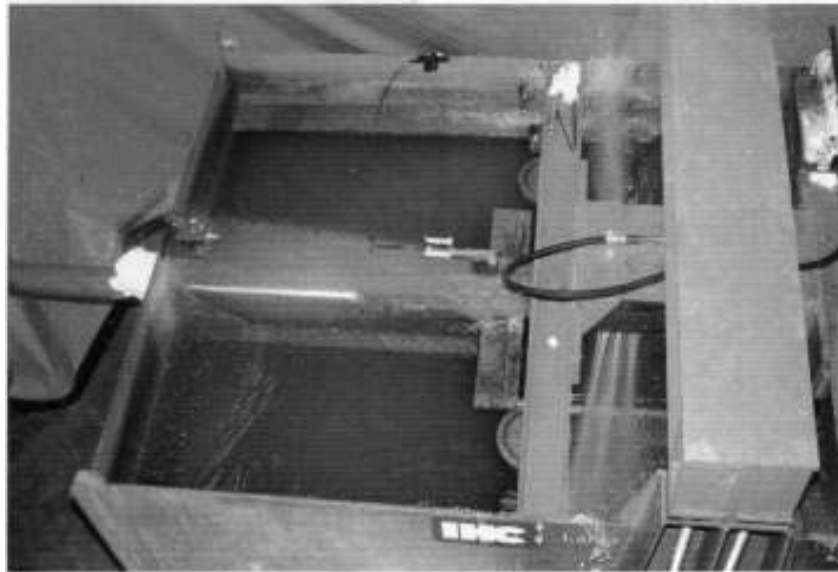


Figure 10.10: 2:1 fender with bearing thickness 5 mm (view I).



Figure 10.11: 2:1 fender with bearing thickness 5 mm (view II).

bearing thickness	surface waviness		
	0 mm	1 mm	2 mm
5 mm	0.020		
22 mm	0.007	0.024	0.047
30 mm	0.006	0.035	
60 mm	0.006	0.053	0.112

Table 10.2: Bearing coefficient for different bearing thicknesses and surface waviness.

CHAPTER 11

Introduction to the numerical study

In the previous chapters a mathematical model has been developed for the analysis of a hydro-support on an elastic track. In this and subsequent chapters this model is further examined with emphasis on the numerical study of this model.

In summary, the mathematical model describes the following physical aspects:

- The nominal film height or gap h between the track and bearing as a result of the initial bearing and track positions and the bearing and track deformations (equation 6.7). This is the distance between the mean planes of the *undeformed roughness* of both the bearing and the track. It does take into account the initial bearing and track positions and their global elastic deformations, but it does not take the surface roughness deformation due to contact into account.
- The true or effective film height h_t (equation 6.11). This is the distance between the mean planes of the *deformed roughness* of both the bearing and the track. This true film height is required for the calculation of the hydrostatic pressure p_h .
- The hydrostatic pressure p_h in the lubricating film with this effective film height between the track and the bearing. In order to determine this hydrostatic pressure the Reynolds' equation 7.9 has to be solved (*PDE No.1*).
- The reduced contact pressure \bar{p}_c and size of the contact areas \bar{a}_c between the bearing and the track (equations 6.28 and 6.27 respectively).
- The combined film pressure p as a result of the hydrostatic and contact pressures (equation 6.6) and the resulting load W (equation 3.1).
- The elastic deformation of the rubber support u_s and in particular the reaction pressure of the rubber support p_s on the bearing (equation 9.8) as a result of this load W (*PDE No.2*). The constant pressure approximation is used for the

calculation of the reaction pressure. The total compression u_s is a result of the (relatively large) uniform displacement u_g of the top plane of the support, and the (relatively small) displacement u_b of the bottom plane of the support.

- The elastic deformation of the bearing u_b . A plate deformation is assumed and the pressures on top and bottom of the bearing (p_s and p respectively) can therefore be combined to give one effective bearing pressure p_b (PDE No.3).
- The elastic deformation of the track u_t as a result of the track pressure p_t (equation 5.3). This track pressure p_t is equal to the combined film pressure p .

A schematic view of the relations between these different physical aspects is given in figure 11.1. This model consists of 3 coupled 2D partial differential equations and some algebraic equations.

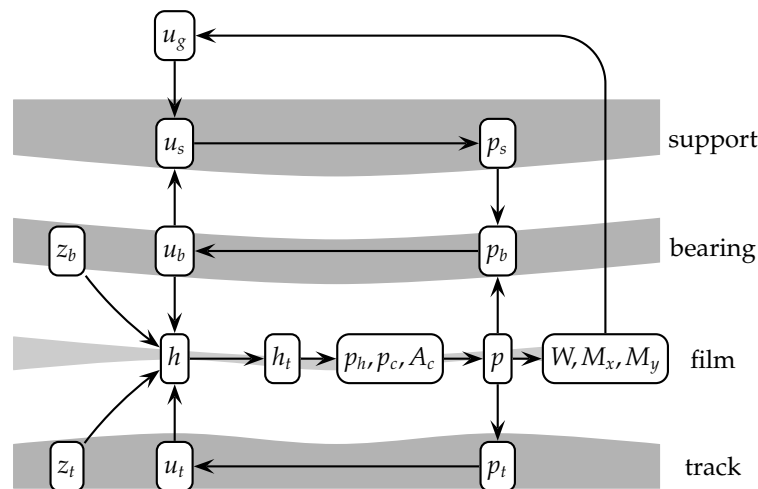


Figure 11.1: The relations between the different components in the model.

The parameters and variables in these equations have been scaled in order to improve numerical stability and accuracy. All dimensions have been scaled using the bearing width B , except for the variables directly related to the film height and various displacements, which have been scaled using a nominal film height h_0 . The pressures and elasticity moduli have been scaled using the supply pressure p_{sup} .

The resulting system of equations has been solved using an iterative numerical approach using the finite element method (BATHE, 1996; SEGAL, 1993b; ZIENKIEWICZ AND TAYLOR, 2000a,b,c). The combination of equations describing the model can not easily be solved using most commercially available finite element software packages. SEPRAN (SEGAL, 1993b) is a flexible and powerful finite element software package that can be used in two ways: (1) As a stand alone application where the user describes his problem using a combination of scripts written in a proprietary script language combined

with user defined functions written in Fortran or (2) as a Fortran subroutine library which the user can call from his program. In order to solve the model the first approach has been used.

The iterative numerical procedure developed in order to solve this system of equations is the subject of the next chapter. The methods used to obtain and improve convergence and the termination criteria will be studied.

CHAPTER 12

Iterative numerical procedure

The elastic deformation of the bearing and the track are directly coupled to the hydrostatic and the contact pressures in the lubricating film and vice versa: On one hand, the hydrostatic and the contact pressures are the cause of the elastic deformation, and on the other, the deformation of the surfaces determines the film height of the lubricating film (and therefore the hydrostatic pressure) and the contact areas and pressure between bearing and track. More over, this coupling is highly non-linear due to the fact that the film height enters the Reynolds' equation to the third power.

Because of this strong non-linear coupling it is impossible to solve the system of equations directly. An iterative procedure is required that hopefully converges to the correct result after a (small) number of iterations. There are two basic methods to solve this kind of system of coupled equations, the so-called fully coupled approach and the weakly coupled approach (see for instance DE HART (2002); ZIENKIEWICZ AND TAYLOR (2000a)).

In the fully coupled approach, at each time step or iteration a new approximation is found for all variables simultaneously. The application of this approach to the solution of the Reynolds' equation in combination with elastic surfaces, requires the Reynolds' equation to be linearized with respect to the film height. The Newton-Raphson method is often used to perform this linearization (see for example VAN HEIJNINGEN AND KASSELS (1986); LUBRECHT (1987)). In combination with the use of SEPRAN this method has been used in VAN HEIJNINGEN AND KASSELS (1986); SEGAL (1993a). The fully coupled approach has been proven to converge quickly, provided that the previous approximation to the solution is sufficiently close to the final solution. However, at each iteration the size of the system of linear equations that has to be solved is much larger than that for the weakly coupled approach. Furthermore, in SEPRAN the finite elements required for the fully coupled approach are not yet implemented, and the development of these elements is beyond the scope of this thesis.

Therefore, the weakly coupled approach (sometimes called a staggered solution process (ZIENKIEWICZ AND TAYLOR (2000a), chapter 19.5)) has been used to solve the system of equations developed in the previous chapters. In the weakly coupled approach the model is split into parts that can be solved separately. Then, at each time step or iteration, a new approximation is found for all variables successively, where the most recent solution of each variable is used to calculate the other variables. Besides the smaller systems of linear equations that have to be solved, this approach allows for the use of independently developed and tested methods and finite elements for each part of the coupled problem. The different parts that can be recognized in our model are:

- The calculation of the support reaction pressure.
- The calculation of the hydrostatic pressure in the lubricating film.
- The calculation of the deformation of the bearing and the track, combined with the calculation of the contact area and pressure.

The calculation of the hydrostatic pressure is straightforward. The calculation of the support pressure and the calculation of the displacements and the contact pressure will be further explained in separate sections.

12.1 Support pressure calculation

The support reaction pressure p_s is a result of the compression of the support u_s . This compression consists of the uniform displacement u_g at the top surface and the deformation of the bearing u_b at the bottom surface. The compression of the support u_s is predominantly determined by u_g . After all, the bearing displacement u_b is in the order of the track surface waviness height, and the top plane is free to descent until the full load is carried. This results in a displacement u_g that is typically more than 25 times that of u_b . In order to simplify the iterative numerical procedure, it is now assumed that the support displacement u_s is *exclusively* determined by the uniform top plane displacement u_g .

Because u_g is uniform, that is constant for the whole top plane of the support, the support pressure p_s is now only dependent on a scalar value u_g . Coupled with the fact that the support deformation is linear, the support pressure can be precalculated for a unit load and then scaled for the actual load W :

1: $u_s := 1$	{assume unit support compression}
2: $p_{s,1} := \mathcal{L}_s(u_s)$	{calculate support pressure}
3: $W_s := \int_A p_s dA$	{support load}
4: $p_{s,1} := p_{s,1}/W_s$	{support pressure for unit load}

Given a load W on the bearing, the support reaction pressure distribution can now easily be calculated using:

$$1: p_s := p_{s,1} * W \quad \{\text{support pressure for load } W\}$$

Remember that this calculation does not take the local variations of the compression due to the bearing deformation into account. Using this precalculation of the support stiffness, the system of relations that was presented in figure 11.1, has been reduced to that in figure 12.1.

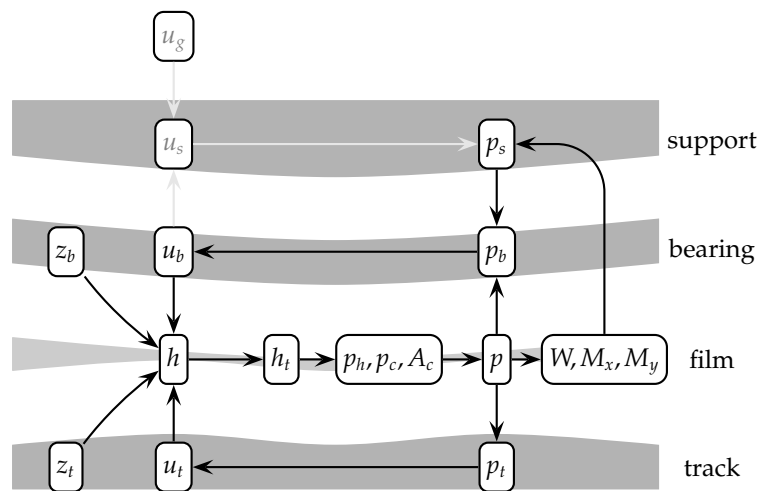


Figure 12.1: The relations between the different components in the model after the precalculation of the support stiffness.

12.2 Displacements and contact pressure calculation

The contact condition between the bearing and the track can be described using the complementarity condition:

$$\begin{cases} \text{contact} & h = t_c & \text{and} & p > p_h \\ \text{no contact} & h > t_c & \text{and} & p = p_h \end{cases} \quad (12.1)$$

where t_c is the contact distance. The contact distance is defined as the distance between the mean planes of the surfaces (excluding surface roughness) in contact conditions. This contact distance is dependent on the contact pressure p_c . If p_c is almost zero, the surfaces are barely in contact and t_c is equal to $3S_q$, with S_q the combined surface roughness. For p_c larger than zero, the surfaces are pressed together and the surface

roughness deforms. t_c becomes smaller than $3S_q$. The relation between t_c and p_c is given by equation 6.28.

Many contact algorithms have been devised for use in numerical procedures (see e.g. ZHONG (1993)). All of these algorithms assume a constant contact distance (usually 0), whereas the contact condition describe above has a variable contact distance t_c .

A new algorithm, combining the contact condition and displacement calculations, has been developed. The bearing and track displacements, u_b and u_t , are given by:

$$\mathcal{L}_b u_b = p - p_s \quad (12.2a)$$

$$-E_t^* u_t = p \quad (12.2b)$$

where p is the total pressure between bearing and track:

$$p = p_h + p_c \quad (12.3)$$

These equations are valid both in the full film and contact areas. However, in the contact areas, the contact pressure p_c is unknown.

In the contact areas the film height h is equal to the contact distance t_c :

$$h = (z_b + u_b) - (z_t + u_t) = t_c \quad (12.4)$$

or:

$$u_t = (z_b + u_b) - (z_t + t_c) \quad (12.5)$$

Substituting this equation into the second of the displacement equations 12.2b yields the following relation between the total pressure p and the bearing displacement u_b :

$$-E_t^* ((z_b + u_b) - (z_t + t_c)) = p \quad (12.6)$$

Substituting this into the first of the displacement equations 12.2a and collecting terms of u_b , yields a relation for u_b valid in the contact areas:

$$(\mathcal{L}_b + E_t^*) u_b = -E_t^* (z_b - (z_t + t_c)) - p_s \quad (12.7a)$$

In the full film areas u_b is described by:

$$\mathcal{L}_b u_b = p_h - p_s \quad (12.7b)$$

These relations have been used in a combined displacement and contact algorithm (algorithm 1). In this algorithm a contact vector C is introduced, which contains 0 in the full film points, and 1 in the contact points. Equations 12.7a and 12.7b can now be combined to:

$$(\mathcal{L}_b + CE_t^*) u_b = (1 - C)p_h - CE_t^* (z_b - (z_t + t_c)) - p_s \quad (12.8)$$

1: $C := 0$	{initialize contact vector}
2: repeat	
3: $W := \int_A p dA$	{load}
4: $p_s := p_{s,1} W$	{support pressure}
5: $t_c := f(p_c)$	{contact distance}
6: $u_b :=$ (equation 12.8)	{solve u_b }
7: $u_t :=$ (equation 12.9)	{solve u_t }
8: $h := (z_b + u_b) - (z_t + u_t)$	{nominal film height}
9: $p_c := -p_h - E_t^* u_t$	{contact pressure}
10: $C := \begin{cases} 0 & \text{if } h > 3S_q \\ 1 & \text{if } h < 3S_q \end{cases}$	
11: until $\epsilon_c < \epsilon_{c,\max}$	

Algorithm 1: Combined displacement and contact algorithm

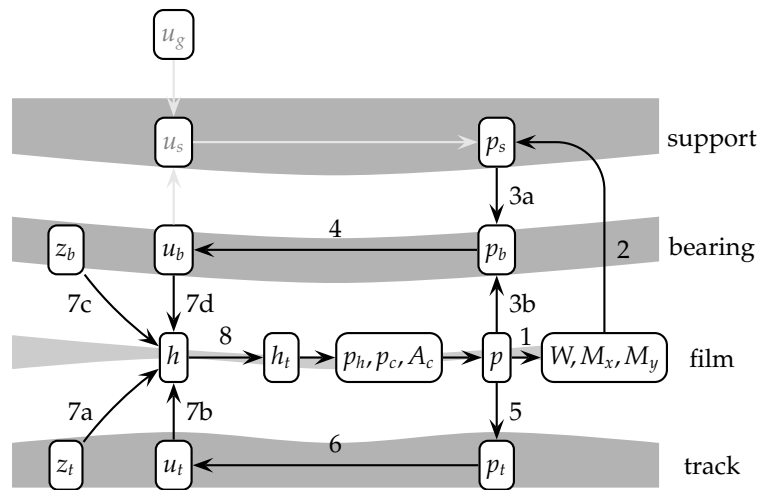


Figure 12.2: Schematic presentation of algorithm 1. The iteration is started with a previous estimate of the pressure p , then the numbered arrows are followed until we are back at the starting point. Note, that in this loop, the *hydrostatic* pressure is kept constant.

Similarly, the track displacement equation becomes:

$$-E_t^* u_t = (1 - C)p_h - CE_t^* ((z_b + u_b) - (z_b + t_c)) \quad (12.9)$$

In figure 12.2 the steps of the algorithm have been presented. Starting with a previous estimate of the pressure p , the steps in the figure are followed until some convergence criterium has been achieved. The following criterium has been used in this thesis:

1: $\epsilon_c := p - p_{old} / p $	{difference in consecutive pressures}
--------------------------------------	---------------------------------------

Besides the convergence of the pressure, the number of contact points is monitored. In some cases, the pressure will not converge and the number of contact points will exhibit some periodic behavior. Then, the calculation is continued as if the calculation had converged.

12.3 Coupled solution

In the previous sections the procedures to calculate the support pressure and the displacements have been presented. The final basic part in the model is the calculation of the hydrostatic pressure. This calculation is fairly straightforward:

1: $h_t := f(h)$	{effective film height}
2: $p_h := \mathcal{L}_h(h_t)$	{hydrostatic pressure}

A basic algorithm to solve the model using a weakly coupled approach is presented in algorithm 2 where the steps in bold have been discussed previously.

- 1: **Precalculate support reaction pressure**
- 2: **repeat**
- 3: **Calculate hydrostatic pressure**
- 4: **Calculate contact and displacements**
- 5: **until** $\epsilon < \epsilon_{max}$

Algorithm 2: Basic algorithm

The iteration is continued until some convergence criterium has been achieved. The following criterium has been used in this thesis:

1: $\epsilon_P := p - p_{old} / p $	{difference in consecutive pressures}
2: $\epsilon_H := h - h_{old} / h $	{difference in consecutive film heights}
3: $\epsilon := \max(\epsilon_H, \epsilon_P)$	{convergence criterium}

Both the pressure and film height are checked in order to ensure convergence of both variables.

It is possible that the basic, Picard-type algorithm 2 does not or only slowly converge. In order to explain the convergence of this basic loop, first the characteristics of the basic calculations inside the central loop must be examined. We distinguish two basic calculations:

$H(P)$: The calculation of the displacements given a pressure distribution.

$P(H)$: The calculation of the pressure given the displacements.

In figure 12.3 the solutions for both basic calculations are schematically presented. The solutions have been reduced to two scalar quantities H and P representing some scalar norm of the film height (and thus displacements) and pressure respectively.

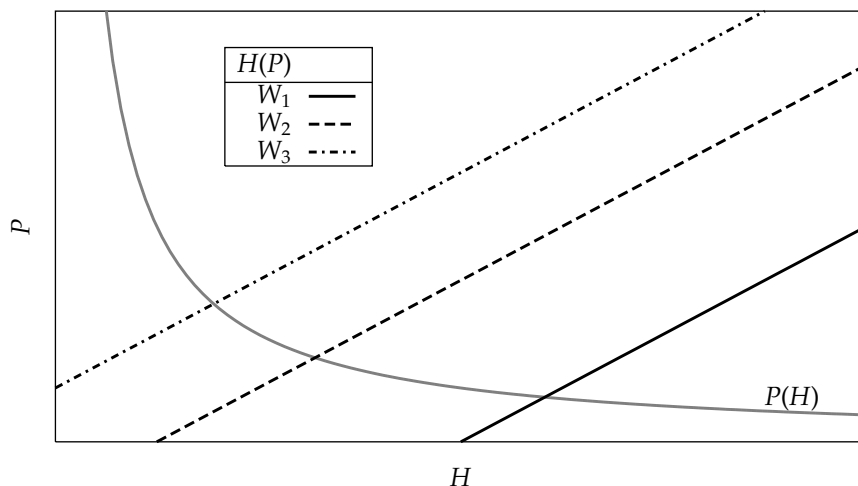


Figure 12.3: Schematic relation between film height and pressure. The line $P(H)$ represents the combined hydrostatic and contact pressure calculated for a given film height. The other lines represent the film height calculated for a given pressure for 3 increasing loads W_1 , W_2 and W_3 respectively.

The calculation $H(P)$ is linear dependent on the pressure. However the other calculation $P(H)$ is strongly non-linear on the film height. For large H (small load) there is no contact and the pressure is equal to the hydrostatic pressure which is relatively independent on the film height. For smaller H (large load) contact will occur and here the pressure will rise much more rapidly. For small loads convergence is easily achieved using the simple Picard-type algorithm, for high loads however convergence is slow or not obtained.

The calculation of the contact pressure is based on the theory developed in chapter 6. Although this theory is based on the assumption that both elastic and plastic deformation occur, the numerical implementation assumes that all deformations are reversible.

The roughness distribution is assumed to remain constant for subsequent iterations and load steps.

Convergence can again be achieved with the use of under-relaxation. Here the calculation is not continued with the new pressure and deformation but with an weighted average of the new and previous pressure and deformation (see algorithm 3). The

- 1: **Precalculate support reaction pressure**
- 2: **repeat**
- 3: **Calculate hydrostatic pressure**
- 4: $p_h := p_{\text{old}} + \omega_p(p_h - p_{\text{old}})$
- 5: **Calculate contact and displacements**
- 6: $h := h_{\text{old}} + \omega_h(h - h_{\text{old}})$
- 7: **until** $\epsilon < \epsilon_{\text{max}}$

Algorithm 3: Adapted algorithm

relaxation factors ω_p and ω_h are adapted during the calculation in order to ensure convergence at any point of the calculation. The heuristics used to adapt these relaxation factors take a large number of parameters into account, including the last 3 values of $|p|$, $|h|$, $|p - p_{\text{old}}|$ and $|h - h_{\text{old}}|$. In case of a (very) thin bearing these relaxation factors can become very small ($\approx 10^{-2}$).

12.4 Height step procedure

In order to improve the numerical stability of the calculations, an iterative procedure is chosen where the central film height h_c is reduced stepwise, starting with a very large initial value and ending with a small value. In this way, the calculation starts with a numerical stable situation, namely a situation where no contact occurs and the deformations of the bearing and track are small compared to the film height. At each height step, the pressures and displacements and the total load and contact load on the bearing are calculated. For the initial values of the variables, the solution at the previous height step is chosen. The calculation is finished when the contact load exceeds a predetermined fraction of the total load. For the calculations presented in this thesis, usually a value of 0.5 was chosen for this fraction. (See algorithm 4.)

It is assumed that due to the relatively small principal wavelengths of the surface waviness the resulting tilting moments are negligible and that therefore the tilt angles α_x and α_y remain zero. If this assumption is dropped then at every height step the tilting angles have to be adjusted to maintain load balance.

The height step size Δh is determined by the previous solution: Initially large steps are taken, then smaller steps when contact occurs or is expected to occur. Heuristics to determine this height step size have been developed experimentally, in order to ensure numerical stability for a large variation of parameters. These heuristics are based on

the current height step h_c , the minimal film height of the nodes not yet in contact h_{\min} , and the surface roughness S_q .

1: $h_c := 1000, \Delta h_c := 100$	{initial central film height, step size}
2: loop	
3: MAIN LOOP (algorithm 3)	
4: $W := \int_A p dA$	{load, contact load}
5: $W_c := \int_A p_c dA$	
6: if $W_c > 0.5W$ then	
7: FINISHED !	
8: end if	
9: $\Delta h_c := f(h_c, h_{\min}, S_q)$	{new height step}
10: $h_c := h_c - \Delta h_c$	
11: end loop	

Algorithm 4: Height step loop

As a result of the pressure and displacement under-relaxation, and the height step loop, the convergence of the program is substantially improved. However, particularly for thin bearings, in the transition between no-contact and contact, convergence is sometimes difficult to obtain. In these cases, the calculation at that problematic film height is halted after a preset number of iterations, and the calculation continues at the next film height. Some of the figures in the chapters 14 and 17 show this problem.

In subsequent chapters the program introduced in this chapter will be used to study the influence of a number of design parameters.

CHAPTER 13

Introduction to the parameter study

In the following chapters the influence of several parameters on the properties and behavior of the hydro-support is studied. Primarily the influence of these parameters on the bearing coefficient has been studied. However, also the influence on the tilting stiffness and flow rate are of interest. The following parameters have been studied:

- Number of recesses.
- Recess width.
- Bearing length/width ratio.
- Bearing thickness.
- Track thickness.
- Track surface waviness.
- Recess pressure.
- Support geometry: massive or 'ideal'.

As stated above, we are primarily interested in the influence of these parameters on the bearing coefficient. The bearing coefficient of a mixed lubricated bearing (partial hydrostatic lubrication, partial contact) is:

$$c_b = \frac{F}{W} = \frac{F_h + F_c}{W_h + W_c} \quad (13.1)$$

where F denotes the total friction force that is equal to the sum of the friction forces as a result of the hydrostatic lubrication F_h and the contact F_c . The total load W is equal

Length	L/B	2.0
Recess width	b/B	0.1
Speed	$\eta UB/h_0^2 p_r$	0.0
Nominal film height	h_0/B	$0.2 \cdot 10^{-3}$
Recess depth	h_r/h_0	50.0
Bearing modulus of elasticity	$E_b h_0 / p_r B$	42.0
Bearing height	t_b/h_0	0.2
Support modulus of elasticity	$E_s h_0 B^2 / p_r t_s^3$	0.025
Support height	t_s/B	0.2
Track modulus of elasticity	$E_t h_0 (1 - \nu_t) / p_r t_t (1 - 2\nu_t)(1 + \nu_t)$	10.0
Track surface roughness	S_q/h_0	0.1
Track surface waviness	h_{wav}/h_0	10.0

Table 13.1: Dimensionless parameters for the reference fender geometry.

to the sum of the hydrostatic load W_h and the contact load W_c . The hydrostatic friction component F_h is in general much less than the contact friction component F_c . In order to reduce the bearing coefficient this last component should be as low as possible.

13.1 Reference fender geometry

The design of the hydro-support depends on a large number of parameters. The amount of work required to study the influence of these parameters using a full factorial study is very time consuming. Therefore a reference hydro-support geometry has been chosen that will be used to study the effect of the change of one parameter at a time. The geometry and material properties for this reference hydro-support have been collected in table 13.1. The parameters in table 13.1 are dimensionless. In table 13.2 the dimensions and material properties of a hydro-support with these dimensionless properties and a nominal load approximately equal to that of the PWA-lock have been gathered.

In figure 13.1 the contact load fraction W_c/W of the reference hydro-support is presented both for the plane track and for the track with surface waviness as a function of the total load. These results are presented relative to those of a hydro-support with the same geometry and recess pressure but with rigid and plane bearing surfaces (see chapter 4). In figure 13.1 the bearing coefficient has been presented on the second vertical axis, assuming a constant coefficient of friction of the track/bearing material combination of 0.1 and assuming that the hydrostatic friction can be neglected.

The track with surface waviness is assumed to have a waviness amplitude equal to 10 times the nominal film height. The track surface is shown in figure 13.2.

On a track with no surface waviness, the load can be increased by a factor of 1.4 relative to that of the hydro-support with rigid surfaces, without the occurrence of contact.

Length	L	1.0 m
Width	B	0.5 m
Recess width	b	0.05 m
Recess height	h_r	5.0 mm
Recess pressure	p_r	$10.0 \cdot 10^5 \text{ N/m}^2$
Velocity	U	0.0 m/s
Viscosity	η	0.001 Ns/m^2
Nominal film height	h_0	0.1 mm
Bearing modulus of elasticity	E_b	$2.1 \cdot 10^{11} \text{ N/m}^2$
Bearing Poisson ratio	ν_b	0.3
Bearing height	t_b	0.1 m
Support modulus of elasticity	E_s	$1.0 \cdot 10^6 \text{ N/m}^2$
Support Poisson ratio	ν_s	0.5
Support height	t_s	0.1 m
Track modulus of elasticity	E_t	$1.0 \cdot 10^9 \text{ N/m}^2$
Track Poisson ratio	ν_t	0.46
Track height	t_t	0.05 m
Track surface roughness	S_q	0.01 mm
Track surface waviness	h_{wav}	1.0 mm/m
Nominal load	W_0	180.0 kN
Nominal flow rate (smooth track)	Q_0	$2.15 \text{ m}^3/\text{h}$

Table 13.2: Example of a fender with the reference geometry.

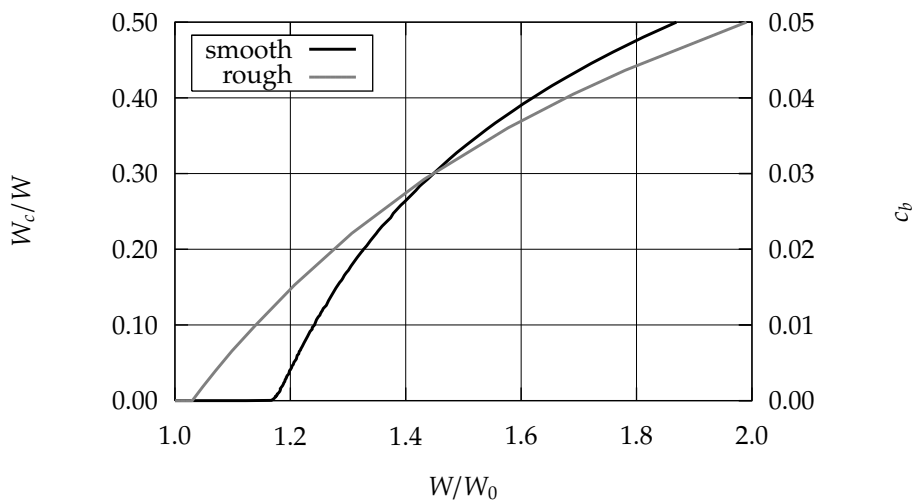


Figure 13.1: Contact load fraction W_c/W and bearing coefficient c_b as a function of the relative load W/W_0 for the reference bearing on both a smooth and a non-smooth track. The load is calculated relative to the load of a fender with the same geometry and rigid surfaces.

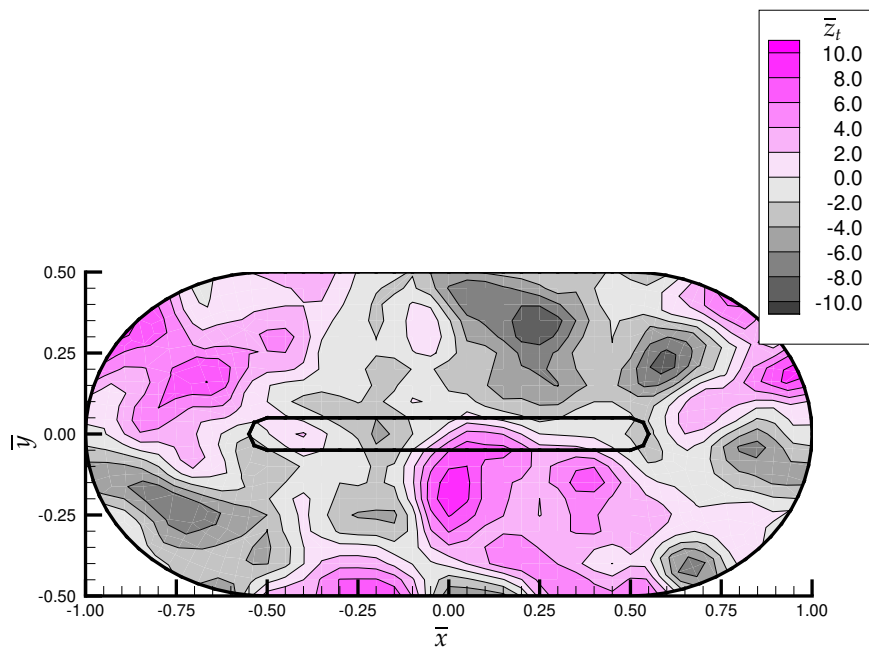


Figure 13.2: Surface of the track for the reference bearing with random surface waviness.

This means that the load carrying capability of the fender is increased by 40% due to the elastic deformation of the surfaces. On the track with surface waviness however, this increase is limited to approximately 5%. Then the fender makes contact with the track before the elastic deformation of the surfaces can increase the hydrostatic load.

In figure 13.3 the contact pressure on a smooth track, is presented for a very low contact load ratio, in figure 13.4 for a higher contact load ratio. In these, and subsequent figures, the (contact) pressure is scaled with the recess pressure ($\bar{p} = p/p_r$). These figures seem to indicate that our choice of the fender geometry (with circular end pieces) ensures an initial contact uniformly distributed on the bearing perimeter.

As a comparison figure 13.5 shows the total pressure (hydrostatic and contact) on a non-smooth track. It is clear that here the contact is not initiated at the bearing edge but anywhere surface peaks occur.

Figure 13.6 shows the load on the reference bearing versus the effective film height h_{eff}/h_0 . The effective film height is defined as that film height a fender with identical geometry and recess pressure but with rigid, plane surfaces must have, in order to exhibit the same flow rate. Figure 13.6 also shows the relation between the load and the flow rate which is presented on the top horizontal axis.

On a smooth track the load increases gradually with decreased flow rate (or film height), whereas on a track with surface waviness the load increases sharply when the flow rate drops below a certain level (figure 13.6). On a smooth track, contact occurs for film thicknesses smaller than $3S_q$. At this film height, the roughness peaks of the surfaces come into contact (see also chapter 5, figure 5.10 and equation 5.16).

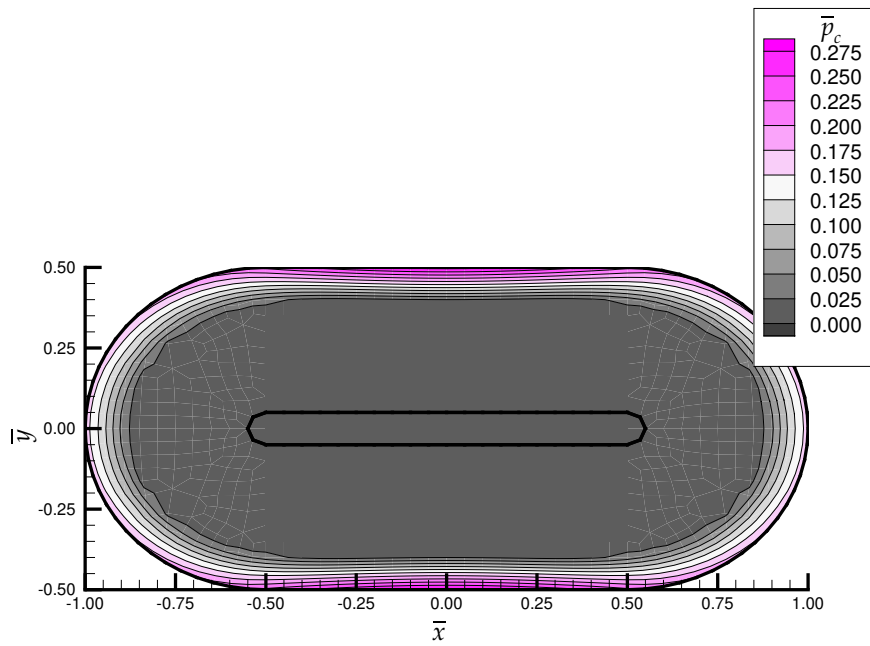


Figure 13.3: Contact pressure distribution on initial contact between bearing and a track with no surface waviness.

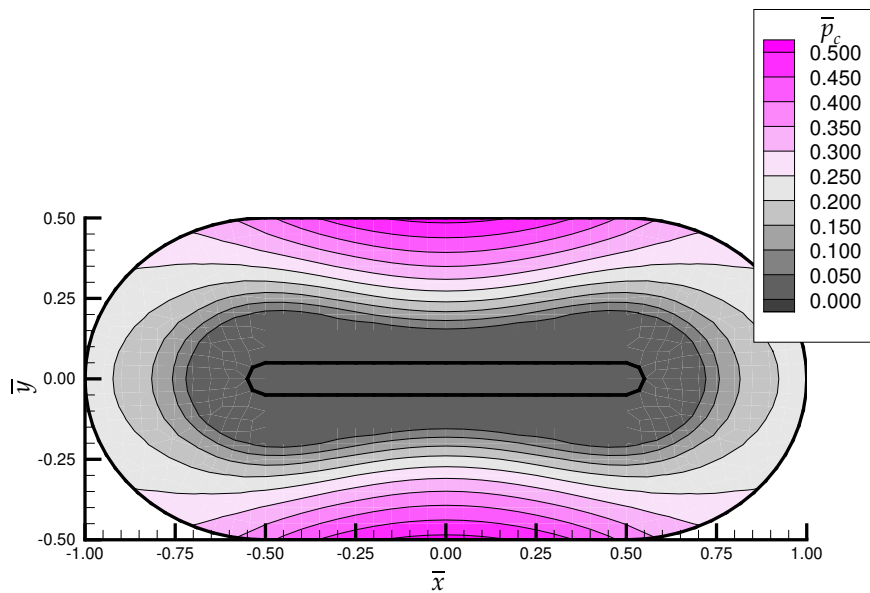


Figure 13.4: Contact pressure at a slightly increased load on a track with no surface waviness.

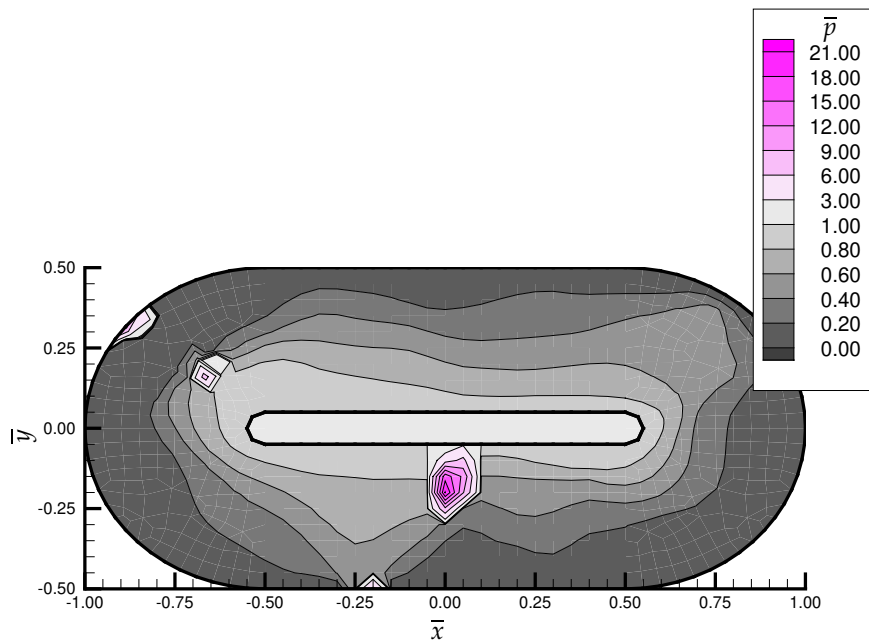


Figure 13.5: Total pressure of the reference bearing on the non-smooth track.

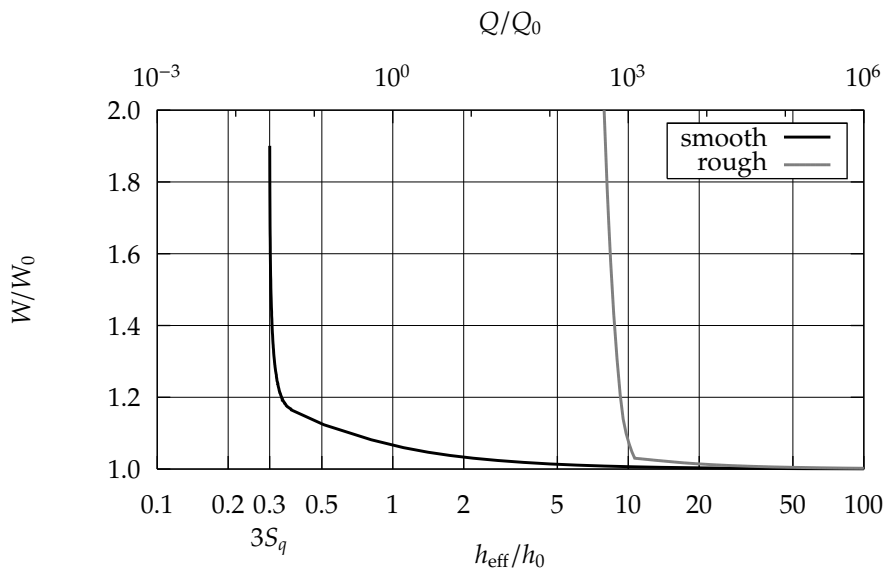


Figure 13.6: Load W/W_0 versus the effective film height h_{eff}/h_0 of the reference bearing for both a smooth and non-smooth track. The effective film height and load are presented relative to those of a fender with the same geometry and rigid surfaces.

Figure 13.7 shows the contact load fraction and bearing coefficient versus the effective film height. On a smooth track the bearing coefficient increases sharply the moment the relative film height is reduced to approximately 0.5, whereas on the non-smooth track this increase occurs at a film height of approximately 10.0.

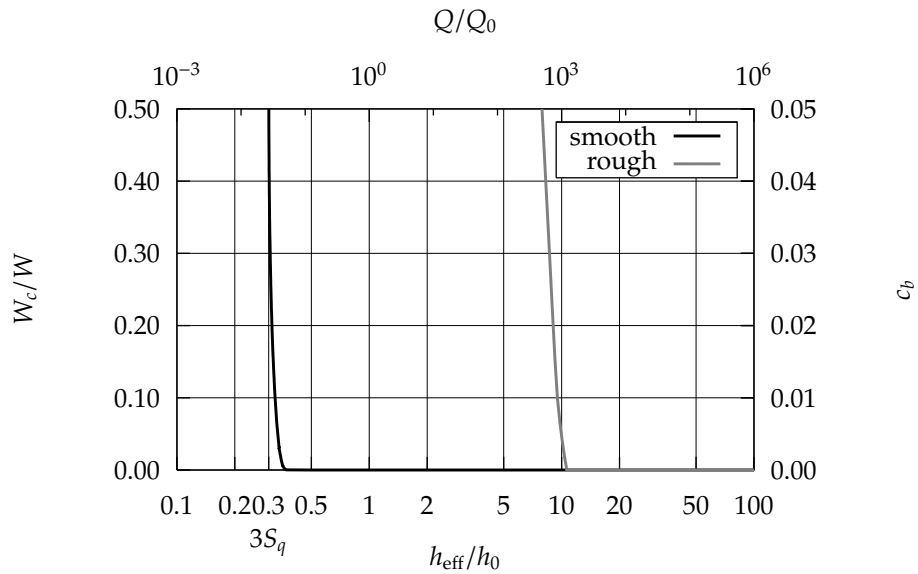


Figure 13.7: Contact load fraction W_c/W and bearing coefficient c_b versus the effective film height h_{eff}/h_0 of the reference bearing for both a smooth and non-smooth track. The effective film height and load are calculated relative to those of a fender with the same geometry and rigid surfaces.

CHAPTER 14

Bearing geometry

In this chapter the influence of several parameters related to the bearing geometry is studied. These parameters are the bearing length/width ratio and the bearing thickness. These parameters are varied while maintaining a constant recess pressure. Furthermore the bearing length/width ratio is varied while maintaining the same load by adjusting the recess pressure.

14.1 Bearing length/width ratio

As was demonstrated in chapter 4, a number of properties of the rigid hydro-fender improve for increased bearing length/width ratio. Namely at equal load both the volume flow rate and the required pumping power decrease. In this chapter the influence of the bearing length/width ratio is studied for elastic surfaces.

The influence of the elastic deformation of the bearing surfaces is most clear for hydro-feet or hydro-fenders with a small bearing length/width ratio (figures 14.1, 14.2 and 14.3).

On a non-smooth track the hydro-foot or hydro-fender with a small bearing length/width ratio is more sensitive to the exact surface geometry of the track (figures 14.4, 14.5 and 14.6).

14.2 Bearing thickness

In this section the influence of the bearing elasticity is studied.

It is assumed that the bearing support is a solid rubber disc with parabolic hollowed edges to reduce the peak stresses at these edges of the support. The reaction pressure

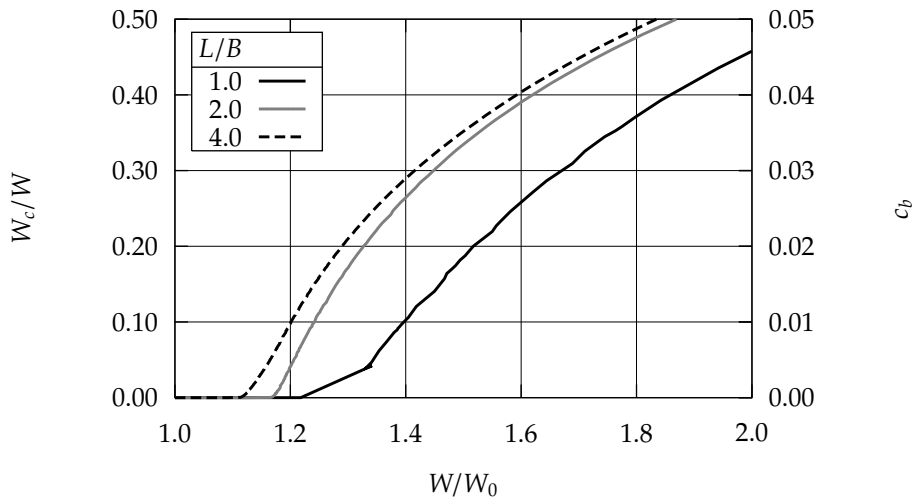


Figure 14.1: Contact load fraction W_c/W and bearing coefficient c_b versus the load W/W_0 for several bearing length/width ratios (L/B) on a smooth track.

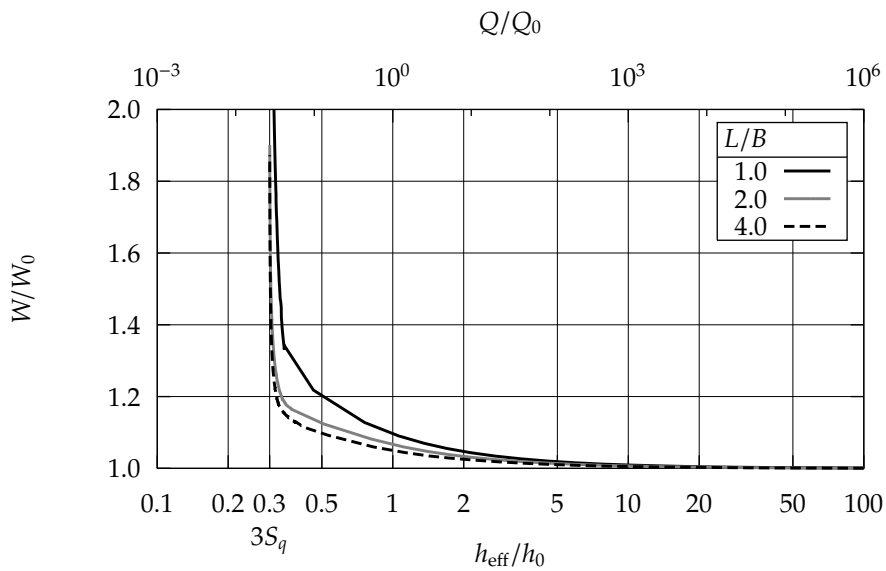


Figure 14.2: Load W/W_0 versus the effective height h_{eff}/h_0 for several bearing length/width ratios (L/B) on a smooth track.

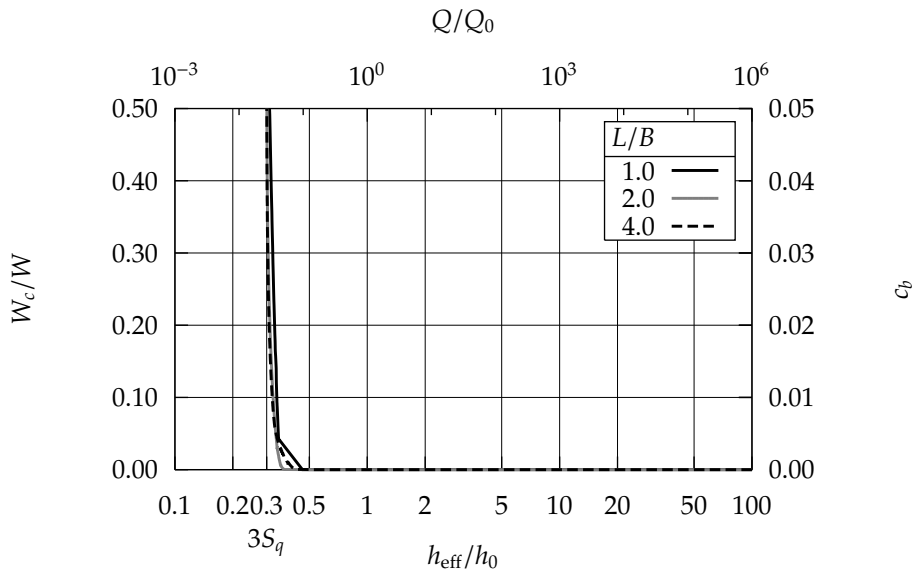


Figure 14.3: Contact load fraction W_c/W and bearing coefficient c_b versus the effective height h_{eff}/h_0 for several bearing length/width ratios (L/B) on a smooth track.

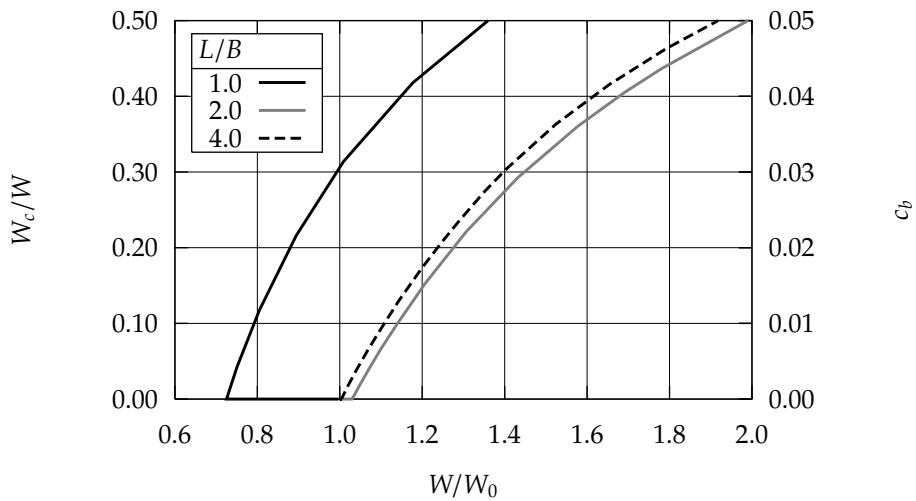


Figure 14.4: Contact load fraction W_c/W and bearing coefficient c_b versus the load W/W_0 for several bearing length/width ratios (L/B) on a non-smooth track.

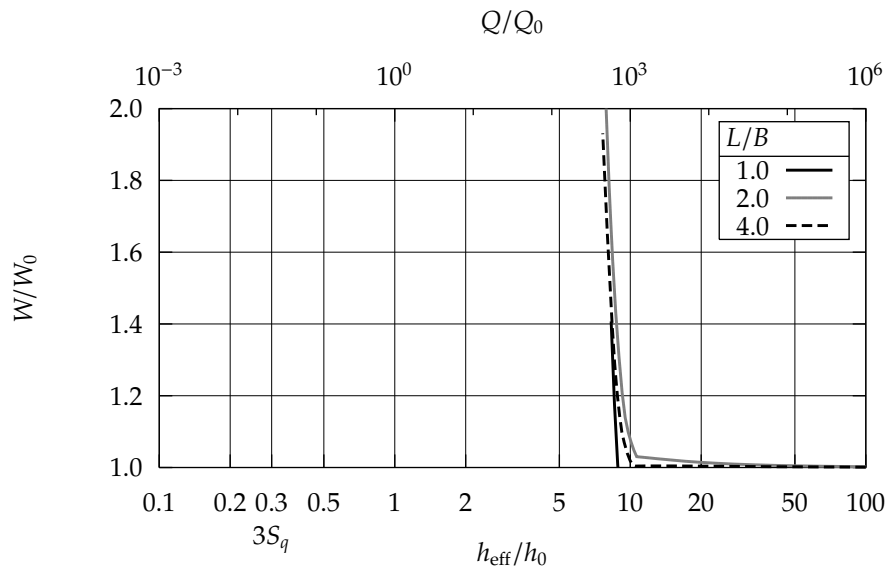


Figure 14.5: Load W/W_0 versus the effective height h_{eff}/h_0 for several bearing length/width ratios (L/B) on a non-smooth track.

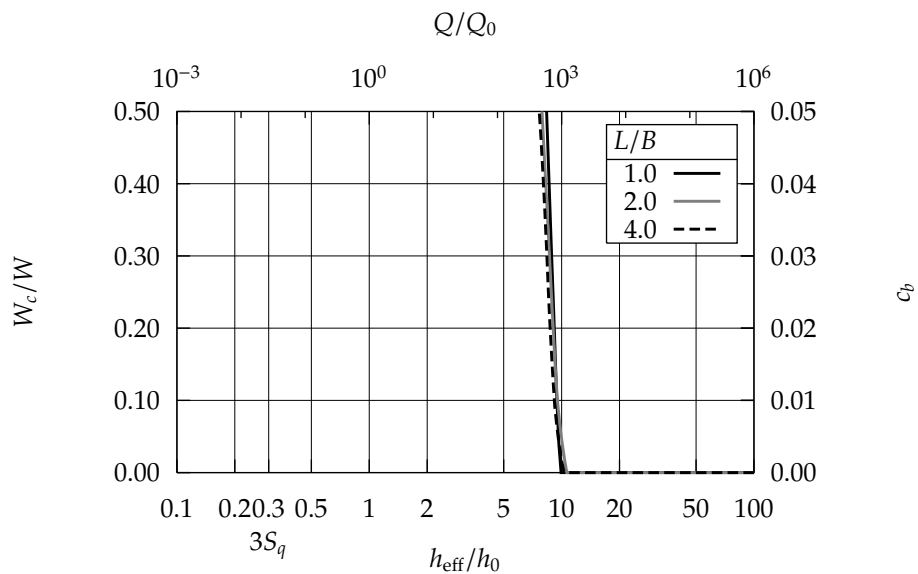


Figure 14.6: Contact load fraction W_c/W and bearing coefficient c_b versus the effective height h_{eff}/h_0 for several bearing length/width ratios (L/B) on a non-smooth track.

distribution as a result of a constant compression of this type of support is accurately modelled using the constant pressure approximation (chapter 9). This reaction pressure distribution is approximately parabolic. It is therefore different from the nominal hydrostatic pressure distribution in the lubricating film which is constant in the recess and then drops approximately linear to the bearing edge. A thin bearing will deform elastically due to this pressure difference between the pressures on top and bottom of the bearing.

The figures 14.7, 14.8 and 14.9 show the contact load fraction, the bearing coefficient, the volume flow rate and the effective film height of the standard hydro-fender with different bearing thicknesses on a plane track. The hydro-fender with the very thin bearing can sustain a load of approximately 1.3 times that of the same hydro-fender with rigid surfaces before contact occurs (figure 14.7). For loads higher than this value the contact contribution increases rapidly. The hydro-fender with a larger bearing thickness can sustain higher loads without a large contact contribution and shows a more gradual increase in the contact load contribution for higher loads. Furthermore the volume flow rate of the thin bearing is higher, for the same load, as that of the thicker bearing (figure 14.8).

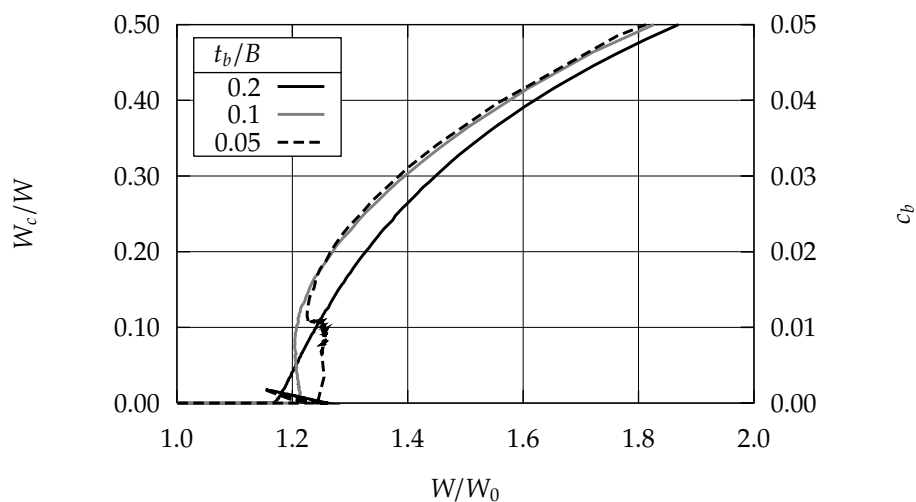


Figure 14.7: Contact load fraction W_c/W and bearing coefficient c_b versus the load W/W_0 for several bearing thicknesses (t_b/B) on a smooth track.

On a non-smooth track the hydro-fender with a (very) small bearing thickness is able to sustain higher loads without or with very little contact compared to the bearing with a larger thickness (figure 14.10). However this increase is coupled with a large increase of the volume flow rate at loads below this contact threshold (figures 14.11 and 14.12). For loads above this contact threshold the volume flow rate of the thin bearing drops below that of the bearing with a large thickness due to the better surface compliance of this thin bearing.

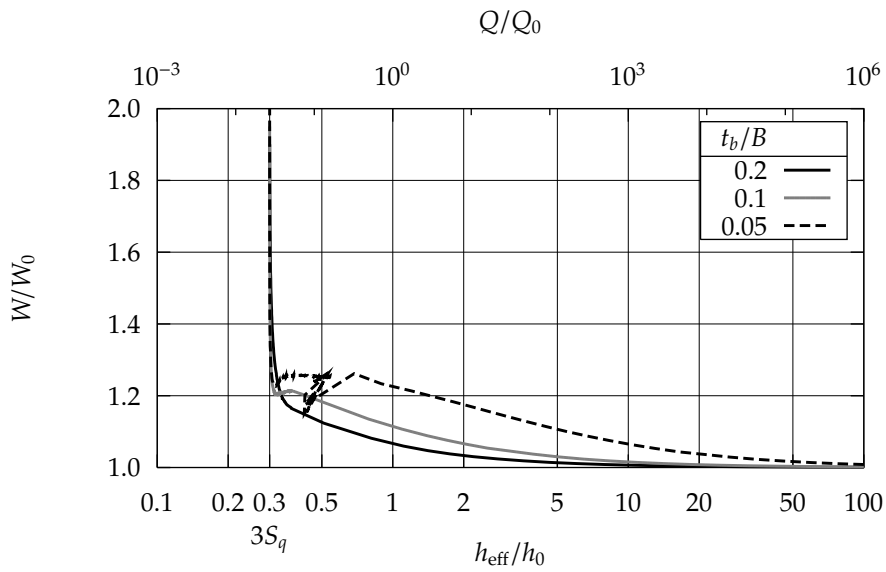


Figure 14.8: Load W/W_0 versus the effective height h_{eff}/h_0 for several bearing thicknesses (t_b) on a smooth track.

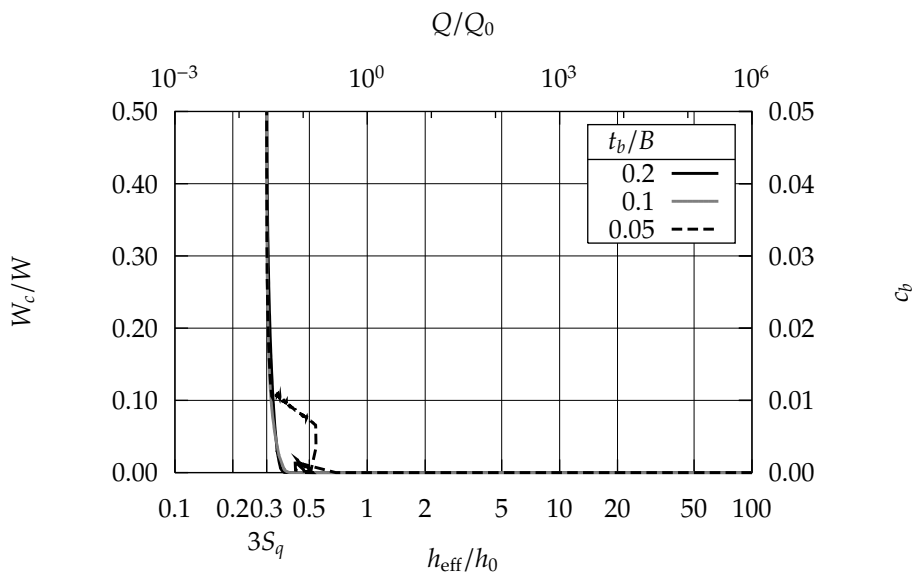


Figure 14.9: Contact load fraction W_c/W and bearing coefficient c_b versus the effective height h_{eff}/h_0 for several bearing thicknesses (t_b/B) on a smooth track.

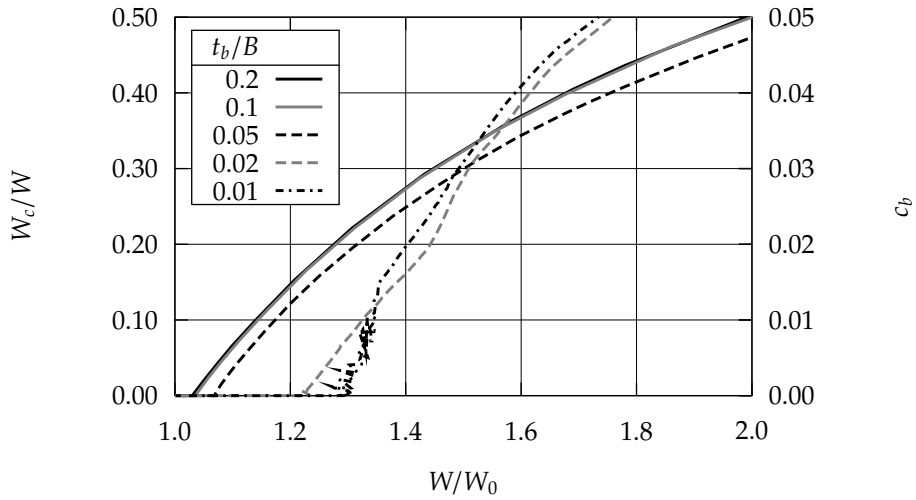


Figure 14.10: Contact load fraction W_c/W and bearing coefficient c_b versus the load W/W_0 for several bearing thicknesses (t_b/B) on a non-smooth track.

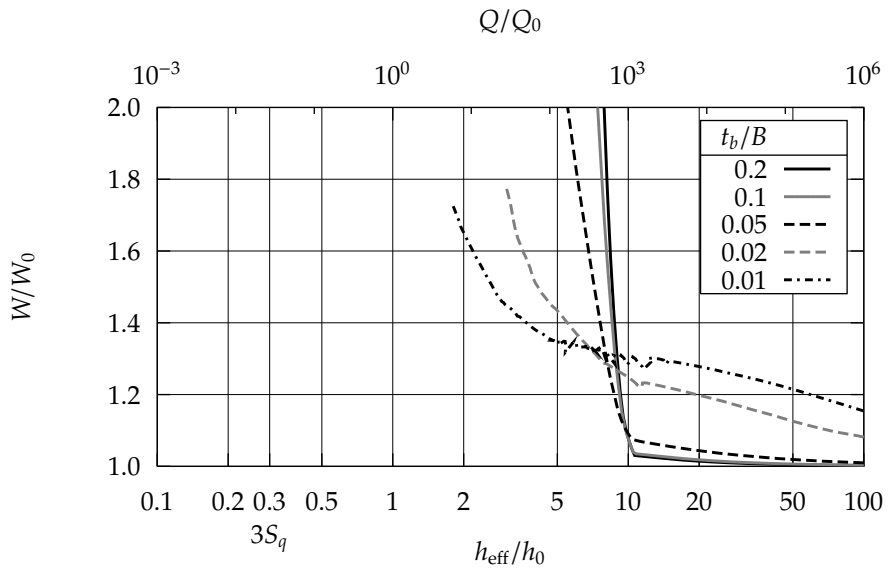


Figure 14.11: Load W/W_0 versus the effective height h_{eff}/h_0 for several bearing thicknesses (t_b/B) on a non-smooth track.

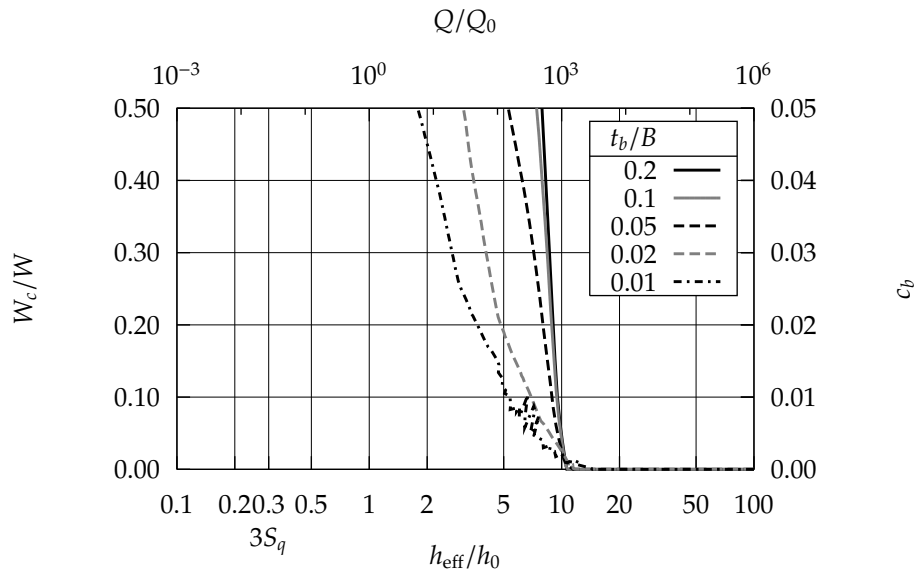


Figure 14.12: Contact load fraction W_c/W and bearing coefficient c_b versus the effective height h_{eff}/h_0 for several bearing thicknesses (t_b/B) on a non-smooth track.

L/R	p_r
1.0	4.258
2.0	1.000
3.0	0.567
4.0	0.395

Table 14.1: Bearing length/width ratio and recess pressure.

14.3 Constant load, variable bearing length/width ratio and recess pressure

The designer of a hydro-support will usually start with a chosen maximum track width and will want to use this track width optimally. Therefore the width of the bearing is fixed whereas the length can be chosen freely. For a given load this means that the recess pressure p_r must become smaller as the bearing length increases.

The bearing coefficient and volume flow rate have been calculated for a number of different bearing length/width ratios and corresponding recess pressures (table 14.1).

On a plane track the hydro-foot especially exhibits a small contact load fraction and therefore small bearing coefficient due to the relatively high recess pressure and elastic deformation (figure 14.13). However this low bearing coefficient is obtained for a relatively high flow rate (figures 14.14 and 14.15).

On a non-smooth track the hydro-foot exhibits a very high contact load ratio for the particular track surface used in this calculation (figure 14.16). The volume flow rate is

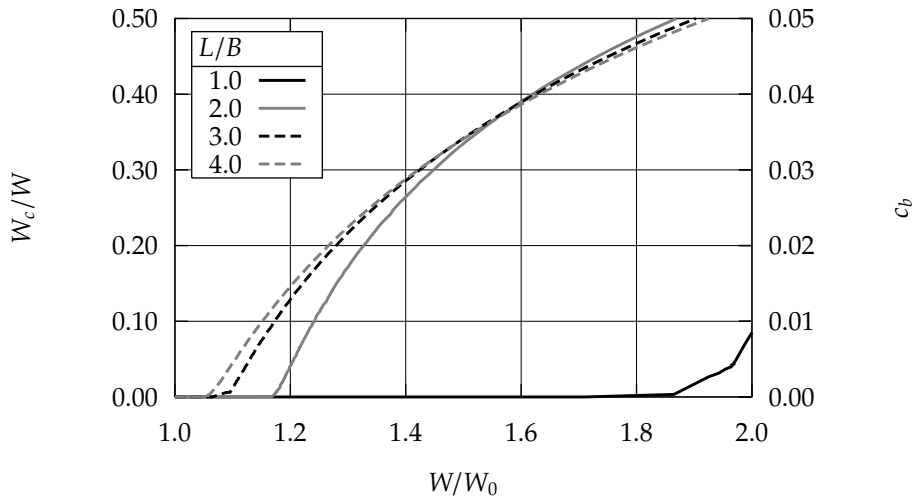


Figure 14.13: Contact load fraction W_c/W and bearing coefficient c_b versus the load W/W_0 for several bearing length/width ratios (L/B) and corresponding recess pressure on a smooth track.

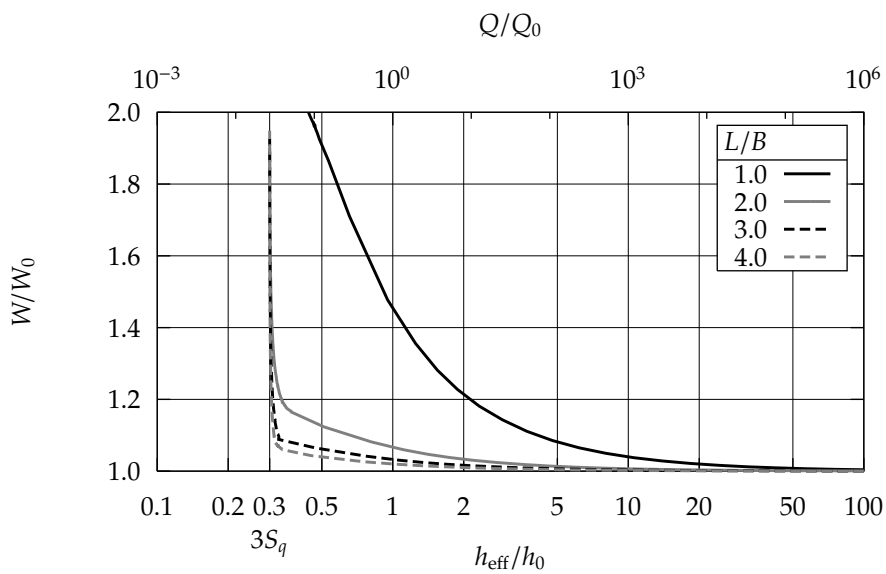


Figure 14.14: Load W/W_0 versus the effective height h_{eff}/h_0 for several bearing length/width ratios (L/B) and corresponding recess pressure on a smooth track.

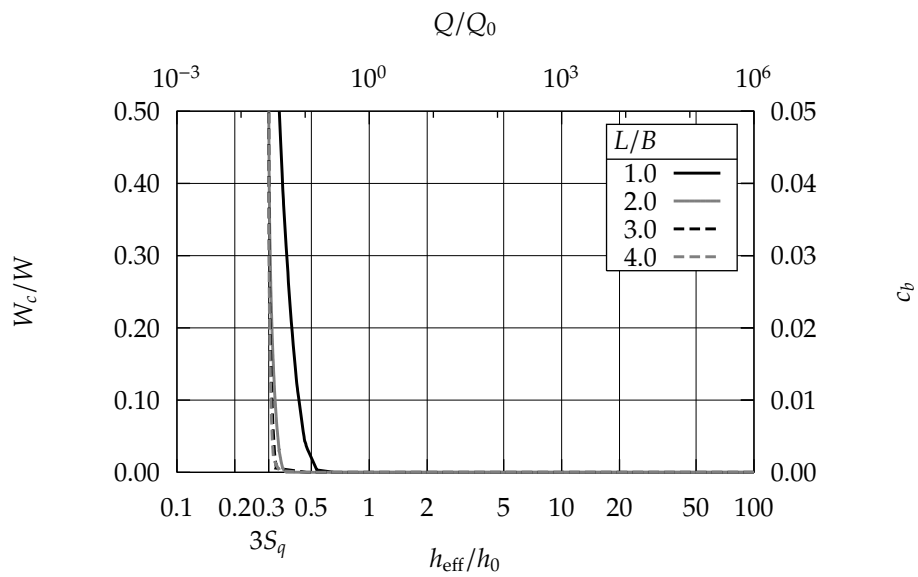


Figure 14.15: Contact load fraction W_c/W and bearing coefficient c_b versus the effective height h_{eff}/h_0 for several bearing length/width ratios (L/B) and corresponding recess pressure on a smooth track.

approximately equal for all bearing length/width ratios (figures 14.17 and 14.18).

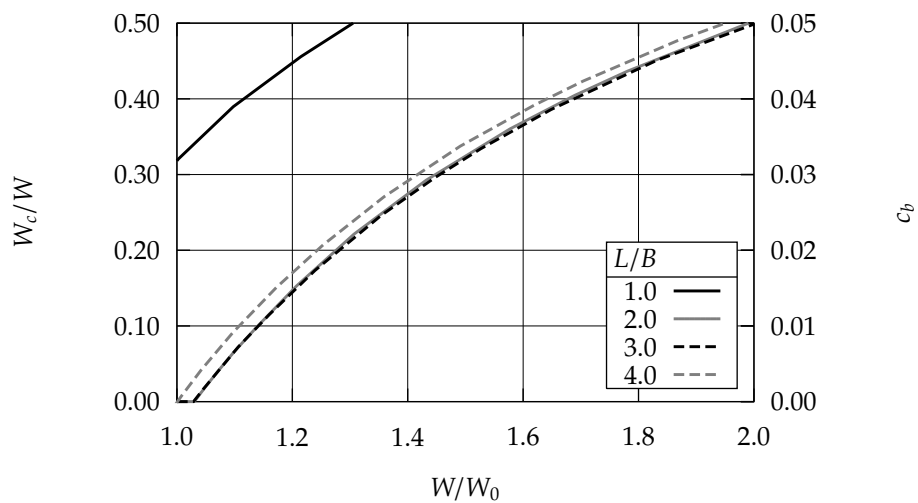


Figure 14.16: Contact load fraction W_c/W and bearing coefficient c_b versus the load W/W_0 for several bearing length/width ratios (L/B) and corresponding recess pressure on a non-smooth track.

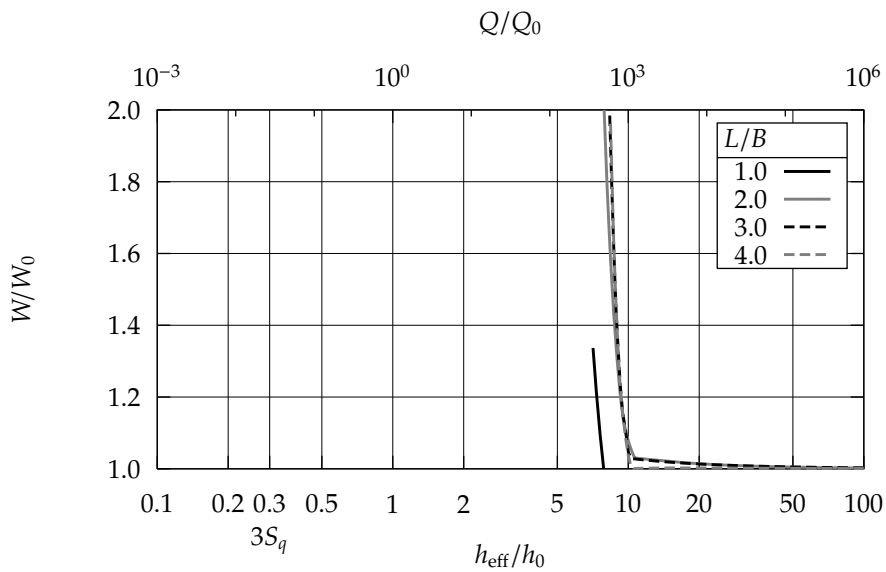


Figure 14.17: Load W/W_0 versus the effective height h_{eff}/h_0 for several bearing length/width ratios (L/B) and corresponding recess pressure on a non-smooth track.

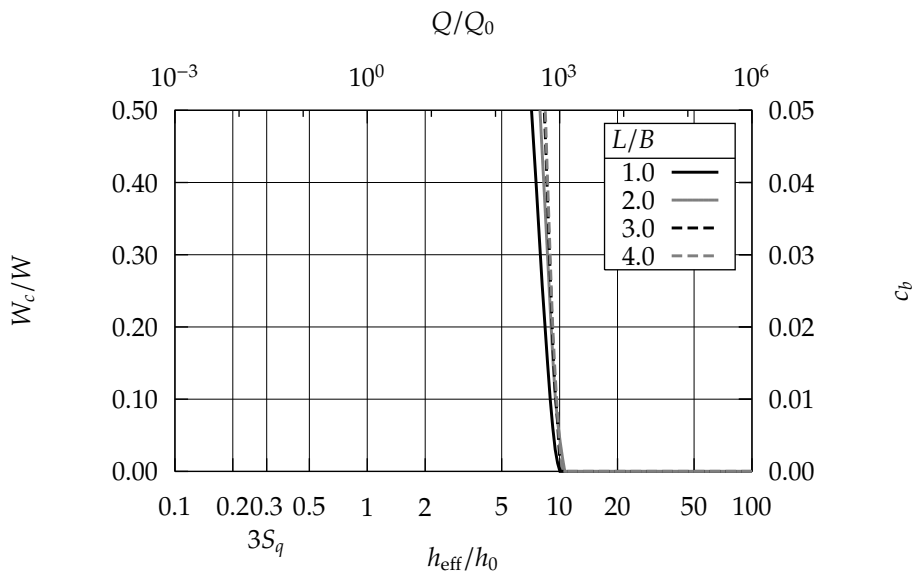


Figure 14.18: Contact load fraction W_c/W and bearing coefficient c_b versus the effective height h_{eff}/h_0 for several bearing length/width ratios (L/B) and corresponding recess pressure on a non-smooth track.

CHAPTER 15

Recess geometry

In this chapter the influence of the recess geometry and recess fluid pressure on the properties of the hydro-fender are studied. The primary parameter of the recess design is the number of recesses of the bearing. In the next section this parameter is varied.

15.1 Number of recesses

The primary parameter pertinent to recess geometry is of course the number of recesses used. In classic hydrostatic thrust bearing design more than one recesses are used in order to increase tilting stiffness. For this reason the hydro-feet in the PWA-lock have four recesses each. A disadvantage of the n-recess design is the necessary use of (1) a separate supply pump or (2) a restrictor for each recess. Both solutions introduce a substantial cost increase.

In this section the tilting stiffness of the 4-recess thrust bearing is compared to that of the 0- or 1-recess bearing. The 1-recess bearing has a recess diameter equal to that of the 4-recess bearing, the 0-recess bearing has a small central recess. Contrary to the calculations in other sections, these calculations have been performed on a hydro-foot instead of a hydro-fender. This in order to compare the tilting stiffness of specifically the hydro-feet in the PWA-lock to its alternatives. All main dimensions have been chosen equal to those of the hydro-feet in the PWA-lock. Furthermore, the load is prescribed and the film height follows from the load balance equation. In order to accurately calculate the properties of the 4-recess bearing, the restrictors to the recesses have to be taken into account. In order to compare the 4-recess bearing with the 0- an 1-recess bearing, these bearings also have to be calculated including the same effective restrictor value.

When the bearing tilts relative to the track an opposing tilting moment will result due to the eccentric hydrostatic pressure or contact pressure. Figure 15.1 shows this tilting

moment \bar{M} versus the tilting angle $\bar{\alpha}$ where:

$$\bar{M} = \frac{M}{\frac{D}{2}W} \quad (15.1)$$

The height h_0 in the tilting angle $\bar{\alpha}$ is a reference film height that is equal to the film height in the center of the bearing if both surfaces are assumed to be rigid. For these calculations this reference film height is equal to 0.1 mm. The track is assumed to be plane.

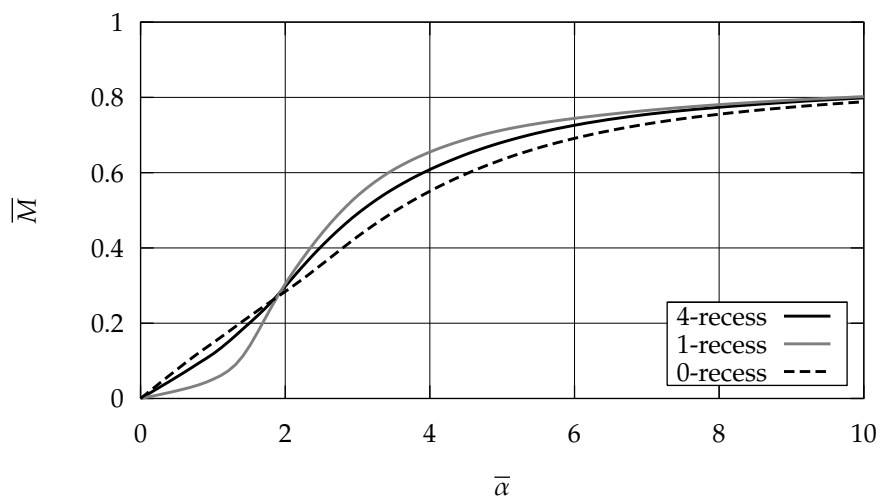


Figure 15.1: Reaction moment \bar{M} versus the tilting angle $\bar{\alpha}$ of the 0-, 1- and 4-recess bearing.

Using figure 15.1, the tilting stiffness of the 4-recess hydro-foot as used in the PWA-lock can be calculated and compared to the stiffness of the rubber support (1.75 MNm/rad, see chapter 2). We are particularly interested in the tilting stiffness for small tilting angles ($\bar{\alpha} < 1.0$). At $\bar{\alpha} = 1.0$, the tilting moment for the 4-recess bearing is $\bar{M} = 0.105$. Assuming a linear relation between tilting angle and moment for small values of $\bar{\alpha}$, and the dimensions for the PWA-lock given in appendix A, the tilting stiffness becomes:

$$\frac{M}{\alpha} = \frac{\bar{M}W\frac{D}{2}}{\bar{\alpha}\frac{h_0}{D/2}} = \frac{0.105 \cdot 250 \cdot 10^3 \text{N} \cdot 0.37 \text{m}}{1.0 \cdot \frac{0.110 \cdot 10^{-3} \text{m}}{0.37 \text{m}}} = 36.0 \text{ MNm/rad} \quad (15.2)$$

And as was assumed in chapter 2, this tilting stiffness is indeed much higher than the tilting stiffness of the rubber support.

The high tilting moment of the 0-recess bearing is noteworthy. It is comparable to that of the 4-recess bearing. Figure 15.2 shows the pressure distribution under the 0-recess bearing where the tilt angle $\bar{\alpha} = 1.0$. The hydrostatic pressure rise is concentrated at that side of the bearing closest to the track resulting in this high tilting moment.

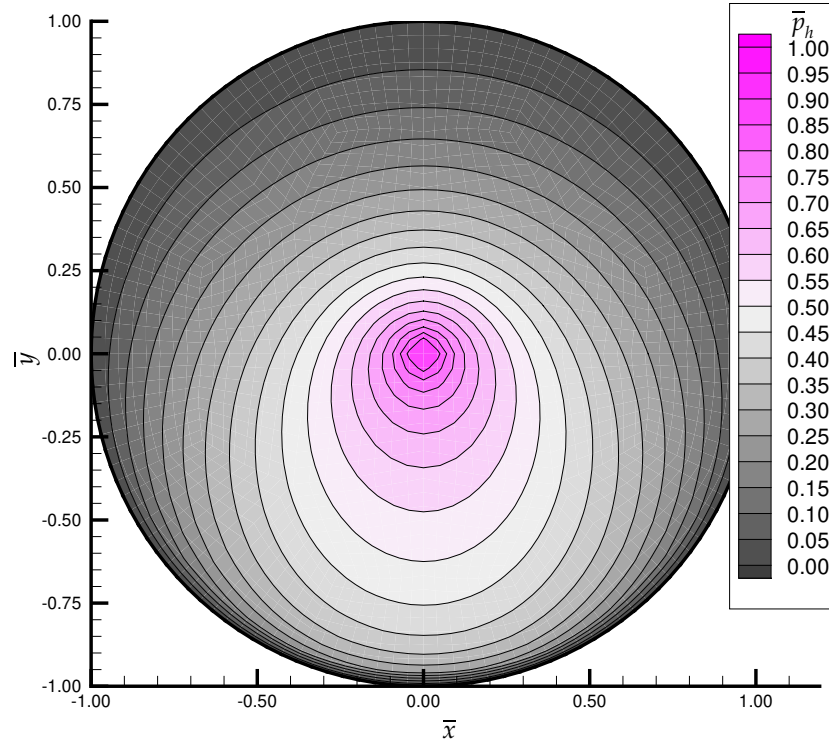


Figure 15.2: Hydrostatic pressure \bar{p}_h of the 0-recess bearing. (Tilting angle $\bar{\alpha} = 1.0$.)

The resulting bearing coefficient c_b is shown in figures 15.3 and 15.4. It is clear that for angles $\bar{\alpha}$ larger than 1.0 contact occurs for all three types of bearing (figure 15.3). However for larger angles the contact load fraction increases more slowly for the 0-recess bearing and fastest for the 1-recess bearing. Furthermore, the 0-recess bearing shows the smallest bearing coefficient for a given tilting moment (figure 15.3).

The 0-recess bearing exhibits a much reduced volume flow rate \bar{Q} compared to the 1-recess and 4-recess bearings (figure 15.5) with:

$$\bar{Q} = \frac{Q\eta}{h_0^3 p_{\text{sup}}} \quad (15.3)$$

This reduction is caused by the high flow resistance in the lubricating film due to the small central recess.

The 0-recess bearing maintains an almost constant height for tilting angles up to approximately 2.0, whereas the 4-recess and in particular the 1-recess bearing show a drop of the central film height for small tilting angles (figure 15.6).

It can be concluded from these calculations that considering the tilting stiffness the 0-recess bearing provides a good alternative for the 4-recess bearing. Compared with the added advantage of the low cost supply system, the 0-recess bearing has been chosen as the main subject of the other calculations.

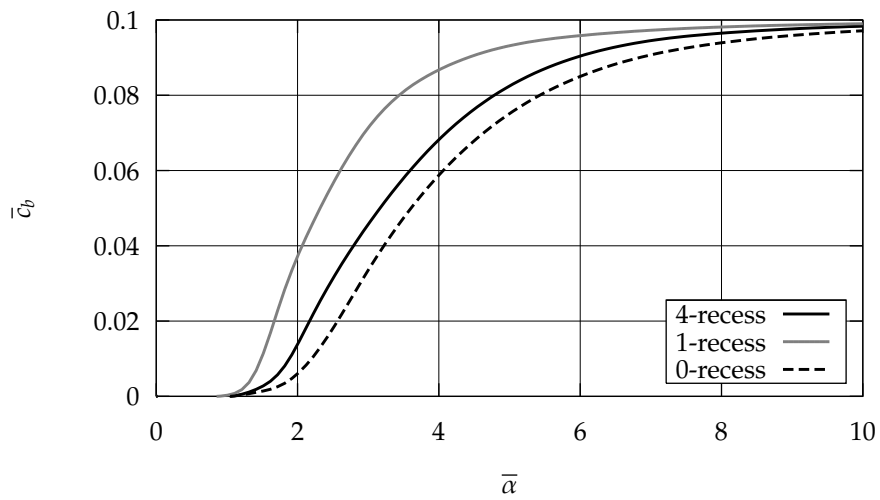


Figure 15.3: The bearing coefficient c_b versus the tilting angle $\bar{\alpha}$.

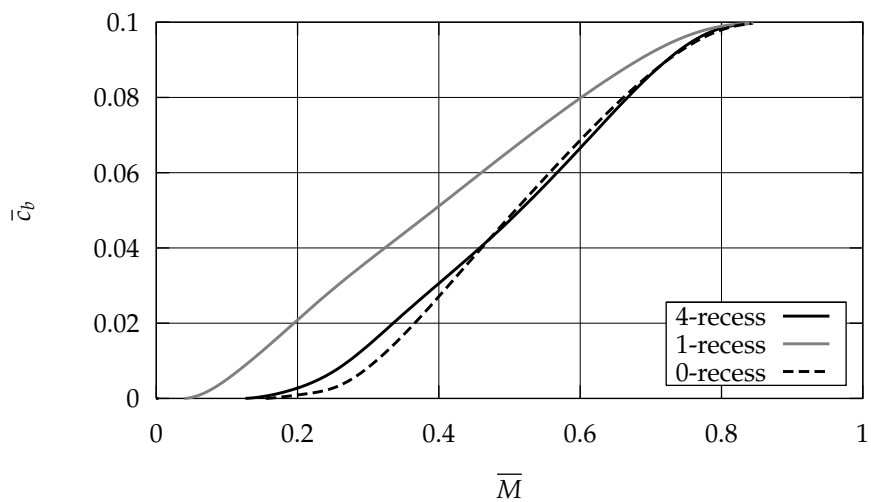


Figure 15.4: The bearing coefficient c_b versus the tilting moment \bar{M} .

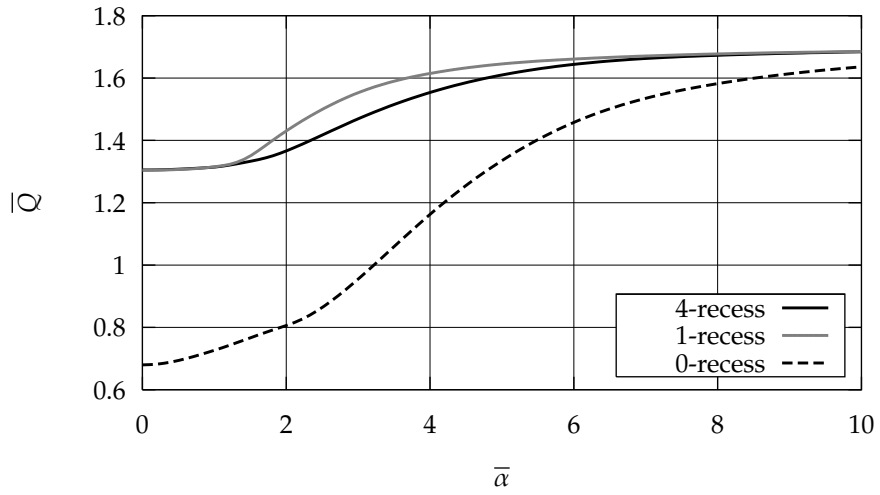


Figure 15.5: flow rate \bar{Q} versus the tilting angle $\bar{\alpha}$.

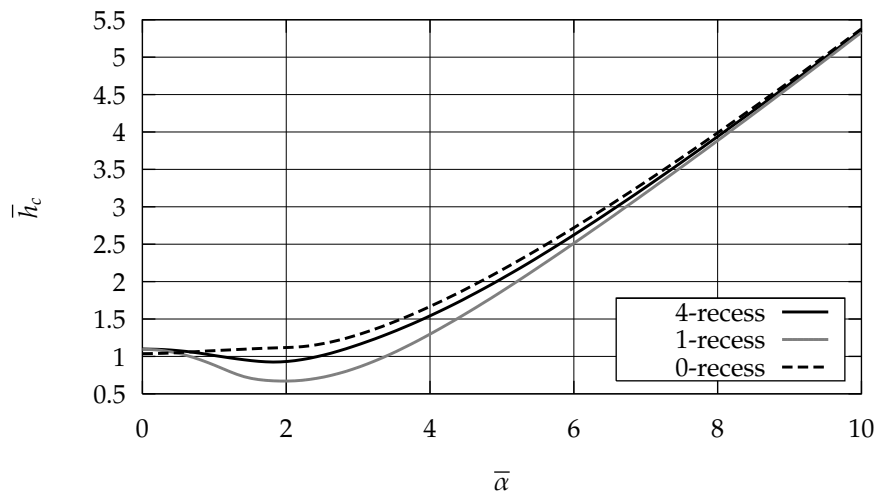


Figure 15.6: Central film height $\bar{h}_c = h_c/h_0$ versus the tilting angle $\bar{\alpha}$.

15.2 Recess width

In this section the bearing/recess width ratio of the reference bearing is varied and the influence of this variation is studied both on a smooth and non-smooth track.

On a smooth track the influence of the elastic deformation of the surfaces decreases strongly for an increased recess width (figures 15.7, 15.8 and 15.9). The bearing coefficient increases clearly for an increased recess width.

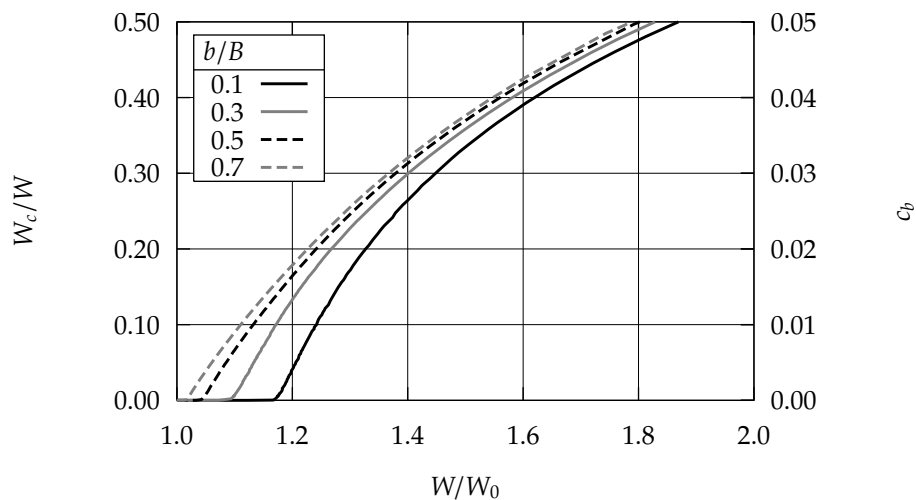


Figure 15.7: Contact load fraction W_c/W and bearing coefficient c_b versus the load W/W_0 for several recess widths (b/B) on a smooth track.

On a non-smooth track the influence of the variation of the recess width is much less pronounced (figures 15.10, 15.11 and 15.12).

15.3 Recess pressure

In this section the influence of the recess pressure on the bearing properties is studied. On a smooth track the influence of the elastic deformation increases as the recess pressure increases (figures 15.13, 15.14 and 15.15).

On a non-smooth track this influence is much less pronounced (figures 15.16, 15.17 and 15.18).

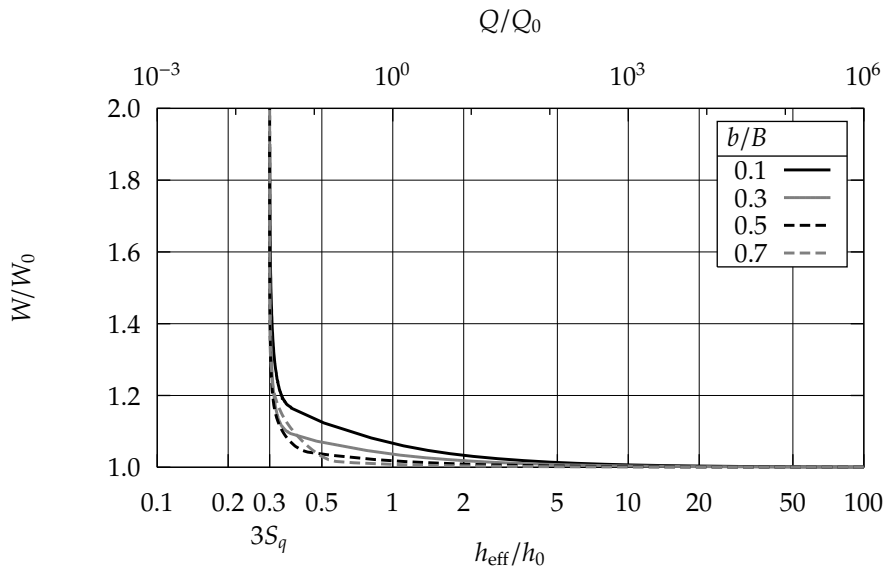


Figure 15.8: Load W/W_0 versus the effective height h_{eff}/h_0 for several recess widths (b/B) on a smooth track.

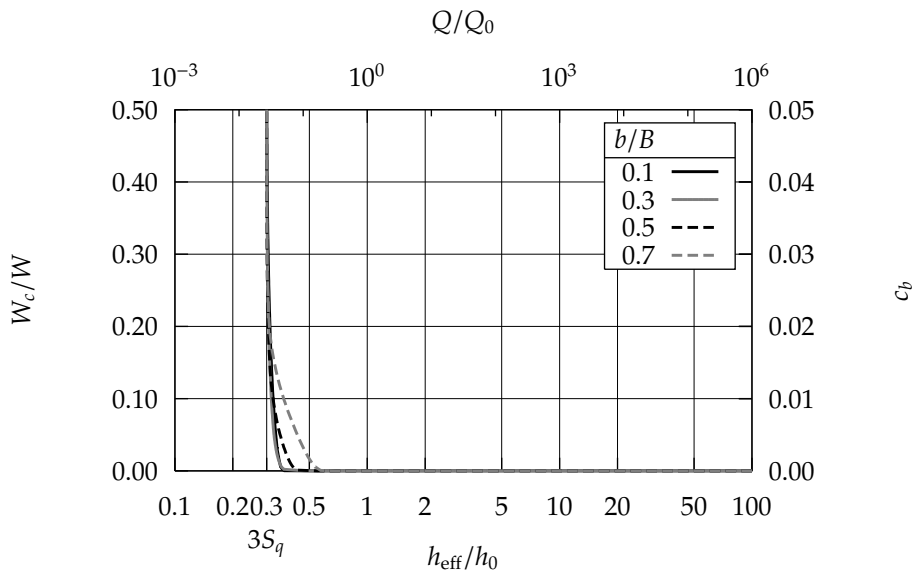


Figure 15.9: Contact load fraction W_c/W and bearing coefficient c_b versus the effective height h_{eff}/h_0 for several recess widths (b/B) on a smooth track.

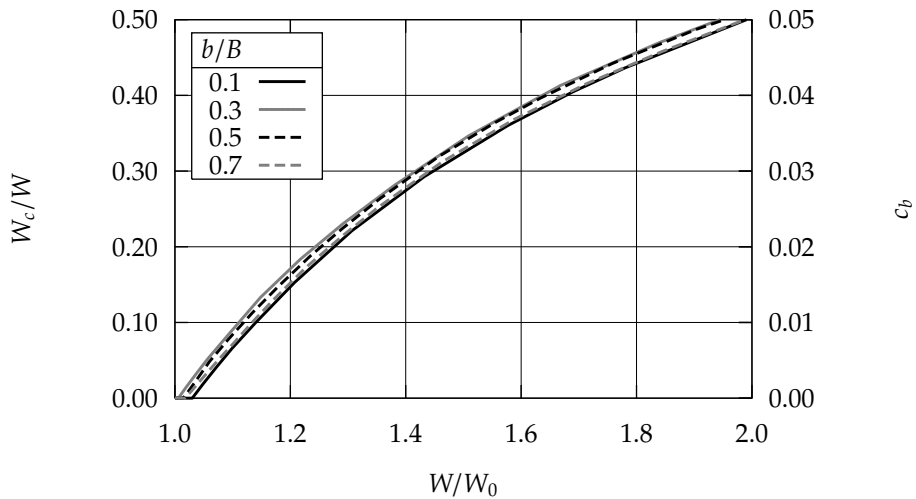


Figure 15.10: Contact load fraction W_c/W and bearing coefficient c_b versus the load W/W_0 for several recess widths (b/B) on a non-smooth track.

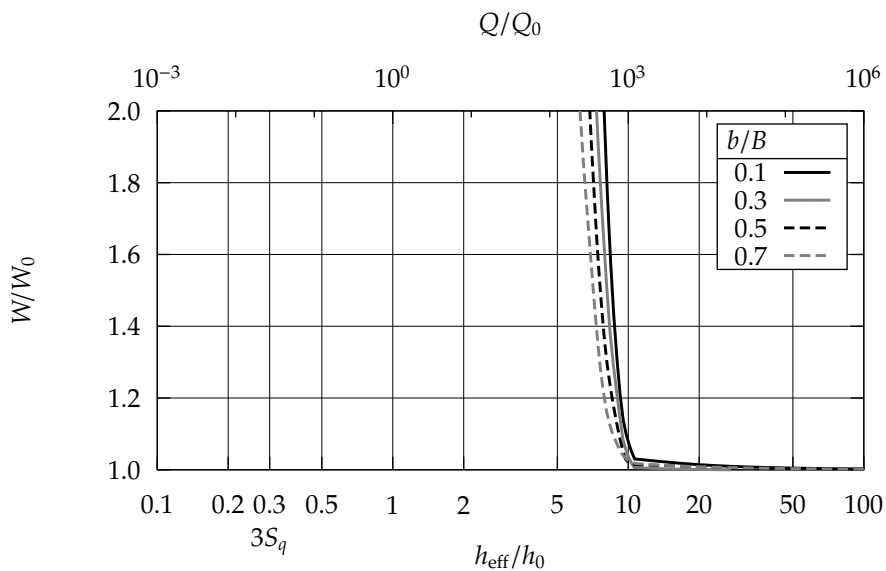


Figure 15.11: Load W/W_0 versus the effective height h_{eff}/h_0 for several recess widths (b/B) on a non-smooth track.

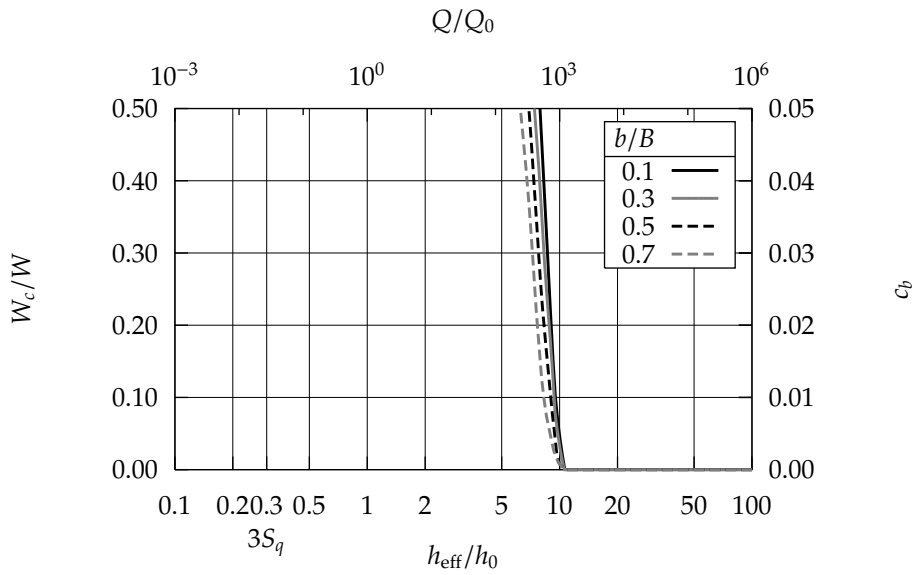


Figure 15.12: Contact load fraction W_c/W and bearing coefficient c_b versus the effective height h_{eff}/h_0 for several recess widths (b/B) on a non-smooth track.

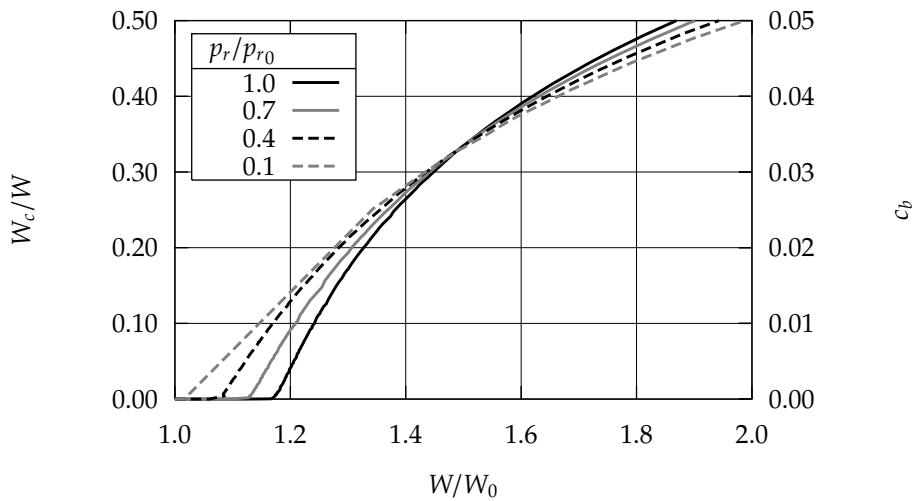


Figure 15.13: Contact load fraction W_c/W and bearing coefficient c_b versus the load W/W_0 for several recess pressures (p_r/p_{r_0}) on a smooth track.

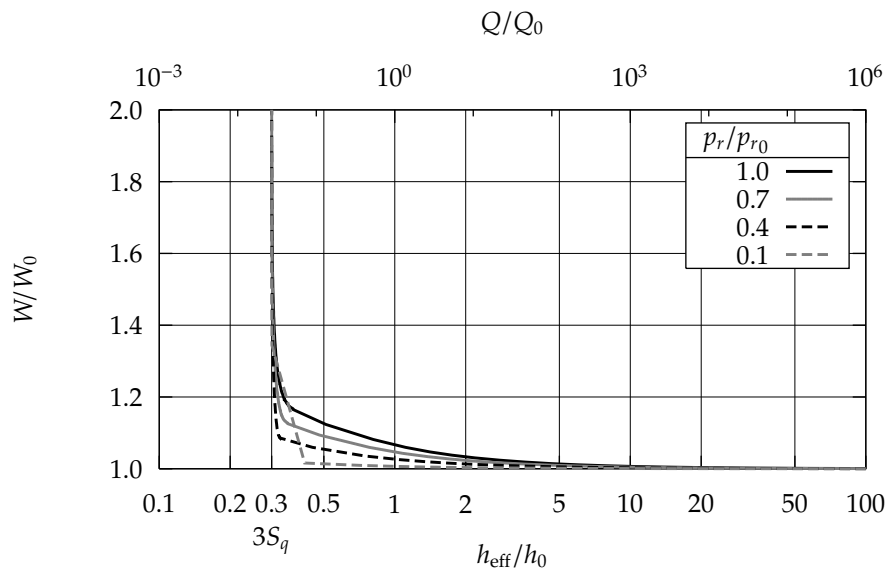


Figure 15.14: Load W/W_0 versus the effective height h_{eff}/h_0 for several recess pressures (p_r) on a smooth track.

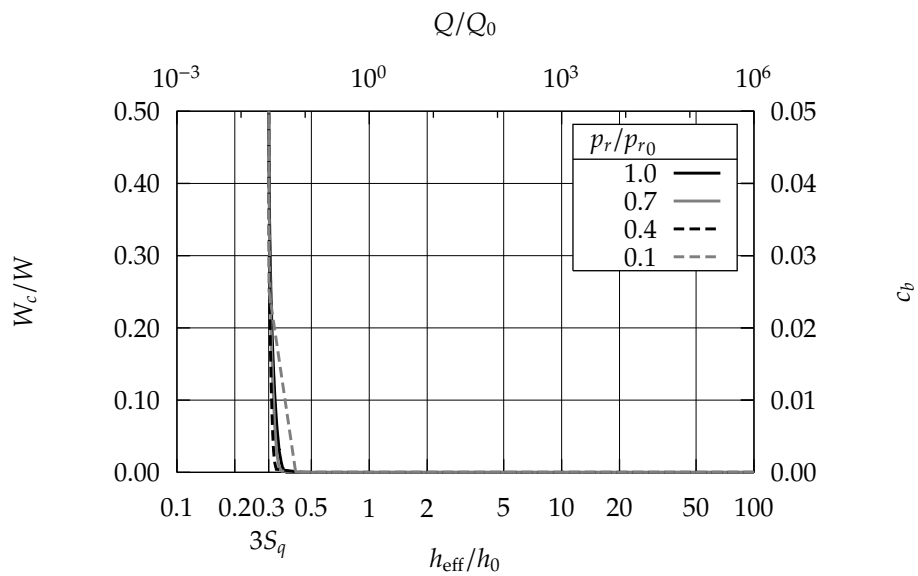


Figure 15.15: Contact load fraction W_c/W and bearing coefficient c_b versus the effective height h_{eff}/h_0 for several recess pressures (p_r/p_{r_0}) on a smooth track.

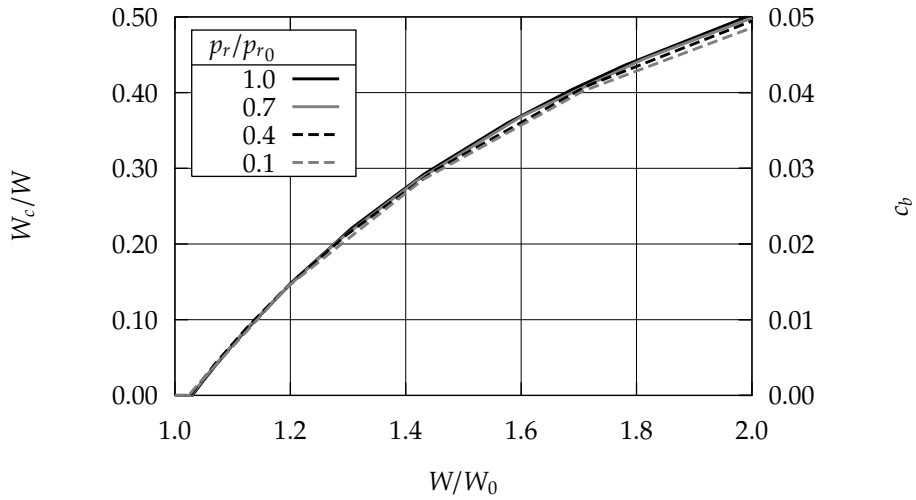


Figure 15.16: Contact load fraction W_c/W and bearing coefficient c_b versus the load W/W_0 for several recess pressures (p_r/p_{r0}) on a non-smooth track.

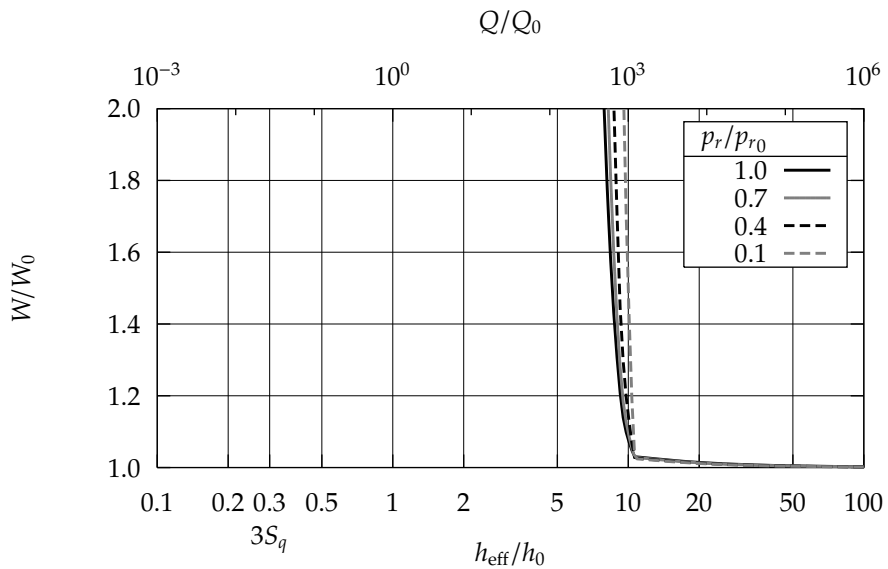


Figure 15.17: Load W/W_0 versus the effective height h_{eff}/h_0 for several recess pressures (p_r/p_{r0}) on a non-smooth track.

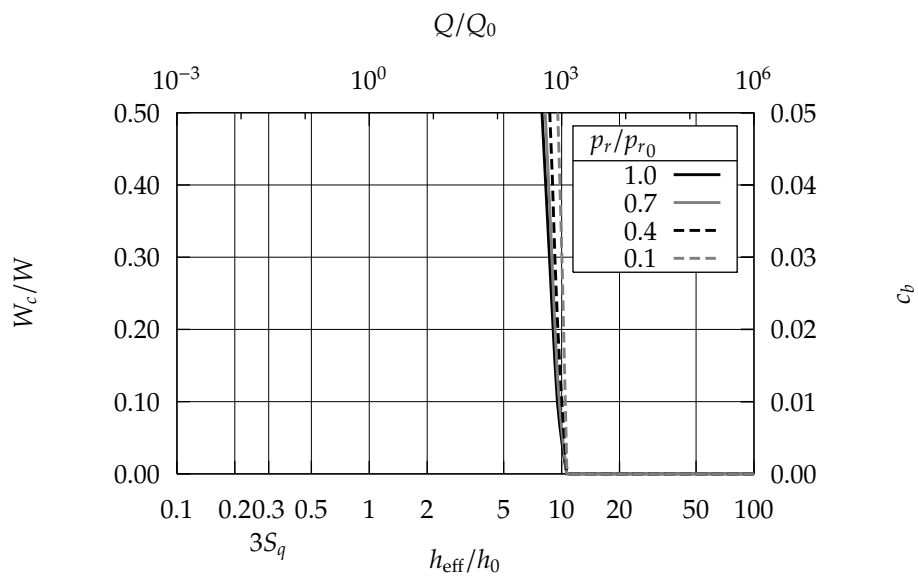


Figure 15.18: Contact load fraction W_c/W and bearing coefficient c_b versus the effective height h_{eff}/h_0 for several recess pressures (p_r/p_{r_0}) on a non-smooth track.

An important aspect of this study is the behavior of the hydro-support on a non-smooth elastic track. This surface waviness is produced using a stochastic process using equation 5.6. Thus the surface waviness is known only in an average sense. The properties of the hydro-support will vary while sliding on a non-smooth track because of local variations of the surface waviness. Furthermore the properties of the hydro-support will differ when sliding on different tracks with different surface waviness. In our model, the track elasticity and track height are combined in one track material constant (equation 5.3). In the following sections the influence of the track waviness geometry and elasticity are studied.

16.1 Surface waviness

As stated previously the variations of the properties of the fender due to the surface waviness are twofold: The properties will vary while sliding on a surface waviness due to the varying actual track surface height distribution and second, the properties will vary while sliding on different tracks with different surface waviness but with the same average surface waviness properties.

16.1.1 Fender position on track

While sliding on a non-smooth track the surface height under the fender will vary continuously and because of that the hydrostatic and contact pressure and flow. Figure 16.1 shows the contact load fraction and bearing coefficient versus the total load for different positions of the fender on the same track surface. The variation of the

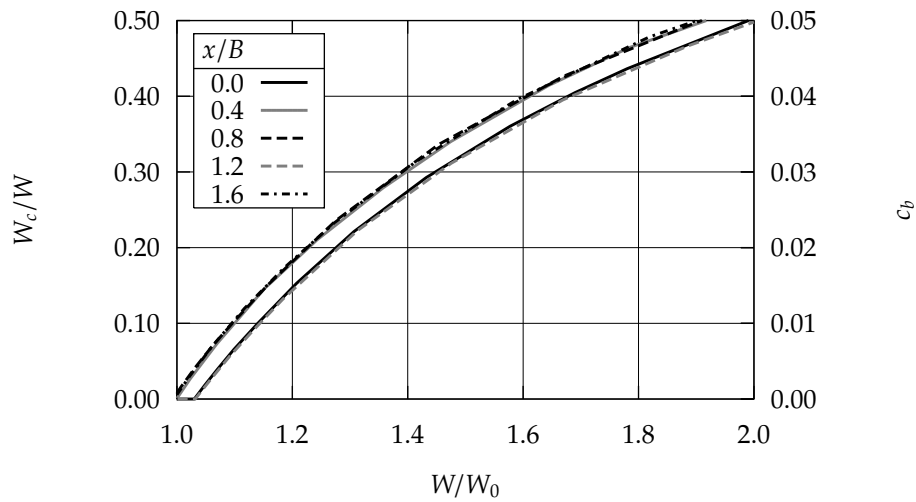


Figure 16.1: Contact load fraction W_c/W and bearing coefficient c_b versus the load W/W_0 for several positions of the bearing on the same track waviness.

bearing coefficient at constant load appears to be independent of the actual load and is approximately equal to 0.004.

Figure 16.2 shows the effective film height and flow rate versus the total load for different positions of the fender. For a constant load this variation is approximately equal to 10%. Therefore the flow rate varies with approximately 30%.

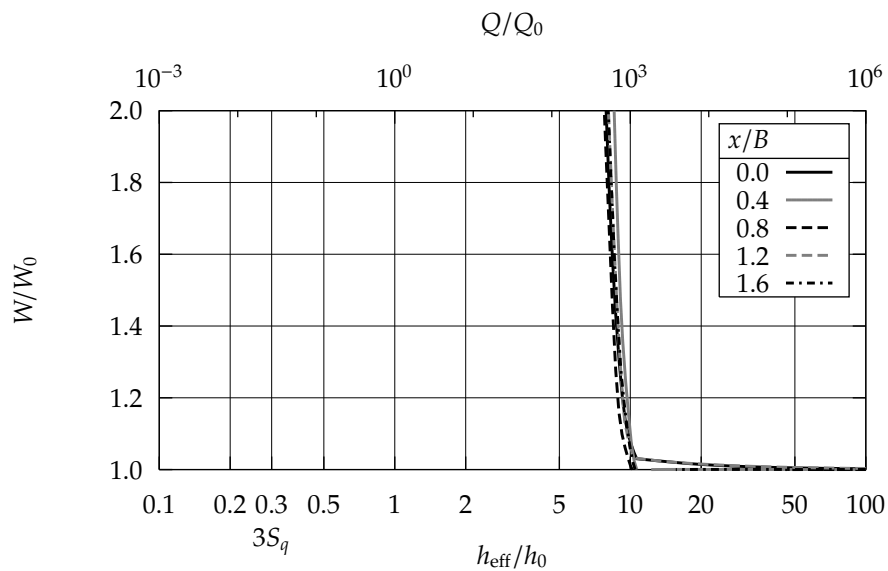


Figure 16.2: Load W/W_0 versus the effective height h_{eff}/h_0 for several positions of the bearing on the same track waviness.

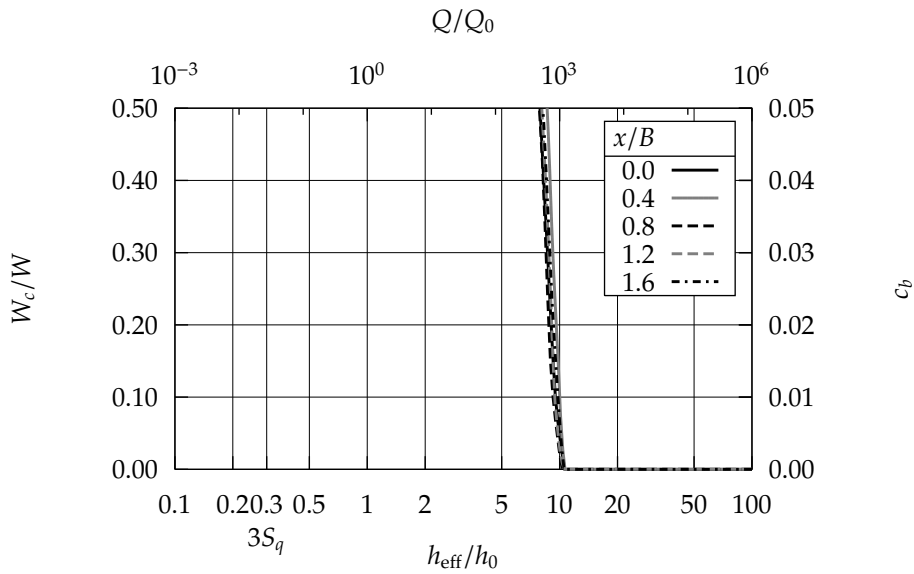


Figure 16.3: Contact load fraction W_c/W and bearing coefficient c_b versus the effective height h_{eff}/h_0 for several positions of the bearing on the same track waviness.

16.1.2 Different random track surfaces

In the previous section the dependance of the fender position on specific non-smooth track on the bearing coefficient and flow rate was studied. However, as stated previously, the waviness of the track surface is only known in an average sense. The exact geometry of the surface waviness is the result of a stochastic process. Therefore, in this section the bearing coefficient and flow rate are studied on tracks with different surfaces. The surface waviness of these surfaces are generated using equation 5.6 with different random parameters a_{mn} , ϕ_{xmn} and ϕ_{ymn} .

The bearing coefficient is clearly dependent on the geometry of the track surface (figure 16.4). The maximum difference of the bearing coefficient between the different tracks is approximately equal to 0.015. Note that this difference is only the maximum difference obtained from 6 different track surfaces. A full stochastic study is required to obtain the variation and distribution of the bearing coefficient for all different track surfaces. The results obtained here, for 6 surfaces only, yields an indication of the variation one can expect.

Figure 16.5 shows the variation of the average film height and therefore the flow rate for the same fender on different tracks. For a constant load the maximum difference of the average film height is approximately 25%, the maximum difference of the flow rate is approximately 60%.

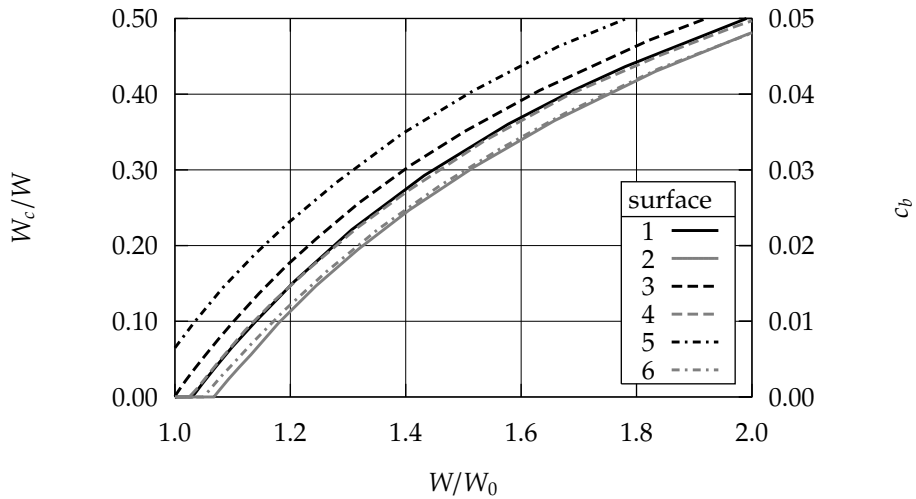


Figure 16.4: Contact load fraction W_c/W and bearing coefficient c_b versus the load W/W_0 for different track waviness with the same amplitude but different (random) geometry.

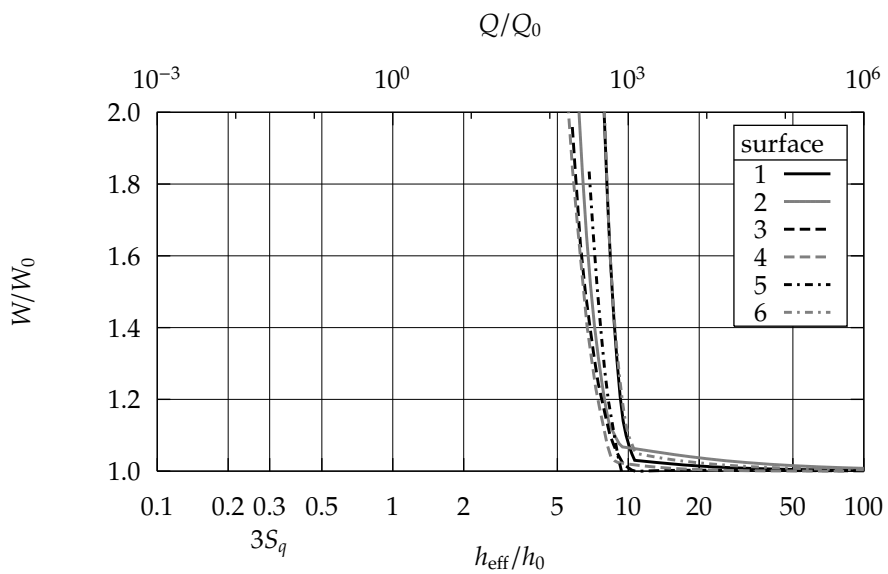


Figure 16.5: Load W/W_0 versus the effective height h_{eff}/h_0 for different track waviness with the same amplitude but different (random) geometry.

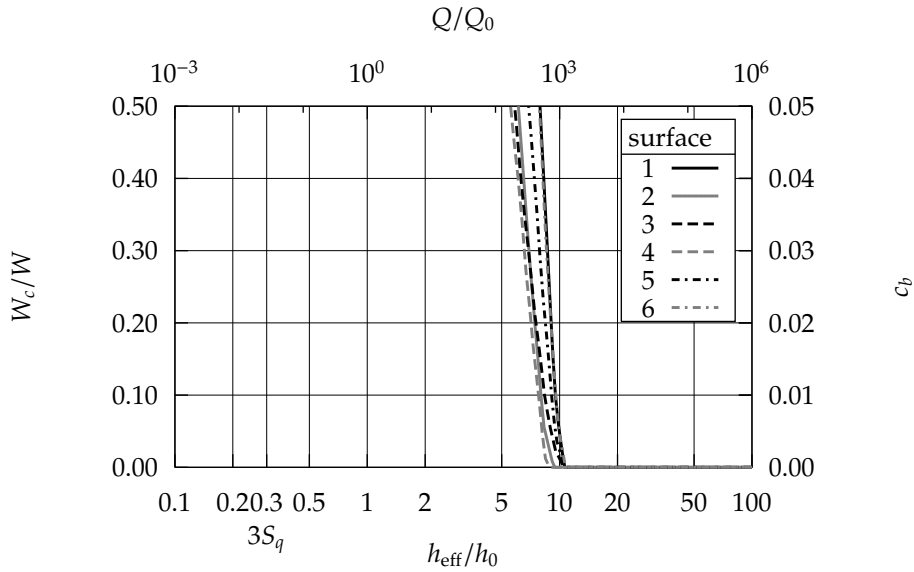


Figure 16.6: Contact load fraction W_c/W and bearing coefficient c_b versus the effective height h_{eff}/h_0 for different track waviness with the same amplitude but different (random) geometry.

16.1.3 Waviness amplitude

The bearing coefficient and flow rate are strongly dependent on the properties of the track surface waviness, in particular the amplitude of the surface waviness. Figure 16.7 shows the contact load ratio and bearing coefficient versus the total load for different amplitudes of the surface waviness. These parameters appear to be only slightly dependent on the waviness amplitude.

The flow rate and effective film height however are strongly dependent on the waviness amplitude (figure 16.8). It appears that the effective film height is approximately equal to the amplitude of the surface waviness.

16.2 Track thickness

The hydro-support slides on an elastic track. The deformation of the track due to the hydrostatic and contact pressure is dependent on the track thickness and elasticity. These properties have been combined in one parameter, the so-called track modulus of elasticity \bar{E}_t :

$$\bar{E}_t = \frac{E_t h_0 (1 - \nu_t)}{p_r t_t (1 - 2\nu_t)(1 + \nu_t)} \quad (16.1)$$

In this section the influence of the track elasticity on the bearing coefficient and volume flow rate are studied.

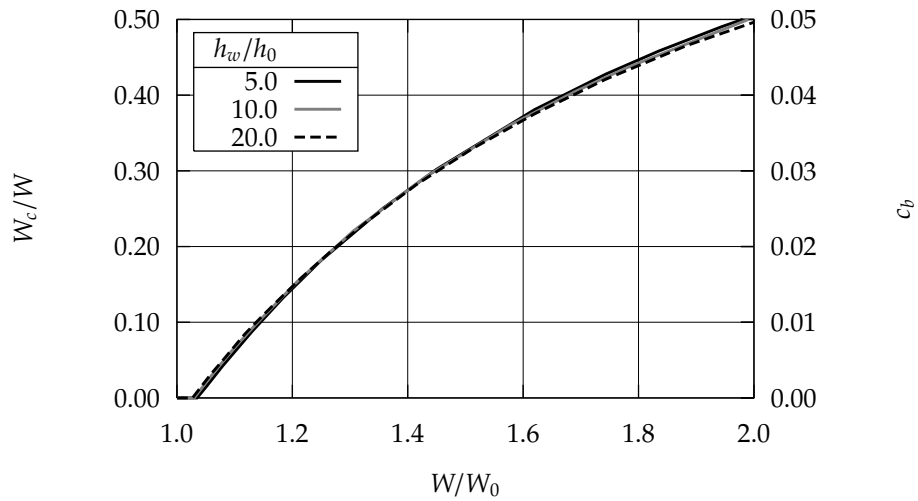


Figure 16.7: Contact load fraction W_c/W and bearing coefficient c_b versus the load W/W_0 for different track waviness with different amplitude (h_{wav}/h_0).

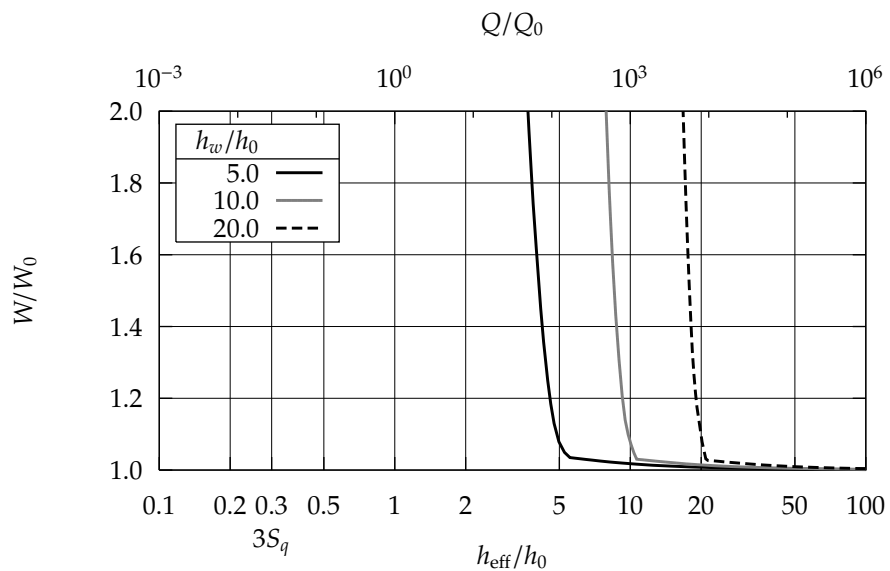


Figure 16.8: Load W/W_0 versus the effective height h_{eff}/h_0 for different track waviness with different amplitude (h_{wav}/h_0).

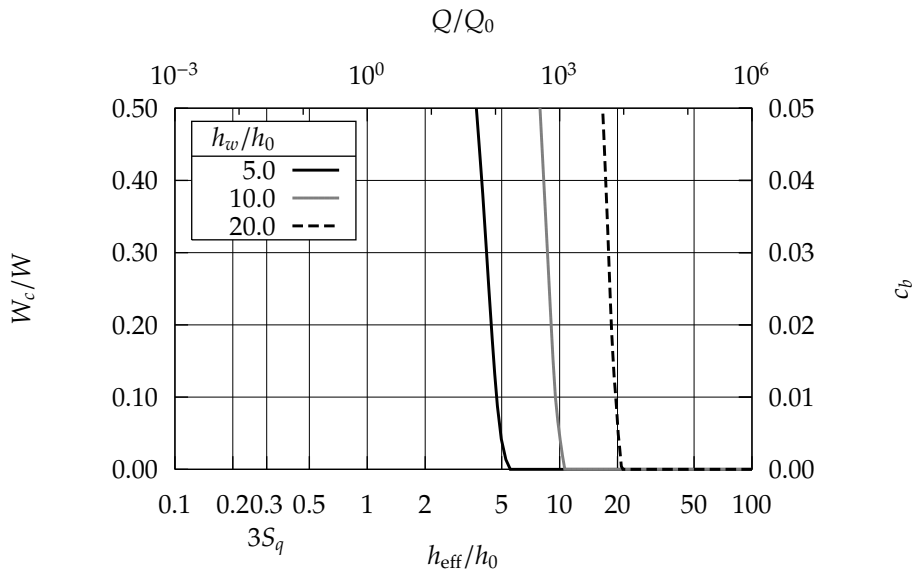


Figure 16.9: Contact load fraction W_c/W and bearing coefficient c_b versus the effective height h_{eff}/h_0 for different track waviness with different amplitude (h_{wav}/h_0).

If the track modulus of elasticity \bar{E}_t is decreased the track deformation due to the hydrostatic and contact pressures will increase as a result. For a given load this will result in a smaller contact load fraction and bearing coefficient (figure 16.10). The load can increase to approximately 1.6 times that obtained with rigid surfaces before contact starts to occur. However this decrease of the bearing coefficient is obtained at the cost of a very much increased volume flow rate (figures 16.11 and 16.12).

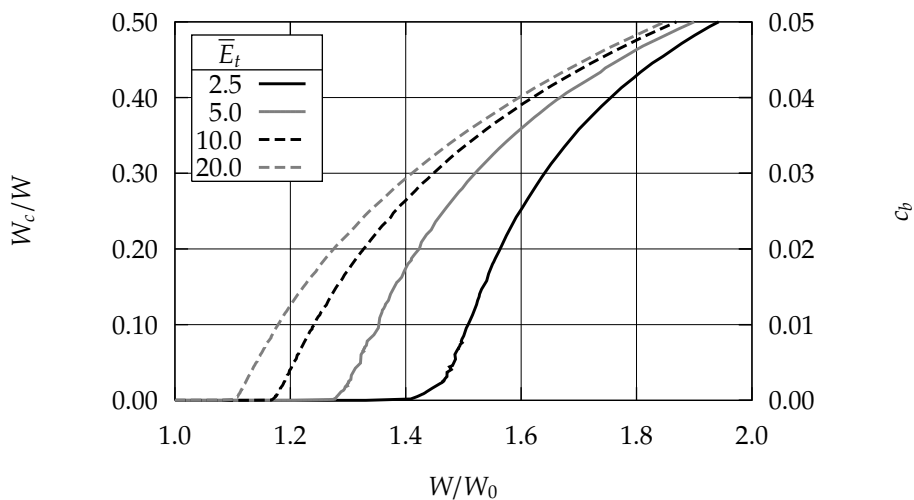


Figure 16.10: Contact load fraction W_c/W and bearing coefficient c_b versus the load W/W_0 for several track elasticities (\bar{E}_t) on a smooth track.

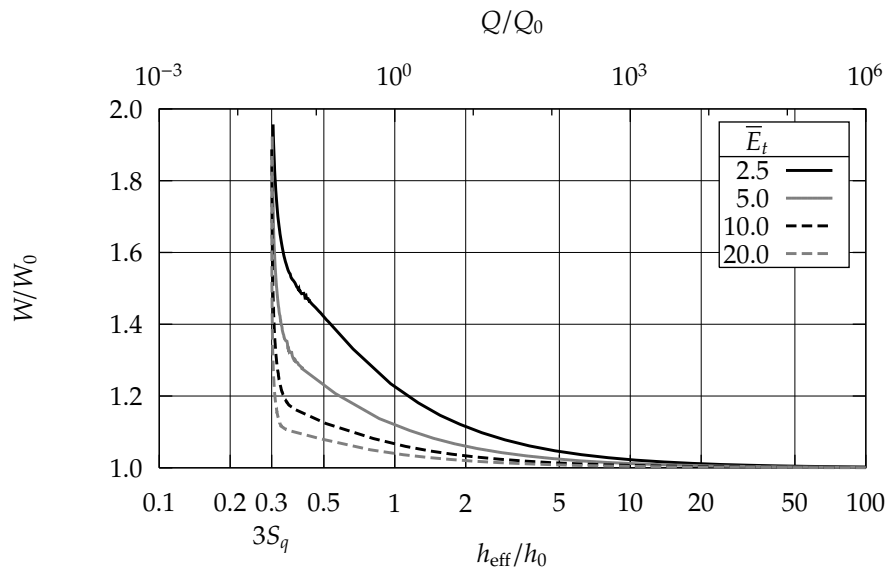


Figure 16.11: Load W/W_0 versus the effective height h_{eff}/h_0 for several track elasticities (\bar{E}_t) on a smooth track.

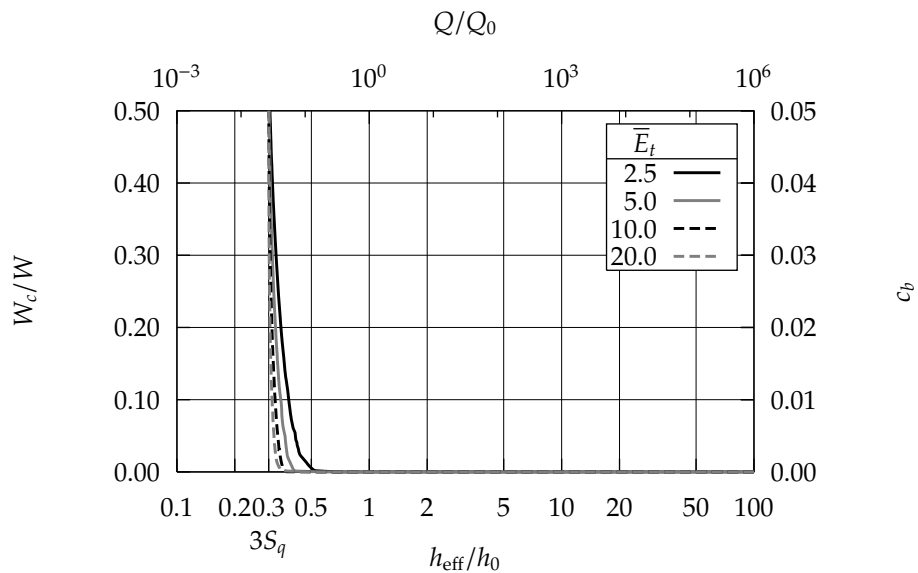


Figure 16.12: Contact load fraction W_c/W and bearing coefficient c_b versus the effective height h_{eff}/h_0 for several track elasticities (\bar{E}_t) on a smooth track.

On a non-smooth track the variation of the bearing coefficient and volume flow rate due to the different track elasticities is much less clear (figures 16.13, 16.14 and 16.15). This small variation in the results, validates the choice of the linear elastic material model in chapter 5.

The decreased effective film height at high loads is caused by the improved surface conformity due to the lower track modulus of elasticity \bar{E}_t .

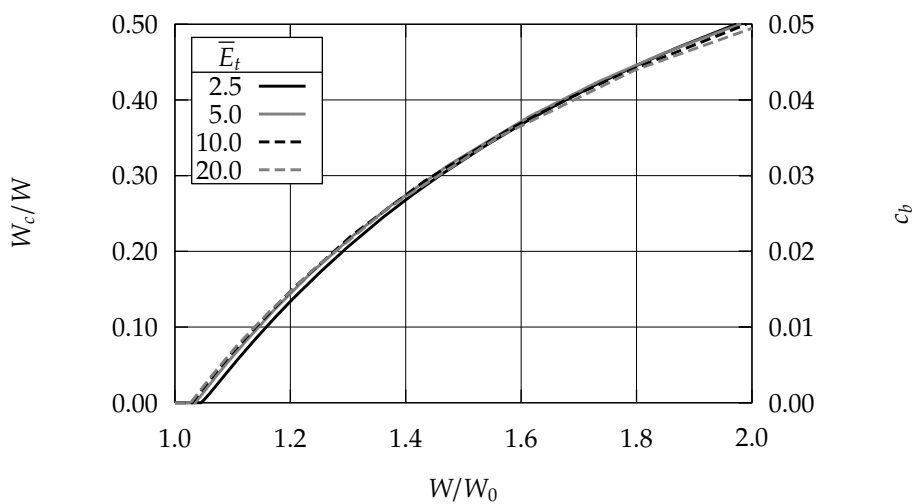


Figure 16.13: Contact load fraction W_c/W and bearing coefficient c_b versus the load W/W_0 for several track elasticities (\bar{E}_t) on a non-smooth track.

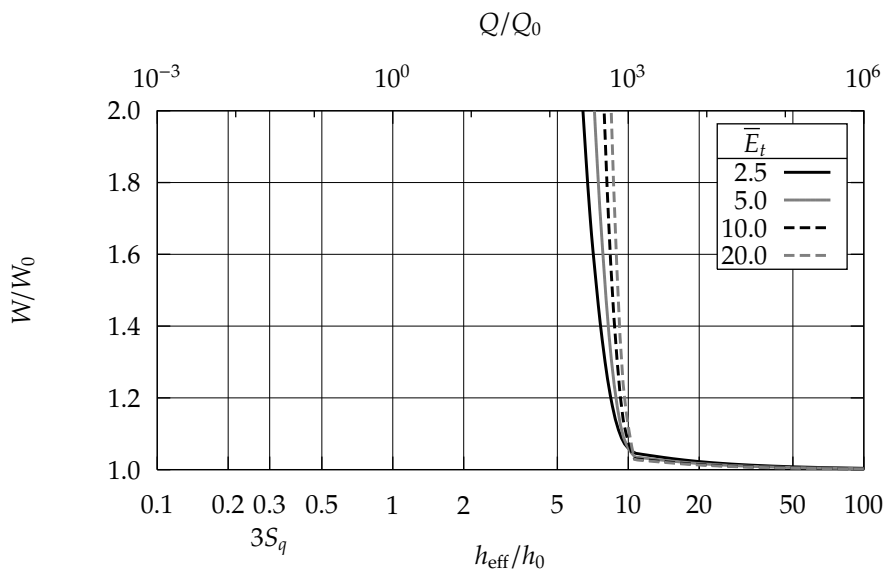


Figure 16.14: Load W/W_0 versus the effective height h_{eff}/h_0 for several track elasticities (\bar{E}_t) on a non-smooth track.

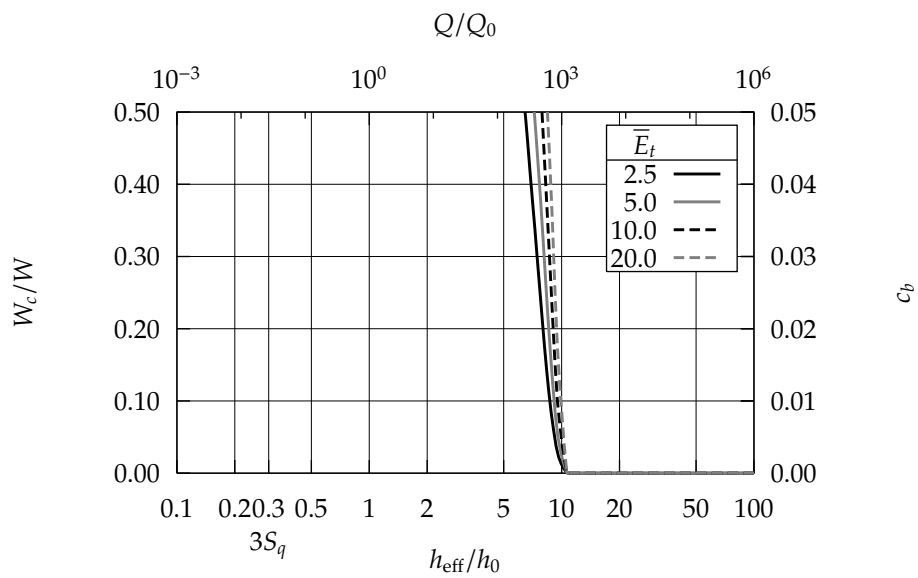


Figure 16.15: Contact load fraction W_c/W and bearing coefficient c_b versus the effective height h_{eff}/h_0 for several track elasticities (\bar{E}_t) on a non-smooth track.

CHAPTER 17

'Ideal' support

In the previous chapters the support was assumed to be a massive rubber disc, the reaction pressure of which could be calculated using the 'constant pressure' approximation. However in chapter 9 the concept of the 'ideal' support was introduced. This type of support is called 'ideal' because it exhibits a specific reaction pressure under uniform compression, that is a reaction pressure equal to the hydrostatic pressure in a parallel lubricating film. Combined with a (very) thin elastic bearing it is assumed that this will result an approximately parallel lubricating film and therefore in a low contact fraction. This hypothesis is tested in the next section.

17.1 Support type: solid or 'ideal'

The properties of a hydro-fender with a solid support are compared to those of one with an 'ideal' support. Because any improvement of the properties is especially expected for thin bearings, these calculations have not only been performed for the reference geometry but also for the hydro-fender with a thin bearing.

Figures 17.1, 17.2 and 17.3 show the results of the comparison on a plane track. The thin bearing with the solid support exhibits a higher hydrostatic load due to the elastic deformation of the bearing, however this higher load is coupled to a much higher volume flow rate. The bearing with the 'ideal' support exhibits a constant load for descending film thickness until contact occurs. At that point the contact load ratio increases. This increase is more pronounced for the thick bearing, whereas the elasticity of the thin bearing results in a more gradual increase of the contact load.

Figures 17.4, 17.5 and 17.6 show the results of the comparison on a non-smooth track. The results are comparable to those obtained on a plane track. However, the thin bearing with the 'ideal' support exhibits a constant hydrostatic load at decreasing film

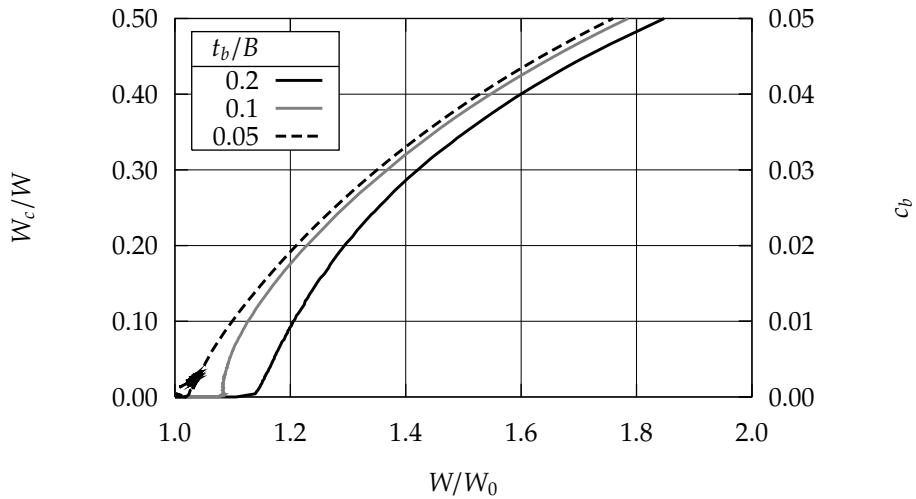


Figure 17.1: Contact load fraction W_c/W and bearing coefficient c_b versus the load W/W_0 for several bearing thicknesses (t_b) on a smooth track. The rubber support is 'ideal'.

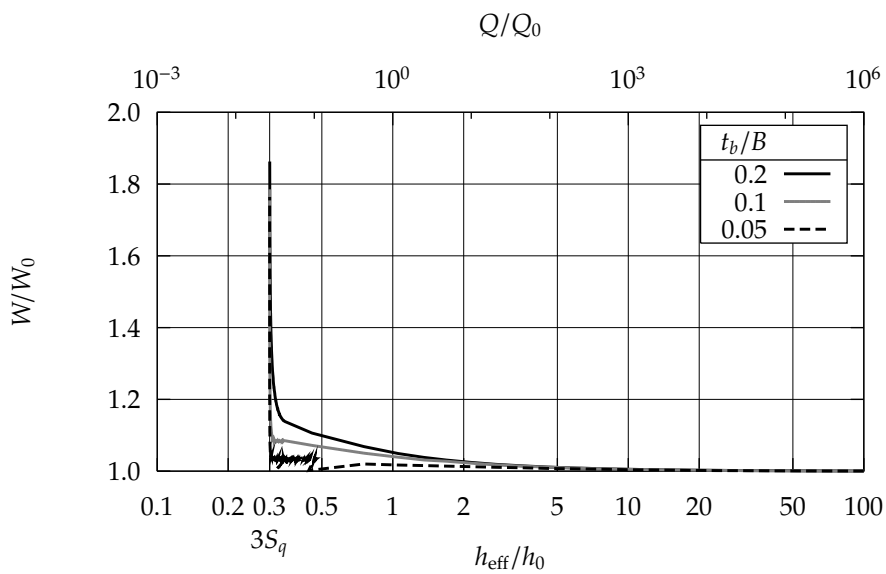


Figure 17.2: Load W/W_0 versus the effective height h_{eff}/h_0 for several bearing thicknesses (t_b) on a smooth track. The rubber support is 'ideal'.

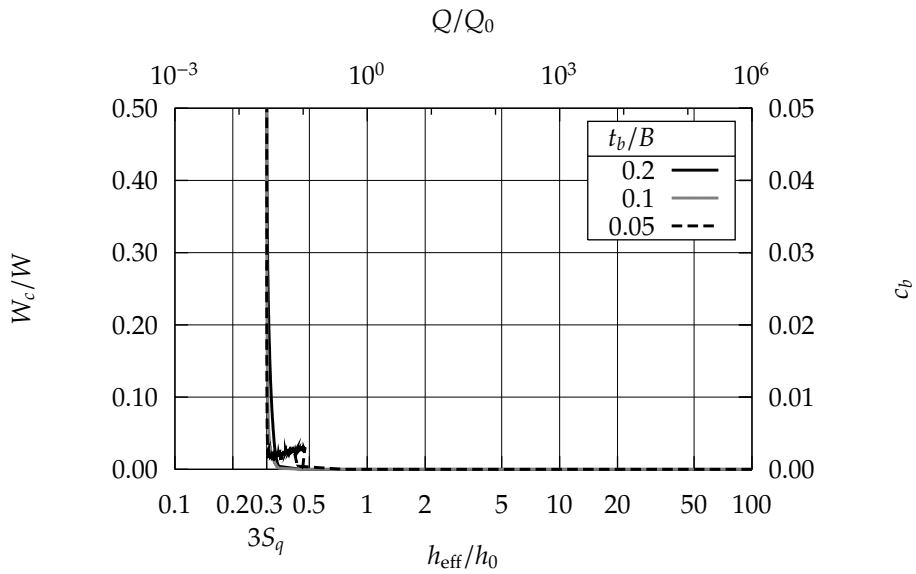


Figure 17.3: Contact load fraction W_c/W and bearing coefficient c_b versus the effective height h_{eff}/h_0 for several bearing thicknesses (t_b) on a smooth track. The rubber support is ‘ideal’.

thickness until contact occurs. This is an indication of the fact that the lubricating film remains parallel, even on a non-smooth track, due to the elastic deformation of the bearing.

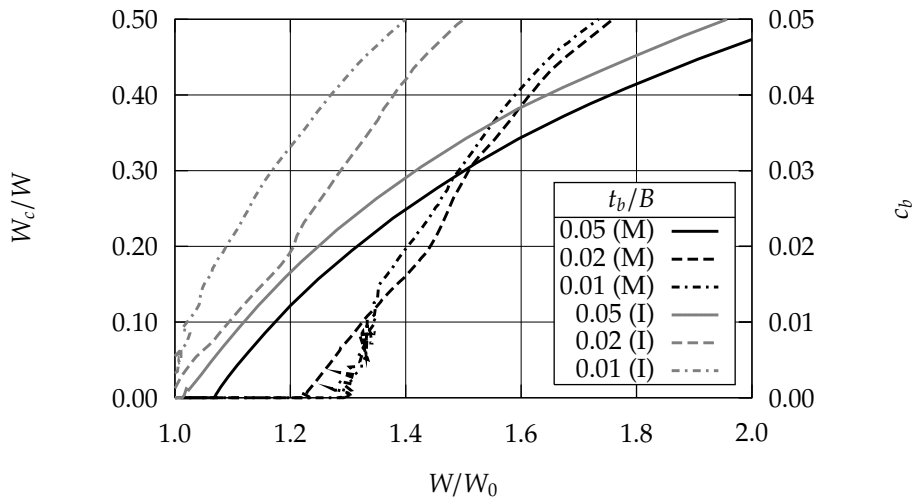


Figure 17.4: Contact load fraction W_c/W and bearing coefficient c_b versus the load W/W_0 for several bearing thicknesses (t_b) on a non-smooth track. The rubber support is ‘ideal’ (I) or massive (M).

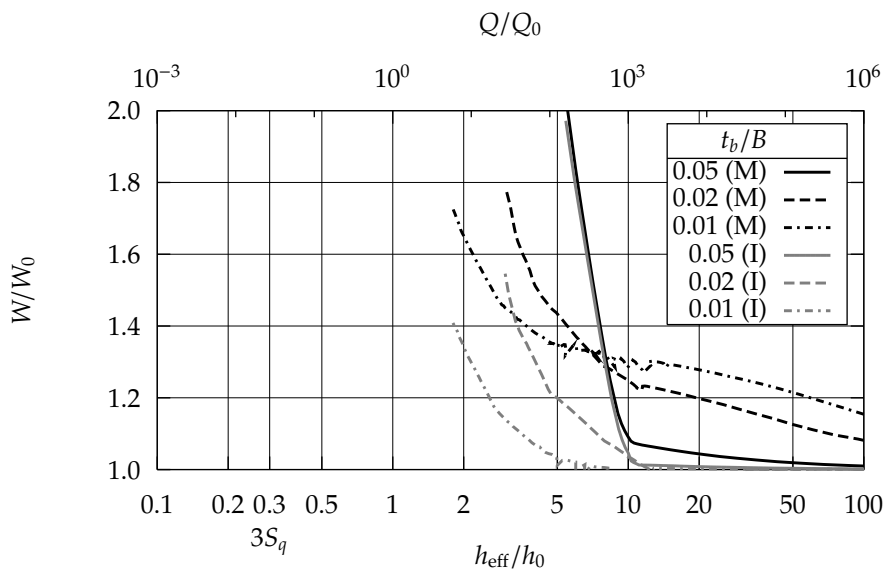


Figure 17.5: Load W/W_0 versus the effective height h_{eff}/h_0 for several bearing thicknesses (t_b) on a non-smooth track. The rubber support is 'ideal' (I) or massive (M).

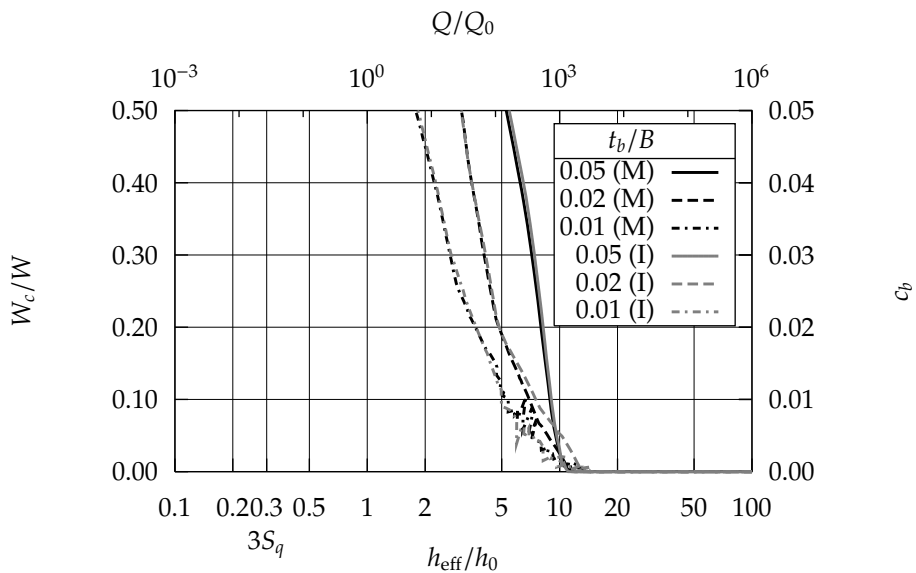


Figure 17.6: Contact load fraction W_c/W and bearing coefficient c_b versus the effective height h_{eff}/h_0 for several bearing thicknesses (t_b) on a non-smooth track. The rubber support is 'ideal' (I) or massive (M).

CHAPTER 18

Parameter study summary

The 0-recess bearing has approximately the same tilting stiffness as the 4-recess bearing, however the supply can be implemented more easily and economically: There is only 1 restrictor necessary instead of 4, and the pressure drop over this restrictor can be smaller, thus reducing the pumping power lost in the restrictor.

An accurate analytical approximation for the load carrying capability (equation 4.26) and volume flow rate (equation 4.28) for the hydro-support with rigid, plane-parallel surfaces has been developed. In figure 4.17 the dimensionless number $QB^2\eta/WH^3$ is presented for various b/B and L/B . This figure shows that for constant load the volume flow rate drops for decreasing recess width and increasing bearing length. The pumping power also decreases for increasing bearing length (see figure 4.15).

Two different bearing supports have been studied: (1) the massive rubber support with parabolically indented edges and (2) the 'ideal' support which exhibits a reaction pressure under compression equal to the hydrostatic pressure in a plane parallel lubricating film. The 'ideal' support combined with a thin bearing is able to follow track surface waviness while maintaining a low volume flow rate. The massive support combined with a thin bearing is also able to follow track surface waviness, however in this case the volume flow rate increases dramatically.

For a given load the volume flow rate is dependent on the position of the fender on the track surface waviness and of the geometry of the track surface waviness. This variation can be as high as 60% and cannot be avoided because of the fact that the track surface waviness is the result of a random process both during the initial manufacturing of the track and during the life span of the track.

The random track surface waviness has been defined using a few parameters: the maximal top to bottom height, the maximal wavelength and an attenuation parameter γ that indicates the measure with which wave components with smaller wavelengths are present in the surface waviness. A fender that is small relative to the maximal

wavelength will be able to tilt as a rigid body and follow this wavelength. In this research it is assumed that the maximal wavelength is smaller than the hydro-support.

The calculations show that the effective film height at the point of initial contact is approximately equal to the amplitude of the surface waviness, regardless of the bearing thickness and other bearing dimensions.

For a hydro-support with a thin bearing the recess is (partly) constructed in the rubber support. Experiments have shown that the hydrostatic pressure in the recess can result in an elasto-plastic buckling of the bearing, particularly if the recess has a large length/width ratio. It is recommended to interrupt the recess in the bearing periodically in order to reduce this recess length/width ratio.

The results of the calculations will be used in the next chapters to develop a design procedure for the hydro-support.

CHAPTER 19

Design tools

In this chapter the results of the previous chapters are used to develop design tools for the hydro-support. Beforehand the following observations can be made:

- For a hydro-support with a given geometry sliding on a non-smooth track and with a required load and bearing coefficient a large spread in the resulting volume flow rate ($\approx 60\%$) can be expected. This because the track surface waviness is only known in an average sense.
- Even if the track surface waviness is exactly known the different positions of the hydro-support on the track will cause a large variation of the volume flow rate.
- The bearing coefficient is virtually linear dependent on the contact force ratio.

$$c_b \approx c_f \frac{W_c}{W} \quad (19.1)$$

with c_b the bearing coefficient, c_f the coefficient of friction of the bearing/track material combination and W_c/W the contact force ratio.

- For a given recess pressure the hydrostatic load can be accurately estimated up to a contact force ratio of approximately 20%. For higher contact force ratios (and thus contact area ratios) the contact areas will influence the flow rate in the lubricating film and reduce the hydrostatic load.
- The hydrostatic load of the hydro-support with non-smooth elastic surfaces is approximately equal to that of the hydro-support with plane rigid surfaces. Because of elastic deformation of the surfaces the load can increase with approximately 30%. However this increase is only feasible for very thin bearings.

- If the designer demands a certain bearing coefficient, a constant pressure supply pump without restrictor should be used. The constant recess pressure will result in a nearly constant hydrostatic load independent of the required volume flow rate and therefore for constant load in a nearly constant contact load ratio and bearing coefficient.
- If the designer demands a certain maximum bearing coefficient, a standard supply pump with any pressure–flow rate characteristic can be used. A restrictor is here not required. The axial stiffness of the hydro–support is here primarily achieved by a variation of the contact load ratio.
- The recess width should be small ($b/B = 0.1$) in order to optimize this axial stiffness.
- The recess in a fender can be constructed as one long groove in the bearing with a depth of $5 \cdot 10^{-3}$ to $10 \cdot 10^{-3}$ m. Supply points can be positioned with regular intervals in the recess in order to provide a homogeneous supply. These supply points can be fed using one pump.
- In a very thin bearing the recess can not be constructed exclusively in the bearing but must also partly be constructed in the rubber support in order to obtain the required depth of the recess. This will result in a large loss of stiffness of the bearing and the bearing may buckle because of this hydrostatic pressure. In order to increase the buckling resistance of the bearing instead of one large supply groove a number of shorter supply grooves must be used.
- A hydro–fender with a high length/width ratio has several advantages: A smaller recess pressure and flow rate for the same load and bearing coefficient. The hydro–fender with a large length/width ratio is furthermore less susceptible to so-called ‘sprays’. A spray is a local increased flow rate due to surface damage, for instance a groove in the track.

Although a large length/width ratio has advantages, the calculations in this thesis have not been conducted for length/width ratios larger than 4. Before employing hydro–supports with a larger length/width ratio it is advisable to perform some additional physical and numerical experiments.

- A (very) thin bearing ($h_b/B < 0.02$) can follow surface waviness. However the combination of a thin bearing and a massive support leads to a large flow rate at low loads. At high loads the flow rate reduces substantially (more so than for a thick bearing).
- Application of a thin bearing does not *postpone* the inception of contact. The flow rate at the start of contact is always approximately equal to the flow rate of a bearing with parallel, rigid and plane surfaces and with a film height equal to the amplitude of the track waviness. With increased load, the flow rate drops faster for a thinner bearing.

-
- The influence of the track thickness on the results is not pronounced.
 - In chapter 4 equations have been derived for the load and flow rate of the hydro-support with parallel, plane and rigid surfaces. These results can also be used to design the hydro-fender with elastic, non-smooth surfaces.

Using these observations a design procedure for the hydro-support with elastic, non-smooth surfaces can be developed:

1. Start.
2. The designer provides the maximum W_{\max} and minimum load W_{\min} on the hydro-support, the maximum allowed bearing coefficient c_b and the expected track waviness h_{wav} .
3. Choose a track width and bearing width. A larger bearing area will result in a smaller supply pressure and flow rate. However a larger track width will increase the cost.
4. Determine the length of the hydro-fender: Choose a large bearing length/width ratio however preferably not larger than 4.
5. Determine the recess width: Choose a small recess/bearing width ratio, e.g. a ratio of 0.1.
6. Determine a bearing thickness: Here a principal choice has to be made: Do we use a thin bearing or a thick bearing. A thin bearing (bearing thickness/width ratio ≈ 0.02) is better capable to follow surface waviness and will result in a smaller flow rate at high loads, however it is more susceptible to surface damage and high contact temperatures. Furthermore an 'ideal' support should be used. A thick bearing (bearing thickness/width ratio ≈ 0.10) is more robust and has successfully been employed in the PWA-lock. However it is less capable to follow surface waviness. A standard massive support can be used.
7. Determine the hydrostatic load at maximum load and maximum bearing coefficient:

$$W_h = W_{\max} \left(1 - \frac{c_b}{c_f} \right) \quad (19.2)$$

8. If a thin bearing is used in combination with a massive support this value has to be corrected for the expected load increase due to elastic deformation:

$$W_h^* = 0.8W_h \quad (19.3)$$

Else:

$$W_h^* = W_h \quad (19.4)$$

9. Given this W_h^* , calculate the recess pressure p_r using the following equation which is derived from equation 4.26:

$$p_r = \frac{W_h^*}{B^2} \left[\frac{\pi}{4} \frac{1 - (b/B)^2}{2 \ln(B/b)} + \frac{1}{2} (L/B - 1)(1 + b/B) \right]^{-1} \quad (19.5)$$

10. Calculate the contact load W_c :

$$W_c = W_{\max} - W_h \quad (19.6)$$

11. If a thin bearing is used in combination with a massive support, calculate the effective film height h_{wav}^* using figures 14.12 or 17.6.
12. Calculate the flow rate Q using equation 4.28:

$$Q = \frac{p_r h_{\text{wav}}^3}{\eta} \left[\frac{\pi}{6 \ln(B/b)} + \frac{L/B - 1}{3(1 - (b/B))} \right] \quad (19.7)$$

13. Given the recess pressure and flow rate a supply pump can be chosen. Choose a supply pump with a constant pressure characteristic. This will reduce the influence of the surface waviness on the bearing coefficient.
14. If the difference between W_{\max} and W_{\min} is less than the contact load W_c , the hydro-support will still operate in the mixed lubrication regime at minimal load and the volume flow will remain equal. If the difference is larger, the hydro-support will operate in the full film regime and the recess pressure and flow rate can be calculated.
15. Done.

A design obtained using this design procedure can be tested and adapted using the results of numerical calculations performed with the program developed in this thesis.

In the following sections two examples of the application of the design procedure are presented.

19.1 Example I: PWA-lock

In this section the design procedure developed in the previous chapter is used to design a new hydro-support for the PWA-lock in Amsterdam. It is assumed that the track in the PWA-lock can be used but that the hydro-feet with their complex 4-recess supply with safety backup is no longer acceptable. We wish to design a 1-recess hydro-fender without restrictor.

It is assumed that the track surface waviness is equal to $0.5 \cdot 10^{-3} \text{ m/m}$ (thus an amplitude of $0.25 \cdot 10^{-3} \text{ m/m}$). The load is $250 \cdot 10^3 \text{ N}$. Furthermore assume a maximum allowed bearing coefficient of 0.005.

The design procedure of the previous chapter is used:

1. Start.
2. $W_{\max} = 250.0 \text{ kN}$, $c_b = 0.005$ and $h_{\text{wav}} = 0.25 \text{ mm}$
3. $B = 0.75 \text{ m}$
4. $L/B = 4$, $L = 3 \text{ m}$
5. $b/B = 0.1$, $b = 0.075 \text{ m}$
6. We choose a thin bearing: $h_L/B = 0.02$, $h_L = 15 \text{ mm}$
7. $W_h = 250.0(1 - 0.005/0.1) = 237.5 \text{ kN}$
8. $W_h^* = 0.8 \cdot 237.5 = 190.0 \text{ kN}$
9. $p_r = 190.0 \cdot 10^3 / (0.75^2 \cdot 1.82) = 1.856 \cdot 10^5 \text{ N/m}^2$
10. $W_c = 250.0 - 237.5 = 12.5 \text{ kN}$
11. According to 14.12 if the contact force fraction is approximately equal to 5% the effective film height reduces by 25%. Therefore the corrected h_{wav} becomes equal to $\approx 0.18 \text{ mm}$.
12. $Q = 1.856 \cdot 10^5 (0.18 \cdot 10^{-3})^3 / 0.001 \cdot 1.34 = 1.45 \cdot 10^{-3} \text{ m}^3/\text{s} = 5.2 \text{ m}^3/\text{h}$
13. The fender has a volume flow rate which is about half that of the PWA-lock hydro-foot. The recess pressure is reduced from $8 \cdot 10^5 \text{ N/m}^2$ to a very low $1.9 \cdot 10^5 \text{ N/m}^2$.

19.2 Example II: west lock Terneuzen

In this section a hydro-support is designed for the western lock in Terneuzen (the Netherlands).

The lock chamber in the western lock in Terneuzen has a width of 40 m and a length of 290 m. The maximum draught of passing ships is 12.25 m. The rolling gates in this lock are 45 m long, 7.5 m wide and 20 m high and have a weight of approximately 10^7 N . Air chambers in the lock-gate are used to reduce the weight of the lock-gate when it is submersed in water. If the gate is carried by two hydro-fenders the load on one fender is at most equal to $2.2 \cdot 10^6 \text{ N}$ and at least equal to $1.1 \cdot 10^6 \text{ N}$. This large difference

in load is caused by the large tide differences in this sea lock. It is assumed that the track surface waviness is equal to $1 \cdot 10^{-3}$ m. The maximum allowed bearing coefficient is 0.01.

The design procedure of the previous chapter is used:

1. Start.
2. $W_{\max} = 2200.0$ kN, $W_{\min} = 1100.0$ kN, $c_b = 0.01$ and $h_{\text{wav}} = 0.5$ mm
3. $B = 1.0$ m
4. $L/B = 6$, $L = 6$ m
5. $b/B = 0.1$, $b = 0.1$ m
6. We choose a very thin bearing: $h_L/B = 0.01$, $B = 10$ mm
7. $W_h = 2200.0(1 - 0.01/0.1) = 1980.0$ kN
8. $W_h^* = 0.8 \cdot 1980.0 = 1584.0$ kN
9. $p_r = 1584.0 \cdot 10^3 / (1.0^2 \cdot 2.92) = 5.425 \cdot 10^5$ N/m²
10. $W_c = 2200.0 - 1980.0 = 220.0$ kN
11. According to 14.12 if the contact force fraction is approximately equal to 10% the effective film height reduces by 60%. Therefore the corrected h_{wav} becomes equal to ≈ 0.17 mm.
12. $Q = 5.425 \cdot 10^5 (0.17 \cdot 10^{-3})^3 / 0.001 \cdot 2.08 = 5.54 \cdot 10^{-3}$ m³/s = 20.0 m³/h

The recess pressure and flow rate at this maximum load are known. The supply pump can now be selected. At minimal load this supply pump will suffice.

The operating point of the supply pump at minimal load is dependent on the characteristic of the supply pump. If we assume that there is no contact at this minimal load the recess pressure becomes:

$$p_r = 1.1 \cdot 10^6 / (1.0^2 \cdot 2.92) = 3.767 \cdot 10^5 \text{ N/m}^2 \quad (19.8)$$

Although the load is halved the variation in the recess pressure is much smaller.

The flow rate required to maintain zero contact at this minimum load is:

$$Q = 3.767 \cdot 10^5 (0.5 \cdot 10^{-3})^3 / 0.001 \cdot 2.08 = 9.79 \cdot 10^{-2} \text{ m}^3/\text{s} = 350.0 \text{ m}^3/\text{h} \quad (19.9)$$

This is an increase by approximately a factor of 20. The selected supply pump could most likely not follow this variation. The supply pump will probably provide a flow rate which is too small to prevent contact. This means that even at minimal load contact will occur, although with a smaller flow rate and bearing coefficient than at maximal load.

CHAPTER 20

Conclusion

In this thesis a model has been developed to describe the properties of a hydro-support: An elastically supported, elastic hydrostatic bearing sliding on a non-smooth elastic track with possible occurring partial contact between track and bearing. The results of this model have been compared qualitatively with experimental data from the hydro-feet in the PWA-lock and from physical model tests.

The properties of the hydro-support with plane rigid surfaces have been derived analytically.

In summary the model for the elastic bearing consists of the following parts:

Hydrostatic lubricating film Reynolds' equation with rough surfaces and partial contact.

Track Elastic deformation using thin layer model.

Bearing Elastic deformation using plate theory.

Support Massive support with a reaction pressure calculated using the constant pressure approximation or an 'ideal' support with a known reaction pressure.

Partial contact

A computer program has been developed incorporating this model. This program has been used to study the properties of a hydro-support. The following conclusions can be drawn from the results:

- The 0-recess hydro-support (or 1-recess support with a small recess width) has a tilting stiffness comparable to that of a 4-recess hydro-support.

- However, when the hydro-support is tilted or when it slides across surface waviness, the variation of the flow rate is larger for the 0-recess hydro-support than for the 4-recess hydro-support.
- The expected surface waviness of a track is only known in an average, stochastic sense. A hydro-support on different track surfaces with different surface wavinesses which are equal stochastically, exhibits very different flow rate and bearing coefficient.
- A hydro-support sliding on a non-smooth track shows large variations in flow rate and bearing coefficient.
- Therefore, the design of a hydro-support can be based on analytical formulae and rules of thumb.
- For a given load and hydro-fender width, a longer hydro-fender has a smaller flow rate, lower recess pressure and thus lower required pumping power.
- A long hydro-fender is less susceptible to 'sprays', that is variations in the flow rate due to local surface damage.
- The application of a thin bearing in combination with an 'ideal' support results in a parallel lubrication film, independent on the surface waviness.
- Buckling of a thin bearing due to the recess pressure can be prevented by using shorter interconnected recesses.
- Use of elastic surfaces (thin bearing) does not postpone contact at increased load. If the effective film height is equal to the amplitude of the surface waviness, contact occurs. However, if the load is increased further the flow rate is reduced, whereas for less elastic surfaces (thick bearing) the flow rate remains approximately equal.

Using the results of the model a design procedure has been developed to design a hydro-support.

The model and the results of the model can be used for other applications. In the next section recommendations for further study have been gathered.

20.1 Recommendations for further research

In this thesis a model has been developed to describe the behavior of a mixed lubricated hydrostatic thrust bearing with elastic surfaces. Apart from the design of hydro-supports for lock-gates, the results of this model can be used to aid in the design of highly loaded, water lubricated, linear guides where partial contact is allowed to

occur or where, due to the inevitable surface waviness, contact *will* occur. Possible applications are the guidance of ship lifts and harbor cranes.

The mathematical model itself can possibly be used in the study of other than hydrostatically lubricated bearings:

- Biological joint lubrication: The lubrication of biological joints is a complex combination of hydrodynamic lubrication and elastic surface deformation. The mixed lubrication model developed in this thesis can possibly be used here.
- Propeller shaft bearing: These bearings are usually constructed from very elastic materials. Here the model is also applicable.

The mixed lubrication model can be improved, in particular with regard to the following aspects:

- A better description of the roughness deformation and true contact area in particular for plastics.
- An integral description of partial contact and lubrication. In the model developed in this thesis, the contact and lubrication description are more or less separated. However, they are mutually dependent and a model should reflect this.
- Further physical experiments in order to study the mixed lubrication model can be used to determine the contact area ratio, the contact force ratio and other pertinent parameters. In particular the study of contact of metal/plastic combinations is interesting.

In this thesis the 'ideal' bearing support has been introduced. The 'ideal' support has a reaction pressure under compression that is equal to the hydrostatic pressure of a hydrostatic thrust bearing with rigid, plane and parallel surfaces. If this support is used, a hydro-support can be constructed with a (very) thin bearing and the hydro-support will follow surface waviness better and approximately maintain a parallel lubricating film.

Although the reaction pressure of the 'ideal' support is known, the actual geometry is not. This geometry can be determined using geometrical or topological optimization techniques with which the geometry of a machine or machine part is adapted iteratively until a certain goal function is optimized. This optimization could include the shape and depth of the recess and the shape and thickness of the bearing in order to match the elasticity of the bearing better with the reaction pressure of the support.

This optimization can be validated using physical experiments. For instance a static hydro-support can be pushed against a track with a certain surface waviness. The height distribution of the lubricating film and possible contact areas and the flow pattern from the bearing are measures of the quality of the support. If a transparent track is used the film height can be observed directly.

In this thesis a design procedure has been developed to design a hydro-support. It deserves recommendation to test the procedure further using physical experiments, especially for the hydro-fender with large bearing length/width ratio and very thin bearing.

APPENDIX A

Operation point, material properties and dimensions of the PWA-lock hydrofoot

Operating conditions:

load	W	$250.0 \cdot 10^3$	N
sliding speed	U	0.24	m/s
sliding time	t_L	100	s

Dimensions of the hydrofoot:

diameter	D	0.750	m
height	t_b	0.120	m
hydraulic diameter	D	0.740	m
hydraulic recess diameter	d	0.530	m
dam width between recesses	d_{dam}	0.050	m
supply pressure (operating point)	p_{sup}	$20.0 \cdot 10^5$	N/m ²
pressure ratio	β	0.4	–
restrictor value	γ	$0.6347 \cdot 10^{-6}$	m ⁴ /s \sqrt{N}

Properties of stainless steel (RVS 316):

specific density	ρ	$7.8 \cdot 10^3$	kg/m ³
specific heat capacity	c	$4.8 \cdot 10^2$	J/kg ^o C
heat conduction coefficient	λ	16.0	W/m ^o C
Youngs' modulus	E	$2.1 \cdot 10^{11}$	N/m ²
Poisson's ratio	ν	0.3	–

APPENDIX A. OPERATION POINT, MATERIAL PROPERTIES AND DIMENSIONS OF THE PWA-LOCK HYDROFOOT

Properties of water (at $T = 10.0^\circ\text{C}$, $p = 1.0 \cdot 10^5 \text{N/m}^2$):

specific density	ρ	1000	kg/m^3
specific heat capacity	c	$4.182 \cdot 10^3$	$\text{J/kg}^\circ\text{C}$
heat conduction coefficient	λ	0.597	$\text{W/m}^\circ\text{C}$
dynamic viscosity	η	0.001	Ns/m^2
Prandtl number	Pr	7.02	–
expansion coefficient	β	$2.0 \cdot 10^{-4}$	$1/^\circ\text{C}$

Dimensions of the rubber ring:

diameter	D_s	0.820	m
internal diameter	d_s	0.290	m
height	t_s	0.080	m
stiffness	k	$50 \cdot 10^6$	N/m
angular stiffness	k_ϕ	$1.75 \cdot 10^6$	Nm/rad

Properties of rubber:

specific density	ρ	1200	kg/m^3
specific heat capacity	c	$1.1 \cdot 10^3$	$\text{J/kg}^\circ\text{C}$
heat conduction coefficient	λ	0.15	$\text{W/m}^\circ\text{C}$
Youngs' modulus	E	$4.6 \cdot 10^6$	N/m^2
Poisson's ratio	ν	0.5	–

Dimensions of the track:

sliding distance	L	25.0	m
width	B	1.1	m
height	t_t	0.07	m
surface waviness (max)	h_{wav}	$0.7 \cdot 10^{-3}$	m/m
gate tilt (max)	dh	$2.2 \cdot 10^{-3}$	m/m

Properties of UHMWPE:

specific density	ρ	940	kg/m^3
specific heat capacity	c	$2.2 \cdot 10^3$	$\text{J/kg}^\circ\text{C}$
heat conduction coefficient	λ	0.4	$\text{W/m}^\circ\text{C}$
Youngs' modulus	E	$1.0 \cdot 10^9$	N/m^2
Poisson's ratio	ν	0.46	–
Hardness	H	$50.0 \cdot 10^6$	N/m^2
Yield stress	σ_y	$20.0 \cdot 10^6$	N/m^2

Heat transfer coefficient from the bearing to the surrounding water:

heat transfer coefficient	α	$\approx 6.0 \cdot 10^2$	$\text{W/m}^\circ\text{C}$
---------------------------	----------	--------------------------	----------------------------

Coefficient of Friction between the track and the bearing (in contact):

coefficient of friction	c_f	0.1	–
-------------------------	-------	-----	---

APPENDIX B

Bearing attitude

The angles of the bearing relative to the lock gate and relative to the track are determined by the equilibrium of the moments caused by the effective pressure (M_x, M_y), the moments caused by the friction between the bearing and the track (M_{w_x}, M_{w_y}) and the tilting moments of the rubber support (M_{s_x}, M_{s_y}):

$$M_{s_x} = M_x + M_{F_x} \quad (\text{B.1a})$$

$$M_{s_y} = M_y + M_{F_y} \quad (\text{B.1b})$$

where M_x and M_y are given by:

$$M_x = \iint_A xp \, dA \quad (\text{B.2a})$$

$$M_y = \iint_A yp \, dA \quad (\text{B.2b})$$

The measures a_x and a_y are the distances in respective the x and y -direction of the center of the load vector and the center of the bearing (figure B.1):

$$a_x = \frac{M_x}{W} \quad (\text{B.3a})$$

$$a_y = \frac{M_y}{W} \quad (\text{B.3b})$$

The eccentricity ϵ_x and ϵ_y is defined to be the dimensionless measure between the center of the load vector and the center of the bearing in x and y -direction respectively.

$$\epsilon_x = \frac{2a_x}{L} \quad (\text{B.4a})$$

$$\epsilon_y = \frac{2a_y}{B} \quad (\text{B.4b})$$

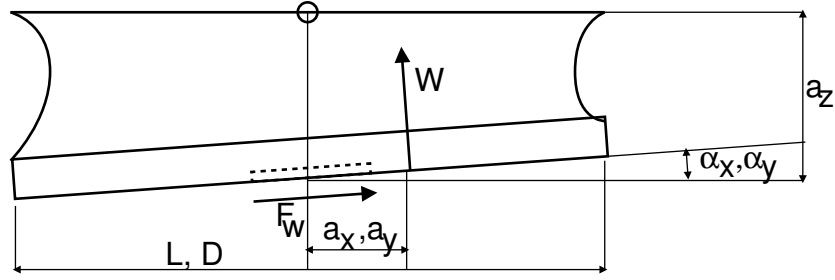


Figure B.1: Global forces operating on the bearing. The angles α_x and α_y are very small.

where L and B are the length of the hydro-support in x and y -direction respectively. An eccentricity of 0 means that the load vector goes exactly through the center of the bearing, an eccentricity of 1 means that the load vector goes through the edge of the bearing.

The moments due to friction M_{F_x} and M_{F_y} are given by:

$$M_{F_x} = F_x a_z \quad (\text{B.5a})$$

$$M_{F_y} = F_y a_z \quad (\text{B.5b})$$

where the measure a_z is the distance in z -direction between the center of the lubricating film and the interface between the support and lock-gate.

The tilting moment of the rubber support is equal to:

$$M_{s_x} = k_{s_x} (\alpha_x - \alpha_{x_0}) \quad (\text{B.6a})$$

$$M_{s_y} = k_{s_y} (\alpha_y - \alpha_{y_0}) \quad (\text{B.6b})$$

where k_{s_x} and k_{s_y} are the tilting stiffness of the rubber support, α_x and α_y the tilting angles of the bearing relative to the initial position and α_{x_0} and α_{y_0} the tilting angles of the top surface of the support relative to the initial position. This tilting angle is a result of the tilting of the lock-gate due to different water levels on both sides of the gate.

Combining equations B.1a and B.6a yields:

$$\alpha_x = (M_x + M_{F_x})/k_{s_x} + \alpha_{x_0} \quad (\text{B.7a})$$

$$\alpha_y = (M_y + M_{F_y})/k_{s_y} + \alpha_{y_0} \quad (\text{B.7b})$$

These equations can be used in order to calculate the tilting angles of the hydro-support.

APPENDIX C

Thermal effects

The bearing/track material combination chosen in the PWA-lock is stainless steel versus UHMWPE. The coefficient of friction of this material combination under wet conditions is approximately 0.1 (HONSELAAR, 1993).

Under normal operating conditions the actual bearing coefficient is much lower than this coefficient of friction, due to the load carried by the hydrostatic pressure and the negligible hydrostatic traction. The heat generated in the bearing/track interface can then easily be transported to the surrounding water. However, if the supply pump has failed and the lock-gate has to be moved without hydrostatic lubrication, the heat generated is much larger and cannot be transported away very easily because there is no forced water flow. In this situation excessive temperature rise in the bearing and track could pose a problem.

In order to calculate the temperature in a complex geometry the so-called 'thermal network method' can be used. This method first introduced by BLOK (1963) and more recently used by VAN OSTAYEN (1988) is based on the analogue between temperature and heat flow on one hand and electric potential and current on the other. A machine is modelled using lumped heat capacities connected by resistors and sources. The resulting thermal network can then be analyzed using methods and computer programs developed for electrical networks. More recently the 'extended thermal network method' was introduced in which general n-node instead of standard 2-node components are used to model the heat flow in machine components.

The development of a thermal network of a complex machine or geometry requires either the use of many small components (resulting in a model comparable to one obtained using a finite element or difference method) or the use of a few but well chosen large components. The advantage of the thermal network method is based in this last approach: using a small network that enables the designer to study the temperature distribution in a construction and the influence of parameters quickly.

In the following sections four different models of the heat flow from the bearing/track interface are presented and used to calculate the temperature rise in the bearing of the PWA-lock.

The temperature rise can be estimated using a number of methods:

Model I: Adiabatic track model.

Model II: Flash temperature model.

Model III: Dutch Department of Public Works model: R.W.S. M870310 (Ros, 1987b).

Model IV: Modified Dutch Department of Public Works model: R.W.S. M870310.

An important aspect of the heat flow from the bearing is the heat transfer coefficient from the bearing surface to the surrounding water. This coefficient is studied in the next section.

C.1 Heat transfer coefficient

The temperature rise in the bearing is determined by two factors viz. the heat production in the bearing/track interface and the heat transport from this interface to the surroundings. The heat transport is partly composed of convective heat transport from the bearing to the ambient water.

In general the heat flow by convection from a warm body to a cooler ambient medium is given by:

$$Q = \alpha A(T - T_a) \tag{C.1}$$

where:

Q	total heat flow	W
α	heat transfer coefficient	W/m ² K
A	surface area of the body	m ²
T	temperature of the body	K
T_a	ambient temperature	K

The heat transfer coefficient α in equation C.1 is dependent on the geometry of the body and the material properties and velocity of the ambient medium. Heat transfer by convection is primarily driven by the velocity with which the ambient medium flows around the body. If this velocity is directly the result of the heat flow itself due to density differences as a result of temperature differences, then this heat flow is caused by 'free' convection. If the ambient medium velocity has an external cause, the heat flow is caused by 'forced' convection.

In general the heat transfer coefficient α of free convection is calculated using (WONG, 1977):

$$Nu = C(GrPr)^n K \quad (C.2)$$

where:

$$\begin{array}{lll} Nu & \text{Nusselt number} & \frac{\alpha D}{\lambda} \\ Gr & \text{Grasshof number} & \frac{g\beta\rho^2\Delta TD^3}{\eta^2} \\ Pr & \text{Prandtl number} & \frac{\eta c}{\lambda} \end{array}$$

and where C , n and K are dependent on the body geometry and:

α	heat transfer coefficient	W/m ² K
D	diameter	m
λ	heat conduction coefficient	W/mK
g	acceleration due to gravity	m/s ²
β	coefficient of thermal expansion	1/K
ρ	mass density	kg/m ³
ΔT	temperature difference between body and ambient fluid	K
η	dynamic viscosity	Ns/m ²
c	specific heat capacity	W/kgK

For the free convection from a vertical cylinder the values of C , n and K are:

$$\begin{array}{ll} C & 0.8 \\ n & 0.25 \\ K & \left(1 + \left(1 + \frac{1}{\sqrt{Pr}}\right)^2\right)^{-0.25} \end{array}$$

The heat transfer coefficient α for forced convection by a cylinder is given by (WONG, 1977):

$$Nu = 0.43 + CRe^n Pr^{0.31} \quad (C.3)$$

where:

$$\begin{array}{lll} Re & \text{Reynolds number} & \frac{\rho UD}{\eta} \\ C & 0.0208 \\ n & 0.814 \end{array}$$

This equation is used to calculate the heat transfer coefficient α from the hydro-foot in the PWA-lock. This hydro-foot has an average diameter of 0.785 m. Values for other pertinent parameters can be found in appendix A. The heat transfer coefficient α is calculated using equation C.3 and the values for the different properties as found in appendix A and is found to be approximately equal to 600.0 W/mK. This value will be used in subsequent calculations.

C.2 Model I: Adiabatic track model

If the hydrostatic water supply is off, the bearing is poorly cooled. The bearing is supported on the top surface by a material with a very low heat conductance viz. rubber. The bottom surface of the bearing rests on an UHMWPE track which also conducts heat poorly. Only the edge of the bearing is directly in contact with water. We can now model the heat transport from the bearing/track interface to the ambient water using these assumptions:

- All heat generated in the bearing/track interface is transported from the bearing by forced convection to the ambient water.
- The temperature difference in the bearing is negligible. (The heat conduction in the bearing is much larger than the heat convection from the surface.)

Then the bearing temperature is described by this differential equation:

$$\rho c A t_b \frac{dT}{d\tau} + \alpha O t_b (T - T_a) = c_b W U \quad (\text{C.4a})$$

with initial condition:

$$T(0) = T_a \quad (\text{C.4b})$$

where:

T	temperature of the bearing	°C
τ	time	s
A	surface area of the bearing	m ²
O	circumference of the bearing	m
h	height of the bearing	m
ρ	specific density of the bearing material	kg/m ³
c	heat capacity of the bearing material	J/kg°C
α	heat transfer coefficient from the bearing to the ambient water	W/m°C
T_a	temperature of the ambient water	°C
c_b	bearing coefficient between the bearing and the track	
W	load on the bearing	N
U	sliding speed of the bearing	m/s

The solution to differential equation C.4a is:

$$T(\tau) = T_a + T_{\max} (1 - e^{-\tau/\tau_c}) \quad (\text{C.5a})$$

with the asymptotic maximum temperature T_{\max} :

$$T_{\max} = \frac{c_b W U}{\alpha O t_b} \quad (\text{C.5b})$$

and the time constant τ_c :

$$\tau_c = \frac{\rho c A t_b}{\alpha O t_b} \quad (\text{C.5c})$$

Figure C.1 shows this temperature rise versus the time.

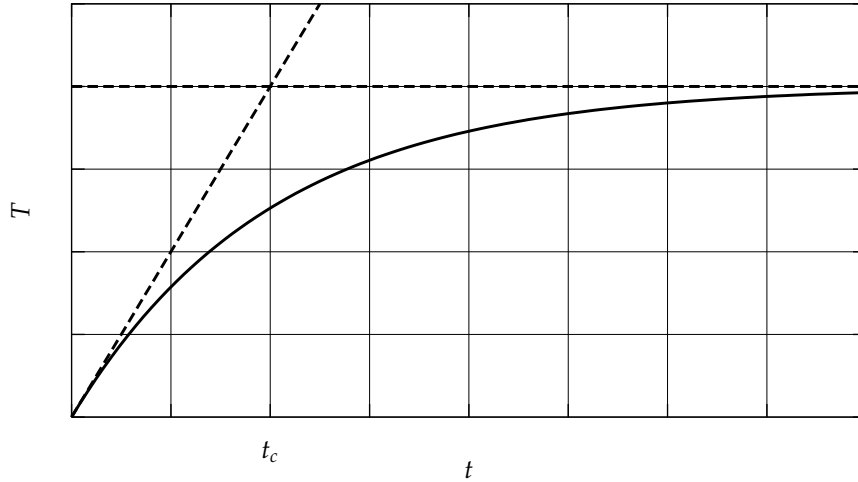


Figure C.1: Temperature rise in the bearing versus time. Method I: Isolated track, uniform bearing temperature and convection from the bearing.

If it assumed that the sliding velocity of the bearing is constant for the total length of the sliding track then:

$$U = \frac{L}{\tau_L} \quad (\text{C.6})$$

where:

- L total sliding distance m
- τ_L time required for total sliding distance s

and the temperature T_L at the end of the total sliding distance L becomes:

$$T_L = T(\tau_L) = T_a + T_{\max} (1 - e^{-\tau_L/\tau_c}) \quad (\text{C.7})$$

with the asymptotic maximum temperature T_{\max} now given by:

$$T_{\max} = \frac{c_b W L}{\alpha O t_b \tau_L} \quad (\text{C.8})$$

If the total sliding time τ_L is much less than the time constant τ_c the end temperature T_L can be approximated by:

$$T_L = T_a + \frac{c_b W L}{\rho c A t_b} \quad (\text{C.9})$$

Note that in this case the end temperature T_L is dependent on the sliding distance L , not on the sliding speed U . Furthermore, the end temperature is not dependent on the heat transfer coefficient α .

The following conclusions can be drawn from the results of this model:

- Because both the heat capacity and the cooling surface increase linearly with the bearing height, the time constant τ_c is independent on the bearing height.
- However, the asymptotic maximum temperature T_{\max} is dependent on the bearing height.

The results of this model are applied on the hydro-foot of the PWA-lock. The temperature rise in the bearing follows from:

$$T(\tau) = 10.0 + \frac{4.22}{t_b} (1.0 - e^{-t_b\tau/1225}) \quad (\text{C.10})$$

The values for all pertinent parameters can be found in appendix A. Table C.1 shows the end temperature T_L for different values of the bearing height t_b . Figure C.2 shows

t_b (m)	T_1 (°C)
0.120	12.8
0.100	13.3
0.050	16.6
0.010	43.1
0.005	76.2

Table C.1: Temperature rise in the bearing of the PWA-lock after 1 movement, calculated for different bearing thicknesses using method I: Isolated track, uniform bearing temperature and convection from the bearing.

the temperature rise in the bearing versus the sliding time for a bearing height of 0.12 m. Due to the fact that the sliding time $\tau_L = 100$ s is so much smaller than the time constant $\tau_c \approx 1200$ s the temperature is still rising linearly.

C.3 Model II: Flash temperature model

In the previous model the track was assumed to be perfectly isolating. But although the track has a very low heat conductance coefficient heat can be transported to the track in that during sliding ‘new’ cold track material is transported into the bearing/track interface and ‘old’ warm material is transported out.

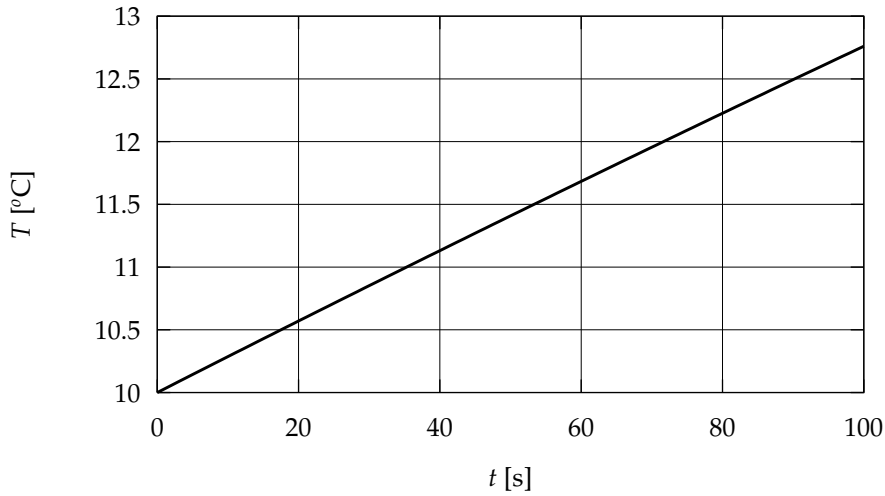


Figure C.2: Temperature rise in the bearing versus time. Method I: Isolated track, uniform bearing temperature and convection from the bearing. Dimensions according to the PWA-lock.

If the Peclet number is high enough ($Pe > 10$), the flash temperature model can be used to calculate the heat flow to the track. The Peclet number is given by:

$$Pe = \frac{\rho c U D}{2\lambda} \quad (\text{C.11})$$

with:

ρ	specific density of the track material	kg/m ³
c	heat capacity of the track material	J/kgK
U	sliding speed of the bearing on the track	m/s
D	diameter of the bearing	m/s
λ	heat conduction coefficient of the track material	W/mK

The Peclet number for the hydro-foot in the PWA-lock is approximately equal to $4.7 \cdot 10^5$ and thus certainly high enough. Assuming a constant heat generation in the bearing/track interface, the average contact temperature is equal to (Bos, 1995):

$$T = \frac{32 \sqrt{2} \Gamma(\frac{3}{4})}{5\pi^2 \Gamma(\frac{1}{4})} \frac{2}{\lambda D \sqrt{Pe}} Q = \frac{0.619910}{\lambda D \sqrt{Pe}} Q \quad (\text{C.12})$$

where:

T	temperature of the track	°C
Q	heat flow in the track	W
D	diameter of the bearing	m

If we assume (like in the previous model) that the bearing temperature is uniform, the following differential equation can be found for the heat generation in the bearing/track

interface and the heat transported by convection from the bearing to the ambient water and to the track:

$$\rho c A t_b \frac{dT}{d\tau} + \left(\alpha O t_b + \frac{\lambda D \sqrt{Pe}}{0.619910} \right) (T - T_a) = c_b W U \quad (C.13)$$

The solution to this equation is:

$$T(\tau) = T_a + T_{\max} (1 - e^{-\tau}) \quad (C.14)$$

with the asymptotic maximum temperature T_{\max} :

$$T_{\max} = \frac{c_b W U}{\alpha O t_b + \frac{\lambda D \sqrt{Pe}}{0.619910}} \quad (C.15)$$

and time constant τ_c :

$$\tau_c = \frac{\rho c A t_b}{\alpha O t_b + \frac{\lambda D \sqrt{Pe}}{0.619910}} \quad (C.16)$$

The results of this model are applied on the hydro-foot of the PWA-lock. The values for all pertinent parameters can be found in appendix A. Table C.2 shows the end temperature T_L for different values of the bearing height t_b . Due to the heat transport to the track the temperature rise remains limited, even for very thin bearings. Figure C.3

t_b (m)	T_2 (°C)
0.120	12.5
0.100	12.7
0.050	13.2
0.010	13.6
0.005	13.7

Table C.2: Temperature rise in the bearing of the PWA-lock after 1 movement, calculated for different bearing thicknesses using method II: Flash temperature track, uniform bearing temperature and convection from the bearing.

shows the temperature rise in the bearing versus the sliding time for a bearing height of 0.12 m.

C.4 Model III: Dutch Department of Public Works model

In a study performed by the Dutch Department of Public Works (Ros, 1987b) a method is presented to calculate the temperature rise in sliding supports.

$$\Delta T = \frac{c_b p U}{A + B + C} \quad (C.17)$$

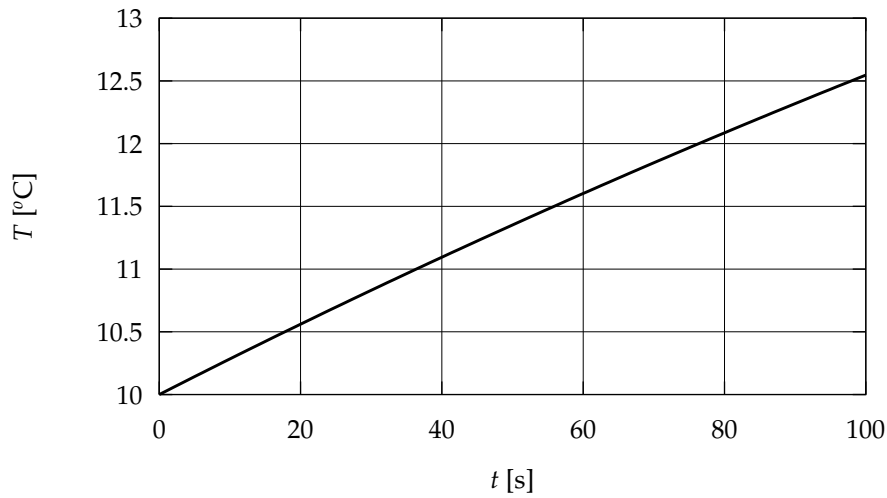


Figure C.3: Temperature rise in the bearing versus time. Method II: Flash temperature track, uniform bearing temperature and convection from the bearing. Dimensions according to the PWA-lock.

In this method the temperature rise is the result of the heat generation per surface area and the sum of three different heat transports:

- through the bearing into the gate (term A).
- through the track into the foundation (term B).
- from the bearing and track to the ambient water (term C).

This model is also applied on the hydro-foot of the PWA-lock. Table C.3 shows the end temperature T_L for different values of the bearing height t_b . Figure C.4 shows the

t_b (m)	T_3 (°C)	A (W/m ² °C)	B (W/m ² °C)	C (W/m ² °C)	$f p v$ (W/m ²)
0.120	32.6	436.7	51.3	83.6	12913.7
0.100	32.6	436.7	51.3	83.6	12913.7
0.050	32.6	436.7	51.3	83.6	12913.7
0.010	104.4	1.8	51.3	83.6	12913.7
0.005	151.7	1.8	5.7	83.6	12913.7

Table C.3: Temperature rise in the bearing of the PWA-lock after 1 movement, calculated for different bearing thicknesses using method III: Department of Public Works method.

temperature rise in the bearing versus the sliding time for a bearing height of 0.12 m. Noteworthy is the large difference in temperature rise between this and the previous methods. All these methods are approximations with justifiable assumptions. Further

research is required to compare all methods and determine the best. This last method has been evaluated against the results of temperature measurements in several locks and other public water works by Ros (1997).

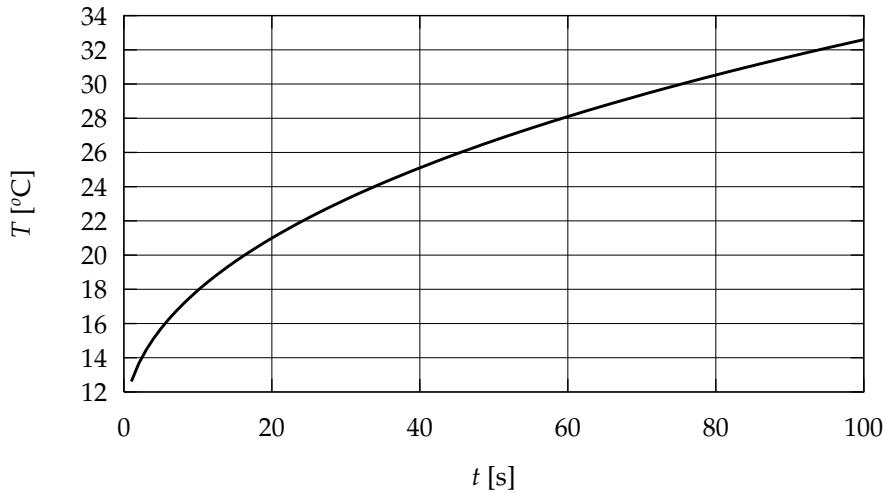


Figure C.4: Temperature rise in the bearing versus time. Method III: Department of Public Works method. Dimensions according to the PWA-lock.

C.5 Model IV: Modified Dutch Department of Public Works model

As mentioned previously, the model used in the previous section takes three heat flows from the bearing/track interface into account. Part C, that is the heat flow to the ambient water, does not take the extra heat resistance due to convection into account. If this resistance is taken into account part C can be written as:

$$C' = \frac{4\lambda_s\alpha_s}{b_s\alpha_s + \lambda_s} + \frac{4\lambda_b\alpha_b}{b_s\alpha_b + \lambda_b} \quad (\text{C.18})$$

This model is also applied on the hydro-foot of the PWA-lock. Table C.3 shows the end temperature T_L for different values of the bearing height h . The modification only slightly increases the calculated temperatures. Figure C.5 shows the temperature rise in the bearing versus the sliding time for a bearing height of 0.12 m.

t_b (m)	T_4 (°C)	A (W/m ² °C)	B (W/m ² °C)	C' (W/m ² °C)	$c_b p v$ (W/m ²)
0.120	32.7	436.7	51.3	80.9	12913.7
0.100	32.7	436.7	51.3	80.9	12913.7
0.050	32.7	436.7	51.3	80.9	12913.7
0.010	106.3	1.8	51.3	80.9	12913.7
0.005	156.0	1.8	5.7	80.9	12913.7

Table C.4: Temperature rise in the bearing of the PWA-lock after 1 movement, calculated for different bearing thicknesses using method IV: Modified Department of Public Works method.

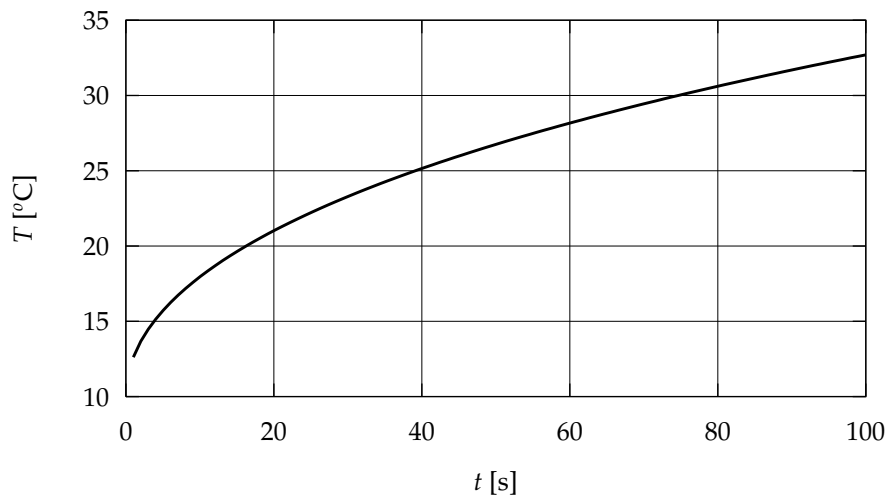


Figure C.5: Temperature rise in the bearing versus time. Method IV: Modified Department of Public Works method. Dimensions according to the PWA-lock.

C.6 Conclusion

In the previous sections 4 methods to calculate the temperature rise in the bearing have been presented and applied on the hydro-foot of the PWA-lock (table C.5). The following observations can be made:

- The results from methods I and II differ substantially with those from methods III and IV.
- The assumption of the uniform bearing temperature probably in the first two methods probably leads to a strong underestimation of the maximum temperature rise.
- Methods III and IV both give similar results, however the model used in method IV is more realistic in that it takes the convection from the bearing to the ambient water into account and should be preferred.

t_b (m)	T_1 (°C)	T_2 (°C)	T_3 (°C)	T_4 (°C)
0.120	12.8	12.5	32.6	32.7
0.100	13.3	12.7	32.6	32.7
0.050	16.6	13.1	32.6	32.7
0.010	43.1	13.6	104.4	106.3
0.005	76.2	13.7	151.7	156.0

Table C.5: Temperature rise in the bearing of the PWA–lock after 1 movement, calculated for different bearing thicknesses using four different methods: (I) Isolated track, (II) Flash temperature in track, (III) Department of Public Works method and (IV) Modified Department of Public Works method.

- All methods show that the temperature rise in the bearing of the PWA–lock will remain acceptable for a nominal sliding speed of 0.24m/s.
- However for a thin bearing the temperature could increase to an unacceptable level, depending on the temperature model used.

APPENDIX D

Matrices for the Lee–Ren contact model

According to the model developed by LEE AND REN (1996), the true contact area \bar{a}_c in a linear elasto–plastic contact is approximately equal to:

$$\bar{a}_c(\gamma, \mathcal{H}, \mathcal{P}_c) = \sum_{i=1}^4 \left\{ \gamma_A^T [A_i] \vec{\mathcal{H}} \right\} \mathcal{P}_c^i \quad (\text{D.1a})$$

and the average gap:

$$\frac{h_t(\gamma, \mathcal{H}, \mathcal{P}_c)}{S_q} = \exp \left\{ \sum_{i=0}^4 \left\{ \gamma_G^T [G_i] \vec{\mathcal{H}} \right\} \mathcal{P}_c^i \right\} \quad (\text{D.1b})$$

with:

$$\mathcal{H} = \frac{2.3 H \beta_x}{\pi E^* S_q} \quad (\text{D.2a})$$

$$\mathcal{P}_c = \frac{2.3 p_c \beta_x}{\pi E^* S_q} \quad (\text{D.2b})$$

and:

$$\vec{\mathcal{H}}^T = [1 \quad \mathcal{H}^{-1} \quad \mathcal{H}^{-2} \quad \mathcal{H}^{-3}] \quad (\text{D.3a})$$

$$\gamma_G^T = [1 \quad \gamma^{-1} \quad \gamma^{-2} \quad \gamma^{-3}] \quad (\text{D.3b})$$

$$\gamma_A^T = [1 \quad \gamma \quad \gamma^2 \quad \gamma^3] \quad (\text{D.3c})$$

and $[A_i], [G_i]$ are matrices filled with constants obtained from curve–fits of the numerical results (For the meaning of the other parameters see chapter 6):

$$\begin{aligned}
 [A_1] &= \begin{bmatrix} 0.634194 & 0.797009 & 0.0368068 & -0.00251425 \\ 0.264131 & -0.185350 & 0.0394701 & -0.00224875 \\ -0.0221767 & 0.0270835 & -0.00742716 & 0.000476956 \\ 0.000480603 & -0.00140638 & 0.00048871 & -0.0000337939 \end{bmatrix} \\
 [A_2] &= \begin{bmatrix} 0.0499357 & -1.33543 & 0.187274 & 0.00479131 \\ -0.241847 & 0.126789 & -0.00294979 & -0.00214404 \\ 0.0136548 & -0.0288007 & 0.0119597 & -0.000609812 \\ -0.0000429514 & 0.00241445 & -0.00159465 & 0.0000917852 \end{bmatrix} \\
 [A_3] &= \begin{bmatrix} -0.0316164 & -0.269988 & 1.79345 & -0.191299 \\ 0.105423 & 0.0902839 & -0.35851 & 0.00860216 \\ -0.0125309 & 0.0120455 & 0.037043 & 0.000706022 \\ 0.000847682 & -0.00240249 & -0.00070782 & 0.000033669 \end{bmatrix} \\
 [A_4] &= \begin{bmatrix} 0.00154307 & 0.111076 & -0.103494 & -0.682262 \\ -0.0331588 & 0.0626379 & -0.186875 & 0.318173 \\ 0.00739703 & -0.0261484 & 0.0532698 & -0.0663717 \\ -0.000583331 & 0.00225497 & -0.00388204 & 0.0040656 \end{bmatrix} \\
 [G_0] &= \begin{bmatrix} 0.157664 & 0.181151 & -0.0835912 & 0.00454632 \\ 0.0989399 & 0.646938 & -0.0853002 & 0.00470051 \\ 0.438505 & -1.85392 & 0.278706 & -0.0157258 \\ -0.329879 & 1.19535 & -0.189829 & 0.010696 \end{bmatrix} \\
 [G_1] &= \begin{bmatrix} -7.91316 & -2.57655 & 0.424767 & 0.0741555 \\ 12.5775 & -16.2802 & 0.584956 & -0.110785 \\ -20.9181 & 38.5601 & -1.26560 & 0.233084 \\ 11.7943 & -23.8217 & 0.778508 & -0.1262 \end{bmatrix} \\
 [G_2] &= \begin{bmatrix} 5.19985 & 8.40891 & 5.36848 & -1.39201 \\ -7.51450 & -14.1747 & 23.1057 & 1.33724 \\ 13.4070 & 11.8043 & -58.1436 & -2.80938 \\ -8.01481 & -3.44203 & 36.8180 & 1.48317 \end{bmatrix} \\
 [G_3] &= \begin{bmatrix} -4.45237 & 8.49363 & -25.8823 & -4.0968 \\ 12.9952 & -55.0575 & 97.4646 & -20.4623 \\ -24.3417 & 109.305 & -158.235 & 48.9041 \\ 13.7624 & -61.1458 & 81.2964 & -29.7077 \end{bmatrix} \\
 [G_4] &= \begin{bmatrix} 0.915562 & -1.24212 & -0.871681 & 12.6861 \\ -1.76901 & -0.234225 & 31.7258 & -64.918 \\ 3.33112 & -1.52263 & -57.7290 & 100.734 \\ -1.86588 & 0.949425 & 31.9972 & -51.5477 \end{bmatrix}
 \end{aligned} \tag{D.4}$$

$$\begin{aligned}
 [G_2] &= \begin{bmatrix} 5.19985 & 8.40891 & 5.36848 & -1.39201 \\ -7.51450 & -14.1747 & 23.1057 & 1.33724 \\ 13.4070 & 11.8043 & -58.1436 & -2.80938 \\ -8.01481 & -3.44203 & 36.8180 & 1.48317 \end{bmatrix} \\
 [G_3] &= \begin{bmatrix} -4.45237 & 8.49363 & -25.8823 & -4.0968 \\ 12.9952 & -55.0575 & 97.4646 & -20.4623 \\ -24.3417 & 109.305 & -158.235 & 48.9041 \\ 13.7624 & -61.1458 & 81.2964 & -29.7077 \end{bmatrix} \\
 [G_4] &= \begin{bmatrix} 0.915562 & -1.24212 & -0.871681 & 12.6861 \\ -1.76901 & -0.234225 & 31.7258 & -64.918 \\ 3.33112 & -1.52263 & -57.7290 & 100.734 \\ -1.86588 & 0.949425 & 31.9972 & -51.5477 \end{bmatrix}
 \end{aligned} \tag{D.5}$$

- ABT-WEST. *Resultaten Beoordeling Proefbalk Oranjesluizen. Technical report*, Adviesbureau voor Bouwtechniek B.V. (1991). In dutch.
- XIAOLAN AI and HERBERT S. CHENG. A transient EHL analysis for line contacts with measured surface roughness using multigrid technique. *Journal of Tribology*, 116:549–558 (1994).
- XIAOLAN AI, HERBERT S. CHENG, DONGYUN HUA, K. MOTEKI, and S. AOYAMA. A finite element analysis of dynamically loaded journal bearings in mixed lubrication. *Tribology Transactions*, 41(3):273–281 (1998).
- M.H. ALIABADI and C. ALESSANDRI, editors. *Contact Mechanics II: Computational Techniques*. Computational Mechanics Publications, Southampton (1995).
- M.H. ALIABADI and C.A. BREBBIA, editors. *Contact Mechanics: Computational Techniques*. Computational Mechanics Publications, Southampton (1993).
- J.F. ARCHARD. Surface topography and tribology. *Tribology International*, 7(10):213–220 (1974).
- G.C. AVONTUUR. *Indrukking UHMW-PE: Correctiefactoren. Technical report*, Bouwdienst Rijkswaterstaat (1993). In dutch.
- BAKKER-RUBBER. *Test Resultaten Vaste Voeten. Technical Report KBR ED 94008*, Bakker Rubber (1994). In dutch.
- T.S. BARRETT, G.W. STACHOWIAK, and A.W. BATCHELOR. Effect of roughness and sliding speed on the wear and friction of ultra-high molecular weight polyethylene. *Wear*, 153:331–350 (1992).
- R. BASSANI and B. PICCIGALLO. *Hydrostatic Lubrication*. Elsevier (1992). ISBN 0-444-88498-X.

BIBLIOGRAPHY

- ROBERTO BASSANI. Hydrostatic Systems Supplied through Flow Dividers. *Tribology International*, 34:25–38 (2001).
- KLAUS-JÜRGEN BATHE. *Finite Element Procedures*. Prentise Hall (1996). ISBN 0-13-301458-4.
- A. VAN BEEK. *Analysis of Rubber Supported Hydrostatic Bearing systems with Elastic Bearing Surfaces*. Ph.D. thesis, University of Technology Delft (1995).
- A. VAN BEEK and H. DAANE. Hydrostatische lagers voor sluisdeuren. *de Constructeur*, pages 44–47 (1995). In dutch.
- A. VAN BEEK and L. LEPIC. Rubber supported hydrostatic thrust bearings with elastic bearing surfaces of infinite length. *Wear*, 201:45–50 (1996).
- A. VAN BEEK and R.A.J. VAN OSTAYEN. Analytical solution for tilted hydrostatic multi-pad thrust bearings of infinite length. *Tribology International*, 30(1):33–39 (1997).
- A. VAN BEEK and A. SEGAL. Het effect van scheefstelling op de lagerkentallen van het hydrostatisch cirkelvormig axiaal lager. *de Constructeur*, pages 50–59 (1991). In dutch.
- A. VAN BEEK and A. SEGAL. Numerical solution for tilted hydrostatic multi-pad thrust bearings of finite length. *Tribology International*, 30(1):41–46 (1997a).
- A. VAN BEEK and A. SEGAL. Rubber supported hydrostatic thrust bearings with rigid bearing surfaces. *Tribology International*, 30(1):47–52 (1997b).
- J.S. BERGSTRÖM, S.M. KURTZ, C.M. RIMNAC, and A.A. EDIDIN. Constitutive modeling of ultra-high molecular weight polyethylene under large-deformation and cyclic loading conditions. *Biomaterials*, in press (2002).
- D. BERTHE and M. GODET. A more general form of Reynolds equation – application to rough surfaces. *Wear*, 27:345–357 (1973).
- BHARAT BHUSHAN. Analysis of the real area of contact between a polymeric magnetic medium and a rigid surface. *Journal of Tribology*, 106:26–34 (1984).
- BHARAT BHUSHAN. *Modern Tribology Handbook, vols. 1 and 2*. CRC Press, Boca Raton and London and New York and Washington D.C. (2001). ISBN 0-8493-8403-6.
- R. BYRON BIRD, WARREN E. STEWART, and EDWIN N. LIGHTFOOT. *Transport Phenomena*. John Wiley and Sons, Inc., New York, London, Sydney, 2nd edition (2002). ISBN 0-471-41077-2.
- S. BJÖRKLUND. The influence of surface roughness in elliptical contacts. *Tribology International*, 34:841–845 (2001).

-
- PETER J. BLAU. The significance and use of the friction coefficient. *Tribology International*, 34:585–591 (2001).
- H. BLOK. Inverse problems in hydrodynamic lubrication and design directives for lubricated flexible surfaces. In B. STERNLICHT, editor, *Proc. Int. Symp. on Lubrication and Wear*, pages 1–151. McCutchan Publ. Corp., Berkeley (1963).
- H. BLOK and H.J.M. MEYER. Squeeze retardation for prolonging the useful life of compliantly lined oscillating bearings. In DOWSON ET AL. (1982), pages 304–312.
- J.F. BOOKER. Basic equations for fluid films with variable properties. *Journal of Tribology*, 111:475–483 (1989).
- J. Bos. *Frictional Heating of Tribological Contacts*. Ph.D. thesis, University of Technology Twente (1995).
- F.P. BOWDEN and D. TABOR. *Friction and Lubrication of Solids*. Clarendon, Oxford, rev. edition (2001). ISBN 0-19-850777-1.
- M.J. BRAUN and J.D. DOUGHERTY. Hydrodynamic analysis and fluid-solid interaction effects on the behaviour of a compliant wall(thick) journal bearing. part 1: Theory. *Journal of Tribology*, 111:70–86 (1989).
- V. CAHOUE, L. BAILLET, M.H. MEURISSE, and B. BOU-SAÏD. Direct and indirect approaches at the plato-hydrodynamic lubrication problem. application to an industrial ironing process. *ASME Paper*, 98(Trib-27) (1998).
- V. CASTELLI, G.K. RIGHTMIRE, and D.D. FULLER. On the analytical and experimental investigation of a hydrostatic, axisymmetric compliant–surface thrust bearing. *Journal of Lubrication Technology*, pages 510–520 (1967).
- L. CHANG. An efficient and accurate formulation of the surface-deflection matrix in elasto–hydrodynamic point contacts. *Journal of Tribology*, 111:642–647 (1989).
- L. CHANG. A deterministic model for line–contact partial elasto–hydrodynamic lubrication. *Tribology International*, 28:75–84 (1995).
- L. CHANG and Y. GAO. Simple numerical method for contact analysis of rough surfaces. In *Proc. of the 1998 ASME/STLE Joint Tribology Conference* (1998).
- W.R. CHANG, I. ETSION, and D.B. BOGY. An elastic–plastic model for the contact of rough surfaces. *Journal of Tribology*, 109:257–263 (1987).
- P.Y.P. CHEN and E.J. HAHN. Use of computational fluid dynamics in hydrodynamic lubrication. *Proc. Instn. Mech. Engrs., Part J*, 212:427–436 (1998).
- H.S. CHENG. The lubrication of rough surfaces. In DOWSON ET AL. (1984), pages 11–20.
-

BIBLIOGRAPHY

- WU CHENGWEI and ZHENG LINQING. An average Reynolds equation for partial film lubrication with a contact factor. *Journal of Tribology*, 111:188–191 (1989).
- T.C. CHIVERS and L.A. MITCHELL. Voidage between rough surfaces: Correlation of measurements and theory. In *International Conference on Fluid Sealing 1971*, pages C2–17–28 (1971).
- H. CHRISTENSEN. Some aspects of the functional influence of surface roughness in lubrication. *Wear*, 17:149–162 (1971).
- H. CHRISTENSEN and K. TØNDER. The hydrodynamic lubrication of rough journal bearings. *Journal of Lubrication Technology*, 95:166–172 (1973).
- W.F. COPY. The hydrodynamic theory of film lubrication. *Proc. Roy. Soc. A*, 197:201–216 (1949).
- J.E. DENNIS and ROBERT B. SCHNABEL. *Numerical Methods for Unconstrained Optimization and Nonlinear Equations*. Prentice-Hall, Englewood Cliffs, New Jersey, 0-89871-364-1 edition (1996).
- D. DOWSON. A generalized Reynolds equation for fluid-film lubrication. *Int. J. Mech. Sci.*, 4:159–170 (1962).
- D. DOWSON. *History of tribology*. Longman, London and New York, 2nd edition (1998). ISBN 1-86058-070-X.
- D. DOWSON and Z. JIN. The influence of elastic deformation upon film thickness in lubricated bearings with low elastic modulus coatings. In DOWSON ET AL. (1989), pages 263–269.
- D. DOWSON and C.M. TAYLOR. Elastohydrostatic lubrication of circular plate thrust bearings. *Journal of Lubrication Technology*, pages 237–244 (1967).
- D. DOWSON, C.M. TAYLOR, and M. GODET, editors. *Proc. of the 16th Leeds–Lyon Symposium on Tribology: Mechanics of Coatings*. Lyon (1989).
- D. DOWSON, C.M. TAYLOR, M. GODET, and D. BERTHE, editors. *Proc. of the 4th Leeds–Lyon Symposium on Tribology: Surface Roughness Effects in Lubrication*. Lyon (1977).
- D. DOWSON, C.M. TAYLOR, M. GODET, and D. BERTHE, editors. *Proc. of the 9th Leeds–Lyon Symposium on Tribology: Tribology of Reciprocating Engines*. Leeds (1982).
- D. DOWSON, C.M. TAYLOR, M. GODET, and D. BERTHE, editors. *Proc. of the 11th Leeds–Lyon Symposium on Tribology: Mixed Lubrication and Lubricated Wear*. Leeds (1984).
- D. DOWSON, C.M. TAYLOR, M. GODET, and D. BERTHE, editors. *Proc. of the 13th Leeds–Lyon symposium on tribology: Fluid-film lubrication – Osborne Reynolds centenary*. Leeds (1986).

-
- D. DOWSON, C.M. TAYLOR, M. GODET, and D. BERTHE, editors. *Proc. of the 13th Leeds–Lyon symposium on tribology*. Lyon (1987).
- D. DOWSON, C.M. TAYLOR, M. GODET, and D. BERTHE, editors. *Proc. of the 20th Leeds–Lyon Symposium on Tribology: Thin Films in Tribology*. Lyon (1993).
- E. DRAGONI and A. STROZZI. Mechanical analysis of a flat, deformable layer underlain by a rigid foundation and indentation by a paraboloidal punch. In M.H. ALIABADI and C.A. BREBBIA, editors, *Contact Mechanics: Computational Techniques*. Computational Mechanics Publications, Southampton (1993).
- H.G. ELROD. A general theory for laminar lubrication with Reynolds roughness. *Journal of Lubrication Technology*, 101:8–14 (1979).
- ABDALLAH A. ELSHARKAWY and LOTFI H. GUEDOUAR. An inverse analysis for steady–state elastohydrodynamic lubrication of one–layered journal bearings. *Journal of Tribology*, 123:524–533 (2001).
- BERNARD FANTINO, JEAN FRENE, and MAURICE GODET. Reynolds equation in viscous film theory. *Journal of Lubrication Technology*, pages 287–288 (1972).
- PATRICK E. FOWLES. A simpler form of the general Reynolds equation. *Journal of Lubrication Technology*, pages 661–662 (1970).
- D.D. FULLER. Mixed friction in lubrication. *Lubrication Engineering*, 10:256–261 (1954).
- Y.C. FUNG. *A first course in Continuum Mechanics for Physical and Biological Engineers and Scientists*. Prentice Hall, Englewood Cliffs, New Jersey, 3rd edition (1994). ISBN 0-13-061524-2.
- R.F. GANS, A.G. JOHNSON, and S.B. MALANOSKI. Radial flow between axisymmetric nonparallel plates of small slope. *ASME Paper*, 87(Trib-38) (1987).
- EDWIN GELINCK. *Mixed Lubrication of Line Contacts*. Ph.D. thesis, Twente University (1999).
- E.R.M. GELINCK and D.J. SCHIPPER. Deformation of rough line contacts. In *Proc. of the 1998 ASME/STLE Joint Tribology Conference* (1998).
- E.R.M. GELINCK and D.J. SCHIPPER. Calculation of stribeck curves for line contacts. *Tribology International*, 33:175–181 (2000).
- A.N. GENT, R.L. HENRY, and M.L. ROXBURY. Interfacial stresses for bonded rubber blocks in compression and shear. *Journal of Applied Mechanics*, pages 855–859 (1974).
- A.N. GENT and P.B. LINDLEY. The compression of bonded rubber blocks. *Proc. Instn. Mech. Engrs.*, 173(3):111–117 (1959).
-

BIBLIOGRAPHY

- A.N. GENT and E.A. MEINECKE. Compression, bending and shear of bonded rubber blocks. *Polymer Engineering and Science*, 10:48–53 (1970).
- I.G. GORYACHEVA. *Contact Mechanics in Tribology*. Kluwer Academic, Dordrecht (1998). ISBN 0-7923-5257-2.
- J.A. GREENWOOD. The area of contact between rough surfaces and flats. *Journal of Lubrication Technology*, 89:81–91 (1967).
- J.A. GREENWOOD. Contact of rough surfaces. In I.L. SINGER and H.M. POLLOCK, editors, *Fundamentals of Friction: Macroscopic and Microscopic Processes*, pages 37–56. Kluwer, Dordrecht (1992).
- J.A. GREENWOOD. Transverse roughness in elastohydrodynamic lubrication. *Proc. Instn. Mech. Engrs., Part J*, 213:383–396 (1999).
- J.A. GREENWOOD and J.H. TRIPP. The contact of two nominally flat rough surfaces. *Proc. Instn. Mech. Engrs*, 165:625–633 (1971).
- J.A. GREENWOOD and J.B.P. WILLIAMSON. Contact of nominally flat surface. *Proc. Roy. Soc.*, A295:300–319 (1966).
- J.A. GREENWOOD and J.B.P. WILLIAMSON. Developments in the theory of surface roughness. In DOWSON ET AL. (1977).
- P.K. GUPTA. Incipient lift-off in preloaded plane externally-pressurized compliant surface bearings. *Proc. Instn. Mech. Engrs*, 188:447–455 (1974).
- M.M. HALL. Pressure distribution over the flat end surfaces of compressed solid-rubber cylinders. *Journal of Strain Analysis*, 6(1):38–44 (1971).
- BERNARD J. HAMROCK. *Fundamentals of Fluid Film Lubrication*. NASA. McGraw-Hill, New York (1994). ISBN 0-07-025956-9.
- C.E. HARDIE and C.M. MCC. ETTLES. The analysis of a self-acting flexible foil slider bearing. *ASME Paper*, 87(Trib-42) (1987).
- SUSAN R. HARP and RICHARD F. SALANT. An average flow model of rough surface lubrication with inter-asperity cavitation. *Journal of Tribology*, 123:134–143 (2001).
- SUSAN R. HARP and RICHARD F. SALANT. Inter-asperity cavitation and global cavitation in seals: An average flow analysis. *Tribology International*, 35:113–121 (2002).
- J. DE HART. *Fluid-structure Interaction in the Aortic Heart Valve: A Three-Dimensional Computational Analysis*. Ph.D. thesis, University of Technology Eindhoven (2002).
- KAZUHIRO HAYASHI and KEIJI HIRASATA. Theoretical investigation on the back-pressured elastohydrostatic thrust bearing. *J. of JSLE (Int. Ed.)*, 26(3) (1982).

-
- G.J.J. VAN HEIJNINGEN. *Verslag van de complete berekening van de Hydro-installatie voor de Nieuwe Oranjesluis te Amsterdam. Technical report, Sectie Werktuigonderdelen en Tribotechniek, TU Delft, Delft (1991). In dutch.*
- G.J.J. VAN HEIJNINGEN and C.G.M. KASSELS. Elastohydrodynamic lubrication of an oil pumping ring seal. In DOWSON ET AL. (1986).
- HOLLANDIA. *Metingen Bovenvlak Dremplaten pos. 1,2 en 3. Technical report, Machinefabriek Hollandia B.V. (1994). In dutch.*
- A.C.M. HONSELAAR. *Wrijvings eigenschappen Kunststoffen: Invloed Glijf snelheid en Vlaktedruk. Technical report, Instituut voor Productie en Logistiek TNO (1993). In dutch.*
- C.J. HOOKE. The behaviour of low-amplitude surface roughness under line contacts. *Proc. Instn. Mech. Engrs., Part J*, 213:275–286 (1999).
- C.J. HOOKE and C.H. VENNER. Surface roughness attenuation in line and point contacts. *Proc. Instn. Mech. Engrs., part J*, 214:439–444 (2000).
- YUKIO HORI, TAKAHISA KATO, and HIROMU NARUMIYA. Rubber surface squeeze film. *Journal of Lubrication Technology*, 103:398–403 (1981).
- HSING-SEN S. HSIAO. Optimum dimensional analysis with applications to elastohydrodynamic lubrication. *Journal of Tribology*, 123:822–827 (2001).
- YUAN-ZHONG HU, GARY C. BARBER, and DONG ZHU. Numerical analysis for the elastic contact of real rough surfaces. *Tribology Transactions*, 42(3):443–452 (1999).
- YUAN-ZHONG HU, HERBERT S. CHENG, TAKAYUKI ARAI, YOICHI KOBAYASHI, and SHUNICHI AOYAMA. Numerical simulation of piston ring in mixed lubrication - a nonaxisymmetrical analysis. *Journal of Tribology*, 116:470–478 (1994).
- YUAN-ZHONG HU, HUI WANG, WEN-ZHONG WANG, and DONG ZHU. A Computer Model of Mixed Lubrication in Point Contacts. *Tribology International*, 34:65–73 (2001).
- YUAN-ZHONG HU and DONG ZHU. A full numerical solution to the mixed lubrication in point contacts. *Journal of Tribology*, 122:1–9 (2000).
- T.J.R. HUGHES and T.E. TEZDUYAR. Finite elements based upon mindlin plate theory with particular reference to the four-node bilinear isoparametric element. *Journal of Applied Mechanics*, 48:587–596 (1981).
- K. IKEUCHI, S. FUJITA, and M. OHASHI. Analysis of fluid film formation between contacting compliant solids. *Tribology International*, 31(10):613–618 (1998).
- K. IKEUCHI and M. OKA. A model analysis of squeeze film effect in a hip joint. In DOWSON ET AL. (1993).

BIBLIOGRAPHY

- A. JEBBINK. *Verslag Metingen Rijkswaterstaat: materialen PTFE 25%C en UHMW-PE. Technical report, Rijkswaterstaat (1996). In dutch.*
- XIAOFEI JIANG, D.Y. HUA, H.S. CHENG, XIAOLAN AI, and Si C. LEE. A mixed elastohydrodynamic lubrication model with asperity contact. *ASME Paper*, 98(Trib-54) (1998).
- Z.M. JIN and D. DOWSON. A general analytical solution to the problem of microelastohydrodynamic lubrication of low elastic modulus compliant bearing surfaces under line contact conditions. *Proc. Instn. Mech. Engrs., Part C*, 211:265–272 (1997).
- K.L. JOHNSON. *Contact Mechanics*. Cambridge University Press (1985). ISBN 0-521-25576-7.
- K.L. JOHNSON, J.A. GREENWOOD, and S.Y. POON. A simple theory of asperity contact in elastohydrodynamic lubrication. *Wear*, 19:91–108 (1972).
- J.J. KALKER. Contact mechanical algorithms. *Comm. in Applied Numerical Methods*, 4:25–32 (1988).
- J.J. KALKER. *Three-Dimensional Elastic Bodies in Rolling Contact*. Kluwer Academic Publishers (1990). ISBN 0-7923-0712-7.
- J.J. KALKER, F.M. DEKKING, and E.A.H. VOLLEBREGT. *Simulation of Rough, Elastic Contacts. Technical Report Report 95-57, TU Delft (1995).*
- C.M. KALKER-KALKMAN. Optimal design with the aid of randomization methods. *Eng. with Computers*, 7:173–183 (1991).
- A.F.C. KANTERS. *On the Calculation of Leakage and Friction of Reciprocating Elastomeric Seals*. Ph.D. thesis, University of Technology Eindhoven (1990).
- YU A. KARPENKO and ADNAN AKAY. A numerical model of friction between rough surfaces. *Tribology International*, 34:531–545 (2001).
- TOSHIHARU KAZAMA and ATSUSHI YAMAGUCHI. Application of a mixed lubrication model for hydrostatic thrust bearings of hydraulic equipment. *Journal of Tribology*, 115:686–691 (1993).
- TOSHIHARU KAZAMA and ATSUSHI YAMAGUCHI. Experiment on mixed lubrication of hydrostatic thrust bearings for hydraulic equipment. *Journal of Tribology*, 117:399–402 (1995).
- C. KLAPPERICH, K. KOMVOPOULOS, and L. PRUITT. Tribological properties and microstructure evolution of ultra-high molecular weight polyethylene. *Journal of Tribology*, 121:394–402 (1999).

-
- P. KLOPPENBURG, E. LEIWAKABESSY, and M. LIGTVOET. *Prins Willem-Alexandersluis: Meting Hydrogeleiding Meting 6 op 970603. Technical report, Techno Fysica B.V., Barendrecht (1997). In dutch.*
- P. KLOPPENBURG, E. LEIWAKABESSY, and M. LIGTVOET. *Prins Willem-Alexandersluis: Meting Hydrogeleiding Meting 7 op 980616. Technical report, Techno Fysica bv., Barendrecht (1998). In dutch.*
- P. KLOPPENBURG, E. LEIWAKABESSY, and M. LIGTVOET. *Prins Willem-Alexandersluis: Meting Hydrogeleiding Meting 8 op 180499. Technical report, Techno Fysica b.v., Barendrecht (1999). In dutch.*
- G. KNOLL, A. RIENÄCKER, V. LAGEMANN, and R. LECHTAPE-GRÜTER. Effect of contact deformation on flow factors. *Journal of Tribology*, 120:140–144 (1998).
- K. KOMVOPOULOS and N. YE. Three-dimensional contact analysis of elastic-plastic layered media with fractal surface topographies. *Journal of Tribology*, 123:632–640 (2001).
- KORS KUNSTSTOFFEN. *Specificaties van Hakorit UHMWPE zwart regeneraat UV-stabiel. Technical report, Kors Kunststoffen (1998). In dutch.*
- G.A. LABOUFF and J.F. BOOKER. Dynamically loaded journal bearings: A finite element treatment for rigid and elastic surfaces. *Journal of Tribology*, 107:505–515 (1985).
- M. LAHMAR, A. HADDAD, and D. NICOLAS. Elastohydrodynamic analysis of one-layered journal bearings. *Proc. Instn. Mech. Engrs., Part J*, 212:193–205 (1998).
- H.R. LE and M.P.F. SUTCLIFFE. Rolling of thin strip and foil: Application of a tribological model for “mixed” lubrication. *Journal of Tribology*, 124:129–136 (2002).
- A.O. LEBECK. Mixed lubrication in mechanical face seals with plain faces. *Proc. Instn. Mech. Engrs., Part J*, 213:163–175 (1999).
- SI C. LEE and H.S. CHENG. On the relation of load to average gap in the contact between surfaces with longitudinal roughness. *Tribology Transactions*, 35(3):523–529 (1992).
- SI C. LEE and NING REN. Behaviour of elastic-plastic rough surface contacts as affected by surface topography, load, and material hardness. *Tribology Transactions*, 39(1):67–74 (1996).
- I. LEE-PRUDHOE, R.S. SAYLES, and A. KADERIC. Investigations into asperity persistence in heavily loaded contacts. In *Proc. of the 1998 ASME/STLE Joint Tribology Conference (1998).*
- M. LEUNG, C.K. HSIEH, and D.Y. GOSWAMI. Application of boltzmann statistical mechanics in the validation of the gaussian summit-height distribution in rough surfaces. *Journal of Tribology*, 119 (1997).
-

BIBLIOGRAPHY

- H.S. LIN, N. MARSAULT, and W.R.D. WILSON. A mixed lubrication model for cold strip rolling – part i: Theoretical. *Tribology Transactions*, 41(3):317–326 (1998).
- P.B. LINDLEY. A finite-element programme for the plane-strain analysis of rubber. *Journal of Strain Analysis*, 10(1):25–31 (1975).
- P.B. LINDLEY. Compression moduli for blocks of soft elastic material bonded to rigid end plates. *Journal of Strain Analysis for Engineering Design*, 14(1):11–16 (1979a).
- P.B. LINDLEY. Plane strain rotation moduli for soft elastic blocks. *Journal of Strain Analysis for Engineering Design*, 14(1):17–22 (1979b).
- YUN LING, PETER A. ENGEL, and WILLIAM L. BRODSKY. Compression of bonded annular rubber blocks. *Journal of Engineering Mechanics*, 121(6):661–666 (1995).
- GENG LIU, QIAN WANG, and CHIH LIN. A survey of contact models for simulating the contact between rough surfaces. *Tribology Transactions*, 42(3):581–591 (1999).
- RONG LIU and D.Y. LI. Modification of archard's equation by taking account of elastic/pseudoelastic properties of materials. *Wear*, 251:956–964 (2001).
- ZHIQIANG LIU, ANNE NEVILLE, and R.L. REUBEN. A numerical calculation of the contact area and pressure of real surfaces in sliding wear. *Journal of Tribology*, 123:27–35 (2001).
- SY-WEI LO. A study on flow phenomena in mixed lubrication regime by porous medium model. *Journal of Tribology*, 116:640–647 (1994).
- A.A. LUBRECHT. *The Numerical Solution of the Elastohydrodynamically Lubricated Line and Point Contact Problem using Multigrid Techniques*. Ph.D. thesis, University of Technology Twente (1987).
- A. MAJUMDAR and B. BHUSHAN. Role of fractal geometry in roughness characterization and contact mechanics of surfaces. *Journal of Tribology*, 112:205–216 (1990).
- A. MAJUMDAR and B. BHUSHAN. Fractal model of elastic–plastic contact between rough surfaces. *Journal of Tribology*, 113:1–11 (1991).
- J.I. MCCOOL. The distribution of microcontact area, load, pressure and flash temperature under the Greenwood–Williamson model. *Journal of Tribology*, 87(Trib-25) (1987).
- JOHN I. MCCOOL. Elastic behaviour of coated rough surfaces. In DOWSON ET AL. (1989), pages 157–165.
- JOHN I. MCCOOL. Extending the capability of the Greenwood–Williamson microcontact model. *Journal of Tribology*, 122:496–502 (2000).

-
- J.D.C. McIVOR and D.N. FENNER. Finite element analysis of dynamically loaded flexible journal bearings: A fast newton-raphson method. *Journal of Tribology*, 111:597–604 (1989).
- H.B. DAKSHINA MURTHY and M.R. RAGHAVAN. Compliance of rough cylinders in compression. *Wear*, 20:353–369 (1972).
- H.B. DAKSHINA MURTHY and M.R. RAGHAVAN. The real area of contact and compliance of rough cylinders in compression. *Wear*, 27:47–60 (1974).
- P. RANGANATH NAYAK. Random process model of rough surfaces. *Journal of Lubrication Technology*, pages 398–407 (1971).
- P.R. NAYAK. Random process model of rough surfaces in plastic contact. *Wear*, 26:305–333 (1973).
- P.W. O'CALLAGHAN and S.D. PROBERT. Real area of contact between a rough surface and a softer optically flat surface. *Journal of Mechanical Engineering Science*, 12(4):259–267 (1970).
- KONG PING OH. The numerical solution of dynamically loaded elasto-hydrodynamic contact as a nonlinear complementarity problem. *Journal of Tribology*, 106:88–95 (1984).
- KONG PING OH. The formulation of the mixed lubrication problem as a generalized nonlinear complementarity problem. *Journal of Tribology*, 108:598–604 (1986).
- R.A. ONIONS and J.F. ARCHARD. The contact of surfaces having a random structure. *J. Phys. D: Phys.*, 6:289–304 (1972).
- R.A.J. VAN OSTAYEN. *Het gebruik van de Thermische Netwerkmethode bij de Beschrijving van de Warmtehuishouding van Werktuigbouwkundige Constructies*. Master's thesis, University of Technology Eindhoven (1988). In dutch.
- F. OSTERLE and E. SAIBEL. The spring-supported thrust bearing. *ASME Paper*, 55(55-A-195) (1955).
- NADIR PATIR and H.S. CHENG. Application of average flow model to lubrication between rough sliding surfaces. *Journal of Lubrication Technology*, 78(Lub-78) (1978a).
- NADIR PATIR and H.S. CHENG. An average flow model for determining effects of three-dimensional roughness on partial hydrodynamic lubrication. *Journal of Lubrication Technology*, 100:12–17 (1978b).
- W. PENG and B. BHUSHAN. Modelling of surfaces with a bimodal roughness distribution. *Proc. Instn. Mech. Engrs., part J*, 214:459–470 (2000).
-

BIBLIOGRAPHY

- WEI PENG and BHARAT BHUSHAN. A numerical three-dimensional model for the contact of layered elastic/plastic solids with rough surfaces by a variational principle. *Journal of Tribology*, 123:330–342 (2001).
- WEI PENG and BHARAT BHUSHAN. Sliding contact analysis of layered elastic/plastic solids with rough surfaces. *Journal of Tribology*, 124:46–61 (2002).
- O. PINKUS. The Reynolds' centennial: a brief history of the theory of hydrodynamic lubrication. *J. of Tribology*, 109:2–20 (1987).
- I.A. POLONSKI and L.M. KEER. Fast methods for solving rough contact problems: A comparative study. *Journal of Tribology*, 123:36–41 (2000).
- ANDREAS A. POLYCARPOU and IZHAK ETSION. Analytical approximations in modeling contacting rough surfaces. *Journal of Tribology*, 121:234–239 (1999).
- J. PULLEN and J.B.P. WILLIAMSON. On the plastic contact of rough surfaces. *Proc. R. Soc. Lond. A.*, 327:159–173 (1972).
- V.S. RADCHIK, B. BEN-NISSAN, and W.H. MÜLLER. Semi-graphical methods for the calculation of real areas of loaded contact by means of the abbot–firestone bearing curve. *Journal of Tribology*, 124:223–226 (2002).
- LORD RAYLEIGH. *Theory of Sound*, chapter part II, section 345, pages 313–. MacMillan, London (1896).
- P. REINSHAGEN. Waterfilm van 0.1 millimeter draagt 25 ton staal. *Delft Integraal*, pages 7–9 (1991). In dutch.
- NING REN and SI C. LEE. Contact simulation of three-dimensional rough surfaces using moving grid method. *Journal of Tribology*, 115(4):597–601 (1993).
- NING REN and SI C. LEE. The effects of surface roughness and topography on the contact behavior of elastic bodies. *Journal of Tribology*, 116(4):804–811 (1994).
- OSBORNE REYNOLDS. On the theory of lubrication and its applications to mr. beauchamp tower's experiments, including an experimental determination of the viscosity of olive oil. *Phil. trans. Roy. Soc. A*, vol. 177, part I:157–234 (1886).
- FRANCOIS ROBBE-VALOIRE. Statistical Analysis of Asperities on a Rough Surface. *Wear*, 249:401–408 (2001).
- S.M. ROHDE, D. WHICKER, and A.L. BROWNE. On the solution of elastohybrid lubrication problems. *ASLE Transactions*, 21(3):264–270 (1978).
- D. Ros. *Drukproeven op UHMPE (Achteraanlagen van de Drielingluis te Maasbracht. Technical report, Bouwdienst Rijkswaterstaat (1984). In dutch.*

-
- D. Ros. Onderzoek glijdeur; einde van een wieltijdperk? *Bruggenspraak* (1987a). In dutch.
- D. Ros. *Onderzoeksinfo M870310: Berekening van de Temperatuurstijging in Schuifgeleidingen door Wrijvingswarmte. Technical report, Bouwdienst Rijkswaterstaat* (1987b). In dutch.
- D. Ros. Waterstaat staat op water; sluisdeuren glijden straks op flinterdunne waterfilm; deel 1. *Bouwdienst Magazine* (1993a). In dutch.
- D. Ros. Waterstaat staat op water; testresultaten hydrogeleiding; sluisdeuren kunnen jarenlang onderhoudsarm op water glijden; deel 2. *Bouwdienst Magazine* (1993b). In dutch.
- D. Ros. Hydrocontact: Effect van lokaal mechanisch contact op draagvermogen film. *Spurwerknieuws* (1996). In dutch.
- D. Ros. Experimentele verificatie onderzoeksinfo m870310 (1997). In dutch.
- E.F. RYBICKI, J.S. STRENKOWSKI, M.A. TAMM, and W.A. GLAESER. A finite element model for compliant bearing lubrication using a minimization algorithm. *Wear*, 47:279–292 (1978).
- P. SAHOO and S.K. ROY CHOWDHURY. A fractal analysis of adhesive friction between rough solids in gentle sliding. *Proc. Instn. Mech. Engrs., part J*, 214:583–595 (2000).
- T. SCHUT. *Beproeven van een laag Hydrofender met dikke glijzool. Technical Report DIV 165 (deel 1), IHC Holland* (1991a). In dutch.
- T. SCHUT. *Meting Kantelstijfheid Hydrostatisch Lager. Technical report, IHC Holland* (1991b). In dutch.
- A. SEGAL. *SEPRAN Standard Problems. Technical report, Ingenieursbureau SEPR, Leidschendam* (1993a).
- A. SEGAL. *SEPRAN Users Manual. Technical report, Ingenieursbureau SEPR, Leidschendam* (1993b).
- M.H. SHARIFF. An approximate analysis of infinitesimal deformations of bonded elastic mounts. *Journal of Strain Analysis*, 23(3):115–120 (1988).
- M.H.B.M. SHARIFF. An analysis of non-linear deformation of bonded rubber blocks. *Journal of Mechanical Engineering Science*, 203:113–119 (1989).
- SATISH C. SHARMA, RAM SINHASAN, and SATISH C. JAIN. An elastohydrostatic study of hole-entry hybrid flexible journal bearings with capillary restrictors. *Tribology International*, 26:93–107 (1993).
-

BIBLIOGRAPHY

- FANGHUI SHI and RICHARD F. SALANT. A mixed soft elastohydrodynamic lubrication model with interasperity cavitation and surface shear deformation. *Journal of Tribology*, 122:308–316 (2000).
- I.L. SINGER and H.M. POLLOCK. *Fundamentals of Friction: macroscopic and microscopic processes*. NATO ASI series. Series E. Applied sciences vol. 220. Kluwer, Dordrecht (1992). ISBN 0-7923-1912-5.
- R. SINHASAN, S.C. SHARMA, and S.C. JAIN. Performance characteristics of externally pressurized orifice compensated flexible journal bearing. *Tribology Transactions*, 34:465–471 (1991).
- G.W. STACHOWIAK and A.W. BATCHELOR. *Engineering Tribology*. Elsevier, 2nd. edition (2001). ISBN 0-7506-7304-4.
- J. STAM. *Metingen Bovenvlak Drempeelplaten, Westhoofd, Nieuwe Oranjesluis te Amsterdam. Technical report*, Machinefabriek Hollandia B.V., Krimpen a.d. IJssel (1994). In dutch.
- A. STROZZI. Analytical modelling of the elastomeric layer in soft layer hip replacements. *Proc. Instn. Mech. Engrs., part H*, 214:69–81 (2000).
- H.W. SWIFT. Theory and experiment applied to journal bearing design. In *IME Proceedings of the general discussion on lubrication and lubricants* (1937).
- T.E. TALLIAN. The theory of partial elastohydrodynamic contacts. *Wear*, 21:49–101 (1972).
- L. VAN DER TEMPEL, H. MOES, and R. BOSMA. Numerical simulation of dynamically loaded flexible short journal bearings. *Journal of Tribology*, 107:396–401 (1985a).
- L. VAN DER TEMPEL, H. MOES, and R. BOSMA. Starvation in dynamically loaded flexible short journal bearings. *Journal of Tribology*, 107:516–521 (1985b).
- TOM R. THOMAS. *Rough Surfaces*. Imperial College Press, 2nd edition (1999). ISBN 1-86094-100-1.
- S. TIMOSHENKO and J.N. GOODIER. *Theory of Elasticity*. McGraw-Hill, 3rd edition (1987). ISBN 0-07-085805-5.
- S. TIMOSHENKO and S. WOINOWSKY-KRIEGER. *Theory of Plates and shells*. McGraw-Hill Book Company, 2nd edition (1987). ISBN 0-07-064779-8.
- R.A.G. VAN TOL. Hydrostatische lagers nieuwe oranjesluis: Gedragen door water. *Land + Water*, pages 58–63 (1992). In dutch.
- K. TØNDER. DDC lubrication: A new concept in tribology. *Journal of Tribology*, 114:181–185 (1992).

-
- K. TØNDER and H. CHRISTENSEN. Waviness and roughness in hydrodynamic lubrication. *Proc. Instn. Mech. Engrs.*, 186(72):807–812 (1972).
- J.H. TRIPP. Surface roughness effects in hydrodynamic lubrication: The flow factor method. *ASME Paper*, 82(82-Lub-45) (1982).
- A.H. UPPAL and S.D. PROBERT. Mean separation and real contact area between surfaces pressed together under high static loads. *Wear*, 23:39–53 (1973).
- A.H. UPPAL, S.D. PROBERT, and T.R. THOMAS. The real area of contact between a rough and a flat surface. *Wear*, 22:163–183 (1972).
- M. VISSCHER. *The Measurement of the Film Thickness and the Roughness Deformation of Lubricated Contacts*. Ph.D. thesis, University of Technology Eindhoven (1992).
- T. VISSER. *Beproeven van holle Hydrofenders op ware grootte*. Technical Report DIV 158, IHC Holland (1989a). In dutch.
- T. VISSER. *Beproeven van Hydrofenders, schaal 1:3*. Technical Report DIV 159, IHC Holland (1989b). In dutch.
- QIAN WANG and HERBERT S. CHENG. A mixed lubrication model for journal bearings with a thin soft coating - part i: Contact and lubrication analysis. *Tribology Transactions*, 38(3):654–662 (1995).
- M.E. WEYLER and CHIH WU. A numerical method for the calculation of lubricant pressures in bearings with mixed lubrication. *Tribology International*, 15(4):89–95 (1982).
- D.J. WHITEHOUSE. Fractal or Fiction. *Wear*, 249:345–353 (2001).
- D.J. WHITEHOUSE and J.F. ARCHARD. The properties of random surfaces of significance in their contact. *Proc. R. Soc.*, A316:97–121 (1970).
- J.B.P. WILLIAMSON. Mechanical contact of heavily loaded surfaces. *Rev. Roum. Sci. Techn-Méc. Appl.*, 16:715–722 (1971).
- J.B.P. WILLIAMSON and R.T. HUNT. Asperity persistence and the real area of contact between rough surfaces. *Proc. R. Soc. Lond. A.*, 327:147–157 (1972).
- W.R.D. WILSON and N. MARSAULT. Partial hydrodynamic lubrication with large fractional contact areas. *Journal of Tribology*, 120:16–20 (1998).
- H.Y. WONG. *Handbook of Essential Formulae and Data on Heat Transfer for Engineers*. Longman, London (1977). ISBN 0-582-46050-6.

BIBLIOGRAPHY

- T.M. WRIGHT, K.L. GUNSALLUS, C.M. RIMNAC, D.L. BARTEL, and R.W. KLEIN. Design considerations from an acetabular component made from an enhanced form of ultra high molecular weight polyethylene. *Transactions of the 37th Orthopedic Research Society*, 248 (1991).
- JIUNN-JONG WU. The properties of asperities of real surfaces. *Journal of Tribology*, 123:872–883 (2001).
- ATSUSHI YAMAGUCHI and HIROSHI MATSUOKA. A mixed lubrication model applicable to bearing/seal parts of hydraulic equipment. *Journal of Tribology*, 114:116–121 (1992).
- W. YAN and K. KOMVOPOULOS. Contact analysis of elastic–plastic fractal surfaces. *J. of Appl. Physics*, 84:3617–3624 (1998).
- X. ZHAI and L. CHANG. An engineering approach to deterministic modeling of mixed-film contacts. *Tribology Transactions*, 41(3):327–334 (1998).
- YATAO ZHANG. Linear deformation of a journal bearing and its relationship to hydrodynamic pressure. *Wear*, 115:41–52 (1987).
- YONGWU ZHAO, DAVID M. MAIETTA, and L. CHANG. An asperity microcontact model incorporating the transition from elastic deformation to fully plastic flow. *Journal of Tribology*, 122:86–93 (2000).
- ZHI-HUA ZHONG. *Finite Element Procedures for Contact-Impact Problems*. Oxford University Press (1993). ISBN 0-19-856383-3.
- D. ZHU and H.S. CHENG. Effect of surface roughness on the point contact EHL. *Journal of Tribology*, 87(Trib-56) (1987).
- O.C. ZIENKIEWICZ and R.L. TAYLOR. *The Finite Element Method, Volume 1: The Basis*. Butterworth and Heinemann, 5th edition (2000a). ISBN 0-7506-5049-4.
- O.C. ZIENKIEWICZ and R.L. TAYLOR. *The Finite Element Method, Volume 2: Solid and Structural Mechanics*. Butterworth and Heinemann, 5th edition (2000b). ISBN 0-7506-5055-9.
- O.C. ZIENKIEWICZ and R.L. TAYLOR. *The Finite Element Method, Volume 3: Fluid Dynamics*. Butterworth and Heinemann, 5th edition (2000c). ISBN 0-7506-5050-8.

Acknowledgements

The research reported in this thesis has been carried out at the Laboratory of Tribology, Engineering Mechanics at the Faculty of Design, Engineering and Production of Delft University of Technology.

I wish to express my sincere gratitude to all my colleagues and former colleagues at the Laboratory of Tribology and Engineering Mechanics for their contributions to this work and for the pleasant atmosphere in which this research could be conducted. In particular, I wish to mention dr. ir. G.J.J. van Heijningen, who first brought me to Delft University of Technology and who introduced me into the research of Tribology and dr. ir. A. van Beek, who brought me back into this field of research after a brief intermission in Computer Aided Education.

I wish to thank the Dutch Ministry of Transport, Public Works and Water Management, Civil Engineering Division, for their financial support of this research. Furthermore, I would like to thank ing. D. Ros and ir. F. Rémercy of the Civil Engineering Division, and my co-promotor dr. ir. A. van Beek for our periodical, extensive and fruitful discussions on the pros and cons of the hydro-support.

I would like to thank my promotor prof. dr. ir. D.J. Rixen, who, although he was only involved in the final year, has brought a fresh perspective to this study and through several long discussions, has helped shape this thesis in its present form. I believe the result is much better because of it.

The algorithms in this thesis have been implemented in the SEPRAN finite element program of Ingenieursbureau SEPRRA. I wish to thank the author ir. A. Segal for his support in the implementation of these algorithms.

I wish to thank all the people who have read the draft version of this thesis, pointed out errors and suggested improvements. Besides my promotor and the other members of the PhD.-committee, I would like to mention my colleague and office room mate ing. A.J. Hoevenaar, my Civil Engineering Division contact ing. D. Ros and in particular my friend ir. A.B. Perduijn. Aside from his (extensive) advise on how to improve this

thesis, he has been of great value in keeping this research going forward. The telephone bill proves it.

Finally, I would like to thank my parents and family for their, mostly non-spoken, but ever present, encouragement and support.

Curriculum Vitae

- 10 juli 1963 Born in Roosendaal, the Netherlands
- 1981—1988 MSc study in Mechanical Engineering at Eindhoven University of Technology. Graduated at the Laboratory of Tribology and Machine Elements under the direction of Prof.dr.ir. M.J.W. Schouten. Title of MSc-thesis (in dutch): “Het Gebruik van de Thermische Netwerkmethode bij de Beschrijving van de Warmtehuishouding van Werktuigbouwkundige Constructies”, *The use of the Thermal Network Method in the Description of the Thermal Balance of Mechanical Designs*.
- 1989—1994 PhD study at the Laboratory of Tribology at Delft University of Technology, headed by Prof.ir. A.W.J. de Gee.
- 1991—1994 Research assistant at the Laboratory of Tribology at Delft University of Technology.
- 1995—1996 Computer Aided Education research assistant at the Department of Mechanical Engineering at Delft University of Technology.
- 1996—present Assistant Professor at Delft University of Technology, Laboratory of Engineering Mechanics, headed by Prof.dr.ir. L.J. Ernst.